



Multi-scale study of mechanical behaviour of two-phase materials during large deformation and ductile damage

Yuchen Zhao

► To cite this version:

Yuchen Zhao. Multi-scale study of mechanical behaviour of two-phase materials during large deformation and ductile damage. Materials and structures in mechanics [physics.class-ph]. Université de Technologie de Troyes, 2017. English. NNT : 2017TROY0018 . tel-02968552

HAL Id: tel-02968552

<https://theses.hal.science/tel-02968552>

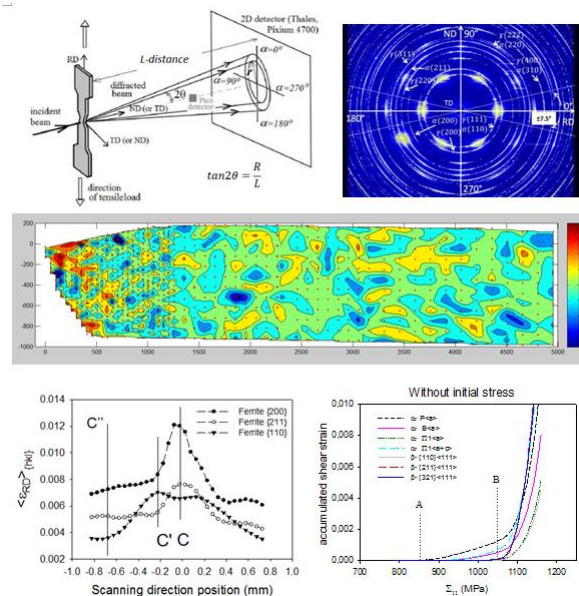
Submitted on 15 Oct 2020

HAL is a multi-disciplinary open access archive for the deposit and dissemination of scientific research documents, whether they are published or not. The documents may come from teaching and research institutions in France or abroad, or from public or private research centers.

L'archive ouverte pluridisciplinaire **HAL**, est destinée au dépôt et à la diffusion de documents scientifiques de niveau recherche, publiés ou non, émanant des établissements d'enseignement et de recherche français ou étrangers, des laboratoires publics ou privés.

Yuchen ZHAO

Multi-scale Study of Mechanical Behaviour of Two-phase Materials during Large Deformation and Ductile Damage



Spécialité :

Matériaux, Mécanique, Optique et Nanotechnologie

2017TROY0018

Année 2017

THESE

pour l'obtention du grade de

DOCTEUR de l'UNIVERSITE DE TECHNOLOGIE DE TROYES

Spécialité : MATERIAUX, MECANIQUE, OPTIQUE ET NANOTECHNOLOGIE

présentée et soutenue par

Yuchen ZHAO

le 17 juillet 2017

Multi-scale Study of Mechanical Behaviour of Two-phase Materials during Large Deformation and Ductile Damage

JURY

| | | |
|-------------------|-----------------------------|---------------------|
| M. A. LODINI | PROFESSEUR EMERITE | Président |
| M. A. BACZMANSKI | PROFESSOR | Directeur de thèse |
| Mme V. FAVIER | PROFESSEURE DES UNIVERSITES | Examineur |
| M. V. JI | PROFESSEUR DES UNIVERSITES | Rapporteur |
| Mme L. LE JONCOUR | MAITRE DE CONFERENCES | Directrice de thèse |
| Mme R. L. PENG | ASSOCIATE PROFESSOR | Examineur |

To my parents

To my dear Yuan

Acknowledgements

As the time flying away, four years of Ph.D. study have fledted soundlessly. These years are a brief moment for the life, but they are the most colourful days I have never experienced. Without your support and assistance, my doctoral dissertation would not have been possible to be accomplished.

My Ph.D. study has been undertaken mainly in the laboratory LASMIS of University of Technology of Troyes (UTT) and partially in the Faculty of Physics and Applied Computer Science of AGH University of Science and Technology.

Foremost, I would like to express my sincere gratitude to my supervisors, Ms. Léa LE JONCOUR and Prof. Andrzej BACZMAŃSKI, for their selfless and generous guidance throughout my study. They enlightened me the first gate of scientific research and taught me not only immense knowledge, which broadened my horizon, but also their personal qualities, such as patience, carefulness, motivation, optimism and enthusiasm, from which I will benefit for the whole life.

Authentic appreciation will also be expressed to Prof. Ru Lin PENG and Prof. Vincent JI, for their valuable comments and advices on my thesis, and to Prof. Véronique FAVIER and Prof. Alain LODINI for their attendance as juries in my Ph.D. defense committee. Their frank suggestions and encouragement greatly improved the scientific quality of this manuscript.

Many thanks go out to the support I received from my colleagues in both UTT and AGH, who gave me lots of help in experimental experiences, equipment usage, specimen preparation, data treatment, information technique and problem discussion. They are Prof. Manuel FRANÇOIS, Prof. Benoît PANICAUD, Mr. Bruno GUELORGET, Mr. Sebastian WRÓŃSKI, Mr. Laurent Daniel, Mr. Mirek WRÓBEL, Mrs. Marianna MARCISZKO, Mr. François WEIL, Prof. Xiaolu GONG and Mr. Zhidan SUN. I am also grateful to my fellow labmates, Mr. Zhaojun TAO, Mr. Jianqiang ZHOU, Mr. Mingchuan WANG, Ms. Elnaz ASADOLLAHIYAZDI, Mr. Donato GALLITELLI, Mr. Kai ZHANG, Mr. Yangcan WU, Mr. Yipeng HUANG, Mr. Feng TAN, Mr. kamil SOŁODUCHA and to my other friends, for their kind assistance and for all the fun we have shared in the last four years.

I would also like to thank Mr. Jan PILCH in the institution UJF in Czech Republic and Mr. Vincent KLOSEK in the laboratory LLB CEA Saclay, for their warm welcome and voluntary guidance during the sleepless nights we were working together.

Last but not the least, I would like to show my deepest love to my father, Prof. Wenming ZHAO, my mother Mrs. Zhengping JIA and, especially, to my dear Yuan. It is them who raised me up when I felt disappointed and encouraged me to carry on. Thank you for your unconditional love, which will always be the strongest support in my life.

Yuchen ZHAO

08th May 2017, in Troyes, France

Summary

| | |
|---|-----------|
| Glossary..... | 4 |
| Introduction | 5 |
| Chapter 1. Research background and material description | 10 |
| 1.1 Description of duplex steels | 12 |
| 1.1.1 Slip mode in duplex steels..... | 13 |
| 1.1.2 Ductile damage in duplex steels..... | 16 |
| 1.1.3 Research status..... | 17 |
| 1.1.3.1 Elasto-plastic deformation of duplex steel | 17 |
| 1.1.3.2 Ductile damage process duplex steel | 20 |
| 1.1.4 Characterisation of studied duplex steels | 22 |
| 1.2 Descriptions of two-phase titanium..... | 25 |
| 1.2.1 Elasto-plastic deformation in two-phase titanium..... | 26 |
| 1.2.2 Ductile damage in two-phase titanium..... | 31 |
| 1.2.3 Characterisation of experimental TIMETAL-18 alloy | 33 |
| 1.3 Conclusion | 37 |
| Chapter 2. Experimental measurements and techniques | 39 |
| 2.1 Measurement by diffraction method | 39 |
| 2.1.1 Physical principles..... | 39 |
| 2.1.2 Influences of microscopic phenomena on scattering patterns | 40 |
| 2.1.3 Tensile testes coupled with in situ diffraction measurements | 43 |
| 2.1.4 Determination of stress state by diffraction method..... | 44 |
| 2.1.4.1 Definition of reference systems..... | 44 |
| 2.1.4.2 Measurements of internal stress by X-ray diffraction | 45 |
| 2.1.4.3 Standard $\sin 2\psi$ method..... | 47 |
| 2.1.4.4 Multi-reflection grazing incidence method | 49 |
| 2.2 Instrumented Indentation Test (IIT) | 51 |
| 2.2.1 Principe of traditional indentation test..... | 51 |
| 2.2.1 Description of Berkovich indenter | 53 |
| 2.3 Electron Backscatter Diffraction (EBSD) | 53 |
| 2.3.1 Scanning Electron Microscope (SEM) | 54 |
| 2.3.2 Electron BackScatter Diffraction (EBSD) system | 55 |
| 2.3.3 SEM Transmission Kikuchi Diffraction (TKD) | 57 |
| 2.4 Methodologies used in the thesis | 58 |
| Chapter 3. Elasto-plastic behaviour modelling with ductile damage process..... | 59 |
| 3.1 Definition of Representative Volume Element (RVE)..... | 60 |
| 3.2 Definition of different scales | 60 |
| 3.3 Approach of scale transition | 61 |
| 3.4 Constitutive equations of multi-scale approach..... | 62 |
| 3.4.1 Localization from RVE to grains | 62 |
| 3.4.2 Modelling of local behaviour..... | 63 |
| 3.4.2.1 Modelling on grains scale | 64 |

| | |
|--|------------|
| 3.4.2.2 Scale transition from grains to slip systems | 64 |
| 3.4.2.3 Modelling at slip systems scale | 65 |
| 3.4.3 Homogenization from lattice to RVE | 65 |
| 3.4.3.1 Homogenization from slip systems to grains scale | 66 |
| 3.4.3.2 Homogenization from grains to RVE scale..... | 67 |
| 3.4.4 Synthesis of elasto-plastic self-consistent model | 68 |
| 3.5 Modelling of nonlinear work hardening and ductile damage | 70 |
| 3.5.1 Damage modelling at grains scale | 70 |
| 3.5.2 Damage modelling at slip systems scale | 72 |
| 3.5.2.1 Modelling of linear hardening | 72 |
| 3.5.2.2 Modelling of nonlinear hardening | 72 |
| 3.5.2.3 Equivalent strain criterion for micro-damage process | 74 |
| 3.5.3 Approach of localization with damage effect | 75 |
| 3.6 Conclusion | 77 |
| Chapter 4. Diffraction study of duplex steel compared with model predictions... 78 | |
| 4.1 Experimental set-up and data treatment..... | 79 |
| 4.2 Initial measurement without external load | 80 |
| 4.3 Strains evolution in the loaded samples during tensile tests..... | 84 |
| 4.4 Analysis for elasto-plastic deformation with model predictions | 88 |
| 4.4.1 Analysis of neutron diffraction data | 88 |
| 4.4.2 Comparison between neutron and synchrotron diffraction data | 92 |
| 4.5 Time depending damage analysis and damage criteria | 93 |
| 4.5.1 Test of equivalent strain criterion for damage | 94 |
| 4.5.2 Tests of equivalent stress criterion for damage..... | 98 |
| 4.5.3 Tests of the total energy criterion for damage | 101 |
| 4.5.4 Conclusion concerning damage criteria | 103 |
| 4.6 Space depending analysis and necking behaviour study | 104 |
| 4.6.1 Experimental data treatment | 107 |
| 4.6.2 Analysis during tensile tests | 108 |
| 4.6.2.1 Analysis on “Sample TD” | 109 |
| 4.6.2.2 Analysis on “Sample ND” | 111 |
| 4.6.3 Analysis of spatial scanning results in the necking area | 112 |
| 4.6.4 Finite Element Method (FEM) simulation | 115 |
| 4.8 Conclusions..... | 119 |
| Chapter 5. Studies of mechanical properties using Instrumented Indentation Test | 121 |
| 5.1 Instrumented Indentation Test on initial specimens | 121 |
| 5.2 Instrumented Indentation Test on fractured specimen | 124 |
| 5.2.1 Evolution of mean hardness and mean Young’s modulus along specimen | 126 |
| 5.2.1.1 Hardness evolution..... | 129 |
| 5.2.1.2 Young’s modulus evolution | 132 |
| 5.2.2 Evolution of hardness vs. Young’s modulus | 133 |
| 5.3 Conclusion | 135 |

| | |
|--|------------|
| Chapter 6. Studies on α-β titanium alloy Ti-18 | 137 |
| 6.1 Tensile test coupled with X-ray diffraction measurements | 137 |
| 6.1.1 Experimental methodology | 137 |
| 6.1.1.1 Determination of elastic lattice strains in transverse direction | 139 |
| 6.1.1.2 Determination of phase stress in loading direction | 139 |
| 6.1.2 Determination of initial stress | 140 |
| 6.1.3 Evolution of stresses in each phase during the tensile test | 141 |
| 6.1.4 Evolution of lattice strain in each phase during the tensile test | 143 |
| 6.2 Confrontation of model prediction with experimental results | 143 |
| 6.2.1 CRSS determined for slip systems | 144 |
| 6.2.2 Evolution of phase strains in transverse direction | 145 |
| 6.2.3 Order of slip activation | 147 |
| 6.2.4 Accumulation of shear strains | 147 |
| 6.2.4.1 Without initial stress | 148 |
| 6.2.4.2 Without initial stress | 149 |
| 6.2.5 Evolution of phase stresses in loading direction | 149 |
| 6.2.6 Evolution of macro-stress in loading direction | 151 |
| 6.3 TKD measurement for Ti-18 microstructure | 153 |
| 6.4 Conclusions | 155 |
| General conclusion | 157 |
| Perspectives | 160 |
| Résumé de la thèse en français | 162 |
| Appendix | 194 |
| References | 243 |

Glossary

CRSS: Critical Resolved Shear Stress

EBSD: Electron BackScatter Diffraction

EPSC : Elasto-Plastic Self-Consistent

FEM: Finite Element Method

IIT : Instrumented Indentation Test

IQ: Image Quality

MGIXD : Multi-reflection Grazing Incidence X-ray Diffraction

ODF: Orientation Distribution Function

RVE: Representative Volume Element

SEM : Scanning Electron Microscope

TKD: Transmission Kikuchi Diffraction

XEC: X-ray Elastic Constants

XSf: X-ray Stress Factors

BCC: Body Centred Cubic

FCC: Face Centred Cubic

HCP: Hexagonal Close Pcking

RD: Rolling direction

TD: Transverse direction

ND: Normal direction

Introduction

Metallic materials, alloys and metal composites are nowadays ones of the most largely used materials. Because of the excellent mechanical properties and the good workability, metallic materials have been applied from underwater operations to the aeronautic and space research. In this case, the quantification of mechanical behaviours of these materials and the understanding of intrinsic properties behind their macroscopic performances are strongly highlighted. On nowadays background of global environmental protection, energy saving and emission reduction, the structure optimization is one of the main topics for industrial design, which urgently requires the characterisation of metallic materials. Besides, despite their outstanding characters, the failure of machine parts caused by large deformation or damage in the metallic materials lead frequently to fatal accidents. In this context, the present thesis is accomplished in the aim of better understanding the mechanical behaviour in metallic materials exhibiting different crystal structures during large deformation, and the intrinsic mechanism of ductile damage process.

Numerous studies have been previously carried out concerning the above mentioned topics [Greenfield 72, Helbert 96, Verhaeghe 97, Helbert 98, Seshacharyulu 00, Filip 03, Krupp 04, Alvarez-Armas 07, Kumar 09, Wang 10, Alvarez-Armas 11, Le Joncour 11, Baczanski 16], however, several issues still remain unsettled. The macroscopic mechanical response of materials is not only determined by the applied external load, but also depends on their internal mechanical state and their microstructures. The polycrystalline materials are constituted by crystal lattice, grains and phases at different scales. This complex constitution and the influence of forming procedures lead to intrinsic heterogeneities of metallic materials, such as crystallographic texture, residual stress and inter-grains or inter-phases incompatibilities. These microscopic heterogeneities and the mechanical behaviours at lattice scale greatly influence the global mechanical behaviour of metallic materials at macroscopic scale.

To the end of investigating intrinsic properties at lattice level and the interaction between grains and phases, multi-scale approach is applied in this work. The multi-scale approach allows localizing macroscopic behaviours of polycrystal materials to grain scale then to lattice scale. During the scale localization, the mechanical behaviours at mesoscopic (grain) and microscopic (lattice) scales could be investigated. In turn, the microscopic mechanical

properties could be used to feedback the mechanical behaviours at mesoscopic scale then to determine the macroscopic performance of materials.

In this work, two typical materials, duplex steels and two-phase titanium, largely applied in the industry field, are taken as the study objects.

The duplex steels are consisted of **austenite** (γ phase) and **ferrite** (α phase) in approximate equal portion. With different **cubic** lattice structures, the duplex steels allow us to study the mechanical properties of cubic lattices, as well as the interaction between them. **α - β titanium** alloy, exhibiting **hexagonal** α phase and **cubic** β phase, is studied in this thesis. This two-phase composition provides us an opportunity to look into the interaction between cubic and hexagonal lattice as well as to characterize the mechanical properties of hexagonal lattice.

Besides the observation of microscopic mechanical behaviour during large deformation, studies of initiation of ductile damage are also an important part of this thesis. Currently, most research work about the ductile damage is based on the ex situ measurement or observation, which makes it difficult to interpret the experimental results. The study of post-fracture samples, for instance the microscopic observation or EBSD (Electron Backscatter Diffraction) analysis on fracture surface or on the cut section along necking, allow obtaining a direct observation on the fracture, but they are limited to static results thus short of information about the dynamic evolution of ductile damage process.

The **diffraction** measurement is considered as an appropriate experimental method to study behaviour of polycrystalline materials at mesoscale, thanks to its selectivity and the possibility of non-destructive measurement. Diffraction-based techniques are powerful tools to study the stress states and the mechanical behaviour of polycrystalline solids at both microscopic and mesoscopic (grains) scales [Baczmanski 99, Gloaguen 02, Baczmanski 04a, Gloaguen 04, Fréour 05, Dakhlaoui 07, Wroński 07, Le Joncour 10, Baczmanski 11, Gloaguen 13]. The selectivity provided by diffraction method allows measuring separately the mechanical properties of each phase in multiphase polycrystalline materials during small deformation stage.

The diffraction techniques in this present work mainly involve the **neutron** and **X-ray** diffraction methods. Due to the low absorption of neutron radiation in certain studied materials, the internal volume of samples can be studied. As well, **high-energy X-ray synchrotron** diffraction are also available for the analysis of internal mechanical properties in

polycrystalline specimen. In addition, the X-ray synchrotron sources provide fine collimation and strong intensity, which make possible high-spatial-resolution measurements.

Besides, the ability of non-destructive measurement enables in situ measurement during the large deformation process. Combining with stress correction method proposed by [Le Joncour 10], the real stress applied along the necking of experimental sample can be determined after appearance of necking phenomenon. Using this method, the mechanical behaviour of aimed material can be followed during the whole tensile test.

In terms of quantification studies, digital simulations based on the self-consistent algorithm are compared to the experimental results. The experimental results obtained from diffraction measurements are compared and fitted by the self-consistent model in order to determine essential parameters related to the elastic and plastic deformation in different phases of materials. A newly developed self-consistent model, which additionally includes the modelling of ductile damage process, is applied to analysis non-linearity work hardening and the initiation of ductile damage.

The aim of present works is to improve our current knowledge on the mechanical behaviour of different metallic materials, moreover to quantify the microscopic strain evolution of different lattices during external mechanical solicitation. This manuscript gathers our studies and thought on the following issues: the evolution of mechanical behaviours in polycrystalline materials, the interaction between grains and phases under external load, the activation of plastic deformation and the initiation of ductile damage, the quantification of material properties by comparing experimental data with digital predations. All of these concerned points will be presented and discussed in four main parts. The main objectives of this work are following:

- **Determination of critical resolved shear stresses and work hardening parameters of slip systems for duplex steel and two-phase Ti-alloy.** To do this, elastic strain of grains aggregate belonging to both phases in two-phase titanium and duplex steel will be studied by diffraction method. Then the experimental results will be compared with self-consistent model.
- **Verification of criterion for damage initiation using ductile damage model integrated in the self-consistent algorithm.** In this aim, the neutron diffraction measurements within

the deformation neck in duplex steel will be compared with model prediction. Different criteria will be used in simulations.

- **Confirmation of previous results on duplex steel obtained by in situ diffraction measurement and further investigation on spatial stress relaxation (damage initiation) during large deformation stage.** The mechanical behaviours of each phase in duplex steel have been studied by Le Joncour et al. [Le Joncour 11]. These results will be confirmed in this thesis using different experimental methods. Then, the heterogeneity of lattice strains along the necking area will be analysed.
- **Observation of hardness evolution and Young's modulus heterogeneity within the necking.** The nano-indentation measurements will be done on the surface of the neck, after fracture of sample made of duplex steel.

In this thesis, the chapter 1 presents bibliographic synthesis about the state of the art on the related studied field. The chapter 1 summarises the background of research work on duplex steels and two-phase titanium alloys. The activation modes of plastic deformation in cubic and hexagonal lattices are also presented. As well, the assumptions proposed by previous literatures about initiation of damage process in both materials are also discussed.

The chapter 2 focuses on the description of techniques employed in the experimental works. The principle of diffraction measurements, the method of stress determination by diffraction, and the **Instrumented Indentation Test (IIT)** are described successively in this chapter.

The chapter 3 presents the modelling of elasto-plastic behaviour of polycrystalline materials based on **multi-scale self-consistent model**. The Eshelby-Kröner grains interaction model is applied in this algorithm. The anisotropy of materials at different scales, such as crystallographic constants of lattices, the grains orientations and the stiffness tensor of different phases, is taken into account. Moreover, a recently developed modelling for ductile damage initiation will be introduced in this chapter, which allows extending the original self-consistent model to the scope of ductile damage process in multi-phase materials.

The chapter 4 is dedicated to the presentation of in-situ diffraction measurements coupled with tensile tests on duplex steels. Then, the experiment results will be analysed by predictions of multi-scale self-consistent models, several essential parameters are determined for the elasto-plastic behaviour of duplex steels, as well as for the **initiation of ductile**

damage in ferritic phase. Studies of stress and strain partitioning between phases in duplex steel during the necking process are described. High resolution in situ synchrotron measurement is applied to perform scans along the neck.

In chapter 5, an original Instrumented Indentation Test (IIT) have been done on duplex steel after the sample fracture, in order to investigate the evolution of microstructure and mechanical properties from the little deformed part of sample until its fracture surface. In comparison with diffraction measurements data, some interesting relationships between phases' mechanical behaviours and the evolution of hardness and Young's modulus are found.

Chapter 6 presents studies on the evolution of stress and strain in each phase of titanium during tensile test using in-situ X-ray diffraction. Fitting of experimental results with model prediction is also performed using elasto-plastic self-consistent model in order to find appropriate values for parameters associated with the **activation of slip systems** in different phases of titanium.

Finally, a general conclusion and perspectives of the presented studies will complete this manuscript.

Chapter 1. Research background and material description

The subject of this thesis focuses on the mechanical behaviour of polycrystalline materials during the plastic deformation as well as the ductile damage processes. This present research concentrates on two-phase materials. Two types of metallic material frequently used in the industry were investigated. They are respectively the duplex stainless steel and the two-phase titanium alloy.

Stainless steels are highly alloyed iron, primarily the carbon. Its mechanical and chemical properties, which depend on the level of different alloying elements, can be strongly varied according to different requirements. Due to its good formability, moderate elaborating cost, and reliable performance, the steel is one of the most widely used materials in the industrial field and in our daily lives. The steels studied in this work are the duplex steels, which are composed of the ferritic phase and the austenitic phase with approximately equal proportions (50%-50%).

Titanium and its alloys are the engineering materials exhibiting excellent properties such as high mechanical strength and excellent corrosion resistance at high temperatures, while they have only half the density of steel. These principal properties make titanium an attractive metal for a wide variety of applications, especially in the aeronautic and aerospace industrial fields. A two-phase titanium alloy is also studied in this work.

The choice of these two above mentioned materials is firstly based on their vast applications in nowadays world. The second reason is their typical crystalline structures, for which the mechanisms of plastic deformation and damage process will be studied:

- In duplex steels, both austenite and ferrite exhibit a cubic crystalline structure. More precisely, the ferrite (α phase) has a **body centred cubic lattice (bcc)** (see Fig. 1.1a) while the austenite (γ phase) has a **face centred cubic (fcc)** unit cell (see Fig. 1.1b). The structure of both phases allows us to figure out the mechanical behaviour of cubic crystals within polycrystalline material under applied load. We can also see the relative difference in mechanical behaviours between two cubic lattices, i.e. bcc and fcc.

- The two-phase titanium alloy studied in this work consists of the α phase having hexagonal lattice (Fig. 1.1c) and the β phase which exhibits a bcc lattice structure. By studying the two-phase titanium alloy, we can observe the variation of mechanical behaviour between the cubic and the hexagonal crystallites under applied external load.

Thorough studies about the mechanism of plastic deformation and the damage process bring a contribution to our current knowledge on steel and titanium, as well as on the activation of slip system in cubic and hexagonal lattice. This knowledge can be used to refine manufacturing methods and improve mechanical performance of the materials, and consequently to expand their practical applications. These two materials are presented briefly in the following sections.

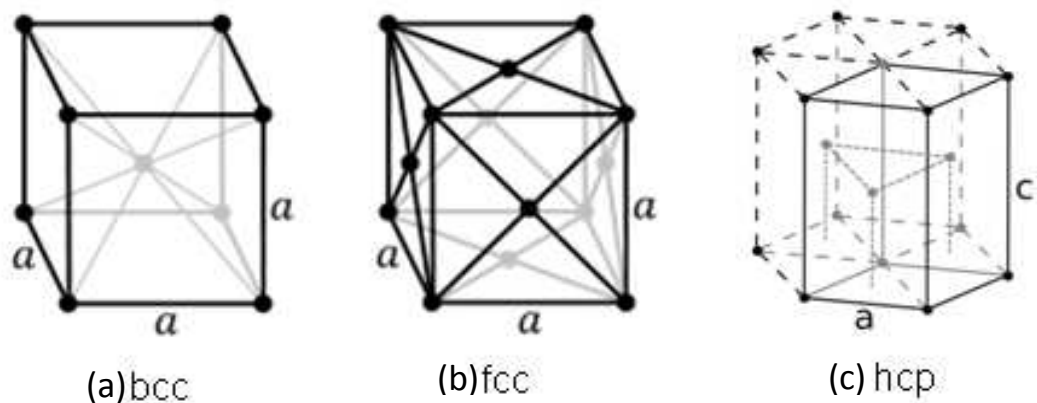


Figure 1.1 Crystal lattice structures: (a) Body centred cubic (bcc); (b) Face centred cubic (fcc); (c) Hexagonal close-packed (hcp). The parameters **a** and **c** indicate lattice parameters of each structure (www.wikipedia.org).

In this chapter, the state of art concerning elasto-plastic deformation and damage process in duplex steels and titanium will be presented. The basic information on the research field of plastic deformation and ductile damage inside the studied materials (duplex steels and two-phase titanium) will be collected from literature and analysed. Especially, the mechanism of elasto-plastic deformation for different phases of steel and titanium is described. The slip systems in different crystal structures and the mechanism of slip system activation have been deeply discussed. The previous results concerning initiation of ductile damage in duplex steel are also presented. However, a further investigation should be processed to identify the processes responsible for damage process occurring in two phase materials.

1.1 Description of duplex steels

In this thesis we were interested in the austeno-ferritic steels, which are named duplex steel, when the phase proportion between austenite and ferrite is close to 50% - 50%. The duplex austenitic-ferritic stainless steel was discovered in the 1920s by J. Hochmann as a result of an error during intergranular corrosion test [Desestret 90]. The Fig. 1.2 shows typical microstructures of duplex steels [DeBold 89]. We can see the austenitic phase in the shape of “islands”, embedded in the ferritic matrix. Once the stainless steel solidifies from melted state it transforms at first to a completely ferritic phase, then during cooling to room temperature, about half of the ferritic grains transforms to austenitic grains, forming a austeno-ferritic microstructure about 50% to 50% in volume fraction.

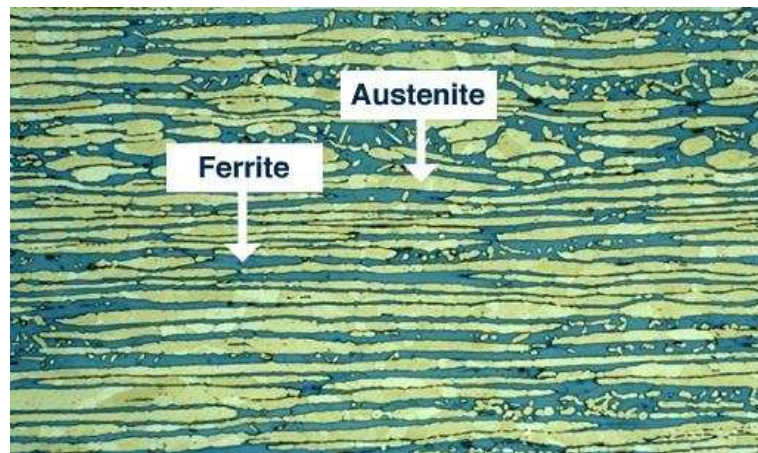


Figure 1.2 Microscopic image of duplex steel [DeBold 89].

In the table 1.1 the representative mechanical properties of ferritic, austenitic and duplex steels are summarized [El Bartali 07].

| Stainless steel | Yield strength (MPa) | Tensile strength Rm (MPa) | Elongation at break A (%) | Young's modulus E (GPa) | Hardness Hv (HB) |
|----------------------------|----------------------|---------------------------|---------------------------|-------------------------|------------------|
| Ferritic | 250-400 | 300-600 | 18-25 | 220 | 190-220 |
| Austenitic | 200-250 | 570-900 | 50-60 | 200 | 210 |
| Duplex Austenitic-ferritic | 450-650 | 730-900 | 25-30 | 200 | 260-290 |

Table 1.1 Mechanical characterisations of different stainless steels [El Bartali 07].

Generally, the ferritic steels have greater yield strength than the austenitic steels, but the ferritic steels are more brittle at low temperature [Lacombe 90, Davis 94]. On the other hand, the austenitic steels show an excellent corrosion resistance as well as a much higher ductility [Lacombe 90, Davis 94]. In duplex steels, ferrite enhances the yield strength level meanwhile the content of austenite improves their ductile behaviour. Therefore austenitic-ferritic duplex steels combine good properties of both ferritic and austenitic phases.

Duplex stainless steels are often applied under corrosive and aggressive working conditions, as in the chemical or oil industry, where the mechanical parts are exposed to a corrosive environment or undergo cyclic loadings. The forged and hot-rolled duplex steel have been studied and presented in several works [Aubin 01, EL Bartali 07, Evrard 08, Le Joncour 11]. A number of studies on a casted duplex stainless steel used in the cooling system of a nuclear power plant have also been published [Bugat 00, M'Cirdi 01]. In the cooling system, these steels are subjected to a slow thermal aging at the working temperature of 320°C, which causes an embrittlement of the ferritic phase ferrite [Bonnet 90, Pumphrey 90]. It is well known that, at temperature lower than 475°C, the spinodal decomposition of ferrite occurs [Lacombe 90, Mateo 97, Park 02]. The transformation of ferrite is essentially caused by the spinodal decomposition leading to the formation of α phase (Cr-poor) and α' phase (Cr-rich) in ferrite, as well as by the nucleation and the growing precipitation of an intermetallic phase rich in nickel, silicon and molybdenum. The rich in chromium α' phase exhibits the same body centre cubic lattice structure as α phase (Fig. 1.1a) [Terada 08]. The presence of α' phase results in the loss of several properties, such as ductility, toughness and corrosion resistance. The detail description of the embrittlement and hardening mechanism occurring during aging of the duplex steel is presented in Appendix 2.

1.1.1 Slip modes in duplex steel

One of the main objectives of this thesis is to study and deepen our knowledge of the plastic deformation occurring in polycrystalline materials. The plastic deformation of crystal materials mainly consists of slipping and twinning. In this thesis, we focus especially on the activation of slip systems and the interaction between slip systems in different phases. The slip mode in different crystal structures during plastic deformation is described in this section.

Several main structure parameters for crystal lattice of ferritic and austenitic phase are presented in table 1.2. The fcc structure of austenite allows the dislocations sliding along 4 planes of $\{111\}$ family, in each of these planes there are 3 possible slip directions $\langle 011 \rangle$ (slip systems $\{111\}\langle 011 \rangle$ as shown in Fig 1.3a). In the bcc structure of ferritic phase, the dislocations slide along 3 different plane families, i.e. $\{011\}$, $\{112\}$, $\{123\}$ and for all the 2 families of slip planes, their slip directions belong to the direction family $\langle 111 \rangle$ (slip systems $\{011\}\langle 111 \rangle$, $\{112\}\langle 111 \rangle$ and $\{123\}\langle 111 \rangle$ as in Fig. 1.3b). Finally for each austenitic grain 12 slip system of $\{111\}\langle 011 \rangle$ and for each ferritic grain 48 slip systems belonging to $\{011\}\langle 111 \rangle$ and $\{112\}\langle 111 \rangle$ can be selected [Schmid 50].

| Phase | Ferrite | Austenite |
|---|-----------------------------------|-----------------------|
| Structure | bcc | fcc |
| Lattice parameter (ambient temperature $\approx 20^\circ\text{C}$) | 2.8664 Å | 3.5770 Å |
| Number of atoms per unit cell | 2 | 4 |
| Packing density | 68% | 74% |
| Slip planes | $\{011\}$, $\{112\}$, $\{123\}$ | $\{111\}$ |
| Slip directions | $\langle 111 \rangle$ | $\langle 011 \rangle$ |
| Atom density on slip plane | $\approx 83\%$ | $\approx 91\%$ |

Table 1.2 Summary of Main parameters of crystal lattice and slip systems for ferrite and austenite [Schmid 50, Person 67, El Bartali 07, Van 14].

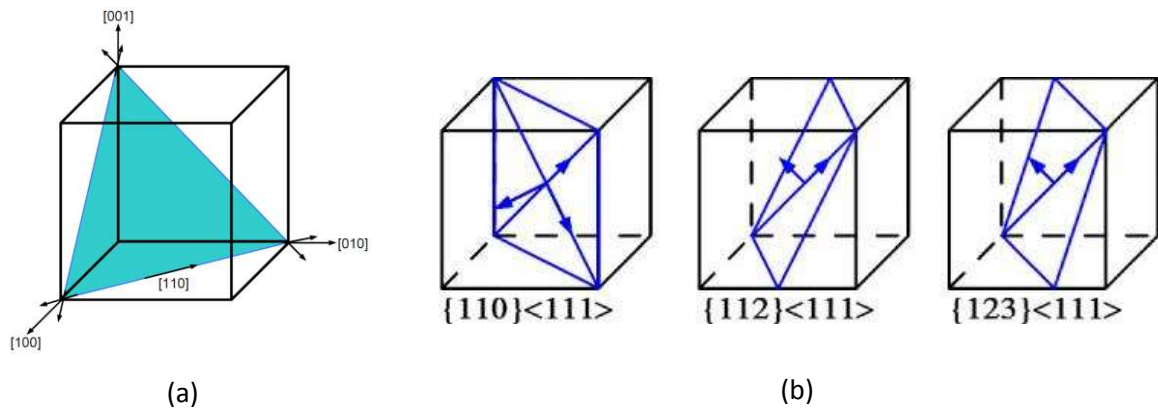


Figure 1.3 Slip systems in fcc lattice (a) and in bcc lattice (b) [El Bartali 07, Van 14].

The mechanism of plastic deformation in the ferritic and austenitic phases has been studied in a number of works [Duval 92, Joly 92, Kruml 97, Bugat 00, Fréchar 06, El Bartali 07, El Bartali 08, Di Gioacchino 15]. The plastic deformation spreads more homogeneously in

austenite and a great number of slip lines can be observed over a large area (Fig 1.4) [Joly 92]. Meanwhile, the plastic deformation mode is relatively localized for ferrite, i.e. less slip lines concentrating in a smaller area can be found (cf. Fig. 1.5a) [Joly 92]. In Fig. 1.5b we can see continuous slip lines over several grains, crossing the phase boundaries and leading to a homogeneous deformation in both phases.

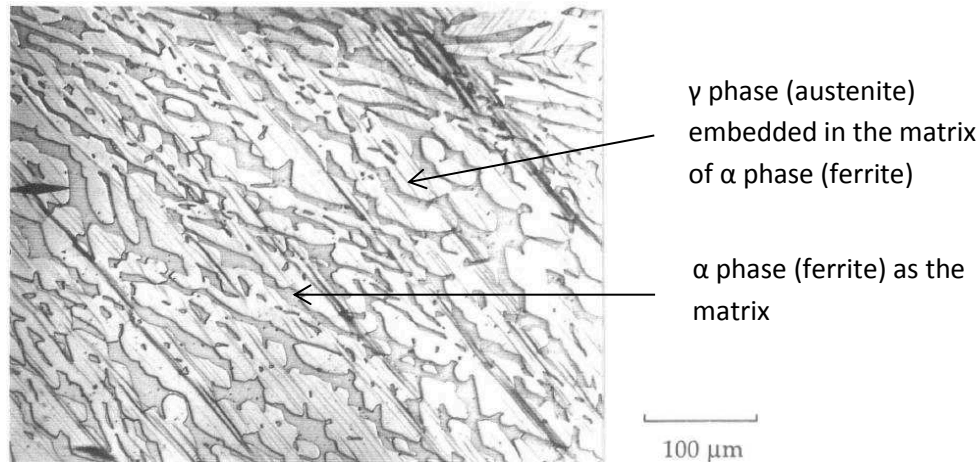


Figure 1.4 Optical micrograph on surface of a duplex alloy (Y4331) sample under tensile load at 20°C. Slip lines can be observed in austenite (γ phase) [Joly 92].

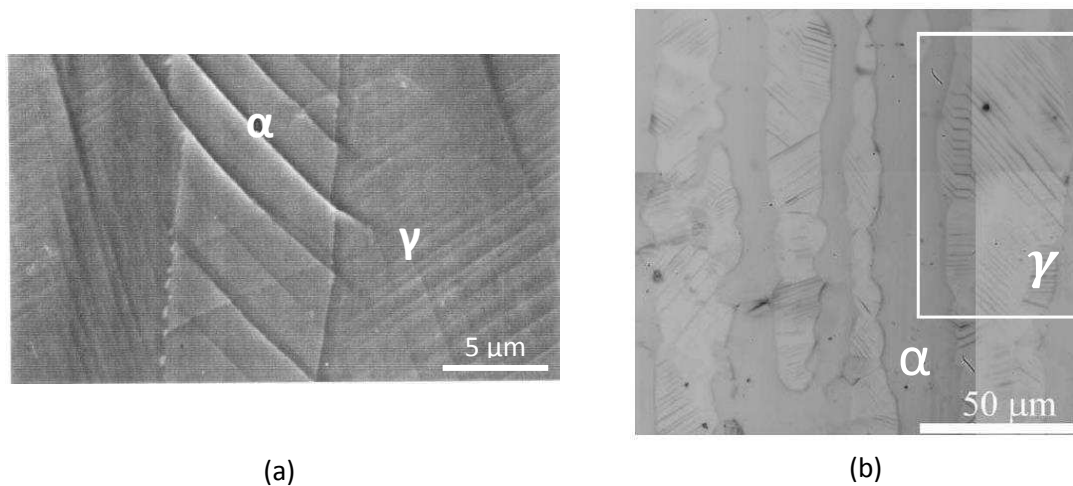


Figure 1.5 (a) Surface of a duplex alloy (Y4331) sample under tensile load at 20°C studied by SEM method. Continuous slip lines between ferrite (α phase) and austenite (γ phase) [Joly 92]. (b) Slip lines occurring in austenite (γ phase) and in the vicinity of grain boundaries (white frame) [El Bartali 07].

Using Scanning Electron Microscope (SEM) method for the sample surface during a fatigue test, it was observed that the slip systems in austenite were activated long before those in ferrite (Fig. 1.5a) [El Bartali 07]. This very early emergence of slip lines in austenite is considered as being coherent with the lower yield strength of this phase, compared with that

of ferrite. It is also seen that the slip systems having high Schmid factors are activated in austenitic phase, however it is not always the case of glides in ferritic phase. The slip lines appear frequently in the vicinity of grain boundaries, and the dislocations tend to accumulate around the grain boundaries during plastic deformation due to the noncontinuity of slip lines (Fig. 1.5b).

| Orientation relationship | Expression | Number of variants |
|--------------------------|--|--------------------|
| Kurjumov-Sachs | $\{111\}_\gamma \{011\}_\alpha$ $\langle 011 \rangle_\gamma \langle 111 \rangle_\alpha$ | 24 |
| Nishijama-Wassermann | $\{111\}_\gamma \{011\}_\alpha$ $\langle 112 \rangle_\gamma \langle 011 \rangle_\alpha$ or $\langle 011 \rangle_\gamma \langle 001 \rangle_\alpha$ | 12 |

Table 1.3 Orientation relationships between slips in ferrite and austenite [Jonas 05].

The continuity of slip lines between phases is caused by some particular orientation relationships between the slip systems in ferrite and austenite, as summarized in table 1.3. Such orientation relationships enable the transfer of gliding from one phase to another. It should be emphasized that in the case of hot-rolled steel used in this present study, the recrystallization effect of material was not completed during rolling process and the later thermal treatment. Thus both phases are not bipercolated anymore and obey almost only the Kurjumov-Sachs relation [Kurjumov 30].

1.1.2 Ductile damage in duplex steels

The ductile damage process in duplex steels has been reported by several literatures. Verhaeghe et al. [Verhaeghe 96] reports that the fracture resulted by tensile load is roughly perpendicular to the tensile axis. Plenty of linear streaks were observed occurring on the cleavage faces and forming the micro-cracks in shape of “fish bone”, which resulted from the emergence of slip plains localized in ferrite. EBSD analysis shows that microcracks initiate in the ferrite ether on slip plans with highest Schmid factor or at the austenite/ferrite boundaries and propagate along slip lines in ferritic grain [Alvarez-Armas 12]. Joly [Joly 92] noted the cleavage cracks initiated at the cutting edge between two twinned crystals in aged ferritic steel.

After the initiation, the most frequently observed ductile damage process at room temperature in duplex steels is the cleavage of ferrite combined with ductile fracture of austenite. The macroscopic cracks through austenite arise by coalescence of cavities formed from the micro-cracks engendered by brittle cleavage of ferrite, as illustrated in Fig. 1.6 [Le Roux 99].

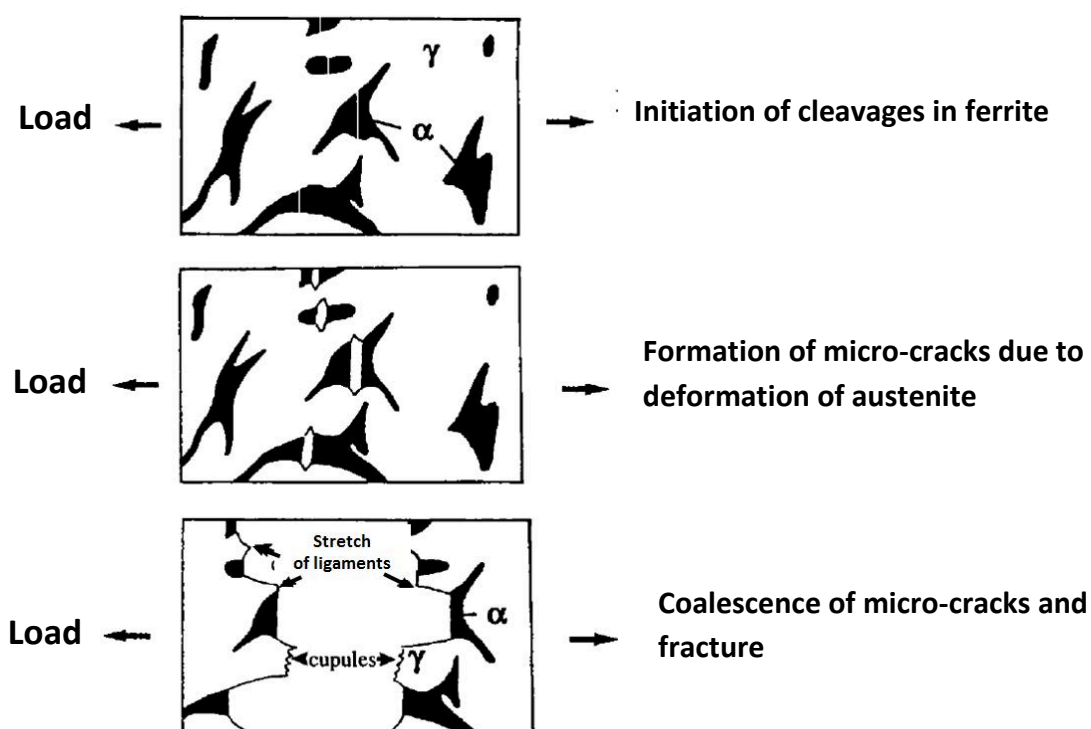


Figure 1.6 Illustration of mechanism of ductile damage in aged duplex steels at room temperature [Le Roux 99].

1.1.3 Research status

The plastic deformation of polycrystalline materials have been already studied by our work team, abundant achievements have been made during these years. In this section, some representative results will be presented, on which is based the thesis work.

1.1.3.1 Elasto-plastic deformation of duplex steel

An interesting study concerning evolution of plastic deformation in the two phases of duplex steel was performed using EBSD method by Wroński et al. [Wroński 12]. By investigating the evolution of IQ (image quality) factor, it was found that estimated deformed volume fraction is higher in the austenitic phase than in the ferritic phase. Moreover the

changes of misorientations in both phases show that the austenitic grains (which build the “islands” of this phase in the initial sample) deformed more homogeneously than the ferritic grains (Fig. 1.7a). In the case of ferrite, changes in the internal substructure lead to significant segmentation inside grains thus the grain size decreased significantly (Fig. 1.7b).

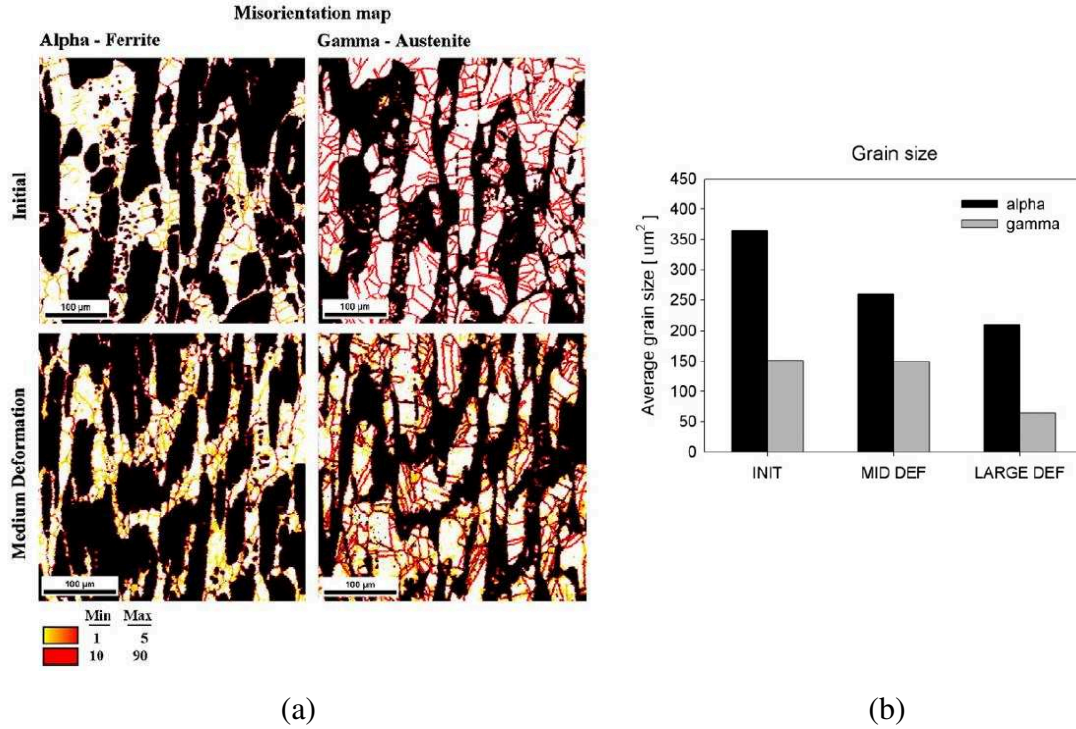


Figure 1.7 (a) Maps of low and high angle boundaries (misorientation angle between grains) for ferritic (alpha) and austenitic (gamma) phases. (b) Grain size for both phases for initial sample (INIT), medium deformation (MID DEF) and large deformation (LARGE DEF).

The mechanism of elasto-plastic deformation in duplex steel has been studied by [Jia 08, Le Joncour 10] and [Baczmański 16] by neutron diffraction during “in-situ” tensile test. The evolutions of interplanar spacing of each $\{hkl\}$ reflection measured in the direction of applied force were drawn in function of the calibrated stress, as illustrated in Fig.1.8 [Le Joncour 11]. Three elasto-plastic deformation steps and the initiation of damage process can be identified from these curves. During the step $E_{\alpha,\gamma}$ from 0 to 250MPa, both ferrite (alpha) and austenite (gamma) are deformed elastically, and a linear dependence of lattice strains in function of the applied stress can be observed for both phases. The slopes of these plots are related to the so called X-ray Elastic Constant (XEC) of each $\{hkl\}$ reflection.

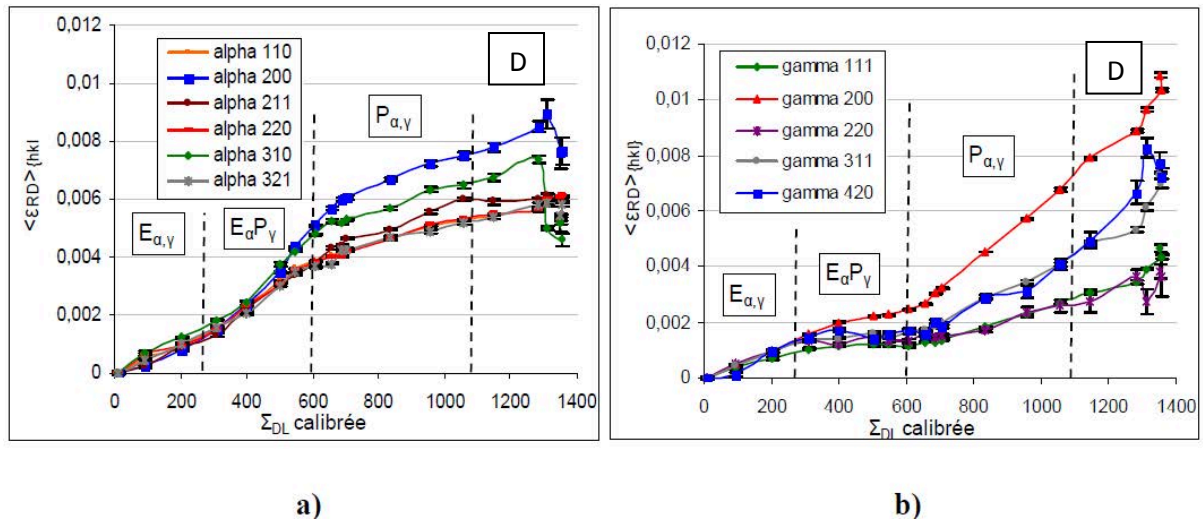


Figure 1.8 Complete evolution curves of micro-strain until initiation of damage process for ferrite (a) and for austenite (b) [Le Joncour 11].

The step $E_{\alpha}P_{\gamma}$ corresponds to the beginning of plastic deformation of austenite, while the ferrite continues elastic deformation. We can see the slopes of all curves for $\{hkl\}$ reflections in austenite declined. Simultaneously, the slopes of $\{hkl\}$ reflections in ferrite rose, indicating that ferrite received a part of stress released by austenite.

During the third step $P_{\alpha,\gamma}$, both phases underwent plastic deformation, but the increase of interplanar spacings in the ferrite was slower than in the austenite, which means that the austenite retook a part of load from the plastically deformed ferrite. It can be concluded that the work hardening rate of the austenitic phase is higher comparing with the ferritic phase. The stage D show the initiation of ductile damage, which will be discussed in the next section.

From the previous study performed by Le Joncour et al. [Le Joncour 10], we can see that different elasto-plastic behaviours of the austenitic and ferritic phases are intrinsically related to their crystal structures as well as the slip modes operating in the crystal lattice.

| Diffraction mode | Neutron | | | Synchrotron | |
|----------------------|----------------|------------|-------------|----------------|------------|
| Material | Quenched UR45N | Aged UR45N | | Quenched UR52N | Aged UR45N |
| Load type | Tension | Tension | Compression | Tension | Tension |
| Ferrite CRSS (MPa) | 220 | 350 | 360 | 290 | 410 |
| Austenite CRSS (MPa) | 140 | 140 | 120 | 180 | 150 |

Table 1.4 Initial CRSS values for ferrite and austenite determined by different experimental methods on different grades of duplex steels [Baczmanski 16].

The activation of slip systems for each phase has been also investigated in the previous work by [Baczmański 16], where the neutron diffraction and synchrotron coupled with in-situ tensile or compression tests were employed on samples of different grades of duplex steels. The predictions with self-consistent model compared with experimental data were carried out to determine the initial Critical Resolved Shear Stress (CRSS) for each phase. The determined values of CRSS are given in table 1.4.

It can be noted that the initial CRSS of ferrite are always higher than that of austenite for all studied duplex steels. This leads to considerably lower yield stress of austenite compared with that of ferrite, and agrees with the above presented experimental observation that slip lines were initiated firstly in the austenitic grains.

1.1.3.2 Ductile damage process duplex steel

As at the end of phase strain evolution curves (Fig. 1.7a), material softening is observed in ferrite after threshold D. It is very interesting to note that the interplanar spacings measured using $\{hkl\}$ reflections significantly decreased in the ferrite. Meanwhile, the austenite took the load released from the ferritic phase. This phenomenon could indicate an initiation of damage process occurs in the ferritic phase, confirming the relatively lower ductility of the ferrite compared to that of the austenite (table 1.1).

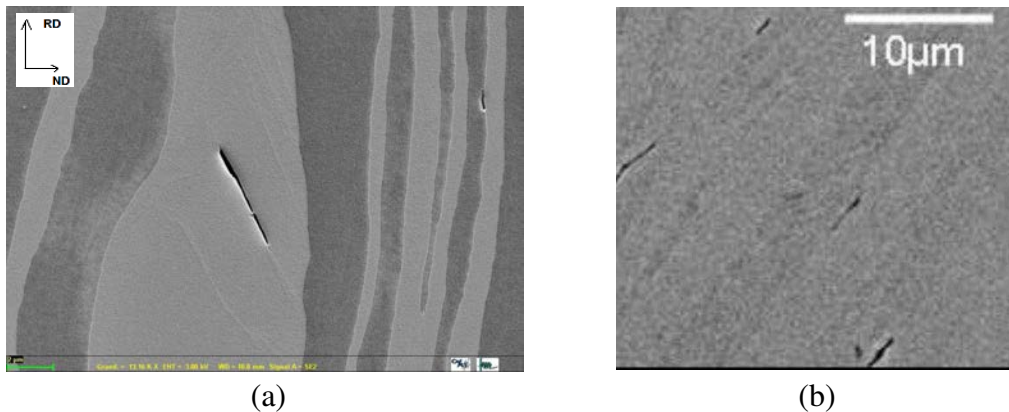


Figure 1.9 SEM picture for initiation of damage, a crack occurred along slip plane within ferritic phase (a); interfacial cracks occurred on the boundaries between two phases (b) [Le Joncour 11].

The initiation of ductile damage process has been studied by Le Joncour and Wronski et al. [Le Joncour 11]. Some microscopic observations confirm the initiation of damage in the ferritic phase. As illustrated in Fig. 1.9a [Le Joncour 10], a crack was observed along the slip line inside ferritic phase, which suggests the cleavage initiates in ferrite; and cracks appeared on the boundaries between two phases (Fig. 1.9b).

[Le Joncour 11] also proposed an assumption for damage process based on the experimental observation, the supposed process of ductile damage is shown by Fig.1.6. This assumption considers that the ductile damage occurs only after the plastification of both phases, and inclusions are supposed occurring homogeneously in both phases.

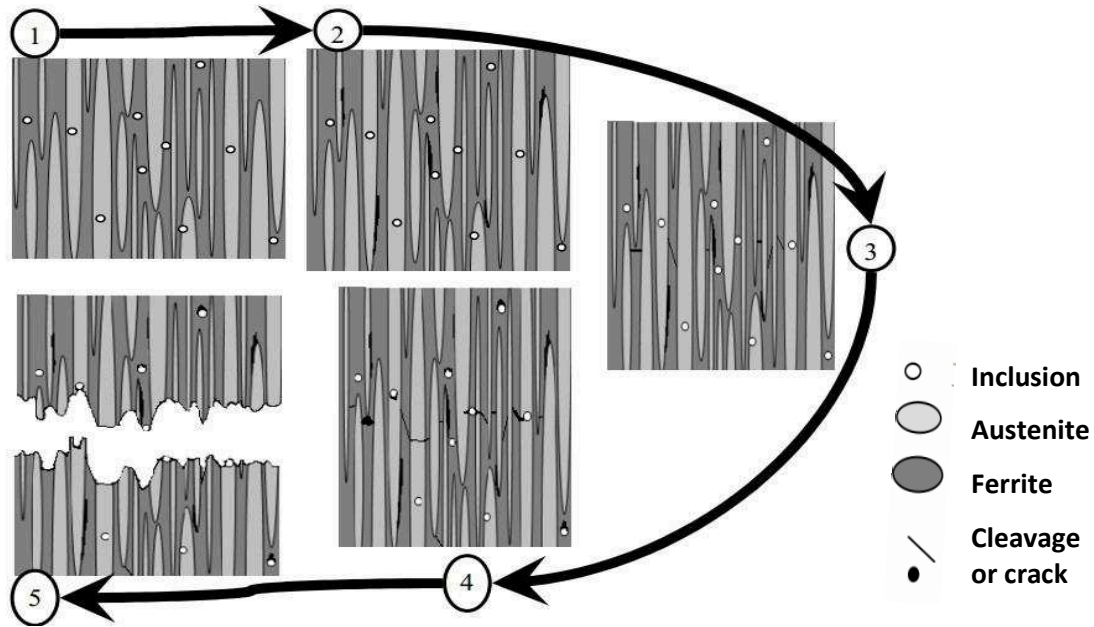


Figure 1.10 Proposition for the process of ductile damage in duplex steels [Le Joncour 11].

1. Both phases are plastified and the damage process is considered beginning only after the plastification of both phases.
2. The interfacial decohesion cracks occurred close to the fracture surface but also observed in the area less deformed. Thus, this type of cracks can be considered as the first appearance of damage (Fig. 1.7 b).
3. The cleavages or cracks along the slip lines in ferrite (Fig. 1.9 a) lead to the relaxation of the ferritic phase (observed by neutron diffraction, Fig. 1.7 a).
4. The inner-ferrite cracks and the interfacial decohesion cracks merge together under the further imposed external load.
5. The ductile fracture occurs by coalescence of all different cracks inside material. The material is finally damaged.

The studies on duplex steel in present thesis are carried out following the current research findings, mainly focus on the initiation of damage process during large deformation stage.

1.1.4 Characterisation of studied duplex steels

The samples prepared for in situ tensile tests are made of two grades of duplex steels, UR45N and UR52N. Both raw alloys are continuously casted and then hot rolled. Subsequently, three experimental specimens are prepared by different thermal treatments from these two materials. UR52N and a portion of UR45N alloys are heat treated at 1050°C and then quenched in water, to avoid precipitation of secondary phases. Another portion of UR45N alloy is subjected to a thermal treatment at 400°C for 1000h in order to age the material. The chemical compositions of the studied duplex steels are given in table 1.5.

| | C | Mn | Cr | Ni | Mo | Cu | S | N |
|-------|-------|------|-------|------|------|------|--------|-------|
| UR45N | 0.015 | 1.6 | 22.4 | 5.4 | 2.9 | 0.12 | 0.001 | 0.17 |
| UR52N | 0.016 | 1.02 | 25.18 | 6.46 | 3.78 | 1.61 | 0.0005 | 0.251 |

Table 1.5 Chemical compositions of duplex stainless steel UR45N and UR52N: mass-percent (Fe=balance).

The microstructure of the studied material is constituted of ferritic phase and austenitic phase in approximately equal volume proportions (50% austenite to 50% ferrite). As shown in the Fig. 1.11 a and b [Dakhlaoui 07], the microstructure of both materials consists of austenitic (γ phase) ‘island’ elongated along the rolling direction and evenly embedded in the ferritic (α phase) matrix.

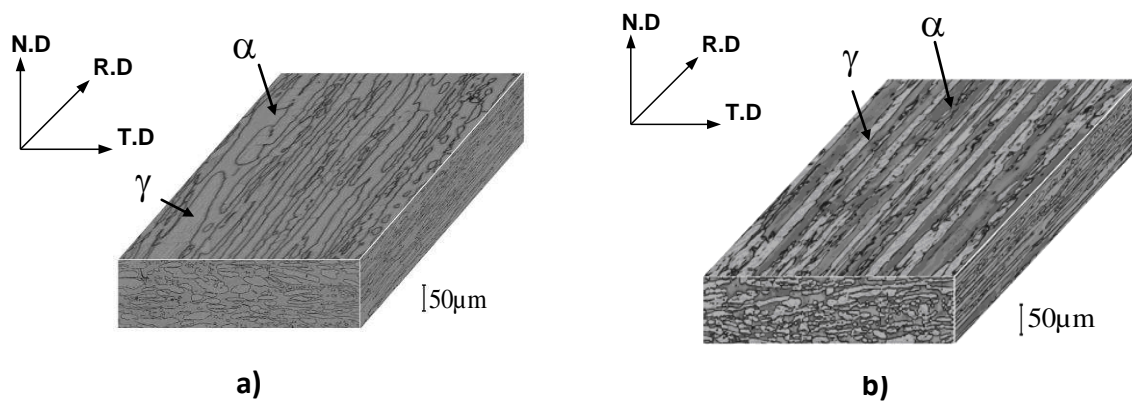


Figure 1.11 Three dimensional microstructure of duplex stainless steel (a) UR45N, (b) UR52N [Dakhlaoui 07].

The EBSD (Electron Backscatter Diffraction) orientation maps [Schwartz 09] made for UR45N steel (Fig. 1.12 [Le Joncour 10]) show that austenite islands are divided into smaller crystallites with different orientations, meanwhile the grains of ferritic phase possess nearly the same crystal orientation resulting from the rolling process.

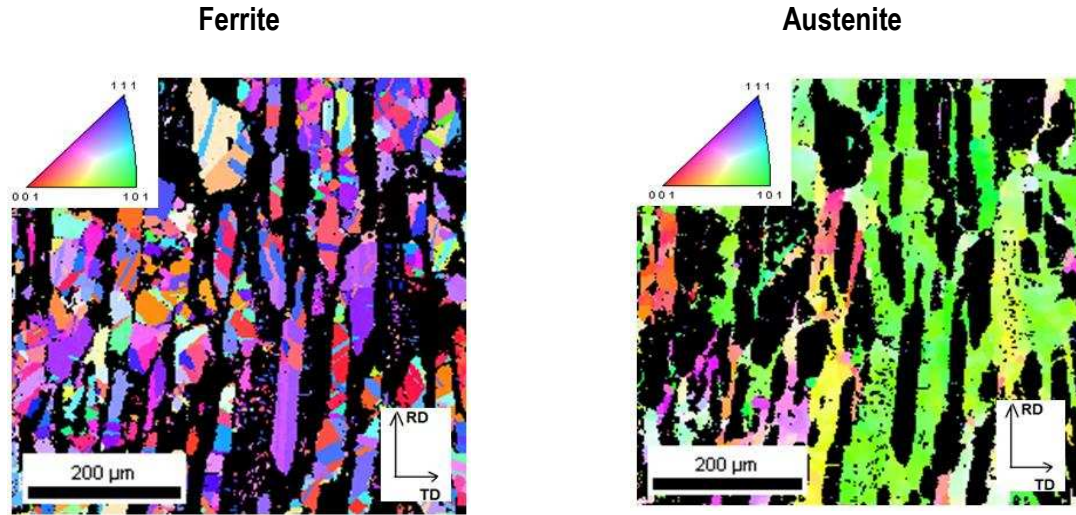


Figure 1.12 Microstructure of the UR45N duplex stainless steel determined by EBSD method. Orientations of austenitic and ferritic grains are shown in the selected phase by colors while the grains of the unselected phase are black [Le Joncour 10].

Subsequently, the experimental pole figures $\{110\}$, $\{200\}$, $\{211\}$ and $\{111\}$, $\{200\}$, $\{220\}$ are measured respectively for the ferrite and the austenite, using Cr radiation X-ray on Seifert four circles diffractometer. The Orientation Distribution Function (ODF) [Bunge 82] is determined independently from the measured experimental pole figures for each phase of both materials (UR52N and UR45N), using the WIMV algorithm [Kallend 90]. Significant anisotropy of grain orientations is found in both phases, and especially pronounced texture is obtained for ferrite, as shown in Fig. 1.13.

| Phase | C_{11} (GPa) | C_{12} (GPa) | C_{44} (GPa) |
|-----------|----------------|----------------|----------------|
| Austenite | 198 | 125 | 122 |
| Ferrite | 231 | 134 | 116 |

Table 1.6 Single-crystal elasticity constants of austenite and ferrite [Simons 71, Inal 99].

The crystallographic textures (Fig.1.13) and typical single crystal elastic constants (given in table 1.6) for ferrite and austenite are used in calculations of the X-ray Elastic Constants (XEC) obtained by the Eshelby-Kröner approach [Eshelby 57; Kröner 61], as proposed by Baczmanski et al. [Baczmanski 03] and Wroński et al. [Wroński 07].

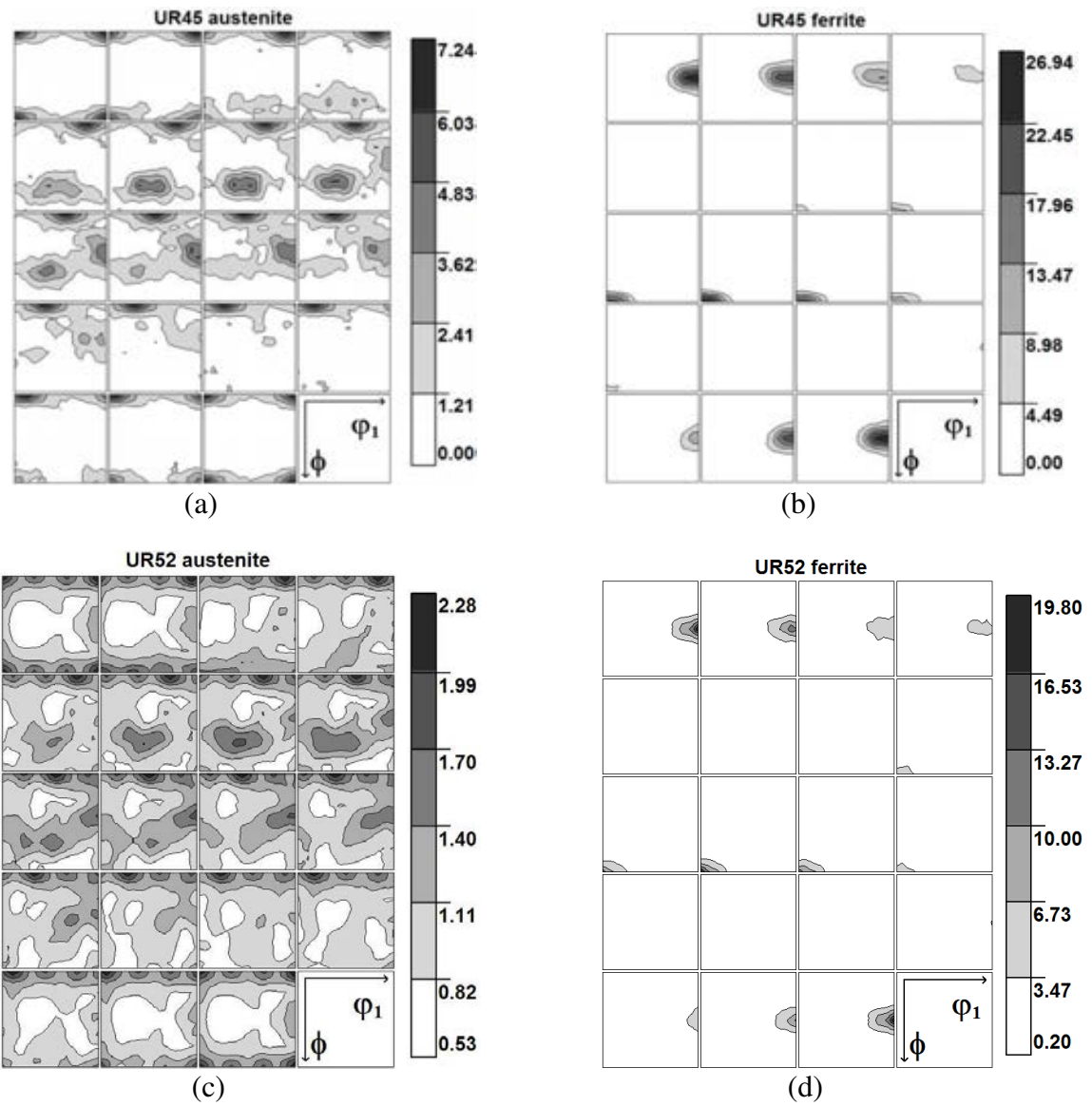


Figure 1.13 Orientation distribution function (ODF) for austenitic phase and ferritic phase of duplex steel UR45N (a and b) as well as of UR52N (c and d), determined by X-ray diffraction (Cr radiation). The sections through Euler space with the step of 5° along the ϕ_2 axis are presented for (a) austenitic and (b) ferritic phases in UR45N sample. The orientation of the sample is: $x_1 \parallel \text{TD}$ (transverse direction), $x_2 \parallel \text{ND}$ (normal direction) and $x_3 \parallel \text{RD}$ (rolling direction).

1.2 Descriptions of two-phase titanium

Two-phase titanium alloy is another material engaged in the studies of this thesis. The microstructure has also a strong influence in the mechanical behaviour of titanium alloys, especially the size and arrangement of the hexagonal α titanium and body-centred cubic β titanium are of prime importance. Lamellar microstructures are originated from cooling out of β titanium field (Fig. 1.14a), and equiaxed microstructures results from recrystallization process. The final microstructure of titanium can either individually exhibits a fine or coarse distribution of grains or both type of grains can be present in a bimodal microstructures (Fig. 1.14b). In the bimodal microstructure, two morphologies can be identified for α titanium as indicated in Fig. 1.14b, i.e. the globular primary α phase (α_p), and the acicular secondary α phase (α_s).

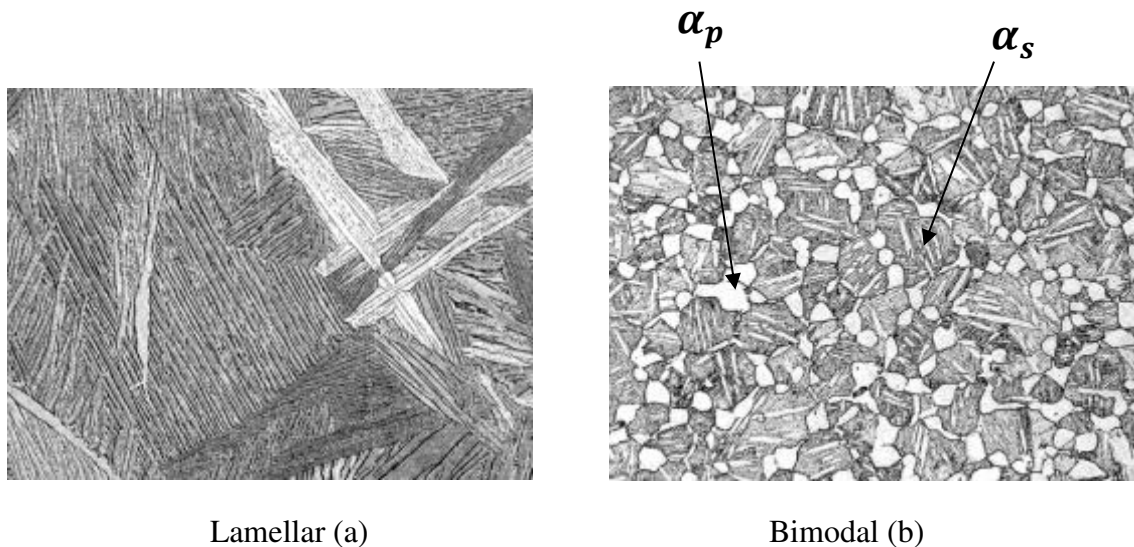


Figure 1.14 Typical microstructures of two-phase titanium alloys: (a) lamellar α -titanium embedded in the matrix of β -titanium; (b) bi-modal microstructure, granular primary α -titanium (α_p) and acicular secondary α -titanium (α_s) embedded in matrix of β -titanium [Peters 03].

Compared with equiaxed microstructures, lamellar structure usually shows better creep behaviour due to their coarser structure, meaning a lower volume fraction of phase boundaries. On the other hand, equiaxed and bimodal microstructures show superior fatigue properties due to their fine microstructures.

1.2.1 Elasto-plastic deformation in two-phase titanium

The crystal structures of α and β titanium are respectively hcp and bcc (cf. unit cells shown in Fig. 1.1 a and c). The main parameters of the lattice for each phase are presented in table 1.7 [Schmid 50, Person 67, Peters 03, Lütjering 07].

The titanium alloys exhibit pronounced anisotropic behaviour, especially concerning their elasto-plastic properties, due to the presence of hexagonal α titanium and pronounced textures. The monocrystal elastic constants of α -titanium varies significantly between 145GPa in the direction vertical to the basal plane and 100GPa in the direction parallel to this plane. [Lütjering 07]. In general, commercial β titanium alloys have lower modulus of elasticity E than α and $\alpha + \beta$ titanium alloys. The typical E values of commercial β phase alloys are in the range of 70 - 90GPa for the as-quenched condition and 100 – 105GPa for the annealed condition, while E is equal approximately 115GPa for commercial $\alpha + \beta$ alloys [Boyer 94].

| Phase | α titanium | β titanium |
|-------------------------------|---|--|
| Structure | hcp | bcc |
| Lattice parameter | $a=2.8664 \text{ \AA}$ $c=4.68 \text{ \AA}$ (measured at $\approx 20^\circ\text{C}$) | 3.32 \AA (measured at 900°C) |
| c/a ratio | 1.587 | |
| Number of atoms per unit cell | 6 | 2 |
| Packing density | 74% | 68% |
| Slip planes | {0001}, {0110}, {0111}, {1122} | {110}, {112}, {123} |
| Slip directions | $\langle 1120 \rangle$, $\langle 1123 \rangle$ | $\langle 111 \rangle$ |
| Atom density of slip plane | $\approx 91\%$ | $\approx 83\%$ |

Table 1. 7 Summary of main parameters of crystal lattice and slip systems for ferrite and austenite [Schmid 50, Person 67, Peters 03, Lütjering 07].

The deformation mechanisms of titanium have been studied over the past decades. Generally, the processes of plastic deformation and of diffusion are strongly related to the crystal structures. In this thesis, we mainly focus on the slip systems in the lattice of titanium and their activation mechanism. Fig. 1.15 [Greenfield 72] shows the continuity of slip lines between α titanium and β titanium and this effect is related to the crystal structures of each phase. As illustrated in Fig. 1.16, α titanium exhibits a hexagonal close-packed crystal structure (hcp). Because of the bcc structure of β titanium, the mechanism of slip systems

activation and slip modes in this phase can be referred to the above described slip systems operating in ferrite.

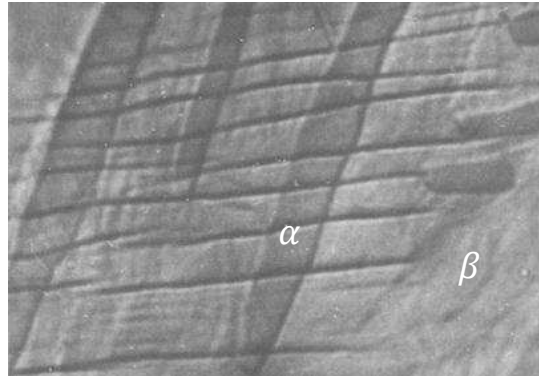


Figure 1.15 Slip lines occurred on lamellar intergranular α platelets in β matrix [Greenfield 72].

The slip planes and slip directions in hcp structure are indicated in Fig 1.16 and summarized in table 1.8 [Patrudge 67, Yoo 81]. The three slip planes (the densely packed planes) are indicated in this figure, i.e. the $\{0001\}$ plane with the highest density, called basal plane; the family of $\{0110\}$ planes, called prismatic planes and the family of $\{0111\}$ and $\{1122\}$ planes, respectively called first order and second order pyramidal planes. The three close-packed directions $\langle 1120 \rangle$ along axes a_1 , a_2 and a_3 are the main slip directions (see Fig.1.16).

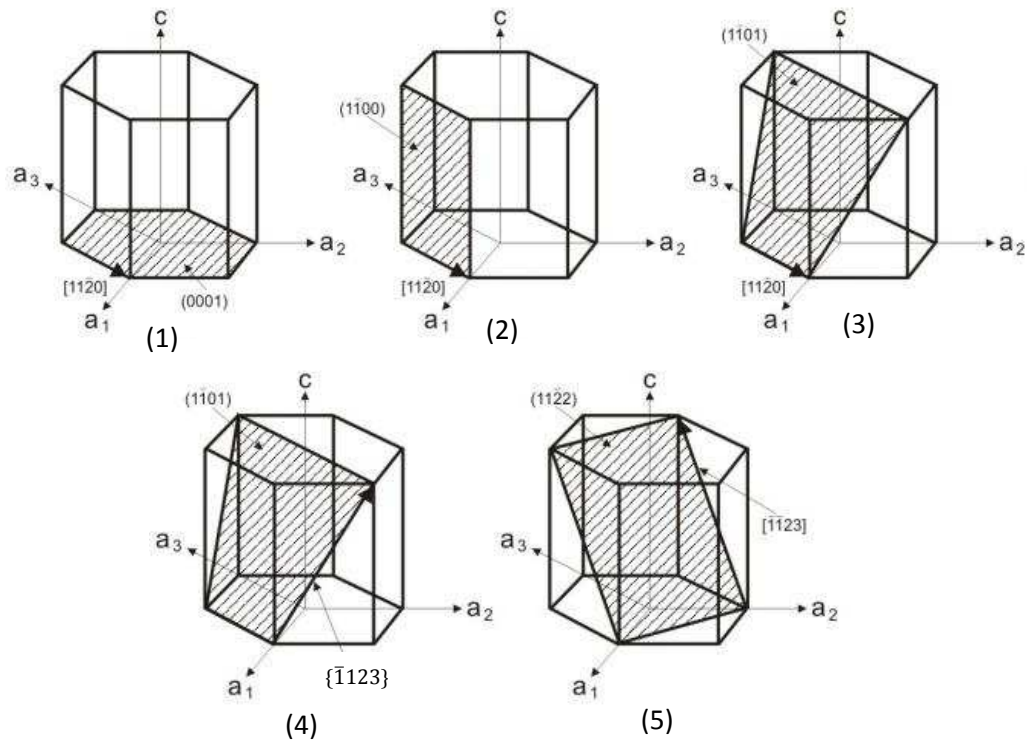


Figure 1.16 Illustration of hcp structure and the slip systems in α titanium [Balasubramanian 02].

Generally, for an hcp crystal, several different deformation modes can be activated during its plastic deformation, such as twinning and gliding process. In this thesis, we mainly discuss the gliding process involving different slip systems of two types. The first type is $\langle a \rangle$ slip system with an \vec{a} Burger's vector $\langle 1120 \rangle$, which can be found on basal plane $\{0001\}$, prismatic planes $\{0110\}$ and first-order pyramidal planes $\{0111\}$. The second type is $\langle c+a \rangle$ slip system with $\vec{c} + \vec{a}$ Burger's vector $\langle 1123 \rangle$, which can be observed on the first $\{0111\}$ and second $\{1122\}$ pyramidal planes.

The plane families $\{0001\}$, $\{0110\}$ and $\{0111\}$ contain \vec{a} type of Burgers vector [Burgers 34, Burgers 39], and these three different slip plane families together with the possible slip direction family $\langle 1120 \rangle$ generate 12 slip systems (table 1.8). The dislocations with Burgers vectors type $\vec{c} + \vec{a}$ have also been observed in several studies by Transmission Electron Microscope (TEM) [Paton 73, Jones 81]. In this experimental the load was applied in the direction parallel to \vec{c} vector, thus neither slip system with \vec{a} nor \vec{c} Burgers vectors can be activated, because the Schmid factors [Schmid 50] for both potential slip directions were equal to zero. However, the angle between the planes $\{1122\}$ containing $\vec{c} + \vec{a}$ Burgers vectors and the c axis is close to 45° , which leads to the highest Schmid factor in a hcp lattice. This is the reason why the most likely activated slip system in α titanium is the so called 2nd order pyramidal system $\langle 1123 \rangle \{1122\}$, shown in the fifth one in table 1.8 [Partridge 67, Yoo 81, Balasubramanian 02]. Another possible slip plane containing dislocations with $\vec{c} + \vec{a}$ are the prismatic $\{0111\}$ planes, which together with $\langle 1123 \rangle$ directions generate the 1st order pyramidal systems $\langle 1123 \rangle \{0111\}$, shown in table 1.8. The latter family of slip systems is frequently taken into account in elasto-plastic deformation model (cf. references in the caption of table 1.8).

| Slip system type | Burgers vector type | Slip direction | Slip plane | No. of slip systems |
|-------------------------------------|---------------------|------------------------|------------|---------------------|
| Basal (1) | \vec{a} | $\langle 1120 \rangle$ | $\{0001\}$ | 3 |
| Prismatic (2) | \vec{a} | $\langle 1120 \rangle$ | $\{0110\}$ | 3 |
| 1 st order pyramidal (3) | \vec{a} | $\langle 1120 \rangle$ | $\{0111\}$ | 6 |
| 1 st order pyramidal (4) | $\vec{c} + \vec{a}$ | $\langle 1123 \rangle$ | $\{0111\}$ | 12 |
| 2 nd order pyramidal (5) | $\vec{c} + \vec{a}$ | $\langle 1123 \rangle$ | $\{1122\}$ | 6 |

Table 1.8 Summary of slip systems in hcp structure, the number of slip system type corresponding to that noted in Fig. 1.16[Partridge 67, Yoo 81, Balasubramanian 02].

According to several previous studies [Patridge 67, Bridier 05, Raabe 07, Wang 10, Beyerlein 10] on titanium alloys, and as illustrated in the work of [Bridier 05], the basal and prismatic slip systems have been shown as the main slipping modes for α phase in Ti-6Al-4V titanium alloy (cf. Fig. 1.17). Only a few 1st order pyramidal slip systems were observed in α_p as a deviated gliding. In Fig. 1.17 we can see that the slip lines occurred in α_p phase during the tensile test were mostly related to prismatic $\langle 1120 \rangle \{0110\}$ and basal $\langle 1120 \rangle \{0001\}$ slip systems.

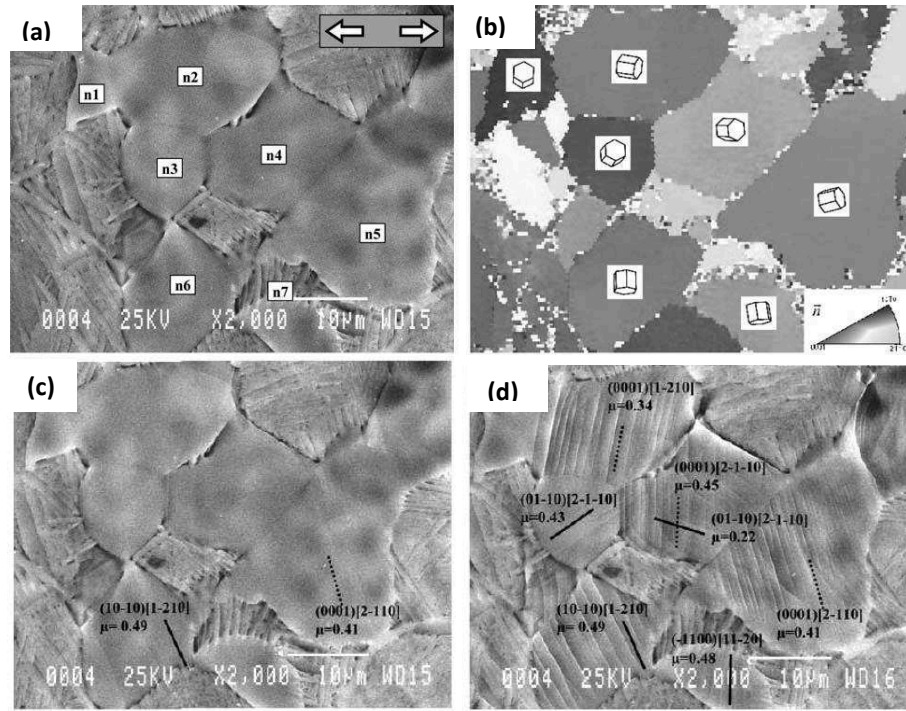


Figure 1.17 Identification of slip systems in α titanium: (a) microstructure before tensile test (arrow indicates tensile direction); (b) corresponding EBSD maps with grains orientation; (c) identification of slip lines at the beginning of plastic deformation of sample; (d) identification of slip lines before fracture of sample [Bridier 05].

The histogram in Fig. 1.18 shows distribution and activation of slip systems at different stress levels, histogram bars represent the occurring frequency of basal or prismatic slip systems in deformed α_p . It clearly presents that the basal slip systems more likely tend to be activated than prismatic systems. Moreover, according to the experimental observation, the coexisting slip systems can be possibly either both prismatic systems and prismatic and basal systems in the same time.

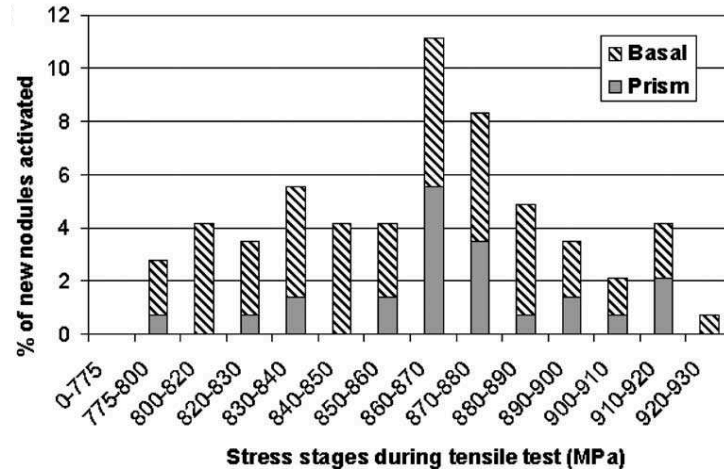


Figure 1.18 Frequency of activated slip systems at different stress stages and their natures [Bridier 05].

According to Bridier's work [Bridier 05], the prismatic $\langle a \rangle$ slip system is the most possibly activated slip system in α titanium at room temperature. And according to [Bridier 08], the predominance of slip along basal and prismatic planes is confirmed. However, by increasing the concentration of α stabilizer elements, which decrease the atomic spacing on basal plane [Raabe 07], the basal $\langle a \rangle$ slip system become easier to active. On the other hand, several previous works [Zambaldi 12, Benmhenni 13, Barkia 15, Gloaguen 15] show that the prismatic $\langle a \rangle$ slip system is the most easily activated system during plastic deformation process in α phase (see table 1.9, the values of critical shear stress for P $\langle a \rangle$ slip system are always the lowest). The presented CRSS values have been evaluated from a combination of experimental observations and micromechanical models.

| | | CRSS values (MPa) of slip system in α titanium | | | |
|--|--------------------------------|---|---|----------|----------|
| Slip systems | Indices | Ref. (1) | Ref. (2) | Ref. (3) | from (4) |
| P $\langle a \rangle$ | $\{0110\}\langle 1120 \rangle$ | 36 | 150 | 92 | 120 |
| B $\langle a \rangle$ | $\{0001\}\langle 1120 \rangle$ | 252 | 349 | 105 | 182 |
| $\pi_1 \langle a \rangle$ | $\{0111\}\langle 1120 \rangle$ | 144 | - | 145 | 149 |
| $\pi_1 \langle c+a \rangle$ | $\{0111\}\langle 1123 \rangle$ | 288 | 1107 | 190 | 241 |
| $\pi_2 \langle c+a \rangle$ | $\{1122\}\langle 1123 \rangle$ | 216 | - | - | - |
| P $\langle a \rangle$: a type prismatic slip system B $\langle a \rangle$: a type basal slip system $\pi_1 \langle a \rangle$: a type 1 st order pyramidal slip system $\pi_1 \langle c+a \rangle$: c+a type 1 st order pyramidal slip system $\pi_2 \langle c+a \rangle$: c+a type 2 nd order pyramidal slip system | | | (1): [Benmhenni 13] (2): [Zambaldi 12] (3): [Gloaguen 15] (4): [Barkia 15] | | |

Table 1.9 CRSS for various possible slip systems in titanium and its alloys, determined by several authors using a combination of experimental observations and micromechanical models.

Analysing the available data concerning modelling of elasto-plastic deformation as well as the experimental data we can find different values of CRSS for slip systems activated in α titanium. However, a great difference exists in the CRSS values for the same slip system, as reported in table 1.9. From these ambiguous results we are not able establish confirmable ranges for the CRSS of each slip system. Therefore, one of the main topics of this thesis is to determine the values of CRSS for slip systems in two phase titanium alloy consisting of α and β phases.

Additionally, in two-phase titanium, the α_s and β phases usually obey a classical Burgers orientation relationship [Burgers 34], i.e. $\{0001\}_\alpha \parallel \{011\}_\beta$ and $\langle 1120 \rangle_\alpha \parallel \langle 111 \rangle_\beta$ [Bhattacharyya 03, Jun 16], and a low energy, semi-coherent interface exists between the phases [Furuhara 95]. At the beginning of plastic deformation, dislocations tends to penetrate the semi-coherent interphase boundaries [Suri 99], then the coherency of interfaces is reduced due to the interaction between boundaries and lattice dislocations [Zhereblsov 10].

1.2.2 Ductile damage in two-phase titanium

As mentioned above, the α titanium exhibits an hcp structure, which is able to lead to a partially different ductile damage process compared with duplex steels. It has been observed that during ductile damage in two-phase titanium, the micro-cracks were nucleated on the interphase boundaries [Greenfield 72]. Generally, the α titanium is considered being softer than β titanium. The difference between the elasto-plastic behaviors of the two phases creates plastic strain incompatibilities at the α/β interfaces [Helbert 96]. In Thompson and Williams's study [Thompson 77], no evident particle nucleation or void have been found on the fractured surface of two-phase titanium alloys Ti-2Al and Ti-6Al-4V. Therefore, other possibilities should be taken into consideration, including twin-matrix interfaces, vacancy clusters, grain boundaries-slip band intersections and slip band-slip band intersections [Helbert 96]. In the studied Ti alloys, the local stresses can be higher in the hexagonal lattice compared with cubic lattice (bcc), due to limited capacity for their relaxation at slip bands intersections. These higher local stresses could result in dislocation coalescence [Stroh 57], which in turn could lead to the generation of micro-cracks.

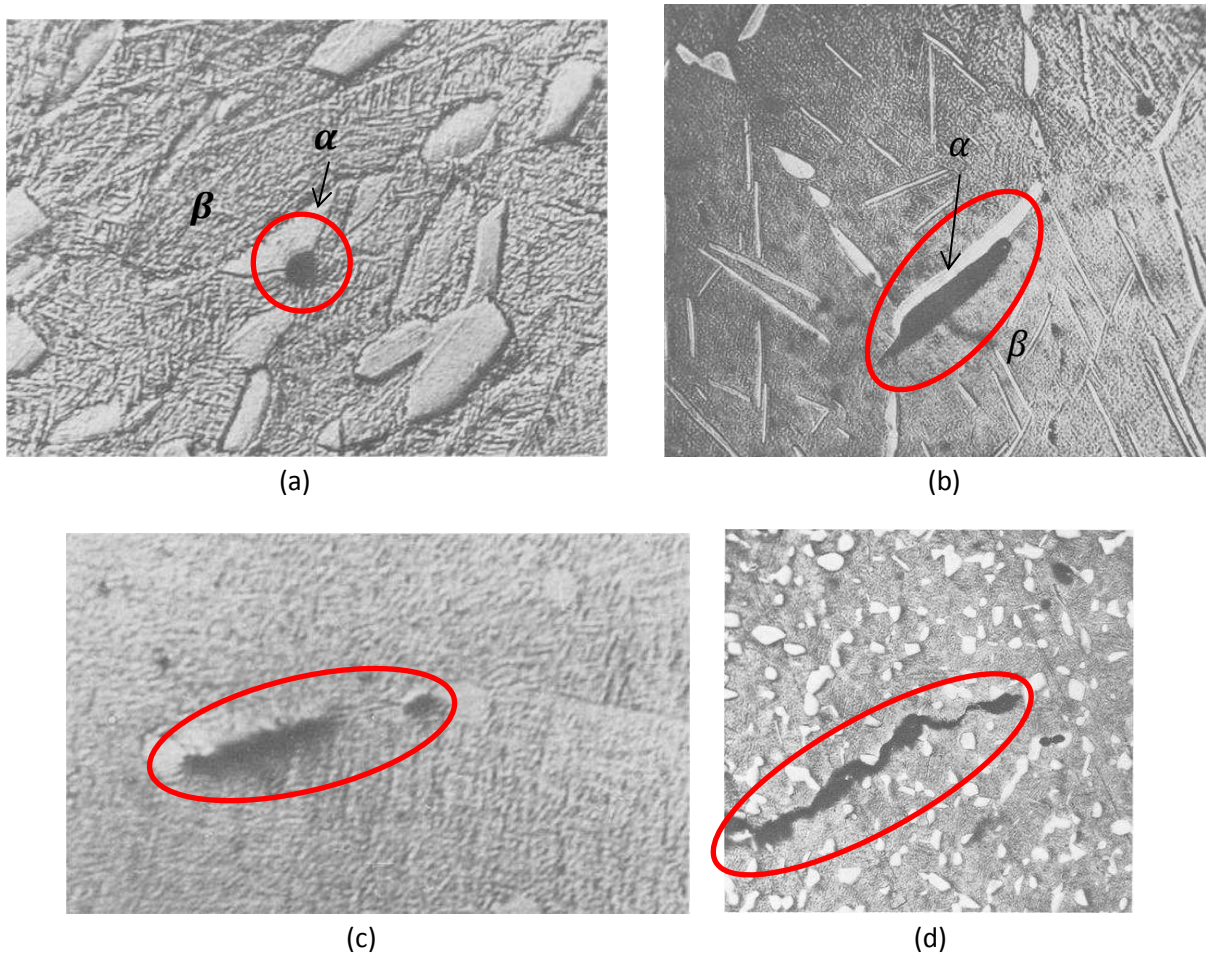


Figure 1.19 Indicated by red circles (a) void nucleation and growth at an equiaxed α - β interphases interface; (b) nucleation of micro-cracks at grain boundary in lamellar α ; (c) Micro-crack growth along β grain boundary; (d) crack propagation in fracture section [Greenfield 72].

In Greenfield's work [Greenfield 72], the void formation occurring at equiaxed α - β interphases after uniaxial tensile test was observed (Fig. 1.19). It was found that the number of micro-cracks increased with the increasing level of applied stress triaxiality in the specimen. Meanwhile, greater void nucleation occurred in the early stage of deformation in samples with larger α particle size. In the lamellar structure of α titanium (Fig. 1.14a), the micro-cracks are formed only at the grain boundaries of α interfaces (Fig. 1.19), and the void nucleation rate increases generally when the grain boundary thickness increases.

In addition, a mechanism involving a pile-up of dislocations in α titanium leads to formation of cracks, which are later converted into a plastic crack. According to [Greenfield 72], void started at α - β interface, then it grown extensively into the β phase. This mechanism, which breaks down the compatibility between α - β interfaces and leads to the nucleation of micro-cracks, should be taken also into account in the description of the damage process

occurring in two phase Ti alloys (Fig. 1.19c). During growth the micro-cracks tended to move around an α particle rather than to break it (Fig. 1.19d). The void grown linearly with strain and occurred preferentially at grain boundary. The growth rate of micro-cracks increased with increasing size of β grain, and the growth of cracks occurred due to local plastic flow at the tip of the void, rather than due to coalescence of smaller voids. Finally when a critical void length-stress relationship was reached, unstable fracture took place.

Using EBSD mapping technique, the crack formation planes have been identified by [Bridier 08]. As illustrated by Fig. 1.20, the crack formation is observed along prismatic (Fig. 1.20a) and basal (Fig. 1.20b) planes. Most prismatic cracks are remained to the primary α_p nodule and parallel to straight and regularly spaced slip bands. In contrary, the basal cracks appear earlier and have propagated through the surrounding microstructure under the same external load, indicating the fatal cracks more likely to form on the basal plane.

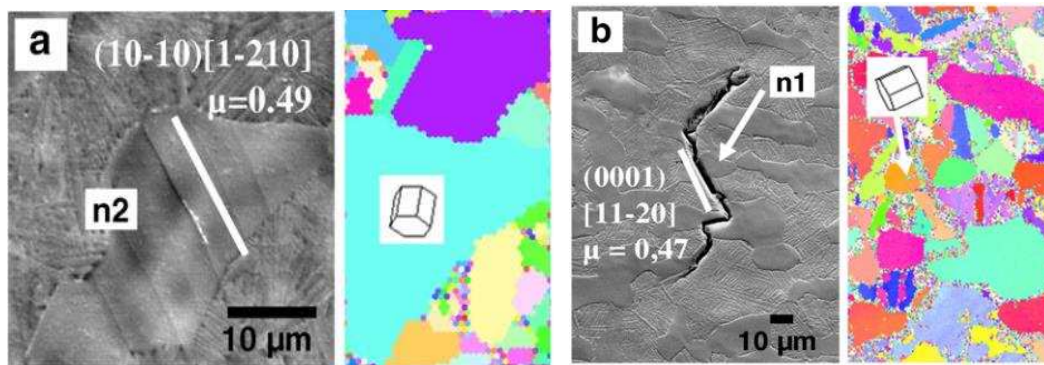


Figure 1.20 Identification of slip planes along which cracks formed. Crack formation on Prismatic plane (a), on Basal plane (b).

1.2.3 Characterisation of experimental TIMETAL-18 alloy

The TIMETAL-18 (mentioned as Ti-18 thereafter) is a high strength near-beta phase titanium alloy, with a nominal composition Ti-5.5Al-5V-5Mo-2.4Cr-0.75Fe-0.15O (in weight percent), produced by TIMET (Valley Creek Blvd. USA).

The studied material was received as a quarter of ingot with a diameter of 250 mm. The as-received ingot was prepared by vacuum arc remelting, then by forging and rolling below the beta transformation temperature (beta transus). After that the material was processed by solution heat treating at a subtransus temperature (1089K) for 2 hours, and then air cooled.

Finally the material was treated by temperature precipitation hardening at 894K for 8 hours and air cooled to form the expected alloy (for the detailed information about Ti-18 please see the patent [Fanning 10]). The designation chemical composition in weight percentage of this alloy is shown in table 1.10.

| Elements | Al | Mo | V | Cr | Fe | O | C | N | Ni | Mo _{eq} | Ti |
|----------|-----|-----|-----|-----|-----|------|------|------|------|------------------|---------|
| Wt% | 5.5 | 5.0 | 5.0 | 2.3 | 0.8 | 0.15 | <0.1 | <0.1 | <0.1 | 13.6 | Balance |

Table 1.10 The chemical composition in weight percentage of Ti-18 alloy [Fanning10].

For the initial material analysis, two small specimens were machined. The investigated surface of the first specimen was parallel to the radial cross section of ingot, while for the second specimen the investigated surface was parallel to the axial cross section of ingot (see Fig. 1.21). Both specimens were metallographically polished with silicon carbide abrasive papers (from 600-grit to 2500-grit) and finally polished by polishing diamond lapping suspension of 1 μ m. Then specimens were chemically etched by a nitric-perchloric acid solution, the concentration of each component is shown in table 1.11. All above mentioned surface treatment were done at room temperature.

| Component | Nitric acid | Perchloric acid | Distilled water |
|---------------|-------------|-----------------|-----------------|
| Concentration | 3% | 5% | 92% |

Table 1.11 The component concentration of chemical etching solution (in volume percentage).

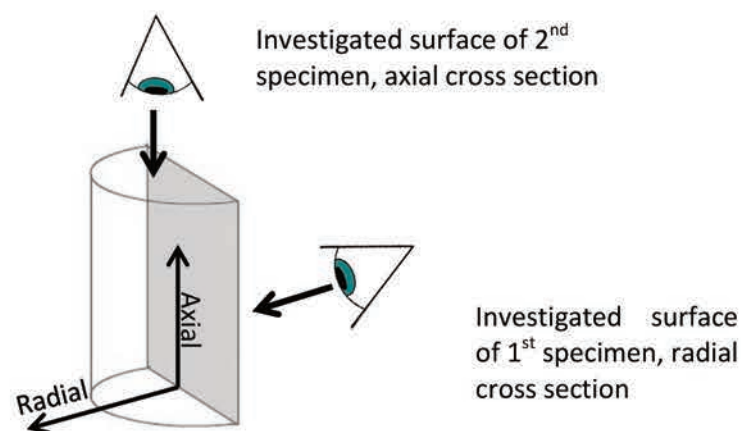


Figure 1.21 Illustration of investigated surface for initial material characterisation of Ti-18. The radial and axial direction is given.

A HITACHI SU-8030 Scanning Electron Microscope (SEM) was employed to perform the microscopic observation [Li 15]. A typical bimodal structure of titanium alloys (cf. section 1.) can be observed, as shown in Fig. 1.22 and Fig. 1.23. At low magnification level, the characteristic microstructure of Ti-18 consists of uniformly spread globular primary α -titanium α_p nodules embedded in β -phase matrix. The shape of α_p nodules is not significantly different between two observed sections (axial and radial). The images obtained with higher magnification are presented in Fig. 1.22 b and Fig. 1.23 b, where lamellar secondary α_s phase is seen. The lamellas were transformed from β -titanium during heat-treatment process.

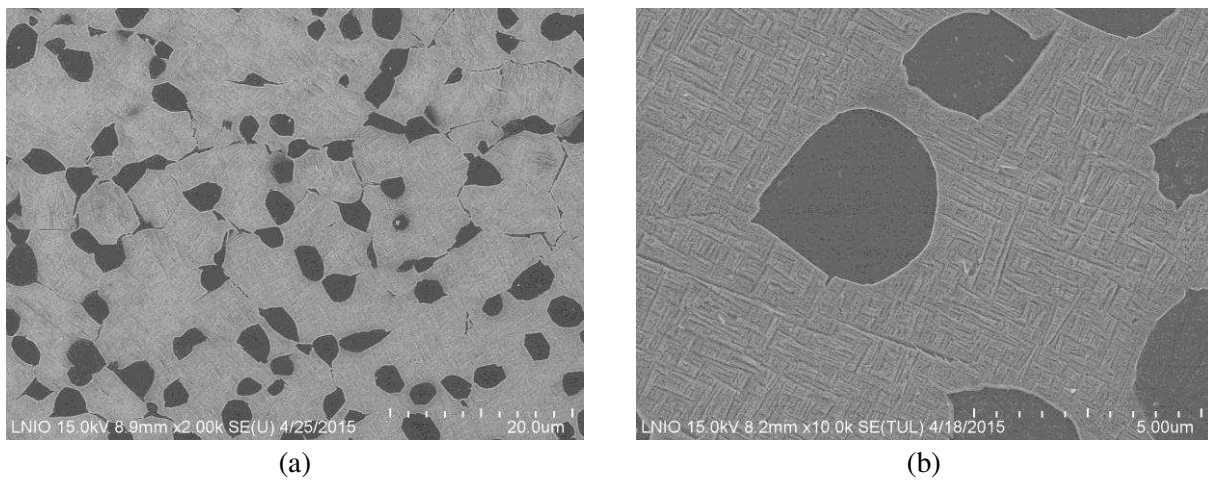


Figure 1.22 SEM images of the microstructure of Ti-18 on ingot radial cross section, (a) low magnification image (2,000x) [Li 15], showing globular primary α -titanium nodules embedded in the transformed β -titanium matrix; (b) high magnification image (10,000x), showing a typical bimodal microstructure, lamellar secondary α -titanium precipitated inside the transformed β -titanium matrix during precipitation hardening process.

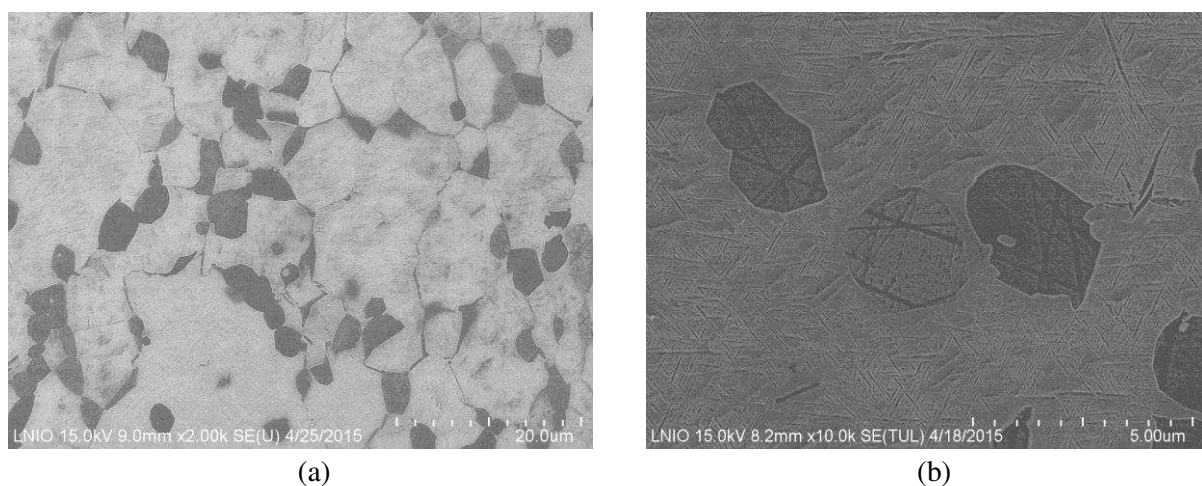


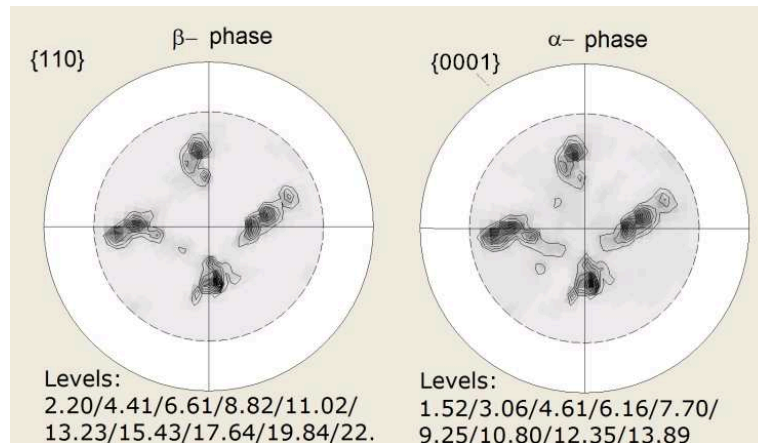
Figure 1.23 SEM images of the microstructure of Ti-18 on ingot axial section, similar bimodal structure as observed on radial section: (a) low magnification image (2,000x) [Li 15]; (b) high magnification image (10,000x).

The estimation of volume fraction for each phase was carried out on both radial and axial cross sections by image processing technique in which the microscopic pictures were converted into binary images (black and white). The detailed estimation steps are described in Appendix 18. Finally, the previous study by [Lebrun 14] shows the volume fraction of α titanium varies between 44% and 52% according to the conditions of heat treatment (see Appendix 18), which agrees with the estimation results (table 1.12). The volume fraction of α titanium is finally determined about 45%. And this volume fraction will be further used in the prediction of elasto-plastic behavior of Ti-18 by EPSC model.

| Section | Surface fraction α_p | Surface fraction α_s in β matrix | Total surface fraction of α titanium |
|---------|-----------------------------|---|---|
| Radial | 18.61% | 34.96% | 47.06% |
| Axial | 24.49% | 23.86% | 42.5% |

Table 1.12 Fractions of α titanium calculated from both the radial and axial cross section.

To characterize crystallographic texture in both phases of the studied Ti alloy, two sets of pole figures, i.e. $\{0001\}$, $\{0110\}$, $\{0111\}$, $\{0112\}$ and $\{011\}$, $\{002\}$, $\{112\}$ were measured respectively for α and β titanium. The measurements were done on the surface perpendicular to axial direction. The similar character of $\{0001\}$ - α and $\{011\}$ - β pole figures (presented in Fig. 1.24a) confirms the Burgers relationship occurring between orientations of the lattices for both phases, i.e., $\{0001\}_\alpha \parallel \{011\}_\beta$ [Newkirk 53]. Moreover, both textures exhibit nearly orthorhombic symmetry. The Orientation Distribution Functions is given in Fig. 1.24b, which are determined for each phase independently from all sets of pole figures, using the WIMV method implemented in the popLA computer package [Kallend 90].



(a)

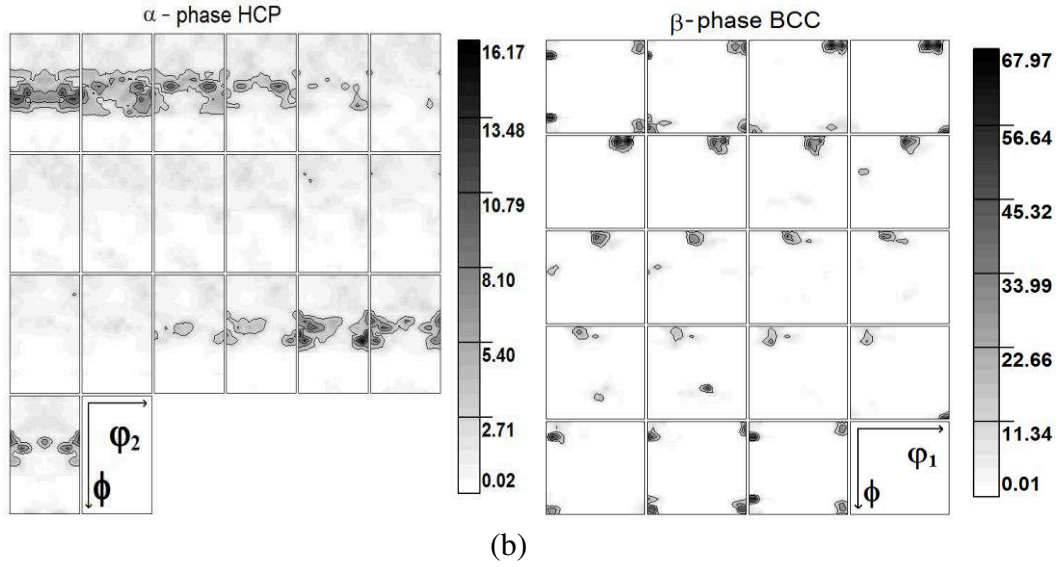


Figure 1.24 (a) Pole figures of $\{0001\}$ - α and $\{011\}$ - β plane families, confirming the Burgers relationship $\{0001\}_{\alpha} \parallel \{011\}_{\beta}$. (b) Orientation distribution functions for both phases of the studied Ti-18 alloy determined by X-ray diffraction (Cu radiation).

The single crystal elastic constants of α and β titanium are presented in table 1.13 [Fréour 05, Hu 10].

| Phase | Structure | c_{11} (GPa) | c_{12} (GPa) | c_{44} (GPa) | c_{13} (GPa) | c_{33} (GPa) |
|----------|-----------|----------------|----------------|----------------|----------------|----------------|
| α | HCP | 162 | 92 | 46.7 | 69 | 181 |
| β | BCC | 174 | 116 | 41 | Calculated | Calculated |

Table 1.13 The single crystal elastic constants of α titanium [Hu 10] and β titanium [Fréour 05].

1.3 Conclusion

In this chapter, the basic information on the elasto-plastic deformation and ductile damage inside studied materials (duplex steels and two-phase titanium) are collected from literature. The mechanism of elasto-plastic deformation for different phases of steel and titanium is described. Especially, the slip systems in different crystal structures and the mechanism of slip system activation have been deeply discussed. The initiation of ductile damage in duplex steel has also been observed in previous works. Most of these previous studies are based on the ex situ observation on material surfaces after experimental tests. In this case, the in situ information inside studied materials is lacked during the aimed processes (large deformation and/or ductile damage), and interferent (impurities, dust, particles, etc.) will be introduced

during the surface treatment, thus a further investigation is necessary to better understand the mentioned mechanism. Moreover, the behavior of duplex steel during large deformation has been studied [Le Joncour 11], a new data calibration was employed to avoid necking geometrical effect on stress determination. This new method gives new possibility for the study of damage at fine-scale.

In the present thesis, studies on elasto-plastic deformation of both phases in two-phase titanium and duplex steel will be continued. Some clues can be found from the literatures and new results will be compared with them. On one hand, in situ measurements by diffraction method will be applied to record simultaneously the interaction between grains and phases in the aimed materials. On another hand, the textured materials are selected in order to observe the influence of grains orientation on the activation of slip systems. Then the experimental results will be verified using self-consistent model and the mechanical behavior of phases within both studied materials will be analysed. As the result, the critical resolved shear stresses and work hardening parameters for slip systems will be characterized.

A further investigation on the ductile damage inside duplex steels will be carried out in this thesis. The initiation of ductile damage process in duplex steels will be observed by diffraction measurement along necking area and simulated using a new version of the self-consistent model integrating a ductile damage modelling, in order to test different damage criterion and to find out the values of some physical parameters related to the initiation of damage process.

In conclusion, by following the previous research results, we wish to determine the parameter values related to the activation of slip systems, to the linear and non-linear work hardening of both duplex steel and two-phase titanium. The ductile damage initiation inside duplex steel is another main topic of this thesis, the distribution of phase strain will be analysed through the experimental observation along necking area, and different damage criterion are proposed and tested by comparing with diffraction data. Instrumented Indentation Test (IIT) are carried out along the sample's necked part after tensile test, evolutions of hardness and elastic modulus will be analysed for both austenite and ferrite.

I hope this thesis would be helpful to extend our current knowledge on the mechanism of plastic deformation and deepen our understanding in the ductile damage process of polycrystalline materials.

Chapter 2. Experimental measurements and techniques

The main idea of this thesis is to find out the basic mechanism of elasto-plastic deformation and ductile damage occurring in multi-phase polycrystalline materials. Therefore, elasto-plastic deformation and ductile fracture process will be investigated for two-phase duplex steels and titanium alloy. In this aim, several classical or advanced experimental techniques have been involved. The studied materials, the experimental techniques as well as the methods of data analysis will be described and illustrated in the following chapter.

2.1 Measurement by diffraction method

Due to its selectivity, diffraction is considered as a powerful nondestructive inspection tool frequently used to analyse the mechanical behaviour of polycrystalline material at phase/grain scale. The diffraction method allows measuring the elastic strain at crystal lattice level inside gauge volume (diffracting volume), thereby determining independently the localized stress in each phase at mesoscopic scale. Besides, the grains inside gauge volume have different orientations and the diffraction method enables to study the variation of elastic lattice deformation for different grains or group of grains having orientations selected by experimental conditions [Ji 89, Gloaguen 02, Lin Peng 02, Ji 03, Almer 03, Gloaguen 04, Baczmański 04a, Dakhlaoui 07, Le Joncour 10, Marciszko 13, Marciszko 16].

2.1.1 Physical principles

The crystal lattice is made up of atoms which constitute $\{hkl\}$ atomic plans (Miller indices), spaced by interplanar spacing d_{hkl} (distance between two atomic plans), as illustrated in Fig. 2.1. Once the crystal is irradiated by X-rays or a beam of particles with wavelength comparable to atomic spacing, the diffraction phenomenon on the lattice occurs. In the case of crystalline solid, the incident beam scattered from lattice planes separated by the interplanar space d_{hkl} , create a constructive interference. In diffraction, the scattering angle 2θ , interplanar spacing d_{hkl} , and wavelength λ fulfill Bragg's law, expressed by Eq. 2.1.

$$2d_{hkl}\sin\theta = n\lambda \quad \text{Eq. 2.1}$$

where n is a positive integer meaning order of the reflection. The reflections in successive crystallographic planes of the crystalline lattice will be then intensified because of the cumulative effect of constructive interference [Myers 02]. Finally a diffraction pattern is obtained by measuring the intensity of scattered waves which create reflection intensity peaks at the points where the scattering angles satisfy the Bragg's condition. Besides of X-rays also the electrons, neutrons and protons can be used as radiation particles for diffraction measurement.

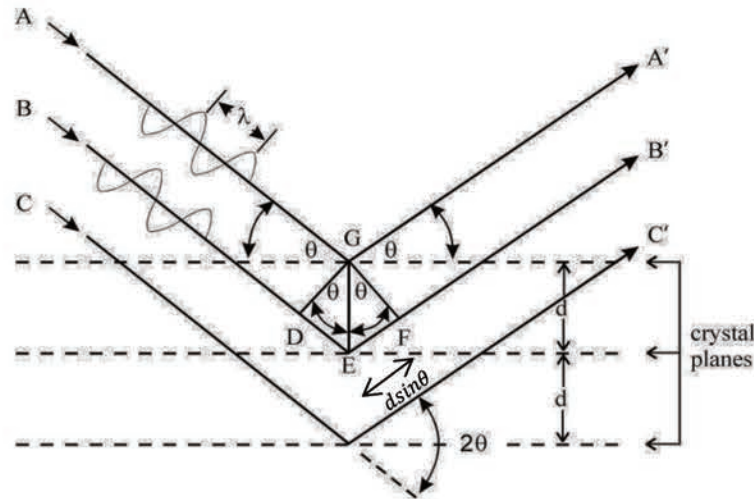


Figure 2.1 Illustration of Bragg's law.

2.1.2 Influences of microscopic phenomena on scattering patterns

Theoretically, the diffraction experiment carried out with perfectly monochromatic and parallel beam on a perfect infinite fine monocrystal will produce diffraction peaks having shape of Dirac distribution [Arfken 00]. The diffraction measurement on a polycrystal material is an average measurement on the gauge volume. The interplanar spacing d_{hkl} is the main measured quantity to determine the macroscopic and the intergranular stress. However, in the experimental data analysis, the variation of peak intensity and the variation of its width should be taken into account. In this aim, such phenomena as twinning, rotation of grains, fragmentation of grains, evolution of defects density and relaxation of the stress during damage process should be studied theoretically and experimentally.

Several microscopic phenomena will occur at different steps when the sample is under external loading. These phenomena can be indirectly observed through the variations of

diffraction peaks during materials' deformation. The relationships between diffraction peaks and micro-mechanical/microstructural phenomenon are briefly illustrated in Fig. 2.2:

- At initial state, the presence of point defects such as vacancy, self-impurity interstitial atom or impurity atom substitution; the line defects (dislocations); and the planar defects such as grain boundaries, stacking faults or twin boundary will locally influence the crystal structures.
- The homogeneous elastic deformation significantly changes the distance between atoms in the lattice. In this case, a slight variation of interplanar spacing d_{hkl} creates a slight displacement in position of diffraction peak (Fig. 2.2 elastic deformation).
- The homogenous plastic deformation results in activation of slips occurring on crystallographic planes or/and twinning phenomena. The effects of plastic deformation seen by diffraction are described in the central part of Fig. 2.2. Such process changes density of dislocations but have no influence on the average lattice parameter.
- During the large deformation process, several effects can be engendered, such as the rotation and fragmentation of polycrystalline grains, as well as the incompatibility between them leading to intergranular stresses (so called 2nd order stresses), resulting in a broadening of reflection peaks. The other phenomenon, such as multiplication of lattice defects, the beam angular divergence and wavelength dispersion can also lead to the peak broadening or shift in peaks' positions. Moreover, the intensity of diffraction peak will depend on the appearance of twinning and the evolution of crystallographic texture.
- According to our recently studies, during the ductile damage process, the creation of micro-cracks and appearance of voids can occur and some softening and relaxation of stress will be caused by the former phenomena. This stress relaxation can be observed as slight variation in interplanar spacing d_{hkl} , which creates a displacement in the position of diffraction peaks (Fig. 2.2 damage).
- Besides, the presence of stacking faults and twins can also change the position of diffraction peak.

One of the goals of this present thesis is to go deeper in the study of ductile damage initiation in the two-phase materials through the large deformation by diffraction measurement.

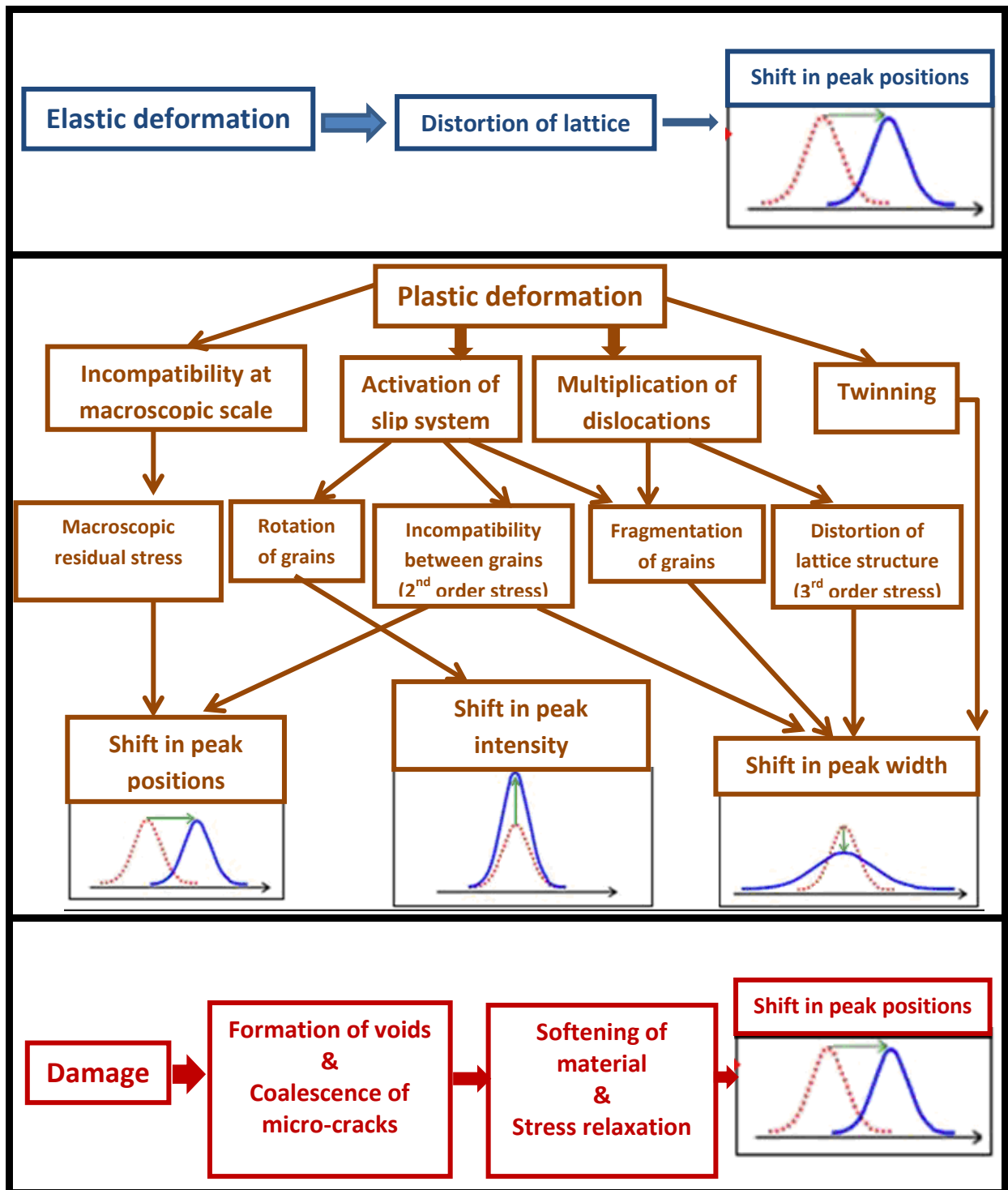


Figure 2.2 Synthesis of influences of deformation and damage mechanism on diffraction pattern described by François et Le Joncour [Le Joncour 11]. The definition of stresses at different scales (orders) is presented in section Appendix 6.

2.1.3 Tensile testes coupled with in situ diffraction measurements

In this thesis, tensile tests are performed in combination with in situ diffraction measurement, in order to real-time record the evolution of crystallites' mechanical behaviour during tensile process. In this work, samples are mounted in a tensile rig, and a uniaxial tensile load is imposed. Incident beam passes into the test sample and then diffracted beam is captured by preseted detectors.

In this work, two types of experimental set-up for diffraction measurements are used. One of the set-up is to receive the diffracted beam situated in the same side of specment as the incident beam (Fig. 2.3 a), another set-up is intended to receive the diffracted beam from the other side of material to the incident beam (Fig. 2.3b). In order to facilitate the understanding and expression of these two techniques, we named them as “**reflection**” mode and “**transmission**” mode. But it should be clear that these two techniques are not related directly to the optical reflection or transmission.

In “**reflection**” mode (Fig. 2.3a), the incident beam and the scattered beam are localized on the same side of sample surface, a detector is also positioned on the same side to receive the signal of scattered beam. In this case, the “reflection” technique is often applied to study thin films or a near-surface volume of the sample.

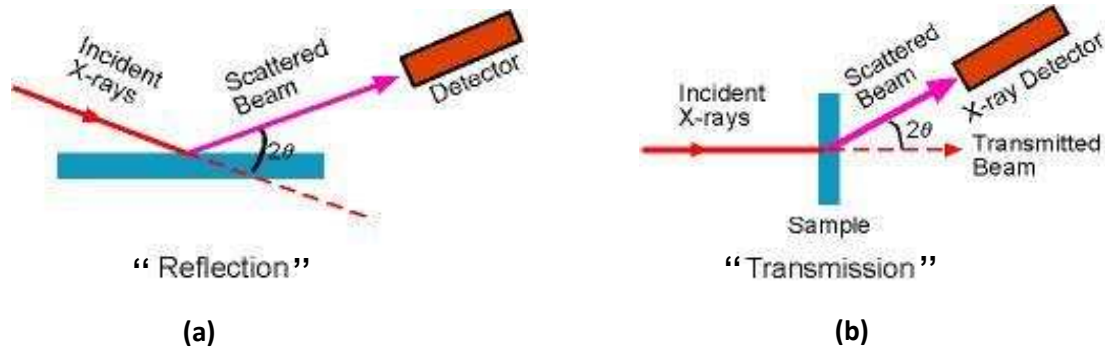


Figure 2.3 Schematic illustration of diffraction in reflection mode (a); in transmission mode (b) [UCSB].

For “**transmission**” geometry, the incident beam cross through the entire sample and the signal of scattered beam is captured by detectors situated on the other side of sample (as illustrated in Fig. 2.3b). The advantage of “transmission” mode is the possibility of measurement on the gauge volume inside specimen. Due to the requirement of deep penetration and “transmission” over the whole sample, extremely high energy of the X-ray radiation is needed (energy level of 50-100KeV for the studied metals). Alternatively, the

neutron diffraction can be used due to a low absorption of the cold or thermal neutrons in the materials, for example the metallic samples having dimensions of mm can be measured in “transmission” mode. Therefore, the measurements using “transmission” technique can be performed only with high energy synchrotron radiation or neutron radiation at large-scale experimental equipment, such as synchrotron, nuclear reactor or neutron spallation source.

2.1.4 Determination of stress state by diffraction method

The stress measurements could be performed both in reflection mode and in transmission mode. Due to the high energy dissipation and high absorption of the X-ray, the stress measurements are performed in reflection mode on experimental laboratory devices. Only in the case of high energy synchrotron radiation or neutron diffraction the measurements can be performed in the transmission mode.

2.1.4.1 Definition of reference systems

The stress state analysis is based on the diffraction measurements of interplanar spacings d_{hkl} in different directions with scattering vector $\vec{\Delta k}$ [Hauk 97]. Thus in order to describe the relative angular position of a diffraction system, it is necessary to define three orthonormal coordinate systems associated with the rotation of studied sample as well as with the scattering vector defined in a fixed frame.

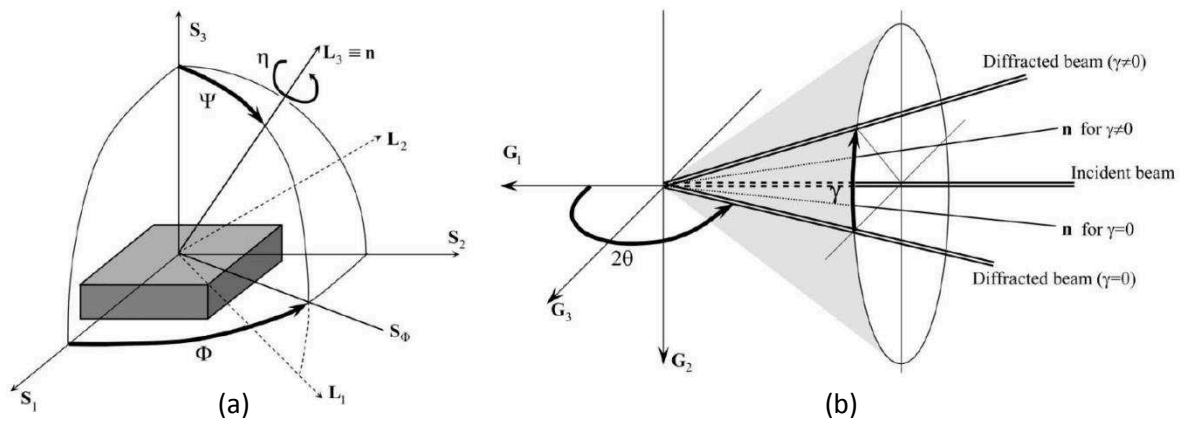


Figure 2.4 (a) Definition of sample reference system S and laboratory reference system L , the angles Ψ , Φ and η describes the relative orientation between systems G and L . And (b) the illustration of Goniometer reference system with respect to the incident and diffracted beams [François 08].

As shown in Fig. 2.4 a and b, each coordinate system is defined in the following way:

The Sample reference system (S) is fixed with respect to the sample. In sample coordinate system three axes are denoted by ($\mathbf{S}_1, \mathbf{S}_2, \mathbf{S}_3$) frame, \mathbf{S}_1 and \mathbf{S}_2 axis coplanar with the sample surface while \mathbf{S}_3 is perpendicular to the surface, the three axes are respectively perpendicular to each other. Generally, if a preferred direction exists on the sample surface, e.g. the rolling direction (RD), the axis \mathbf{S}_1 is usually chosen along this direction.

The Laboratory reference system (L): The laboratory coordinate system is denoted by ($\mathbf{L}_1, \mathbf{L}_2, \mathbf{L}_3$) frame. Axis \mathbf{L}_3 is defined parallel to the scattering vector \vec{n} , axis \mathbf{L}_2 lies on the surface plane.

Then the angular relationship between sample system \mathbf{S} and laboratory system \mathbf{L} can be described by two angles Ψ and ϕ . Ψ defines the angle between axis \mathbf{S}_3 and \mathbf{L}_3 , ϕ describes the angle between axis \mathbf{S}_1 with respect to the projection of axis \mathbf{L}_3 onto the surface plane. Another supplementary angle η is given to describe the rotation angle of laboratory system around the scattering vector.

The Goniometer reference system (G): is denoted as ($\mathbf{G}_1, \mathbf{G}_2, \mathbf{G}_3$) and used to describe the rotation of goniometer system. \mathbf{G}_1 is parallel to the incident beam, \mathbf{G}_2 represents the axial direction of goniometer (as illustrated in figure 2.4b). \mathbf{G}_3 is chosen to receive the orthonormal reference system.

2.1.4.2 Measurements of internal stress by X-ray diffraction

The analysis of stress state using X-ray diffraction measurement has been presented in literature, as for example in [Noyan 87, Hauk 97, Inal 99, Baczmański 05, Welzel 05] and developed for many special applications.

The principles of X-rays stress determination is based on the measurement of interplanar spacings $\langle d_{\vec{n}}(\phi, \psi) \rangle_{\{hkl\}}$ along scattering vector and the determination of elastic lattice strains $\langle \varepsilon_{\vec{n}}(\phi, \psi) \rangle_{\{hkl\}}$ according to Eq. 2.2,

$$\langle \varepsilon_{\vec{n}}(\phi, \psi) \rangle_{\{hkl\}} = \frac{\langle d_{\vec{n}}(\phi, \psi) \rangle_{\{hkl\}} - \langle d_{\vec{n}}^0(\phi, \psi) \rangle_{\{hkl\}}}{\langle d_{\vec{n}}^0(\phi, \psi) \rangle_{\{hkl\}}} \quad \text{Eq. 2. 2}$$

where the interplanar spacing $\langle d_{\vec{n}}(\phi, \psi) \rangle_{\{hkl\}}$ can be calculated from the position of diffraction peak for a given given $\{hkl\}$ plane family using the Bragg's law (Eq. 2.1) and

$\langle d_{\vec{n}}^0(\phi, \psi) \rangle_{\{hkl\}}$ is the strain free interplanar spacing. The $\langle \rangle_{\{hkl\}}$ brackets denote the average value of a physical quantity over the diffracting volume measured only from diffracting grains for which the scattering vector \vec{n} is perpendicular to the $\{hkl\}$ planes.

If we take the simplest case of the stress analysis for which the polycrystalline material consists of independent elastically isotropic crystallites, the macro-strain tensor $\langle \varepsilon_{ij}^S \rangle_{\{hkl\}}$ expressed in the sample frame **S** can be calculated from the tensor of first order stresses $\sigma_{ij}^{I,S}$ using Hook's law [Welzel 05],

$$\langle \varepsilon_{ij}^S \rangle_{\{hkl\}} = S_{ijkl} \langle \sigma_{kl}^{I,S} \rangle = \left[S_1 \delta_{ij} \delta_{kl} + \frac{1}{2} S_2 \frac{1}{2} (\delta_{ik} \delta_{jl} + \delta_{il} \delta_{jk}) \right] \sigma_{kl}^{I,S} \quad \text{Eq. 2. 3}$$

where δ_{ij} is the Kroneckers delta, S_{ijkl} are the elements of compliance tensor for isotropic material, S_1 and $\frac{1}{2} S_2$ are the independent components of the tensor S_{ijkl} which can be related to Young's modulus E and Poisson's ration ν of material through the relations:

$$S_1 = -\frac{\nu}{E} \quad \text{Eq. 2. 4}$$

$$\frac{1}{2} S_2 = \frac{(1 + \nu)}{E} \quad \text{Eq. 2. 5}$$

Taking into consideration the coordinate system transformation from sample reference system **S** to laboratory reference system **L**, the $\langle \varepsilon_{ij}^L(\phi, \psi) \rangle_{\{hkl\}}$ strain defined in **L** system can be related to the components of macro-stress tensor (first order stresses $\sigma_{ij}^{I,S}$) defined with respect to the **S** system:

$$\begin{aligned} \langle \varepsilon(\phi, \psi) \rangle_{\{hkl\}} = & \frac{1}{2} S_2^{\{hkl\}} \sin^2 \psi [\sigma_{11}^{I,S} \cos^2 \varphi + \sigma_{12}^{I,S} \sin 2\varphi + \sigma_{22}^{I,S} \sin^2 \varphi] \\ & + \frac{1}{2} S_2^{\{hkl\}} [\sigma_{13}^{I,S} \cos \varphi \sin 2\psi + \sigma_{23}^{I,S} \sin \varphi \sin 2\psi \\ & + \sigma_{33}^{I,S} \cos^2 \psi] + S_1^{\{hkl\}} (\sigma_{11}^{I,S} + \sigma_{22}^{I,S} + \sigma_{33}^{I,S}) \end{aligned} \quad \text{Eq. 2. 6}$$

The technique of stress analysis using above mentioned equations is called $\sin^2 \psi$ method. The hkl-dependent X-ray diffraction elastic constant $S_1^{\{hkl\}}$ and $\frac{1}{2} S_2^{\{hkl\}}$ can be calculated from

crystallite coupling models such as Voigt, Reuss and Eshelby-Kröner models, which are presented in Appendix 8.

2.1.4.3 Standard $\sin^2\psi$ method

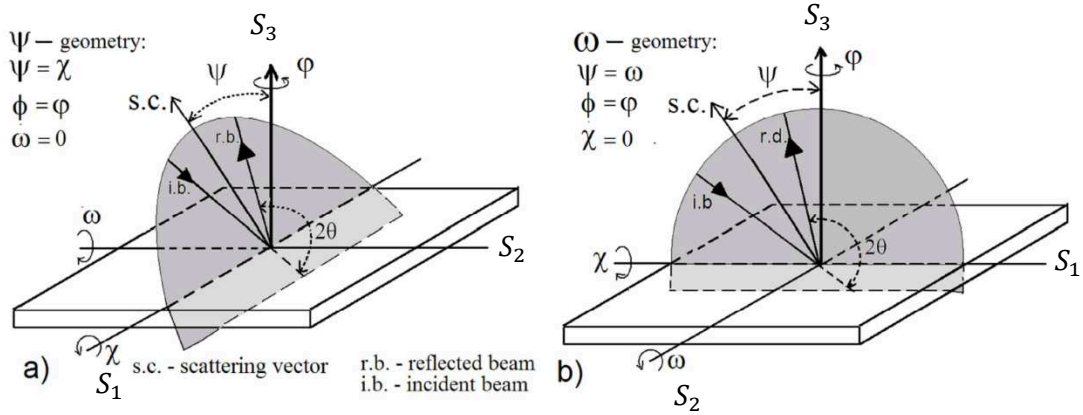


Figure 2.5 Illustration of sample position and rotation during standard $\sin^2\psi$ method measurement and the concerned frame of reference [Marciszko 13b]. (a) ψ -geometry, (b) ω -geometry.

The standard $\sin^2\psi$ method is widely used in the non-destructive analysis of stress state in polycrystalline material. In this case, as illustrated in Fig. 2.5 [Marciszko 13b]. The angle ψ is the angle between scattering vector and the axis S_3 . It exists two possible ways to change ψ angle: the first one is by tilting diffraction plane (ψ -geometry, Fig. 2.5a); the second one is by rotating the incident and diffracted beams in diffraction plane (ω -geometry, Fig. 2.5b), in this case the diffraction plane is perpendicular to the sample surface. Angle χ and ω are introduced to accomplish rotations around axis S_1 and/or around S_2 respectively. Another rotation is characterized by the azimuth angle ϕ rotating the sample around the normal to the surface, i.e. axis S_3 .

X-ray diffraction tests with rotations by ϕ and ψ angles allow determining all the six independent components of the stress tensor at a given penetration depth τ of X-ray beam using linear least squares method for the measured strains $\langle \varepsilon(\phi, \psi) \rangle_{\{hkl\}}$ expressed by Appendix 7 (the values of $F_{ij}(\phi, \psi, f)_{\{hkl\}}$ must be known). To determine six components of the stress tensor it must be assumed that the normal stress $\sigma_{33}^I = 0$, which is reasonable for the low energy X-ray radiation penetrating a shallow layer of the studied material (a few micrometers in metallic samples).

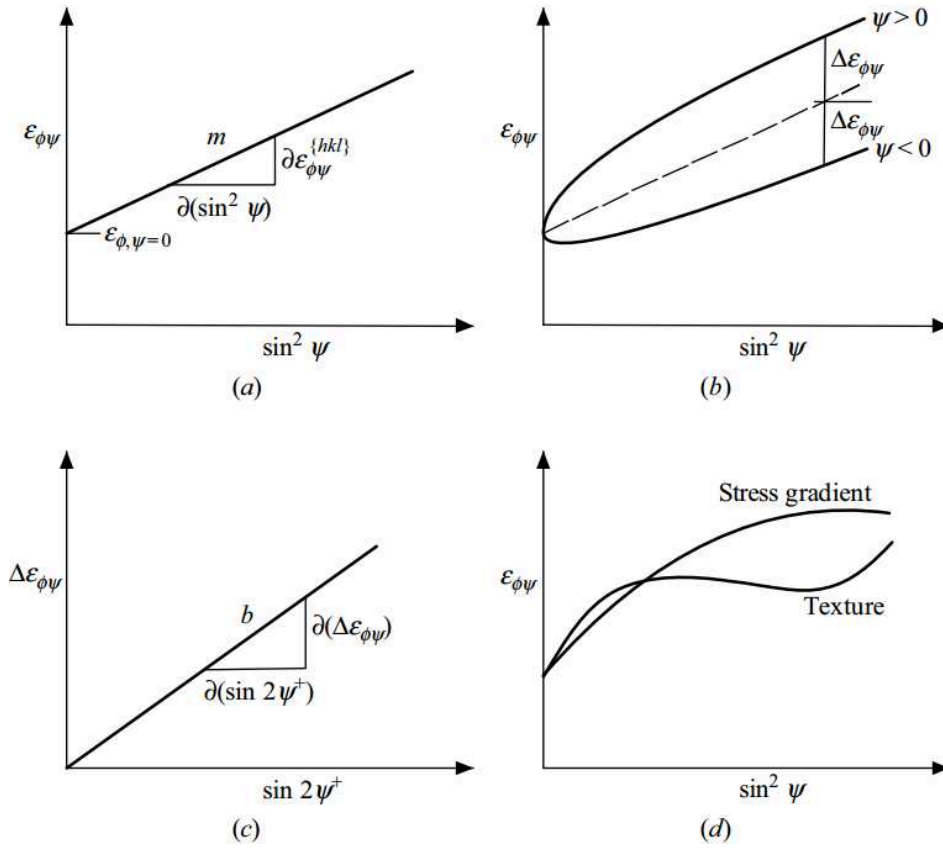


Figure 2.6 Illustration of linear least squares regression for $\sin^2\psi$ method, (a) linear plot when $\tau = 0$; (b) ψ -splitting effect when $\tau \neq 0$; (c) linear $\Delta\epsilon(\phi, \psi)_{\{hkl\}}$ vs. $\sin^2\psi^+$ curve for an isotropic material and $\tau \neq 0$, where ψ^+ means positive rotation of angle ψ ; (d) non-linear plot due to crystallographic texture, stress or composition gradient [He 11].

As illustrated in Fig. 2.6a [He 11], if shear stress components τ in the stress tensor are negligible and specimen is quasi-isotropic, the $\langle \epsilon(\phi, \psi) \rangle_{\{hkl\}}$ vs. $\sin^2\psi$ would be a linear function. In this case, the normal stress components can be calculated from the slope m of the plot using simple linear regression for Eq. 2.6 (the $S_1^{\{hkl\}}$ and $S_2^{\{hkl\}}$ constants must be known). If we take into consideration of the shear stress components τ in quasi-isotropic materials, the $\langle \epsilon(\phi, \psi) \rangle_{\{hkl\}}$ vs. $\sin^2\psi$ plot exhibits characteristic splitting of $\langle \epsilon(\phi, \psi) \rangle_{\{hkl\}}$ vs. $\sin^2\psi$ function measured for ϕ_1 (in Fig. 2.6b denoted by $\psi > 0$) and $\phi_2 = \phi_1 + 180^\circ$ (in Fig. 2.6b denoted by $\psi < 0$). The normal stresses again can be calculated using linear regression for the arithmetic mean from the measurements performed for ϕ_1 and ϕ_2 (Fig. 2.6b).

Additionally the shear stresses can be calculated from the slope b of different function $\Delta\langle \epsilon(\phi, \psi) \rangle_{\{hkl\}}$ vs. $\sin^2\psi$ plot (compared Fig. 2.6 b and c). To do this, the Eq. 2.6 must

be applied for a known values of $S_1^{\{hkl\}}$ and $S_2^{\{hkl\}}$ constants. For strongly textured materials the $\langle \varepsilon(\phi, \psi) \rangle_{\{hkl\}}$ vs. $\sin^2\psi$ plot is not linear and the component of the stress tensor can be calculated only from Eq. A7.5 (see Appendix 7) using the least square method for known $F_{ij}(\phi, \psi, f)_{\{hkl\}}$ factors (see Fig. 2.6c). Finally, in the presence of stress or composition gradient inside the tested material or presence of second order stresses, non-standard methods must be used for stress analysis.

2.1.4.4 Multi-reflection grazing incidence method

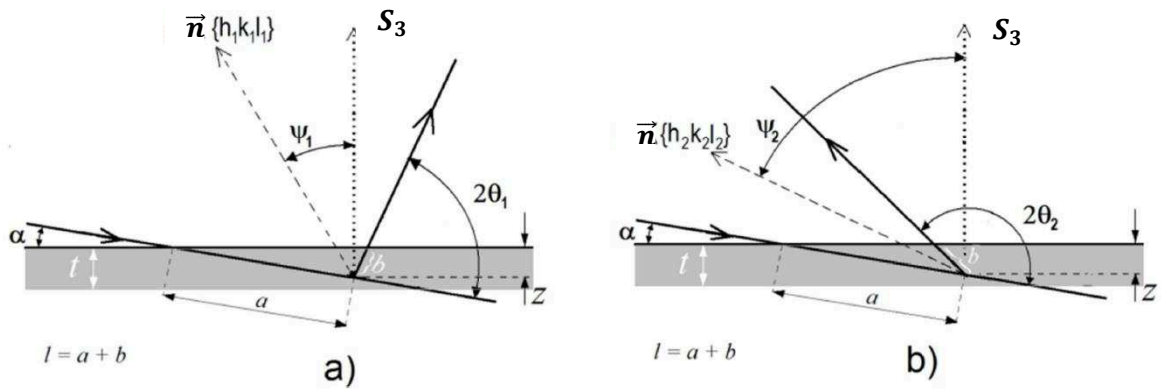


Figure 2.7 Geometry of grazing X-ray diffraction method (MGIXD). The incident angle between the sample surface and the incident beam is constant during measurement, while the orientation of the scattering vector is characterized by angle $\psi_{\{hkl\}}$ [Marciszko 13b].

The multi-reflection grazing incidence X-ray diffraction (MGIXD) [Van Acker 93, Skrzypek 01, Baczmański 04b, Genzel 05, Peng 06], called also multi $\{hkl\}$ grazing incidence method [Welzel 05], is a modification of the conventional symmetrical Bragg-Bretano geometry (theta/2theta) [Zevin 12] used in the standard $\sin^2\psi$ method. The advantage of MGIXD is the possibility of keeping constant gauge volume during measurement and enabling the stress analysis for different depths below the sample surface. This method is characterized by a small constant incident angle α with variation of scattering vector orientations, as illustrated in Fig. 2.7 [Marciszko 13b], where the angle $\psi_{\{hkl\}}$ between the normal to the sample surface and the scattering vector of a given $\{hkl\}$ reflection can be expressed by equation:

$$\psi_{\{hkl\}} = \theta_{\{hkl\}} - \alpha \quad \text{Eq. 2. 7}$$

where $2\theta_{\{hkl\}}$ is the diffraction angle corresponding to the $\{hkl\}$ reflection [Lim 87, Ma 02, Baczmański 04a, Marciszko 13a].

The effective penetration depth z can be calculated using Eq. 2.8 [Marciszko 13a], where μ is the linear X-ray absorption coefficient for the studied material:

$$z = \left(\frac{\mu}{\sin\alpha} + \frac{\mu}{\sin(2\theta_{\{hkl\}} - \alpha)} \right)^{-1} \quad \text{Eq. 2. 8}$$

Instead of the measurement of average interplanar spacing $\langle d(\phi, \psi) \rangle_{\{hkl\}}$, the equivalent lattice parameter $\langle a(\phi, \psi, z) \rangle_{\{hkl\}} = \sqrt{h^2 + k^2 + l^2} \langle d(\phi, \psi, z) \rangle_{\{hkl\}}$ at the effective penetration depth z are determined for each $\{hkl\}$ reflection. The $\langle a(\phi, \psi, z) \rangle_{\{hkl\}}$ lattice parameters are related to the first order stress tensor $\sigma_{ij}^I(z)$ for a given depth z , using the $F_{ij}(\phi, \psi, f)_{\{hkl\}}$ factors and the strain free lattice parameter a_0 :

$$\langle a(\phi, \psi, z) \rangle_{\{hkl\}} = [F_{ij}(\phi, \psi, f)_{\{hkl\}} \sigma_{ij}^I(z)] a_0 + a_0 \quad \text{Eq. 2. 9}$$

The advantage of MGIXD grazing incidence method compared with the standard $\sin^2\psi$ method is that it allows performing the measurement of stress gradient at a nearly constant depth below the sample surface. Moreover by changing appropriately the angle α the material can be investigated at different depths below the sample surface (at a micrometric scale and even less).

The grazing incidence method is chosen for our study mainly because of its advantages compared to traditional $\theta:2\theta$ method, such as a relative low requirement on the coupling between sample surface and detector, a constant penetration depth under sample surface and the possibility of measuring a highly textured material.

In this thesis, the tensile tests are performed on duplex steels with in situ diffraction measurements by neutron and synchrotron radiation. The tensile test is also carried out on two-phase titanium Ti-18 coupled with stress measurement on the sample near-surface volume with X-ray radiation. Uniaxial tensile loads are applied to the samples, while the diffraction measurements are performed for each loading step. More details concerning the experimental methods will be given in chapters 4 for duplex steels and in chapter 6 for Ti-18.

2.2 Instrumented Indentation Test (IIT)

The Instrumented Indentation Tests (IIT), is called also depth-sensing indentation or nano-indentation. Due to its possibility of applying very low loads and nano-scale measurements, the IITs have been done to investigate the mechanical behaviour of materials in the past twenty years. Various mechanical properties of materials can be measurement by this technique, such as Young's modulus, hardness [Olivier 92], yield strength [Field 95, Swain 98], work-hardening [Dao 01], fracture toughness [Jang 08] and so on.

Although the diffraction measurement, as a non-destructive method, possesses numerous advantages in the research field of crystalline materials, some limitations of this method restrict its application in several cases. In this context, the IIT is carried out in the present study as a complementary method to the diffraction measurements, to observe the evolutions of Young's modulus and hardness along the sample after its fracture for a first investigation.

2.2.1 Principe of traditional indentation test

Usually, a very hard indenter tip whose mechanical properties are known (frequently made of diamond) and with a known high precision geometry (usually a Berkovich tip [Berkovich 50]) is pressed into the sample surface. The load imposed on the indenter tip increases when the tip penetrates further into the sample until the user-defined depth. During the whole indentation process the penetration depth (denoted as h) of tip is recorded, and the load imposed on the tip (denoted as P) is measured. After nano-indentation process, a load-displacement curve (called also P - h curve, shown in Fig. 2.8) can be plotted and some desired mechanical properties can be derived from it (for instance, the Young's modulus and hardness).

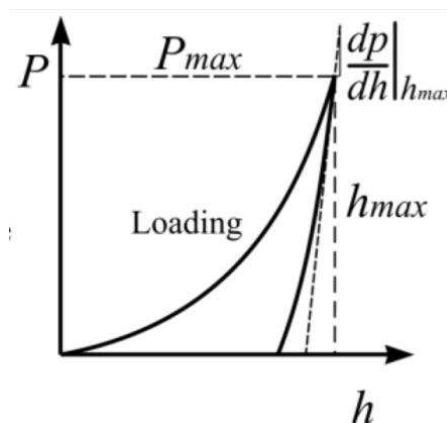


Figure 2.8 Typical load-displacement curve for indentation test [Li 14].

Once the P-h curve is obtained, the contact stiffness S_c corresponding to the initial slop of unloading curves will be firstly calculated using equation [Hay 09]:

$$S_c = \left. \frac{dP}{dh} \right|_{h=h_{max}} \quad \text{Eq. 2. 10}$$

Then the contact area A_c determined as a function of contact depth h , called “area function”. The exact expression of area function varies according to the geometries of indenter tips. For an ideal diamond Berkovich tip, the area function can be given as [Fischer-Cripps 11]:

$$A_c = 24.56h^2 + Ch \quad \text{Eq. 2. 11}$$

where C is a constant used to calibrate the uncertainty caused by the real geometry of Berkovich intender tip, in the case when the total indentation depth is less than 2 μm . The value of constant C is determined empirically by indenting a known material.

Afterwards the reduced modulus E_r [Oliver 92] can be deducted from the contact stiffness S_c and the contacted area A_c [Hay 09]:

$$E_r = \frac{\sqrt{\pi}}{2} \frac{S_c}{A_c} \quad \text{Eq. 2. 22}$$

Then the Young’s modulus E of tested material could be calculated from the reduced modulus E_r , the Young’s modulus E_i and Poisson’s ratio ν_i of indenter tip, and the Poisson’s ratio ν of tested material, using the following [Oliver 92]:

$$E = (1 - \nu^2) \left[\frac{1}{E_r} - \frac{1 - \nu_i^2}{E_i} \right]^{-1} \quad \text{Eq. 2. 13}$$

The hardness H of tested material is also calculated from the contact area A_c and load P :

$$H = \frac{P}{A_c} \quad \text{Eq. 2. 14}$$

In this thesis, the ITT method was employed on a specimen of duplex stainless steel to identify the spatial evolution of Young’s modulus and hardness after the failure of material. The measurements were performed either inside or outside the deformation necking area.

2.2.2 Description of Berkovich indenter

The Berkovich type indentation tip was used in this work. This indenter consists of a three-sided pyramid which is geometrically self-similar. The angle between the centreline and the three faces is 65.3° (as illustrated in Fig. 2.9a).

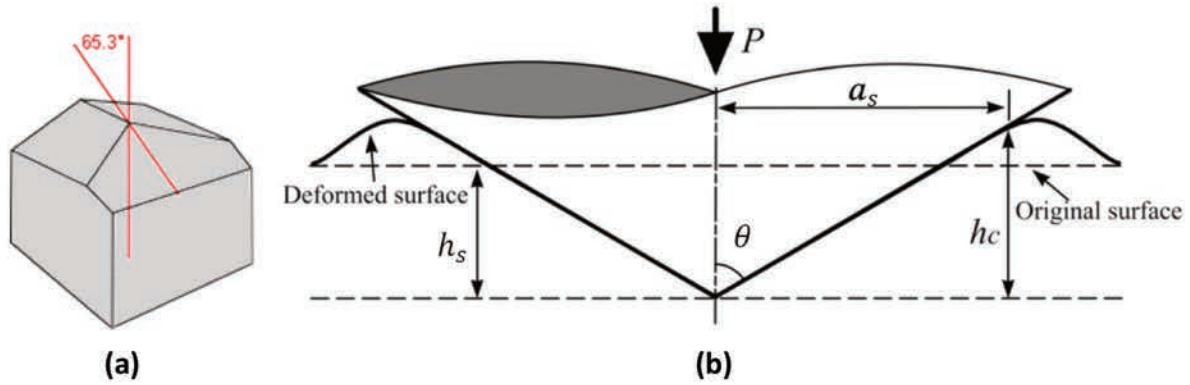


Figure 2.9 Illustration of Berkovich tip (a) and the scheme of equivalent conical indenter (b) [Li 15].

The Berkovich indenter can be simplified into an equivalent conical indenter as illustrated in Fig. 2.9b, for which the equivalent semi-apex angle θ is equal to 70.3° , a_s is the equivalent projected radius of indenter, while the h_s is the penetration depth with respect to the original surface and h_c is the penetration depth with respect to the deformed surface of the tested material [Li 15]. The a_s can be calculated from the equivalent contact area A_c :

$$A_c = \pi a_s^2 \quad \text{Eq. 2. 15}$$

This simplified model of equivalent indenter will be employed in the estimation of plastified zone created by indentation imprint (see Appendix 12).

2.3 Electron Backscatter Diffraction (EBSD)

In this thesis, the EBSD technique is used to identify the microstructure of Ti-18 alloy consisting of globular primary α_p phase and the lamellar secondary α_s embedded in β titanium.

The EBSD is a diffraction technique, allowing to measure the crystallographic orientations of grains so as to observe the microstructure of a crystalline material [Randle 00]. The history of EBSD technique can be traced back to 1928, i.e. to the first discovery of diffraction

phenomenon resulted from the back-scattered electrons by Shoji Nishikawa and Seichi Kikuchi [Nishikawa 28]. Such obtained diffraction pattern, shown by Fig.2.10, is called a Kikuchi pattern [Boersch 37].

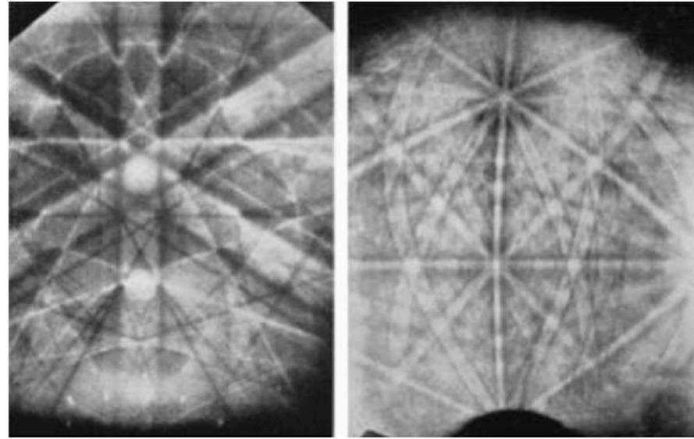


Figure 2.10 Kikuchi pattern obtained by Boersch on iron surface [Boersch 37].

Then, with introduction of Scanning Electron Microscope (SEM), the EBSD has been developed a lot since 1970s. In 1984, Dingley [Dingley 84] continued the work of Venables et al. [Venables 73] with phosphor screen and Charge Coupled Device (CCD) cameras, and added computer assisted indexation system, creating a prototype of modern EBSD system. In the following text, the principles of SEM, EBSD and Transmission Kikuchi diffraction (TKD) will be presented.

2.3.1 Scanning Electron Microscope (SEM)

The Scanning Electron Microscope (SEM) is a type of electron microscope which produces microscopic images of sample using focused beam of electrons. The major advantage of this technique is the possibility to obtain high resolution microscopic images of the studied specimen. The level of magnification allows observations at nanometric scale.

The principle of SEM is presented in Fig. 2.11 [Britannica 16]. The beam of electron emitted by high voltage cable is accelerated by electron gun, and then focused by the condenser playing a role of lenses. The objective lenses will subsequently refocus the electron beam as a very tiny spotlight with a diameter lower than 200 Å on the surface of specimen. The movement of electron beam is controlled by the scan coils to realize the scanning on the surface of specimen.

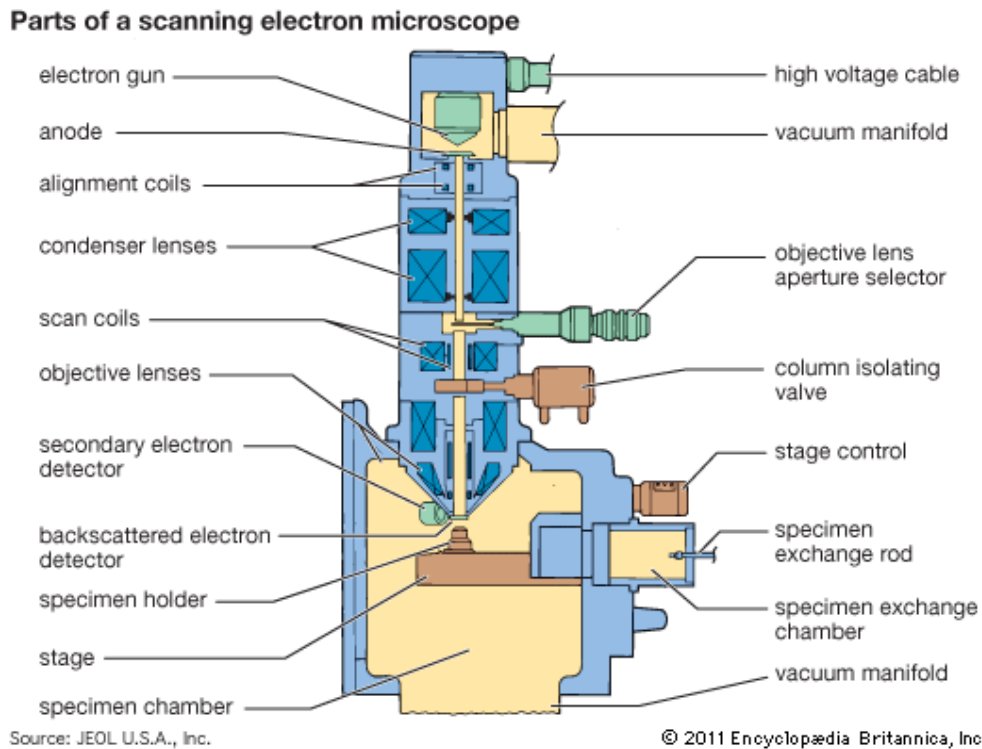


Figure 2.11 Structure of typical Scanning Electron Microscope [Britannica 16].

Under the impact of electron beam several electron signals are produced, such as: backscattered electrons of incident beam, low energy secondary electron emission, X-ray, ultra-violet photons and so on. All of these mentioned signals can help to form images, but the images are constituted basically from the signals of backscattered and secondary electrons received by detectors.

2.3.2 Electron BackScatter Diffraction (EBSD) system

Generally, the system of EBSD consists of a SEM equipped with an Electron Beam Scattering Pattern (EBSP) detector. The EBSP detector has at least one phosphor screen, one compact lens and a low-light CCD camera (as shown by Fig. 2.12).

To perform an EBSD measurement, a flat and highly polished polycrystalline specimen should be placed in the SEM sample chamber, and typically tilted 20° with respect to the incident beam (Fig. 2.12), in order to increase the contrast of diffraction pattern. The phosphor screen is inside the SEM sample chamber and coupled with a compact lens to focalize the backscattered pattern from the phosphor screen to the CCD camera.

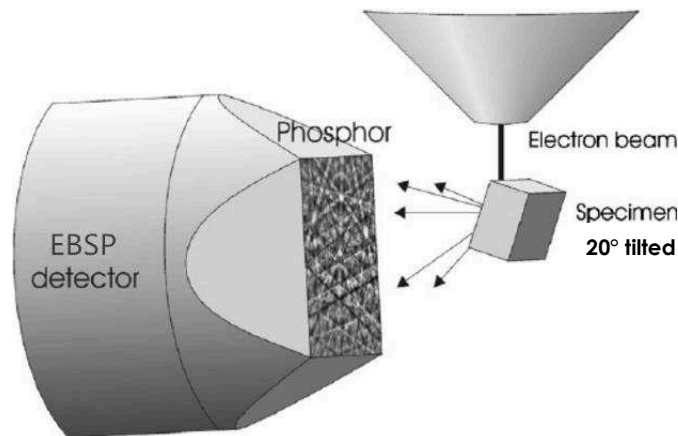


Figure 2.12 Schematic illustration of EBSD system [Winkelmann 07].

When the electron beam interacted with the crystal lattice (as shown by Fig. 2.13a), the backscatter electrons which satisfy the Bragg condition create diffraction bands on the phosphor screen, as shown in Fig. 2.13a, these bands are called Kikuchi lines, and the pattern is called Kikuchi pattern.

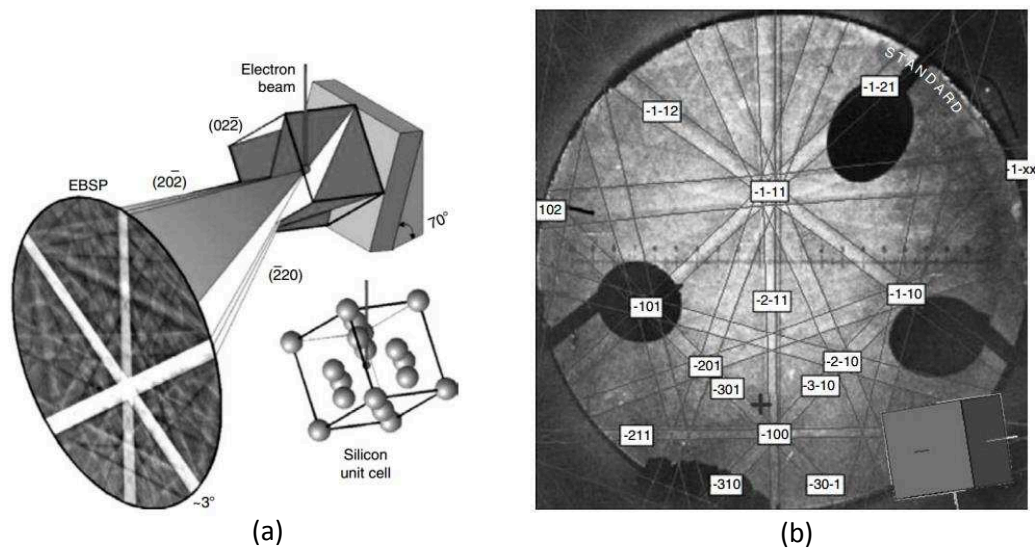


Figure 2.13 (a) Interaction of electrons with crystalline material [Day 01]. (b) Illustration for correspondence of Kikuchi lines with diffracting lattice planes [Mitland 07].

The Kikuchi lines, corresponding to lattice planes, can be individually indexed by Miller indexes (Fig. 2.13b) and used to describe the orientation of grains situated inside gauge volume by specialised software.

2.3.3 SEM Transmission Kikuchi Diffraction (TKD)

The Transmission Kikuchi Diffraction (TKD) technique has been recently introduced as a SEM based method, used to improve the spatial resolution of microscopic images by up to nanoscale (better than 10nm) [Trimby 12]. The TKD technique is based on existing EBSD hardware and software, but requiring electron transparent specimens. The specimens should be highly polished and thin enough (50 to 150nm) to receive transmission signal from the electron beam passing through the sample.

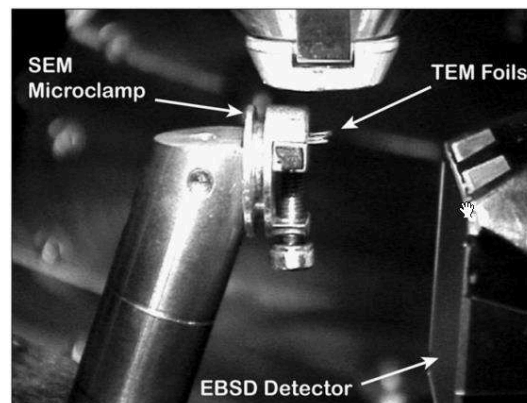


Figure 2.14 Experimental set-up of TKD measurement [Trimby 12].

As shown by Fig. 2.14, the samples are mounted horizontally in the SEM chamber, at a level above the top of the detector used in the EBSD method. The foils (samples) are mounted horizontally by tilting the SEM stage by 20° towards the EBSP detector. The samples are positioned at a short working distance (typically about 5mm). Subsequently, orientation maps can be collected without tilt correction or dynamic focus during analysis thanks to the horizontal positioning of the sample [Trimby 12].

The main advantages of TKD compared with conventional EBSD technique are:

- Higher spatial resolution (5-10nm) allowing characterizing truly nanocrystalline materials.
- Horizontally positioned samples avoiding tilt correction and the non-uniform spatial resolution on the tiled sample.
- Good contrast for image obtained by TKD.
- High-speed data acquisition and possible automate data acquisition
- The possibility of using existing EBSD hardware and software.

In this thesis, the TKD technique is used to analysis the microstructure evolution of globular α_p and lamellar α_s in Ti-18 (see chapter 6).

2.4 Methodologies used in the thesis

In this chapter, the experimental methodologies and techniques employed in this thesis are illustrated. The main experimental technique used in this work is the diffraction method. Firstly diffraction will be applied to characterize the initial stress existing within test samples. Then, the in situ diffraction measurements will be performed during tensile tests in order to study the mechanical behaviours of different phases in the investigated materials at a mesoscopic scale. Finally, the stress evolution inside studied material will be determined during the tensile test by grazing incidence method.

Both evolutions of micro-strain and internal stress provide experimental data for the later model predictions (which will be presented and explained in chapter 3). By means of the model predictions, several physical parameters concerning the plastic deformation and the initiation of ductile damage process can be identified. The identification of physical parameters, which is an important part of this thesis, contributes to the knowledge concerning the activation of slip systems in different type of lattice structures and the initiation of ductile damage within two-phase materials.

In the case of duplex steels, instrumented indentation tests will be performed on the post-fracture sample. The tested points will be spread from the fracture edge to the nearly no-deformed area, in order to observe the spatial evolution of hardness and Young's modulus for austenite and ferrite.

Moreover, the contrast tomography will be applied to observe the behaviour of different phases in titanium alloys, however with this method it is hardly possible to identify the phases due to their similar X-ray absorption (see Appendix 26).

At the end, a study on the microstructure consisting of lamellar α_s and β phases in Ti-18 will be carried out using SEM TKD technique.

Chapter 3. Elasto-plastic behaviour modelling with ductile damage process

The constitutive models are widely used in the analysis of effective mechanical behaviour for homogenous or heterogeneous polycrystalline materials. Undoubtedly, application of modelling is very helpful for the post treatment of experimental results. The constitutive models enable the quantitative determination of material properties in a more efficient way, and allow us to obtain more accurate results with much lower cost.

The earliest elastic multi-grains models were proposed by Voigt [Voigt 28] and Reuss [Reuss 29], which are based respectively on the assumptions of homogeneous strain and stress (see Appendix 8). Later, a new elastic self-consistent model was introduced by Kröner [Kröner 58, Kröner 61] for heterogeneous material. Eshelby [Eshelby 57] derived the tensor describing elastic interactions between ellipsoidal inclusion and surrounding medium. This tensor was commonly used to calculate the interaction between a grain and polycrystalline aggregate in **elasto-plastic self-consistent models** of elasto-plastic deformation. The constitutive formulation of the **rate-independent self-consistent model** was firstly proposed by Hill [Hill 65]. This formulation assumes that the stress rate is proportional to the strain rate, and the hardening process occurs due to the evolution of dislocation density. Then another version of elasto-plastic self-consistent model was proposed by Berveiller et al. [Berveiller 79] and generalized by Lipinski et al. [Lipinski 89, Lipinski 95]. This model describes the mechanical behaviour of a polycrystalline material under large elasto-plastic deformation. The rotation of grains during deformation process is also taken into consideration. The model generalized and improved by Lipinski has been used in a number of studies, in which the elasto-plastic deformations and the evolution of crystallographic texture have been predicted (by calculation of the rotation of grain lattice [Zattarin 00, Bonfoh 03, Franz 09, Nicaise 10]). This model has been also applied to compare with the experimental results obtained from diffraction measurement performed for two-phase materials [Lebensohn 93, Clausen 98, Baczmański 05, Le Joncour 10, Zecevic 15, Baczmański 16].

In the present work, an elasto-plastic rate-independent self-consistent model, based on the Lipinski and Berveiller's work [Berveiller 89, Lipinski 89, Lipinski 95], was applied to investigate the evolution of elasto-plastic properties of the studied materials. Moreover,

ductile damage modellings based respectively on hypotheses of equivalent strain, equivalent stress and total specific surface energy [Sannouni 96, Panicaud 11] are integrated in the elasto-plastic self-consistent model in order to determine the adjustable parameters of ductile damage process. The theoretical data predicted by self-consistent model will be then compared with experimental data obtained by in situ diffraction measurement during tensile test.

3.1 Definition of Representative Volume Element (RVE)

The simple grain-medium interaction models [Sachs 28, Voigt 28, Reuss 29, Taylor 38] are dedicated to identify the macroscopic behaviour of a given material, using appropriate constitutive equations based on the assumption of homogeneous stress or strain. The basic hypothesis of more advanced multi-scale models supposes that the material is not homogenous, thus the microstructure of material should be taken into account. In this case, the concept of **Representative Volume Element** (RVE) should be introduced. A RVE is defined as the smallest sub-volume of a heterogeneous material having sufficient size to represent all necessary statistic information about the microstructure of material. The RVE should be able to characterize the distribution and morphology of heterogeneous properties of studied materials [Besson 01]. In order to define an elementary representation of continuous medium, the constitutive equations must be introduced with respect to the whole structure of material. Hence, the RVE should be selected big enough to ensure that all effects occurring on the finer scales are taken into account. In polycrystalline materials, the RVE is defined as an aggregate of grains, where the number of grains can vary from dozens to thousands. The mechanisms, such as activation of slip systems, initiation of damage process are carried out at the mesoscopic (grains) or microscopic (lattice) scales.

3.2 Definition of different scales

Multi-scale modelling involves different scales, their definitions are given below:

Macroscopic scale refers to the scale of RVE, physically corresponding to the aggregate of grains or polycrystals (in this work corresponding to the gauge volume of diffraction measurements). The global behaviours of material are modelled at this level, using purely phenomenological continuous theories.

Mesosopic scale is an intermediate scale corresponding to the behaviour of grains or of single crystals. At this level, the evolution of stress and strain at grains scale related to the inter-crystalline interaction is approximated by interaction of the inclusion and surrounding average medium. The calculations are performed accounting for elastic/plastic anisotropy of grain and matrix, as well as rotation of the lattice leading to texture variation.

Microscopic scale is the most localized scale, where the plastic slip mechanism including the activation of slip systems and their work hardening (due to multiplication of dislocations) is modelled.

3.3 Approach of scale transition

The scale transition process is essential for multi-scale self-consistent modelling. The approach of scale transition is divided into three main steps. They are respectively **localization**, **local behavior calculation** and **homogenization**.

1st step: Localization

The **localization** is applied to transform physical quantities from macroscopic scale (RVE) to a finer scale. The approach involved in our modelling is called **Mean-filed**, which is more appropriate for heterogeneous microstructure.

In this approach, the localization procedure is based on the existence of fourth rank concentration tensors A_{ijkl} , related to the localization of macroscopic tensor of a physical quantity Q_{ij} . The expression of the localization process from global scale quantity Q_{ij} to local scale quantity q_{ij} is given by Eq. 3.1.

$$q_{ij}(\vec{x}, \vec{\chi}) = A_{ijkl}(\vec{x}, \vec{\chi}, \vec{x}', \vec{\chi}'): Q \quad \text{Eq. 3.1}$$

The vector \vec{x} represents the current position of localization, and $\vec{\chi}$ provides other information of grain such as orientation, the shape and the phase to which the grain belongs. The sign ' denotes the variables related to vicinity of the concerned grain.

2nd step: Modelling of local behaviour

Behaviours on mesoscopic (grains) and microscopic (lattice) scales are modelled and processed with scale transition steps of localization. The behaviours of grains and the

interaction between slip systems are computed sequentially at mesoscopic and microscopic scales.

3rd step: Homogenization

The homogenization is a process allowing to feedback the computed results on the inferior scales to the calculation of macroscopic behaviour. This step is often carried out by calculating the weighted arithmetic average of physical quantities over inferior scales, until the related macroscopic physical quantities are obtained (as shown in Fig. 3.2, page 68).

3.4 Constitutive equations of multi-scale approach

An elasto-plastic self-consistent model developed from [Hill 65] has been proposed by [Berveiller 79, Lipinski 89, Lipinski 95]. This model allows describing the mechanical behaviours of polycrystal materials under large deformation, taking into account the rotation of grains. This model can be used to predict the elasto-plastic deformation and texture evolution in polycrystalline materials. In the following text the approach of self-consistent model as well as its constitutive equations will be described step by step [Lipinski 89, Lipinski 95, Le Joncour 11, Panicaud 11].

3.4.1 Localization from RVE to grains

This step aims at finding the concentration tensor A_{ijkl} (described by Eq. 3.1), which allows to carry out the localization of macroscopic strain rate \dot{E}_{ij} to local strain rate $\dot{\epsilon}_{ij}^g$ at grain scale. It is useful to introduce the effective macroscopic elasto-plastic tangent modulus L_{ijkl}^{eff} to characterize the relation between macroscopic strain rate \dot{E}_{ij} and stress rate $\dot{\Sigma}_{ij}$ in the polycrystalline material, expressed as Eq. 3.2.

$$\dot{\Sigma}_{ij} = L_{ijkl}^{eff} \dot{E}_{kl} \quad \text{Eq. 3.2}$$

This tangent modulus tensor L_{ijkl}^{eff} is known at the beginning of elasto-plastic deformation because it is supposed to be initially equal to the overall elastic tensor C_{ijkl}^{el} of material during the elastic deformation stage.

The determination of the concentration tensor A_{ijkl} is based on two principal assumptions. Firstly, the Eshelby's model is taken into account, i.e. the grains are considered as ellipsoidal inclusions embedded in a homogeneous medium. Second assumption postulates that the strain

rate and the tangent relation do not vary inside inclusions. In consideration of these above mentioned hypotheses, the formula of concentration tensor A_{ijkl}^g for each grain g can be given as [Lipinski 89, Lipinski 95]:

$$\underline{\underline{A}}^g = \left[\underline{\underline{I}} - \underline{\underline{T}}^{gg} : (\underline{\underline{l}}^g - \underline{\underline{L}}^{eff}) \right]^{-1} \quad \text{Eq. 3.3}$$

where $\underline{\underline{I}}$ is the fourth rank identity tensor, $\underline{\underline{T}}^{gg}$ is the tensor which describes the interactions between matrix and the ellipsoidal inclusion g , $\underline{\underline{l}}^g$ is the local tangent modulus at grain level.

Generally, the interaction tensor can be defined by following expression:

$$T_{ijkl}^{gh} = \frac{1}{V_g} \int_{V_g} \int_{V_h} \Gamma_{ijkl}(\mathbf{r} - \mathbf{r}') dV_h dV_g \quad \text{Eq. 3.4}$$

where $\Gamma_{ijkl}(\mathbf{r} - \mathbf{r}')$ is a transformed Green's tensor [Mura 93, Baczmański 05] used to express the component of displacement rate at position \mathbf{r} when a unit rate of body force is applied at the position \mathbf{r}' . When $g \neq h$, the Eshelby's tensor describes the interactions between grains at long distance, which can be neglected if compared with the short distance interactions in the “one site” model. In the latter model only the T_{ijkl}^{gg} tensor (i.e. when $g = h$) is calculated and used in the Eq. 3.3 [Lipinski 89, Lipinski 95]. In this case we consider only the interaction of the inclusion with the matrix.

The T_{ijkl}^{gg} tensor is related with the Eshelby's tensor S_{ijkl}^{esh} through relation:

$$S_{ijkl}^{esh} = T_{ijmn}^{gg} L_{mnkl}^{eff} \quad \text{Eq. 3.5}$$

The concentration tensor A_{ijkl}^g then is used to localize the rate of macroscopic total strain \dot{E}_{ij} to the local one on grain scale $\dot{\varepsilon}_{ij}^g$:

$$\dot{\varepsilon}_{ij}^g = A_{ijkl}^g \dot{E}_{kl} \quad \text{Eq. 3.6}$$

3.4.2 Modelling of local behaviour

The local behaviours at grains and lattice scales will be calculated in order to predict the plastic deformation and interactions between grains. The plastic deformation is mainly created

by slip and twinning phenomena. This presented model is our first approach for elasto-plastic behaviour modelling, only slip phenomenon in cubic and/or hexagonal lattice is taken into account. The twinning and the modelling of other phenomena can be the next objective of our work. The constitutive equations of local behaviours at grains and lattice scales will be described.

3.4.2.1 Modelling on grains scale

In general case of nonlinear elasto-plastic deformation, the strain rate $\dot{\epsilon}_{ij}^g$ for a given grain or single crystal g under local stress rate $\dot{\sigma}_{ij}^g$ can be expressed by the relation:

$$\dot{\sigma}_{ij}^g = l_{ijkl}^g \dot{\epsilon}_{kl}^g \quad \text{Eq. 3.7}$$

where l_{ijkl}^g is the local tangent modulus for a grain.

For the elastic deformation the above equation takes form:

$$\dot{\sigma}_{ij}^g = c_{ijkl}^g \dot{\epsilon}_{kl}^{g\,el} \quad \text{Eq. 3.8}$$

where c_{ijkl}^g is the single crystal stiffness tensor of a grain.

The elastic deformation is modelled at grain level, while the plasticity of material is calculated at the level of slip systems.

3.4.2.2 Scale transition from grains to slip systems

The process of plastic deformation is modelled at lattice level. In this case, it is necessary to calculate the shear stress on each slip systems s from stress tensor defined at a grain scale. This can be done using the symmetric Schmid's tensor $M_{ij}^{s\,sym}$, as given below:

$$\tau^s = \sigma_{ij}^g : M_{ij}^{s\,sym} \quad \text{Eq. 3.9}$$

where τ^s is the shear stress imposed on the slip system, the $M_{ij}^{s\,sym}$ can be calculated by:

$$M_{ij}^{s\,sym} = \frac{1}{2} (n_i m_j + m_i n_j) \quad \text{Eq. 3.10}$$

where m_i is the unit vector parallel to gliding direction, n_i is the unit normal vector to the gliding plane.

3.4.2.3 Modelling at slip systems scale

Then the slip system is activated if the shear stress τ^s reaches the critical resolved shear stress (CRSS) τ_c^s :

$$f = \tau^s - \tau_c^s \quad \text{Eq. 3.11}$$

If the criterion ≥ 0 , it means $\tau^s \geq \tau_c^s$, the slip system is activated, otherwise still elastic deformation occurs.

During the plastic deformation, the multiplication and the spatial evolution of dislocations in the grain lead to work hardening, i.e. an increasing in CRSS. In this part of model, only linear work hardening is modelled. The latent hardening or self-hardening can be expressed by components H^{ts} of the hardening matrix characterizing the interactions between slip systems t and s [Lipinski 89, Lipinski95]:

$$\dot{\tau}_c^t = \sum_s H^{ts} \dot{\gamma}^s \quad \text{Eq. 3.12}$$

where $\dot{\gamma}^s$ is the rate of plastic glide on the active slip system s interacting with slip system t :

$$\dot{\gamma}^s = \sum_t N^{st} M_{ij}^{t \text{ sym}} c_{ijkl}^g \dot{\epsilon}_{kl}^g \quad \text{Eq. 3.13}$$

where N^{ts} is the matrix calculated for all active slip systems:

$$N^{st} = (H^{ts} + M_{ij}^{ts \text{ sym}} : c_{ijkl}^g : M_{ijkl}^{st \text{ sym}}) \quad \text{Eq. 3.14}$$

The constitutive equations for nonlinear work hardening will be later presented in the modelling of large deformation.

3.4.3 Homogenization from lattice to RVE

After calculations of local behaviours, the feedback calculations should be done in order to relate the local results to the superior scales and to predict the macroscopic behaviour at RVE scale.

3.4.3.1 Homogenization from slip systems to grains scale

The glide of slip systems will lead to significant rotation and plastic deformation on the grain as illustrated in Fig. 3.1. The rate of plastic deformation rate $\dot{\varepsilon}_{ij}^{g pl}$ can be expressed by the symmetric Schmid tensor $M_{ij}^{s sym}$ and the plastic glide rate $\dot{\gamma}^t$ on the scale of slip systems:

$$\dot{\varepsilon}_{ij}^{g pl} = \sum_s M_{ij}^{s sym} \dot{\gamma}^s \quad \text{Eq. 3.15}$$

while the rotation rate for the grain can be given by the anti-symmetric Schmid tensor $M_{ij}^{s anti}$ as:

$$\dot{\omega}_{ij}^{g pl} = \sum_s M_{ij}^{s anti} \dot{\gamma}^s \quad \text{Eq. 3.16}$$

where the anti-symmetric Schmid tensor $M_{ij}^{s anti}$ is defined as:

$$M_{ij}^{s anti} = \frac{1}{2} (n_i m_j - m_i n_j) \quad \text{Eq. 3.17}$$

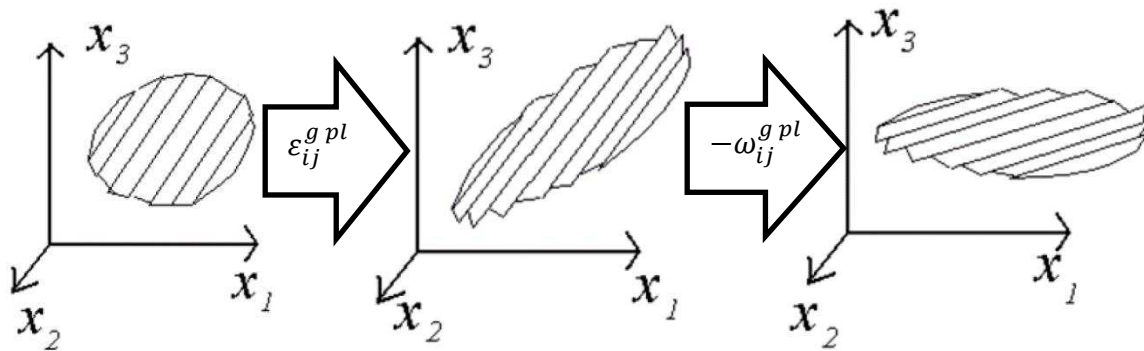


Figure 3.1 Schematic illustration of plastic and rotating behaviour of a grain during plastic deformation [Baczmanski 05].

This step can be considered as the homogenization between microscopic (slip systems) scale and the mesoscopic (grain) scale. The formula for calculation of the elasto-plastic tangent modulus l_{ijkl}^g for an undamaged grain g can be deducted from the active slip systems and it was derived by Lipinski et al., 1989 [Lipinski 89]:

$$l_{ijkl}^g = c_{ijkl}^g - \sum_{st}^{N^{st active}} c_{ijmn}^g : M_{mn}^{s sym} N^{st} M_{op}^{t sym} : c_{opkl}^g \quad \text{Eq. 3.18}$$

3.4.3.2 Homogenization from grains to RVE scale

This approach of homogenization from grains to RVE is to calculate the new macroscopic elasto-plastic tangent modulus at each iterative step.

In the case of elastic deformation of undamaged material, the effective macroscopic elastic modulus C_{ijkl}^{eff} is computed from the single crystal elastic constants c_{ijkl}^g , the concentration tensor A_{ijkl}^g , and the volume fraction f^g of each grain:

$$C_{ijkl}^{eff} = \sum_1^{N^g} f^g c_{ijmn}^g : A_{mnkl}^g \quad \text{Eq. 3.19}$$

Then, when the material undergoes plastic deformation, the effective macroscopic tangent modulus L_{ijkl}^{eff} can be calculated from analogical equation:

$$L_{ijkl}^{eff} = \sum_1^{N^g} f^g l_{ijmn}^g : A_{mnkl}^g \quad \text{Eq. 3.20}$$

where l_{ijkl}^g is the local tangent modulus.

3.4.4 Synthesis of elasto-plastic self-consistent model

To summarize, the steps of scale transitions and physical entities concerned on each scale were illustrated in Fig. 3.2:

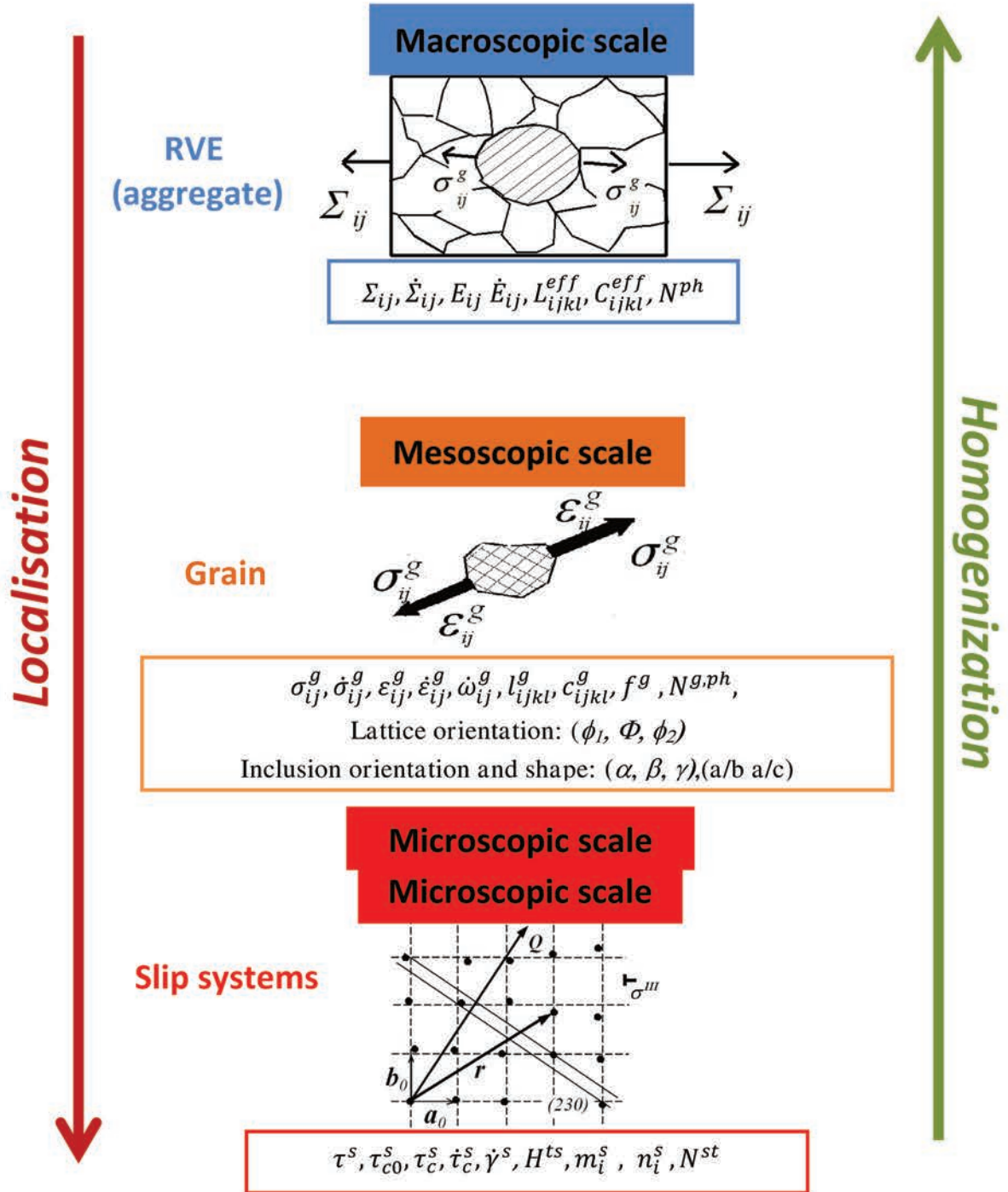


Figure 3.2 Schematics of multi-scale transition. The parameters of model are explained in table 3.1.

Among parameters presented in Fig. 3.2, the input parameters of model are picked out and listed in the table 3.1:

| Scale | Notation | Physical signification |
|--------------|---|--|
| RVE | N^{ph} | Number of phases in the material |
| Grains | N^g | Number of grains in RVE (respective for each phase) |
| | f^g | Volume fraction of individual grain |
| | c_{ijkl}^g | Stiffness tensor for each grain |
| | (ϕ_1, Φ, ϕ_2) | Euler angles defining lattice orientation (statistically described by ODF) |
| | a/b and a/c; α, β, γ | Aspect ratios of the inclusion axes; Euler angles defining orientation of the inclusion axes |
| Slip systems | N^s | Number of slip systems (respectively for each phase) |
| | $\{hkl\}\langle uvw \rangle$ and m_i^s, n_i^s | Slip systems with corresponding vectors: parallel to gliding direction and normal to the gliding plane |
| | τ_{c0}^s | Initial CRSS |
| | H^{ts} | Work hardening parameter or parameters of hardening law (for example Voce law given by Eq. 3.30) |

Table 3.1 Synthesis of input parameters of used self-consistent model.

- The number of phase N^{ph} are given and fixed according to the real number of phases in the material.
- The number of grains N^g are given and fixed preliminary and enough to ensure the representativeness of RVE.
- The initial orientation of grains (ϕ_1, Φ, ϕ_2) is given by Euler angles [Bunge 69], according to the measured orientation distribution function (ODF) - $f_0^g(\phi_1, \Phi, \phi_2)$. (f^g : Volume fraction of individual grain).
- The stiffness tensors c_{ijkl}^g for different single crystals are taken from the literatures [Simons 71, Inal 99, Fréour 05, Hu 10].

- Aspect ratios of the inclusion axes (a/b and a/c , the ratios between major axis and minor axis of grains are defined as 1 for simplest assumption of homogeneous grains shape in this study) and Euler angles defining orientation of the inclusion axes (α, β, γ).
- The number of slip systems $\{hkl\}\langle uvw \rangle$ and their vector m_i^s as well as the vector n_i^s are found from the literatures [Schmid 50, Patridge 67, Person 67, Yoo 81, Balasubramanian 02, Peters 03, El Bartali 07, Lütjering 07].
- The initial CRSS τ_{c0}^s is the critical shear stress identified by fitting the experimental curves with prediction results.
- Work hardening parameter H or parameters of hardening law (for example Voce law given by Eq. 3.30), which reflects the interaction between slip systems t and s .

The classification of these three scales and the corresponding physical quantities are defined with respect to the observation of plastic deformation. The micro-mechanical models compared with the experimental observation allow us to trace back to the original reasons of elasto-plastic deformation and damage process.

3.5 Modelling of nonlinear work hardening and ductile damage

The pre-existing self-consistent model has been developed by introducing the ductile damage effect [Panicaud 11] and used in this work. The ductile damage is modelled with the assumption of energy equivalence [Saanouni 96] applied at grains scale.

3.5.1 Damage modelling at grains scale

The conceptions of effective total strain tensor $\tilde{\varepsilon}_{ij}^g$ and of effective stress tensor $\tilde{\sigma}_{ij}^g$ for each grain g in the fictive undamaged configuration is based on the equations:

$$\tilde{\varepsilon}_{ij}^g = \varepsilon_{ij}^g \sqrt{1 - d^g} \quad \text{Eq. 3.21}$$

$$\tilde{\sigma}_{ij}^g = \frac{\sigma_{ij}^g}{\sqrt{1 - d^g}} \quad \text{Eq. 3.22}$$

d^g is a scalar parameter used to represent the damage magnitude at grain scale (or mesoscopic), ε_{ij}^g and σ_{ij}^g are the strain and stress in the considered damaged grain.

Then the relation between the rate of local effective total strain and effective stress rate is rewritten as:

$$\dot{\sigma}_{ij}^g = l_{ijkl}^g \dot{\varepsilon}_{kl}^g \quad \text{Eq. 3.23}$$

while the same relation for damaged grain takes form:

$$\dot{\sigma}_{ij}^g = \tilde{l}_{ijkl}^g \dot{\varepsilon}_{kl}^g \quad \text{Eq. 3.24}$$

where \tilde{l}_{ijkl}^g and l_{ijkl}^g are the local tangent modulus tensors for damaged and fictive undamaged grains, respectively.

Substituting Eq. 3.21 and Eq. 3.22 into Eq. 3.23, the relation between the rate of local total strain and effective stress rate for damaged grain can be expressed through:

$$\dot{\sigma}_{ij}^g = (1 - d^g) l_{ijkl}^g \dot{\varepsilon}_{kl}^g - \frac{1}{2} (l_{ijkl}^g \varepsilon_{kl}^g + \frac{1}{1 - d^g} \sigma_{ij}^g) \dot{d}^g \quad \text{Eq. 3.25}$$

When we suppose that the damage parameter d^g is a function of local stress σ_{ij}^g and local strain ε_{ij}^g , such as $d^g = f(\sigma_{ij}^g, \varepsilon_{ij}^g)$, the formula Eq. 3.25 can be rewritten as:

$$\begin{aligned} \dot{\sigma}_{ij}^g = & (1 - d^g) l_{ijkl}^g \dot{\varepsilon}_{kl}^g - \frac{1}{2} (l_{ijkl}^g \varepsilon_{kl}^g + \frac{1}{1 - d^g} \sigma_{ij}^g) \left(\frac{\partial d^g}{\partial \varepsilon_{ij}^g} \dot{\varepsilon}_{ij}^g \right) \\ & - \frac{1}{2} \left(l_{ijkl}^g \varepsilon_{kl}^g + \frac{1}{1 - d^g} \sigma_{ij}^g \right) \left(\frac{\partial d^g}{\partial \sigma_{ij}^g} : \dot{\sigma}_{ij}^g \right) \end{aligned} \quad \text{Eq. 3.26}$$

Comparing the above equation with Eq.3.23, the equivalent elasto-plastic tangent modulus for a damaged grain can be obtained:

$$\begin{aligned} \underline{\tilde{l}}^g = & \left(\underline{I} + \frac{1}{2} \left(\underline{l}^g : \underline{\varepsilon}^g + \frac{1}{1 - d^g} \underline{\sigma}^g \right) \otimes \frac{\partial d^g}{\partial \underline{\varepsilon}^g} \right)^{-1} : \\ & \left(\left(\underline{I} - d^g \right) \underline{l}^g - \frac{1}{2} \left(\underline{l}^g : \underline{\varepsilon}^g + \frac{1}{1 - d^g} \underline{\sigma}^g \right) \otimes \frac{\partial d^g}{\partial \underline{\varepsilon}^g} \right) \end{aligned} \quad \text{Eq. 3.27}$$

3.5.2 Damage modelling at slip systems scale

If the ductile damage is taken into consideration, the criterion of plasticity should also be modified to include the damage process.

The effective plastic glide $\tilde{\gamma}^s$ as well as the effective CRSS $\tilde{\tau}_c^s$ can be defined on the damageable material as in Eq. 3.28 and Eq. 3.29:

$$\tilde{\gamma}^s = \gamma^s \sqrt{1 - d^g} \quad \text{Eq. 3.28}$$

$$\tilde{\tau}_c^s = \frac{\tau_c^s}{\sqrt{1 - d^g}} \quad \text{Eq. 3.29}$$

3.5.2.1 Modelling of linear hardening

Hence, according to this approach the classical linear yielding criterion for the activation of a given slip system can be expressed as [Panicaud 11, Baczmański 16]:

$$f_{linear}^s = \tilde{\tau}_c^s - \left(\tau_{c0}^s + \sum_t H^{ts} \tilde{\gamma}^t \right) \leq 0 \quad \text{Eq. 3.30}$$

where τ_{c0}^s is the initial CRSS on the slip system s , and H^{ts} is the hardening matrix in the undamaged material.

3.5.2.2 Modelling of nonlinear hardening

However, a nonlinear hardening process is necessary in the case of large deformation. The Voce law [Tomé 84] is usually employed in the self-consistent prediction model to describe the nonlinear evolution of slip systems. In this case, the criterion of plasticity can be given by following formula [Follansbee 88, Kocks 88, Bouvier 05, Panicaud 11, Baczmański 16]:

$$f_{voce}^s = \tilde{\tau}_c^g - \left(\tau_{c0}^{ph} + (\tau_1^{ph} + \theta_1^{ph} \tilde{v}^g) \left[1 - \exp \left(-\frac{\theta_0^{ph}}{\tau_1^{ph}} \tilde{v}^g \right) \right] \right) \leq 0 \quad \text{Eq. 3.31}$$

where \tilde{v}^g is the sum of plastic shear strain accumulated on all slip systems in a given grain g :

$$\tilde{v}^g = \sum_s \tilde{\gamma}^s \quad \text{Eq. 3.32}$$

τ_0^{ph} , τ_1^{ph} , θ_0^{ph} and θ_1^{ph} are parameters of Voce law which should be identified for different phases. The τ_0^{ph} is the initial CRSS as well as τ_1^{ph} is the asymptotic tangent CRSS for phase ph obtained from the final hardening region (straight line as shown in Fig. 3.3). The θ_0^{ph} is the initial hardening ($H_{initial}^{ts} = \theta_0^{ph}$) while the θ_1^{ph} is the final hardening ($H_{final}^{ts} = \theta_1^{ph}$) of phase ph . The significations of Voce parameters are synthesized in table 3.2. In the case of multi-phase modelling these mentioned parameters will be determined respectively for each phase.

It is noteworthy that the microscopic damage related to the effective CRSS is the same for all slip systems within a given grain.

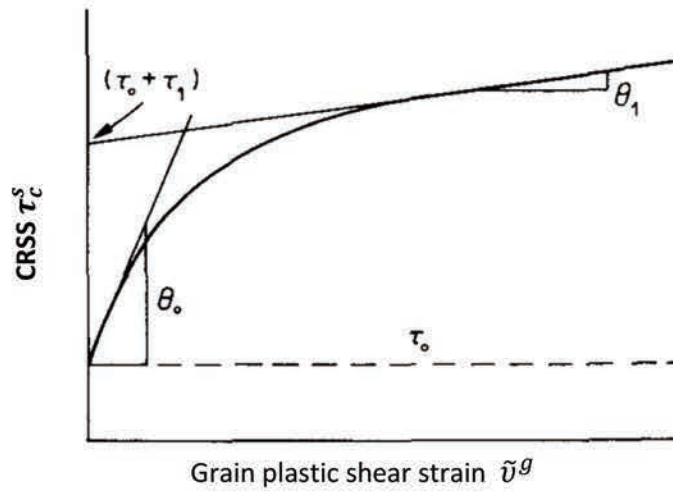


Figure 3.3 Schematic representation of the dependence of the CRSS τ_c^s on the sum of plastic shear strain $\tilde{\nu}^g$ accumulated over all slip system s in grain g [Tomé 84].

| Process | Parameter | Physical meaning of parameter | Effects of the parameter on the results of diffraction or mechanical experiments |
|---------------------------|------------------|--|--|
| Small plastic deformation | τ_{c0}^{ph} | Initial value of CRSS | Determines the yield stress for the phase ph . |
| | θ_0^{ph} | Initial hardening of the slip system for small deformation | Determines the slopes and non-linearity of the hardening in each phase. |
| Large plastic deformation | τ_1^{ph} | Back extrapolated CRSS | |
| | θ_1^{ph} | Hardening of the slip system for the large deformation | |

Table 3.2 Synthesis of Voce law parameters used in the self-consistent model [Baczmański 16].

The variation rate of CRSS can be thus obtained by differentiating Eq. 3.28 and Eq. 3.29 and using the plasticity criterion Eq. 3.30 [Panicaud 11]:

$$\begin{aligned}\dot{\tau}_c^s &= (1 - d^g) \sum_t H^{ts} \dot{\gamma}^t - \frac{1}{2} \left(2 \sum_t H^{ts} \gamma^t + \frac{1}{\sqrt{1 - d^g}} \tau_0^s \right) \dot{d}^g \\ &= (1 - d^g) \sum_t H^{ts} \dot{\gamma}^t - \frac{1}{2} \left(\sum_t H^{ts} \gamma^t + \frac{1}{1 - d^g} \tau_c^s \right) \dot{d}^g\end{aligned}\tag{Eq. 3.33}$$

Furthermore, if the anisotropic hardening based on Voce law is applied, the component H^{ts} of hardening matrix in Eq. 3.33 can be expressed as [Le Joncour 10, Panicaud 11]:

$$H^{ts} = \frac{\partial \tau_c^g}{\partial \tilde{\nu}^g} h^{ts}\tag{Eq. 3.34}$$

h^{ts} is a component of the matrix which indicates the proportion of latent hardening or self-hardening between slip systems s and t .

3.5.2.3 Equivalent strain criterion for micro-damage process

To describe micro-damage process occurring in the grain, the parameter of isotropic damage evolution \dot{d}^g at the grain scale is established in function of the equivalent grain strain ε_{eq}^g , expressed as model [Baczmański 16]:

$$\dot{d}^g = \xi^{ph} (\varepsilon_{eq}^g - \varepsilon_0^{ph})_+^{n^{ph}} (\dot{\varepsilon}_{eq}^g)_+\tag{Eq. 3.35}$$

where ε_0^{ph} , n^{ph} , ξ^{ph} are phase-dependent parameters for a given phase, $(\mathbf{x})_+$ are the Macaulay brackets, denoting the positive part of the variable \mathbf{x} , i.e. $(\mathbf{x})_+ = \mathbf{x}$ if $\mathbf{x} > 0$, $(\mathbf{x})_+ = 0$ if $\mathbf{x} \leq 0$. ε_{eq}^g is the second invariant of the total strain tensor for a grain g , calculated as:

$$\varepsilon_{eq}^g = \sqrt{\frac{2}{3} \left(\tilde{\varepsilon}_{ij}^g - \frac{1}{3} tr(\tilde{\varepsilon}_{ij}^g) I_{ij} \right) : \left(\tilde{\varepsilon}_{ij}^g - \frac{1}{3} tr(\tilde{\varepsilon}_{ij}^g) I_{ij} \right)}\tag{Eq. 3.36}$$

where ε_{ij}^g is the total elasto-plastic deformation of a grain g during whole process.

ε_0^{ph} , n^{ph} , ξ^{ph} are the adjustable parameters related to the relaxation and damage effect of the given phase. Their physical meanings are synthesized in table 3.3:

| Process | Parameter | Physical meaning of parameter |
|-------------------|----------------------|---|
| Damage initiation | ε_0^{ph} | Critical value of equivalent total strain in a given phase for initiation of damage. The ε_0^{ph} describes the initiation of damage process, and can be unambiguously determined for each phase by comparing the theoretical prediction results with the experimental diffraction results (as it is explained in the next chapter 4). |
| Damage evolution | n^{ph} | Parameters describing the stress relaxation occurring in a given phase, interpreted as ductile damage occurring in this phase. ξ^{ph} changes the slop and n^{ph} adjusts nonlinearity of ($\langle \varepsilon_{app} \rangle_{ph}$ vs. Σ_{app} plot, and influence the macroscopic Σ_{app} vs. E_{app} plot in loading direction. |
| | ξ^{ph} | |

Table 3.3 Synthesis of adjustable parameters used to describe the damage process [Baczmanski 16].

In this section, we present only the equivalent strain damage criterion, other criteria for ductile damage (the equivalent stress criterion and total energy criterion) will be presented and compared in chapter 4.

3.5.3 Approach of localization with damage effect

Once the damage process is initiated, the strain rate localization given by Eq. 3.6 should be modified. For the fictive undamaged material the localization process can be rewritten as:

$$\dot{\varepsilon}_{ij}^g = A_{ijkl}^g \dot{E}_{kl} \quad \text{Eq. 3.37}$$

Differentiating the Eq. 3.8 between local strain and effective local strain, we can obtain a relation between the rate of local strain $\dot{\varepsilon}_{ij}^g$ and the rate of effective local strain $\dot{\varepsilon}_{ij}^g$ [Panicaud 11]:

$$\dot{\varepsilon}_{ij}^g = \Xi_{ijkl}^g \dot{\varepsilon}_{kl}^g \quad \text{Eq. 3.38}$$

$$\text{with: } \Xi_{ijkl}^g = \left((\sqrt{1-d^g}) \underline{I} - \frac{\underline{\varepsilon}^g}{2\sqrt{1-d^g}} \frac{\partial d^g}{\partial \underline{\varepsilon}^g} \right)^{-1} \quad \text{Eq. 3.39}$$

under the assumption that the damage depends only on the total strain at grain scale.

The relation between the increment of strain \dot{E}_{ij} and the rate of effective strain $\dot{\tilde{E}}_{ij}$ on macroscopic scale should also be introduced:

$$\dot{\tilde{E}}_{ij} = Z_{ijkl} \dot{E}_{kl} \quad \text{Eq. 3.40}$$

Applying Eq. 3.37 and Eq. 3.38 into Eq.3.39, a new localizing relation can be found:

$$\dot{\varepsilon}_{ij}^g = \Xi_{ijmn}^g A_{mnop}^g Z_{opkl} \dot{E}_{kl} \equiv \tilde{A}_{ijkl}^g \dot{E}_{kl} \quad \text{Eq. 3.41}$$

The fourth rank tensor Z_{ijkl} can be calculated by the integration of mesoscopic strains over RVE:

$$\dot{E}_{ij} = \frac{1}{V} \int_V \dot{\varepsilon}_{ij}^g dV \quad \text{Eq. 3.42}$$

$$\Rightarrow \underline{\underline{Z}} = \left(\frac{1}{V} \int_V \underline{\underline{\Xi}}^g \underline{\underline{A}}^g dV \right)^{-1} \quad \text{Eq. 3.43}$$

$$\text{Or } \underline{\underline{Z}} = \left(\sum_g f^g \underline{\underline{\Xi}}^g \underline{\underline{A}}^g \right)^{-1} \quad \text{Eq. 3.44}$$

where f^g is the volume fraction of grain g . Using the expression for \tilde{A}_{ijkl}^g (Eq.3.41) and the explicit form of Z_{ijkl} (Eq. 3. 44), the strain localization tensor \tilde{A}_{ijkl}^g for damaged material can be obtained as [Panicaud 11, Baczmański 16]:

$$\underline{\underline{\tilde{A}}}^g = \underline{\underline{\Xi}}^g : \underline{\underline{A}}^g : \underline{\underline{Z}} = \quad \text{Eq. 3.45}$$

$$\left((\sqrt{1-d^g}) \underline{\underline{I}} - \frac{\underline{\underline{\varepsilon}}^g}{2\sqrt{1-d^g}} \otimes \frac{\partial d^g}{\partial \underline{\underline{\varepsilon}}^g} \right)^{-1} : \underline{\underline{A}}^g : \left(\sum_g f^g \left((\sqrt{1-d^g}) \underline{\underline{I}} - \frac{\underline{\underline{\varepsilon}}^g}{2\sqrt{1-d^g}} \otimes \frac{\partial d^g}{\partial \underline{\underline{\varepsilon}}^g} \right)^{-1} : \underline{\underline{A}}^g \right)^{-1}$$

$$\text{Eq. 3.46}$$

3.6 Conclusion

The elasto-plastic self-consistent model allows describing the mechanical behaviour of a polycrystalline and two-phase material during elasto-plastic deformation and taking into account the evolution of crystalline texture (grains rotation). A possible formulation of this model for damage process has been recently proposed by [Panicaud 11] and improved by [Baczmanski 16]. This model is based on the total energy equivalence assumption, while the non-linear work hardening is modelled applying the Voce law. The damage process is simulated at mesoscopic scale and transformed to macroscopic scale using self-consistent approach.

The presented model is proposed in order to predict correctly the evolution of material behaviour under tensile load at three different scales (macroscopic scale for RVE, mesoscopic scale for grains and microscopic scale for slip systems). The values of physical parameters related to the plastic deformation and damage process can be thus determined, such as τ_{c0}^s , τ_1^{ph} , θ_0^{ph} , θ_1^{ph} (Voce law) for plastic deformation and ε_0^{ph} , n^{ph} , ξ^{ph} (damage law) for ductile damage. To do this, the model calculations are compared with lattice strain measured within the deformation neck during in situ tensile test.

However, some features should be further improved, for example the twinning modes during plastic deformation. Though twinning is also one of the major plastic deformation modes, especially for non-cubic lattice, its complexity raises difficulties in the digital modelling. Compared with slip, twinning not only contributes to the incremental reorientation of grains as slip does, but also varies the volume fraction of a grain with different orientations. So in this first attempt of digital modelling we take only slips in consideration, the modelling with twinning effect is under developpement. Moreover, we will see in chapter 6 that the twinning mechanism is not observed on our studied material. We also know that the damage process could be coupled with other various physical phenomena (nucleation, coalescence, micro-cracks, etc.). Due to the complexity of coupling these phenomena with other major effects, this first attempt of damage modelling concentrates on the study of damage criterion.

In the following chapters, the multi-scale self-consistent model will be performed to calculate theoretically the mechanical behaviours for duplex steels and Ti-18 alloy. The obtained theoretical results will be then compared with experimental results to carry out quantitative analysis, in the aim of finding out the values of material parameters related to elasto-plastic deformation as well as the ductile damage process.

Chapter 4. Diffraction study of duplex steel compared with model predictions

Duplex steel is one of the materials studied in this thesis. In situ tensile tests combined with neutron and synchrotron radiation measurement were carried out, in order to study the elasto-plastic behaviour under the uniaxial tensile load. In this chapter, the initiation and the evolution of ductile damage process during the large deformation stage are also investigated for each phase [Baczmański 16].

Time depending studies of ductile damage process in duplex steel were carried out with a stress correction during the large deformation stage. Different behaviours of lattice strains are determined for the aged UR45N sample at the end of tensile test. The evolution of strains and stresses in both phases will be explained using a new version of self-consistent model accounting for ductile damage process. The theoretical results calculated by self-consistent model are then compared with the experimental results with different values of adjustable parameters. Thus some parameters related to the intrinsic properties of different lattice structures are determined for each phase. For example, the Critical Resolved Shear Stress (CRSS), the parameters of hardening law and the parameters related to ductile damage process are identified. The properties of both phases in duplex steel are studied here with help of synchrotron and neutron radiation. The neutron diffraction was applied also to compare elasto-plastic deformation occurring at grain scale in different types of duplex steel.

Subsequently, for the first time, space depending scanning along the necking of the aged UR45N samples during ductile damage process was carried out with synchrotron diffraction measurements in a transmission mode. An X-ray synchrotron radiation was applied to examine the mechanical behaviour of both phases by scanning the necking zone of sample. The diffraction measurements were performed at the ID15B synchrotron beamline in ESRF (cf. Fig. 4.1a). The experimental results from the scanning of necking zone deepened our comprehension about the local mechanism of ductile damage during large deformation. To help understanding the experimental data, Finite Elements Method (FEM) was applied for a 3D model created on the basis of the real sample and the shape of the necking size. Moreover, the lattice strains measured using different reflections were compared with the prediction of the self-consistent model.

4.1 Experimental set-up and data treatment

The in situ tensile tests combined with synchrotron X-ray diffraction measurements were performed at European Synchrotron Radiation Facility (ESRF) at Grenoble, France. The beamline ID15B was employed to carry out diffraction measurements in transmission mode (see Fig 4.1a), by applying a monochromatic X-ray radiation (wavelength $\lambda=0.14256\text{\AA}$, energy of incident beam of about 87KeV), with a beam size of $100 \times 100 \mu\text{m}^2$. The initial cross section of sample along the measurement position was squared by $1.5 \times 1.5\text{mm}$ (sample's technical drawing in Appendix 9).

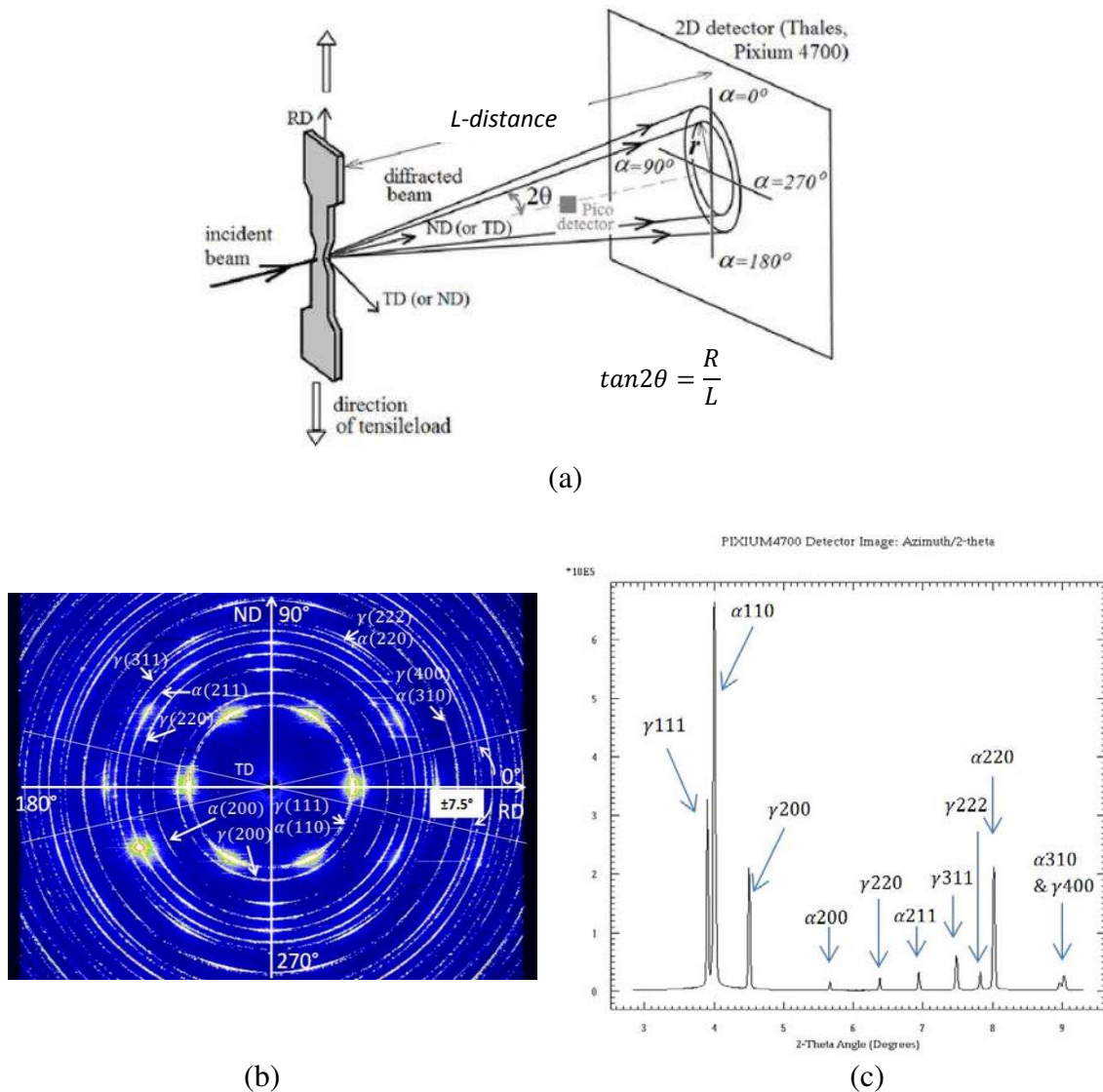


Figure 4.1 (a) Synchrotron diffraction performed in transmission mode at the ID15B beamline using a 2D detector. Orientations of the sample with respect to the experimental setup are shown. (b) Example of image obtained on CCD detector, the fan-sector (eg. between $\eta = 0^\circ \pm 7.5^\circ$ and $180^\circ \pm 7.5^\circ$ for loading direction and $\eta = 90^\circ \pm 7.5^\circ$ and $270^\circ \pm 7.5^\circ$ for transverse direction) is called "cake shape", the reference coordinates and orientation angles are shown. (c) 1D spectrum converted form one "cake shape" sector of diffraction image.

In order to determine lattice strains for different hkl reflections, their diffraction patterns were recorded with a 2D detector, model PIXIUM 4700, manufactured by Thelas [Daniels 09], as shown in Fig.4.1b and c.

Before each in situ diffraction measurement, the calibration of distance L between sample and 2D detector should be performed, in order to get accurate 2θ angles for diffraction peaks during in situ tensile test (the calibration process is illustrated in Appendix 10).

Subsequently, software MULTIFIT was used to determine diffraction peak position by fitting the peak profile with a pseudo-Voigt function [Thompson 87]. The advantage of MULTIFIT program is the possibility of automatic peak profile fitting, providing the individual diffractograms from each “cake shape” sector for many diffraction patterns measured during tensile test or stress determination experiment. From these diffractograms we can get the necessary information in certain orientations of the scattering vector, for example the elastic lattice strain in the loading or transverse direction.

In addition, in situ neutron measurements were previously carried out by Baczmanski et al. [Baczmanski 16] on quenched and aged duplex stainless steels. The neutron measurements were performed during unidirectional tensile and compression tests using Time Of Flight (TOF) method on the instrument ENGIN-X at the spallation neutron source ISIS, RAL, UK. The experimental results of neutron measurements will be used to compare with the results of synchrotron measurements.

4.2 Initial measurement without external load

The initial stress, caused by the manufacturing process or/and the heat treatment and remained in the specimen, should be determined before the tensile-test. To determine initial stresses, the interplanar spacings $\langle d \rangle_{\{hkl\}}$ were measured for different orientations of the initial unloaded samples with respect to the scattering vector.

To measure initial stresses in the aged duplex steel the high energy synchrotron diffraction in the transmission mode was applied. The measurements were done for two sample orientations shown in Fig. 4.1a, where the RD (Rolling direction), ND (Normal direction) and TD (Transverse Direction) define the axes of the sample frame (cf. Fig. 1.11 page 22). For the first orientation, the incident beam was parallel to ND, while the second orientation was

obtained through rotation of the sample around RD by 90° (in this case the incident beam was parallel to TD). The intensities of the diffraction rings, corresponding to different hkl reflections were integrated within “cake shape” sectors (Fig. 4.1b), where α swept the 2D pattern with steps of 15° over the whole 360° range of the azimuth angle. Finally, for each sample orientation the inter-planar spacings $\langle d \rangle_{\{hkl\}}$ were determined for 24 orientations of the scattering vectors with respect to the sample and using different reflections. Next, the arithmetical mean $\langle a(\phi, \psi) \rangle_{\{hkl\}}$ lattice parameters were calculated for symmetrically equivalent α and $\alpha + 180^\circ$ angles.

The multi-reflection method was used to determine the initial stress remained in the specimen for each phase (see section 2.3.3 and [Wroński 07]). As the result, the deviatoric initial stresses in each phase were independently determined from the $\langle a(\phi, \psi) \rangle_{\{hkl\}}$ values (table 4.1).

| | | Neutron diffraction (ISIS) | | | Synchrotron (ESRF) |
|---------------------|-----------|----------------------------|--------------|------------------|--------------------|
| | | UR45N (quenched) | UR45N (aged) | UR52N (quenched) | UR45N (aged) |
| σ_{RD} (MPa) | austenite | 61 ± 12 | 87 ± 9 | 85 ± 10 | 134 ± 15 |
| | ferrite | -50 ± 15 | -57 ± 11 | -24 ± 15 | -155 ± 19 |
| σ_{TD} (MPa) | austenite | 59 ± 12 | -7 ± 9 | 50 ± 10 | 84 ± 15 |
| | ferrite | -29 ± 15 | -19 ± 12 | -122 ± 15 | -44 ± 19 |
| σ_{ND} (MPa) | austenite | -120 ± 12 | -80 ± 9 | -135 ± 10 | -218 ± 15 |
| | ferrite | 79 ± 15 | 76 ± 9 | 144 ± 15 | 199 ± 18 |

Table 4.1 Initial stresses determined in both phases of the studied specimens, the gray cells are the results determined for previous experiments measured by neutron diffraction.

The measured $\langle a(\phi, \psi) \rangle_{\{hkl\}}$ vs. $\sin^2\psi$ plots and the fitting results obtained for both phases are presented in Fig. 4.3 a and b for different ϕ angles (0°, 90°, 180°, 270°). The ϕ and ψ angles, representing the orientation of the scattering vector with respect to the sample, are defined in Fig. 2.4. In the multi-reflection method for stress determination, the experimental data for different hkl reflections in each phase were fitted simultaneously by a least square procedure [Baczmański 03, Wroński 07]. Similarly as the neutron diffraction (Fig. 4.2), it can be concluded that the second order stresses aren't significant within each phase of the studied initial sample. Actually, the $\langle a(\phi, \psi) \rangle_{\{hkl\}}$ vs. $\sin^2\psi$ measured plots are well fitted using Kröner approach of XEC. However important mismatch stress between austenitic and ferritic phases was found, as shown in table 4.1.

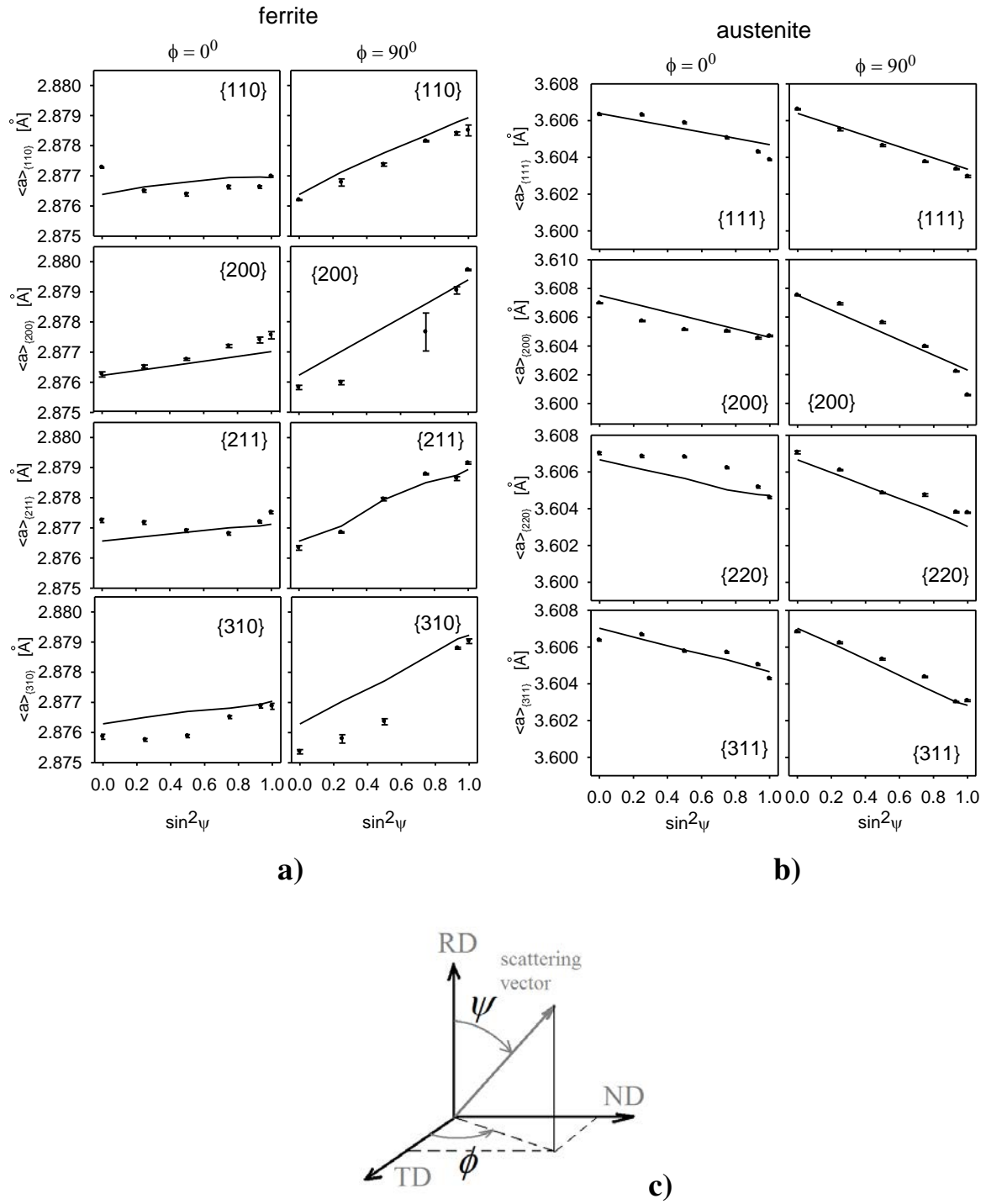
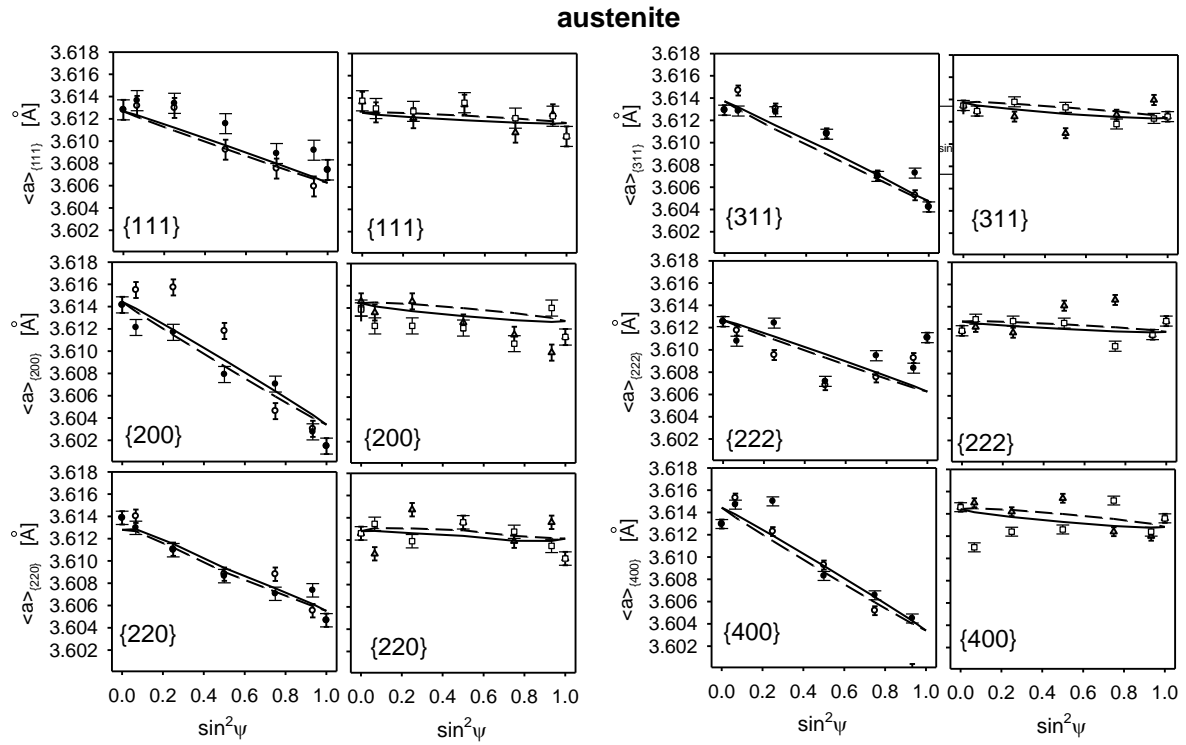
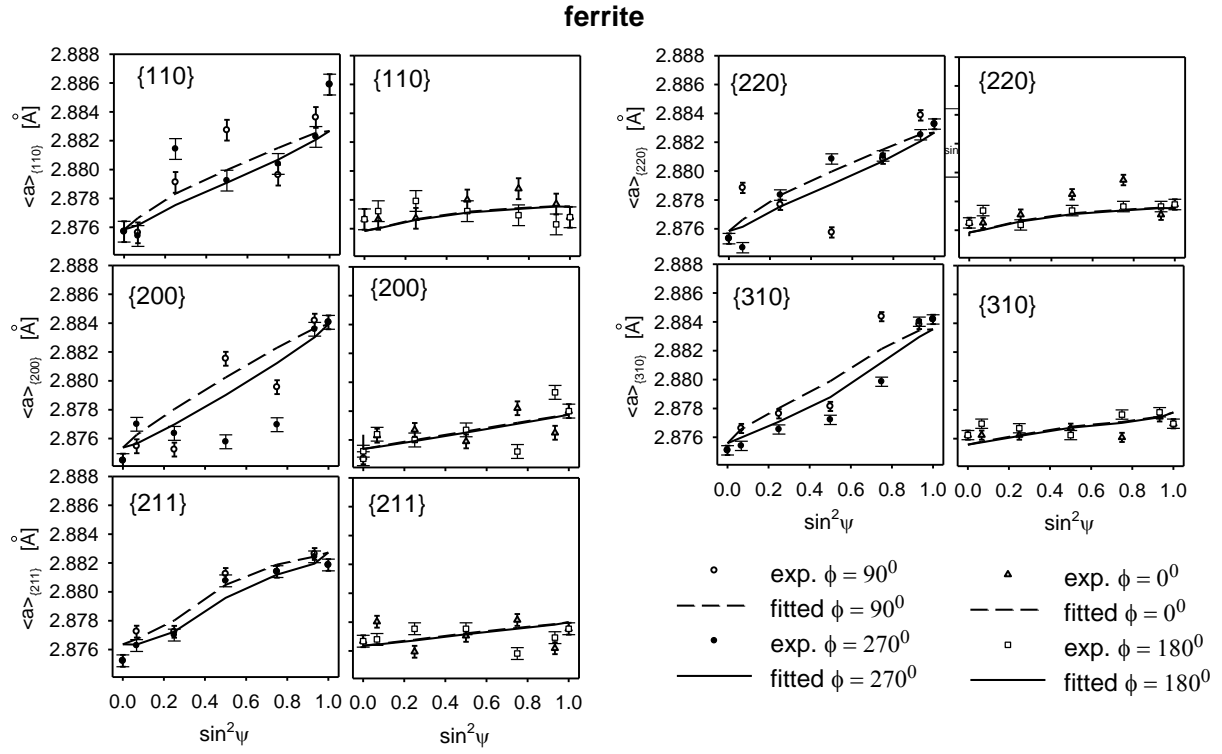


Figure 4.2 Lattice parameters (points) measured using neutron diffraction and theoretical results of fitting (continuous lines) for the initial UR45N aged sample. The experimental data for various hkl reflections analysed for (a) ferritic and (b) austenitic phases, separately (XECs were calculated for the textures given in Fig. 1.13 (page 24) using Kröner method). (c) The orientation of the scattering vector with respect to the sample frame is shown.



b)

Figure 4.3 Similar as in Fig. 4.2 presentation of the measured lattice parameters (points) and theoretical results of fitting (continuous lines) for the initial UR45N aged sample. In this case the measurement was done using synchrotron diffraction. The coordinate is the same as in Fig. 4.2.

Analysing the stress tensors measured using neutron and synchrotron diffraction, it is found that approximate absolute values of stress components, but with opposite signs, are found for austenite and ferrite. Which means a positive stress is measured in ferrite, the negative stress can be measured in austenite (table 4.1). Opposite slopes can be also seen in the $\langle a(\phi, \psi) \rangle_{\{hkl\}}$ vs. $\sin^2\psi$ plots between austenite and ferrite (Fig. 4.2 and 4.3). In other words, the initial stresses were balanced over both phases exhibiting equal volume fractions. Moreover, the slopes of $\langle a(\phi, \psi) \rangle_{\{hkl\}}$ vs. $\sin^2\psi$ plots were well reproduced by the theoretical lines for both phases, which means that the anisotropy of XECs was well predicted using the Kröner model.

4.3 Strains evolution in the loaded samples during tensile tests

Series of in situ diffraction (neutron or synchrotron) measurements were performed during tensile tests until fractures of the samples. During the tests the total sample deformation was determined from the recorded actuator position, while the applied force was controlled by a load cell sensor. In the case of neutron experiment the strain for small deformation was also measured by the strain gauge.

In order to observe the evolution of lattice strains in a given direction, the relative strains $\langle \varepsilon_{\vec{n}} \rangle_{\{hkl\}}^{ph}$ along loading direction or transverse direction are determined for different hkl reflections belonging to each phase ph (cf. Eq. 2.2). \vec{n} represents the scattering vector with respect to the sample frame.

Due to the heterogeneity of sample's cross section caused by large deformation, the local stress applied inside gauge volume is difficult to be interpreted by macroscopic stress recorded using tensile grip. In this case, a new calibration of local macroscopic stress should be performed for large deformation range using the method proposed by Le Joncour et al. [Le Joncour 11]. The aim of this calibration is to avoid the influence of sample narrowing occurred during tensile test (see Appendix 11).

During in situ synchrotron X-ray diffraction measurement, uniaxial tensile test was performed on the aged UR45N steel. A hydraulic 5 kN rig was used to apply load along RD (rolling direction) in the rate equal to 1 N/s (i.e. 0.44 MPa/s for the stress rate) until sample fracture. Diffraction data were collected with exposure time equal to 10 s separated by 5 s intervals without acquisition. The sample strain was monitored by the position of the

hydraulic actuator. The macro-mechanical true stress vs. true macro-strain Σ_{RD} vs. E_{RD} plot is shown in Fig. 4.4.

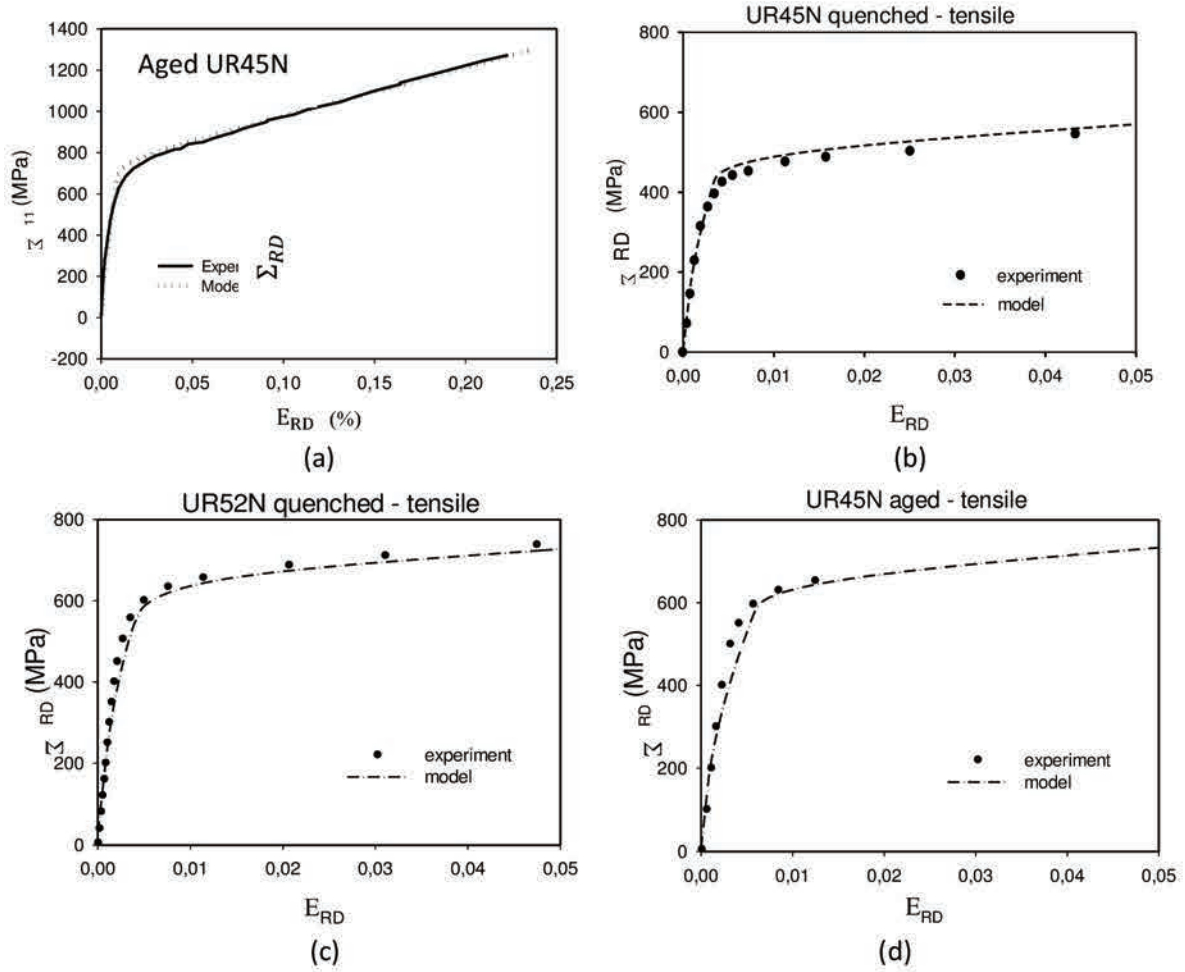


Figure 4.4 Macro-mechanical Σ_{RD} vs. E_{RD} plots for: (a) aged UR45N during synchrotron measurement; (b) quenched UR45N, (c) quenched UR52N, (d) and aged UR45N during neutron measurement subjected to tensile test. Experimental results (points) are compared with model predictions (lines) for elasto-plastic deformation range.

The interplanar spacings are determined for the direction along the applied load (RD) and perpendicular to the applied load (TD). As for initial measurements in these directions the intensities of the diffraction rings are integrated within “cake shape” sectors (Fig. 4.1b) and the arithmetical mean $\langle d \rangle_{\{hkl\}}$ spacings were calculated for symmetrically equivalent angles α and $\alpha + 180^\circ$. Then the relative lattice strains $\langle \varepsilon_{RD} \rangle_{\{hkl\}}$ in the direction of applied load (RD) and in the direction perpendicular to the load (TD) were calculated. For the strain analysis the following hkl reflections were chosen: 111, 200, 220, 331 in austenite and 110, 200, 211, 310 in ferrite. The relative lattice strains vs. applied macro-stress are shown in Fig. 4.5.

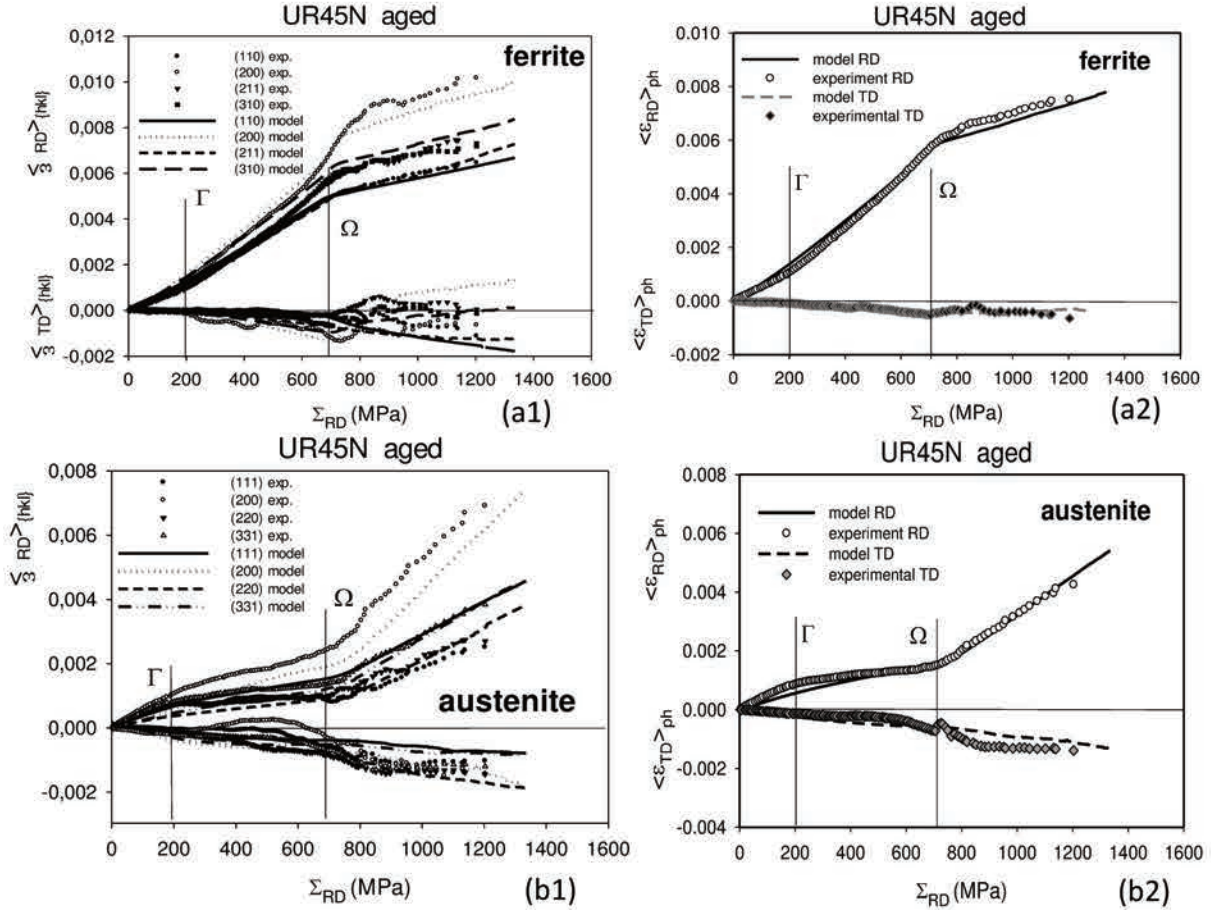


Figure 4.5 The evolution of lattice strain vs. applied stress (points) of different hkl reflections measured by synchrotron for austenite (a1) and ferrite (b1) and the evolution of phase strains vs. applied stress (points) for austenite (a2) and ferrite (b2) measured over gauge volume, in RD and TD. The model predictions (lines) are also compared with the experimental results.

Subsequently, the arithmetic averages $\langle \epsilon_{RD} \rangle_{ph}$ and $\langle \epsilon_{TD} \rangle_{ph}$, respectively over all measured lattice strains $\epsilon_{RD}^{>\{hkl\}}$ and $\epsilon_{TD}^{>\{hkl\}}$ were calculated for each phase ph and shown in Fig. 4.5 a2 and b2. According to [Baczmański 11], the $\langle \epsilon_{RD} \rangle_{ph}$ and $\langle \epsilon_{TD} \rangle_{ph}$ averages describe elastic behaviour of the grains belonging to the studied phases ph .

In Fig. 4.5 and Fig. 4.6 two thresholds Γ and Ω determining the changes in the trend of plots can be identified. These limits correspond respectively to the yield point of austenite and the yield point of ferrite, as it was interpreted by Le Joncour et al. [Le Joncour 10, Le Joncour 11]. The results of neutron diffraction measurements are also shown in Fig. 4.6, where the relative lattice strains (Eq. 2.2) measured in the direction of applied load (RD) for different hkl reflections belonging to ferrite or austenite are respectively presented.

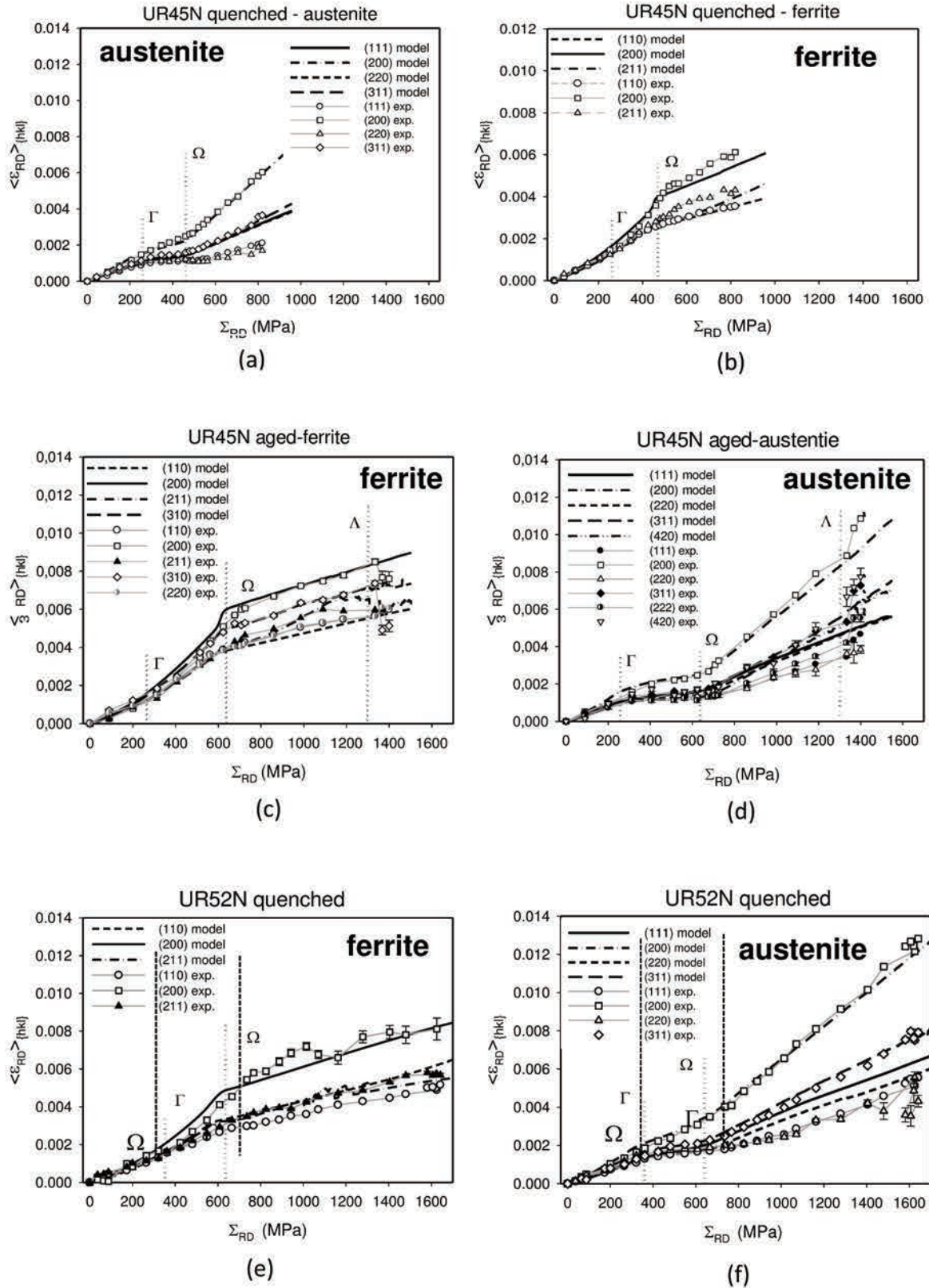


Figure 4.6 Experimental measured by neutron (points) elastic lattice strains ($\langle \epsilon_{RD} \rangle_{\{hkl\}}$) parallel to the load direction (RD) versus the calibrated macro-stress Σ_{RD} for samples of quenched UR45N during tensile test (a, b), aged UR45N during tensile test (c, d), and quenched UR52N during tensile test (e, f), compared with model predictions (lines) for tensile test.

4.4 Analysis for elasto-plastic deformation with model predictions

In this section, a self-consistent model was used to compare with the experimental results in the elasto-plastic deformation range. The parameters of Voce law are determined in this way for each phase of the studied duplex steels. The parameters allow us to characterize the mechanical behaviour of each phase within polycrystalline material. In the following text the interpretation of experimental results during elasto-plastic deformation range and that during the damage process are respectively presented.

4.4.1 Analysis of neutron diffraction data

According to Fig. 4.5 and Fig. 4.6, two threshold Γ and Ω can be identified during the elasto-plastic deformation range. As previously observed from the study of tensile test combined with in situ neutron diffraction measurements on duplex steel UR45N and UR52N [Baczmański 04a, Le Joncour 10, Le Joncour 11], the thresholds Γ and Ω correspond respectively to the yield point of austenite and ferrite. From the beginning of tensile test until the threshold Γ , both ferrite and austenite deformed elastically. A linear dependence of lattice strains vs. applied stress can be seen for this stage. The slopes of these curves are related to the X-ray elastic constants corresponding to each reflection.

Between the threshold Γ and Ω , the austenite undergoes plastic deformation. At point Γ , we can see the change of the slopes in lattice strain-stress curves measured in the loading direction. The plots of austenite became more flat due to the plastification of this phase. Meanwhile, the ferrite continues its elastic deformation, and in contrary to austenite an increase of the lattice strains vs. applied stress rate can be observed. This increase indicates that the stress relieved in austenite is probably transferred to ferrite, until the yield point of ferritic phase.

At threshold Ω , the ferrite reached its yield point, and after that, both phases deformed plastically. Over this limit a lower increasing rate of lattice strain in ferrite can be found compared with that of austenite. It means that the work hardening of austenite is stronger than ferritic phase.

The self-consistent model without damage effect modelling was employed to study the behaviour of UR45N by comparison. This approach allows determining the Voce's parameters for each phase of the studied duplex steel.

The simulation was performed with 20,000 spherical inclusions representing grains belonging to the ferrite (10,000) and the austenite (10,000). This set of inclusions having lattice orientations determined from experimental textures (Fig. 1.13 page 24) provides enough statistics for comparison with the diffraction results. The number of grains studied during experiment can be estimated as the ratio of the studied gauge volume to the grain size. After a rough estimation by analyzing Fig. 1.11 page 22 and Fig. 1.12 page 23, millions of grains can be included in the gauge volume of neutron measurement and tens of thousands of grains can be included in that of synchrotron measurement (estimation process cf. [Le Joncour 11]). Such large numbers of grains cannot be used in calculations.

In the model calculation, the initial orientations of crystallites defined according to the experimental textures (Fig. 1.13 page 24), the single crystal elastic constants (table 1.6 [Simons 71, Inal 99] page 23), and the initial stresses determined by initial measurement (section 4.2) are taken as the input data for each phase.

To adjust the model strains $\langle \varepsilon_{RD} \rangle_{\{hkl\}}$ (and additionally $\langle \varepsilon_{TD} \rangle_{\{hkl\}}$ measured at synchrotron radiation) to the experimental data the values of the CRSS were varied for both phases. As above mentioned, the first threshold I , corresponding to the yield point of the austenite, can be used to determine its initial critical resolved shear stress (CRSS) τ_0^{ph} , related to the beginning of plasticity for austenitic phase. Meanwhile, the second threshold Ω enables the determination of initial CRSS τ_0^{ph} for ferritic phase. Simultaneously, the macroscopic experimental Σ_{RD} vs. E_{RD} curves were also fitted by model predictions. This fitting allows determining the Voce parameters τ_1^{ph} , θ_0^{ph} and θ_1^{ph} , which are related to the working hardening of material during the plastic deformation.

The results of model at microscopic scale are shown in the above figures (from Fig. 4.5 and Fig. 4.6). The model predictions are compared with the evolution curves of experimental lattice strains in loading direction (RD direction, either in tension or in compression) and in transverse direction (TD in tensile test during synchrotron measurement). Fig. 4.6 a and c, Fig. 4.5a and Fig. 4.6 b, d, Fig. 4.5b present respectively the comparison between the experimental and model predicted results for individual hkl reflections belonging to ferritic phase and austenitic phase under tensile load.

From above figures, we can see that the predicted results agree well with the measurements for ferrite and austenite, either for macroscopic Σ_{RD} vs. E_{RD} curves (Fig. 4.4), or for $\langle \varepsilon_{RD} \rangle_{\{hkl\}}$ vs. Σ_{RD} curves (Fig. 4.5 and 4.6). Such agreements prove that the employed self-consistent model is able to predict correctly the micro-mechanical behaviour of grains, as well the partitioning of stresses between phases.

The values of Voce parameters determined from each test are presented in table 4.2. In the case of aged UR45N and quenched UR52N samples measured by neutron diffraction, the tensile tests were performed until large deformation, i.e. up to the sample fracture. These experimental data allow determining the τ_1^{ph} and θ_1^{ph} for each phase. For the other tests, only the initial CRSS τ_0^{ph} and the initial hardening parameter θ_0^{ph} were found.

Comparing the results obtained on quenched UR45N and aged UR45N samples, a considerably lower τ_0^{ph} in ferrite can be noticed for the quenched steel. However, almost the same values of τ_0^{ph} for austenite have been found on all UR45N samples. This phenomenon is caused by the spinodal decomposition of ferrite into α and α' phase during the aging process and the precipitation of secondary phases leading to increase of the ferrite hardness [Calonne 01], while the structure and mechanical properties of austenite remain unchanged (cf. Appendix 2).

| | | Neutron diffraction (ISIS) | | | Synchrotron (ESRF) |
|-----------------------|-----------|----------------------------|--------------|------------------|--------------------|
| Material | | UR45N (quenched) | UR45N (aged) | UR52N (quenched) | UR45N (aged) |
| Deformation mode | | tension | tension | tension | tension |
| τ_0^{ph} (MPa) | austenite | 140 | 140 | 180 | 150 |
| | ferrite | 220 | 350 | 290 | 410 |
| θ_0^{ph} (MPa) | austenite | 225 | 225 | 225 | 380 |
| | ferrite | 110 | 110 | 110 | 190 |
| τ_1^{ph} (MPa) | austenite | not determined | 280 | 280 | not determined |
| | ferrite | | 150 | 140 | |
| θ_1^{ph} (MPa) | austenite | | 6 | 6 | |
| | ferrite | | 5 | 3 | |

Table 4.2 Parameters of plastic deformation determined in tensile and compression tests (the load was applied along rolling direction - RD), the gray cells are the results determined for previous experiments measured by neutron diffraction.

By analysing the mechanical properties of quenched UR45N and the quenched UR52N (neutron measurements), which are subjected to the same thermal treatment but with different chemical compositions, we can see the yield strength and the initial CRSS τ_0^{ph} of both phases are higher in the case of UR52N, the similar results have also been found by [Dakhlaoui 07] using X-ray diffraction.

The higher yield stress in quenched UR52N can be explained by a compound effect. In one hand, the initial stresses influence the measured yield stresses. From table 4.1, we can see the initial stresses in quenched UR52N are higher (about 20MPa) than those in UR45N for both phases, which increase the yield stress in quenched UR52N. In another hand, the higher yield strength of ferrite in UR52N compared with that of UR45N can be explained by its relatively higher contents of chromium and molybdenum (table 1.5 page 22) which increase the yield strength of both phases but mostly that of ferrite. The higher yield strength of austenite in UR52N can be associated with the higher presence of nitrogen (table 1.5 page 22) [Bugat 01]. In this fact both phases contribute to the higher value of macroscopic yield strength of UR52N steel. Meanwhile, it should be stated that the values of the parameters related to the work hardening of ferrite are lower than that of austenite for all samples, regardless of the sample preparation (quenched or aged) or the chemical composition (UR45N or UR52N). This phenomenon suggests that the difference between the mechanical properties of investigated materials is significantly affected by the initial CRSS τ_0^{ph} and the initial stresses.

An asymmetry can be observed from the lattice strains vs. applied macro-stress (Σ_{RD}) curves of each phase between the tensile test performed on aged UR45N (Fig. 4.6). However, the macroscopic yield strength (Fig. 4.4 b,c,d) and the determined Voce parameters (table 4.2) are very similar for both deformation modes. Hence, this asymmetry appearing on the behaviour at the level of lattice strains can be explained by the presence of initial stresses in each phase. As presented in table 4.1, initially the ferrite was under compression state due to its negative initial stress along RD, while the austenite was under tensile state due to its positive initial stress. The applied load superposed with the initial stress during the tensile test, leading to a higher yield stress for ferrite and a lower yield stress for austenite.

An opposite effect occurred during the compression test. Despite of the deformation mode, the initial stress is able to increase the yield strength of one phase while to decrease the yield strength of another phase by approximately the same values. Consequently, the stresses

between phases do not result in a significant change in the macroscopic yield strength of the material (cf. Fig. 4.4) [Dakhlaoui 07].

4.4.2 Comparison between neutron and synchrotron diffraction data

The role of initial stresses is also confirmed by the result obtained from the synchrotron radiation measurement performed on UR45N sample under tensile load. Sufficient numbers of grains are included in the large enough gauge volumes during both measurements, allowing them to be RVE during measurements. This makes it possible to compare the results from two experiments.

A higher value of initial stress is found in the case of synchrotron measurements than those measured by neutrons (cf. table 4.1). This means that the studied aged UR45N is heterogeneous or the samples were not prepared exactly under the same condition (the aged samples for neutron and synchrotron measurements were prepared separately). The mean values of elastic lattice strains were calculated over all measured hkl reflections belonging to each phase ($\langle \epsilon_{RD} \rangle_{\{hkl\}}$ and $\langle \epsilon_{TD} \rangle_{\{hkl\}}$ in Fig. 4.5). A good agreement between experimental and theoretical mean lattice strains (Fig. 4.5), as well as macro-mechanical Σ_{RD} vs. E_{RD} curves are obtained.

Analysing Fig. 4.6 a,b and Fig. 4.5 a2 and b2, it can be noticed that the yield stress in the gauge volume studied by synchrotron radiation is higher for ferrite and lower for austenite in comparison with the average values determined by neutrons over a larger gauge volume (cf. the positions of Γ and Ω thresholds). This means that the difference of the elastic limits between each phase increases with higher local residual stresses. Moreover, the values of CRSS obtained for ferritic phase in both experiments are also different, while no significant difference in τ_0^{ph} was found for the austenite (Table 4.2). The higher value of CRSS for ferrite causes also higher value of macroscopic yield stress for the sample used in synchrotron experiment (cf. Fig. 4.4).

The residual stresses could be considered inhomogeneous in different phases. The CRSS of ferrite are also different in the samples separately prepared for neutron and synchrotron experiments (with different manufacturing process and different sample shapes). The variation of stresses within phases could be explained by temperature gradients during sample cooling after aging treatment, while the CRSS variation in ferritic phase may be caused by

differences or heterogeneities of the precipitation process during aging. The mechanical properties and microstructure of austenitic phase was not changed during aging.

Finally, the evolution of work hardening during the tensile tests measured by synchrotron and neutron should be compared. In this case, the main difference between tests is the control mode, by stress (synchrotron experiment) or by strain (neutron measurements). The high beam energy of synchrotron radiation enables short measurements time (exposure time equal to 10s, separated by 5s intervals without acquisition) during continuous tensile test. In the case of neutron measurements, the diffraction measurements were performed at a given constant sample strain during long time (a few minutes of acquisition). Moreover, the neutron measurements were done after sample relaxation, the sample relaxed 10-15min at each load step (for constant strain the applied stress decreased with time). Therefore, different macro-mechanical Σ_{RD} vs. E_{RD} curves were obtained. The curves obtained from synchrotron and neutron measurement correspond respectively to the macroscopic material behaviour with and without relaxation during continuous uniaxial tensile deformation. The parameters of Voce law ($\tau_1^{ph}, \theta_0^{ph}, \theta_1^{ph}$), given in table 4.2, show that the work hardening in both phases is much higher in the case of continuous tensile test because the stress relaxation does not occur.

4.5 Time depending damage analysis and damage criteria

As reported in the section 4.3, the neutron diffraction measurements were performed on samples of aged UR45N and quenched UR52N steels during tensile tests until fracture. Comparing the diffraction data for both materials, different behaviour of lattice strains was found at the end of tensile test, i.e. after threshold Δ (as seen in Fig.4.6). A significant decrease of lattice strains in ferrite and an increase of lattice strains in austenite were observed for the aged UR45N steel, while such phenomenon was not observed for the quenched UR52N steel. This phenomenon indicates a relaxation of the phase stress occurring in the ferrite, which was simultaneously compensated by the increasing of phase stress in austenite. From the analysing of thermal aging process in duplex steel (Appendix 2), the ferrite is considered more fragile under thermal effect and more sensible to the external load. In this case, the following tests of damage criterion are based on the assumption that the ferrite is the only phase in which initiates damage process. This evolution of micro-strains in both phases

will be explained using a new version of self-consistent model accounting for ductile damage process.

In order to study the initiation of ductile damage in UR45N, modelling of ductile damage is integrated in the current self-consistent model, which enables the explanation of damage process in both phases above the threshold Δ . Calculations were performed for the data measured by neutron diffraction, but additionally different damage criteria were tested.

4.5.1 Test of equivalent strain criterion for damage

The equivalent strain criterion has been described in section 3.3. Both the predicted macroscopic tensile curve Σ_{RD} vs. E_{RD} (Fig. 4.7a) and the lattice strains (Fig. 4.8) were compared with the experimental results. The experimental tensile curve Σ_{RD} vs. E_{RD} was obtained from a tensile test including the large deformation range with the new local stress calibration proposed by Le Joncour et al. [Le Joncour 10] and Baczmański et al. [Baczmański 11]. In this method the strains were measured in the deformation neck during large deformation range by using DIC (digital image correlation) technique [Le Joncour 10]. It should be underlined, that in model calculations, the damage was assumed to be initiated only in the ferritic phase according to the previous experimental observation (cf. section 1.1).

| Damage criterion | Phase | Parameters | Values |
|--------------------------------------|---------|----------------------|--------|
| Equivalent strain Eqs. 3.35, 3.36 | Ferrite | ε_0^{ph} | 0.8 |
| | | n^{ph} | 0 |
| | | ξ^{ph} | 0.2 |

Table 4.3 Values of adjustable parameters describing the damage process in ferrite, determined using self-consistent model with **equivalent strain** damage criteria.

The results of model adjustment to experimental data are shown in Fig. 4.7a and Fig. 4.8, the values of damage parameters (cf. Eqs. 3.35, 3.36 page 74 and table 3.3 page 75) are given in table 4.3. In this analysis it was assumed that the damage development depends only on the equivalent von Mises strain (“equivalent strain criterion”), as originally proposed by Baczmański et al. [Baczmański 16].

From Fig. 4.7a we can see the calculated Σ_{RD} vs. E_{RD} curves show still linearity after the sample fracture on experimental curve. This phenomenon means the fracture effect is not taken into account in this current damage modelling, this modelling mainly focuses on the

initiation of ductile damage. Additionally, Fig. 4.7b presents the predicted dependence of total lattice strain $\langle \varepsilon_{RD} \rangle_{mean}^{aus+fer}$ (defined by Eq. A11.2 in Appendix 11) vs. macro-stress along applied load (RD). The average micro-strain in function of calibrated macro-stress Σ_{RD} is also shown (this linear dependence was extrapolated from the elastic range and next used to calibrate macro-stress Σ_{RD}). Comparing with the experimental data, it is well seen that linear function is obtained by model prediction, and the model calculated curve is very close to the experimental curve and still linear even in the damage region (above threshold Λ). Thus the calibration of the macro-stress in the gauge volume (as proposed in Appendix 11) is also available for the damaged material.

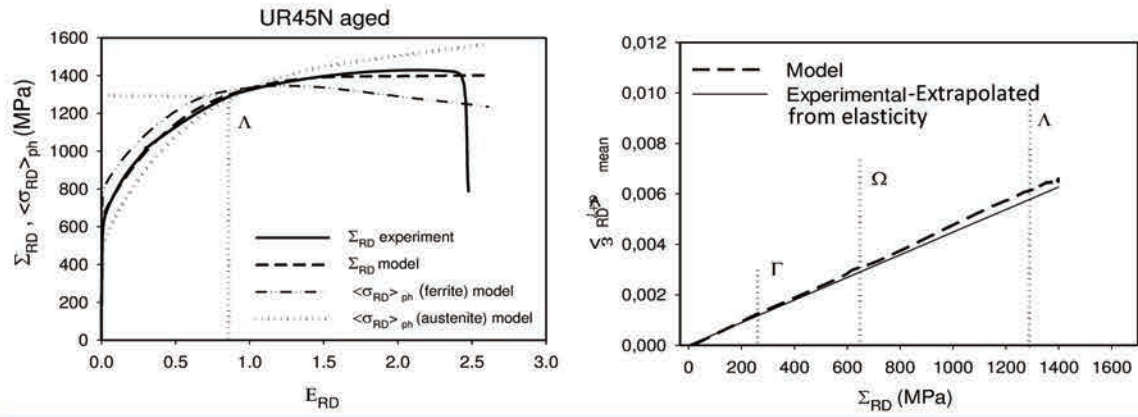


Figure 4.7 The result of mechanical tensile test performed along RD compared with model prediction (a) for damage criterion of equivalent strain. Additionally, the theoretical mean stresses (along RD) are shown in function of the total sample strain E_{RD} . In figure (b) the predicted dependence of total lattice strain $\langle \varepsilon_{RD} \rangle_{mean}^{aus+fer}$ (defined by Eq. A11.2, Appendix 11) vs. macro-stress along applied load (RD).

The stress transfer between phases during damage process is confirmed by model prediction, when the “equivalent strain” criterion is applied to define the damage parameter d^{fer} (Eqs. 3.35 and 3.36). The relaxation of the mean stress $\langle \sigma_{RD} \rangle_{fer}$ in ferrite and the increase of mean stress $\langle \sigma_{RD} \rangle_{aus}$ in austenite develop gradually (as seen in Fig. 4.7a) at the end of the macroscopic tensile curve Σ_{RD} vs. E_{RD} . This tendency of stress transfer between two phases after threshold Λ is also well seen in Fig. 4.8, where the lattice strains measured in both phases vs. stress Σ_{RD} (calibrated for the gauge volume) are presented. In this figure, the experimental lattice strains are compared with model predictions performed with and without damage modelling. The good agreement between the most of the $\langle \varepsilon_{RD} \rangle_{\{hkl\}}$ vs. Σ_{RD} curves and the model prediction for measured hkl reflections confirms the reliability of the used model, when damage was taken into account.

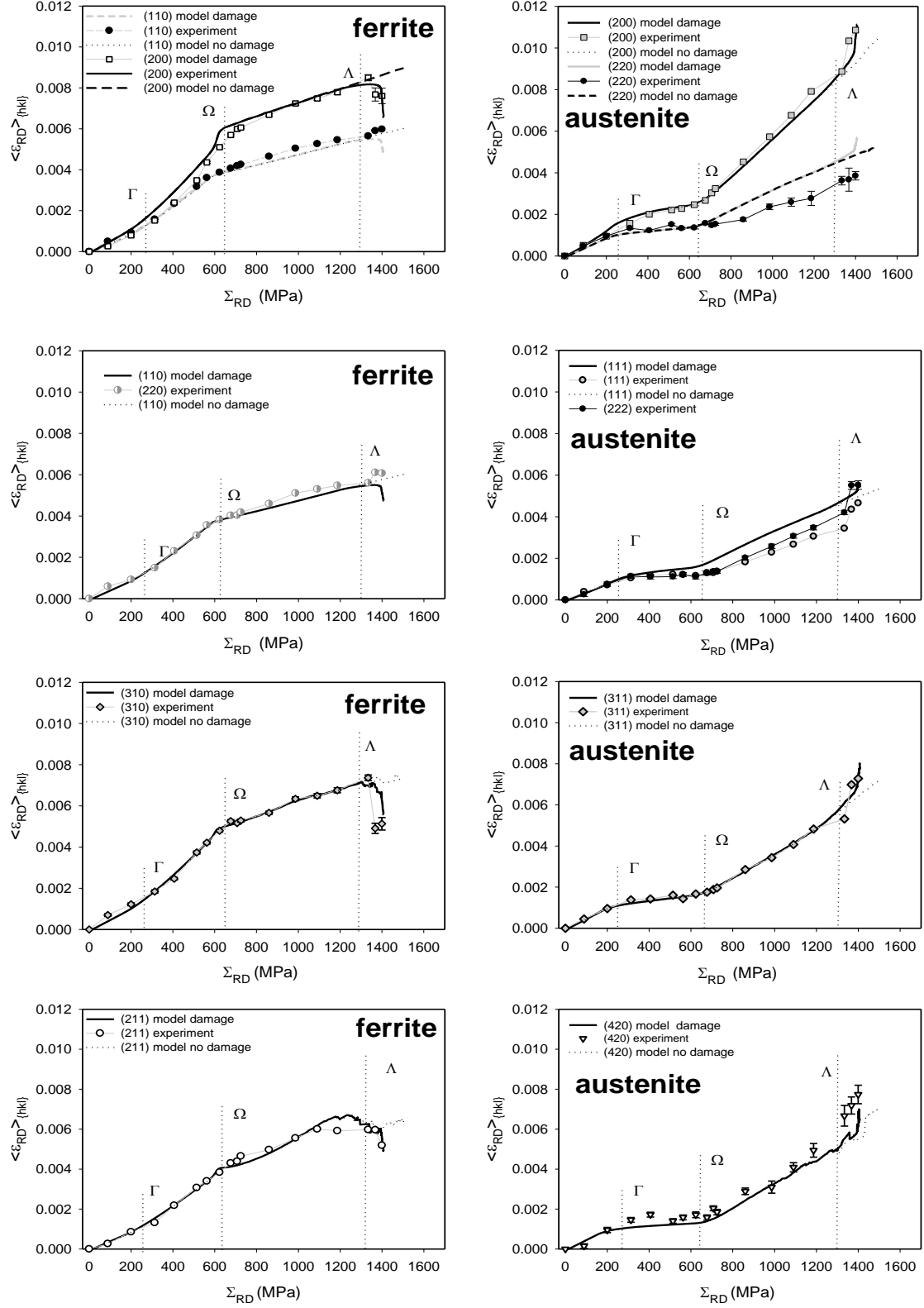


Figure 4.8 The measured elastic lattice strains $\langle \epsilon_{RD} \rangle_{\{hkl\}}$ vs. applied stress Σ_{RD} in the aged UR45N sample fitted by self-consistent model with and without prediction of the damage effect (**equivalent strain criterion**).

A presentation of the phase behaviour is shown in Fig. 4.9, where the arithmetical mean lattice strains ($\langle \varepsilon_{RD} \rangle_{ph}$) calculated for each phase are presented.

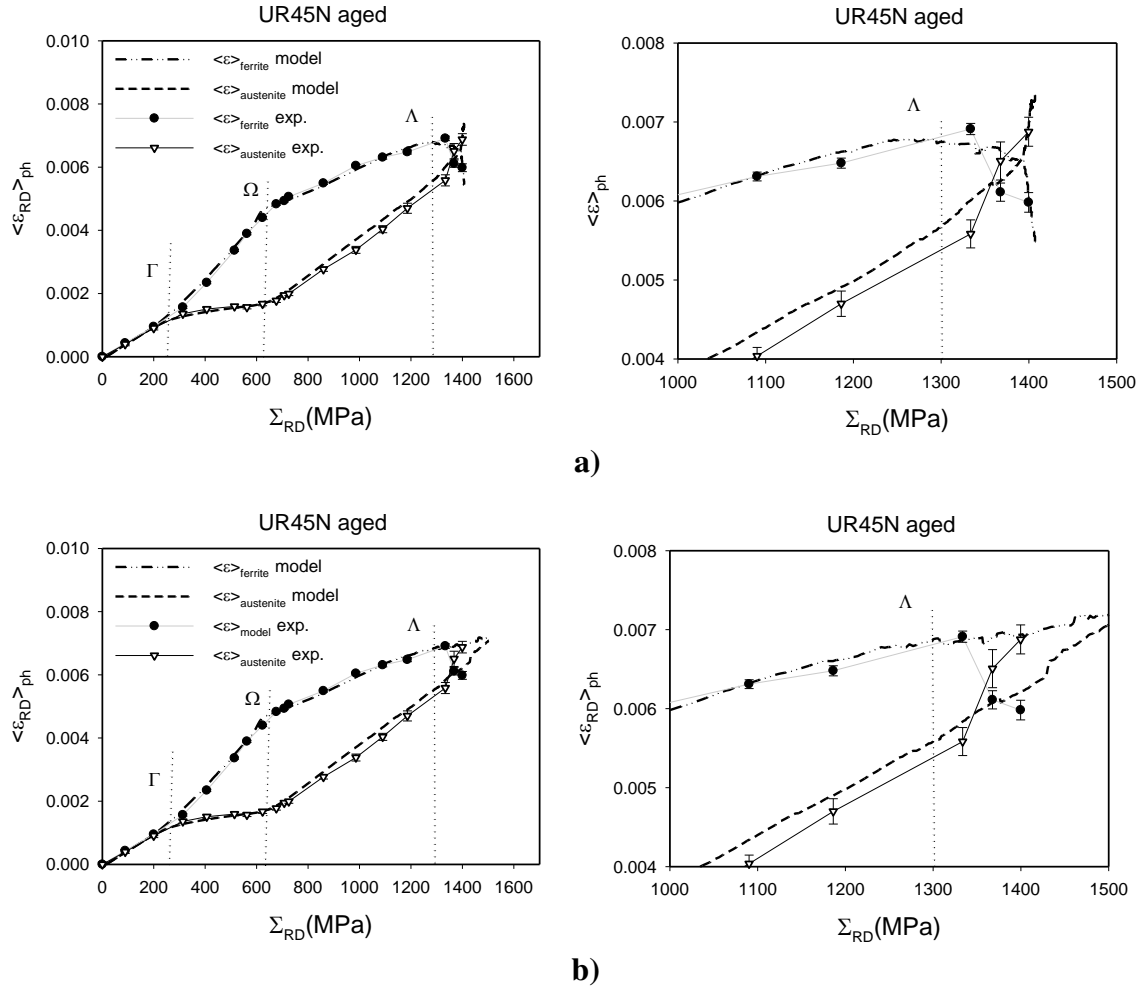


Figure 4.9 The mean values of the measured elastic phase strains vs. applied stress, in the UR45N sample fitted by self-consistent model (damage criterion of **equivalent strain**) with damage (a) and without damage (b). On the right, magnification of the range close to sample fracture is shown.

It is well seen that the tendency of the $\langle \varepsilon_{RD} \rangle_{ph}$ vs. Σ_{RD} curves cannot be correctly simulated without damage process. Again it is confirmed that significant load transfer between each phase can be predicted if damage/softening in ferritic phase is taken into account. The observed relaxation of stress in ferrite can be identified as the result of the damage occurring at the grain scale. The significant damage effect can be observed for the macro-stresses over 1300 MPa (above threshold Λ), i.e. when a growing number of ferrite grains fulfil the condition: $\varepsilon_0^g > \varepsilon_0^{ph} = 0.8$ for large sample deformation (cf. Eq. 3.35). As mentioned, the mean phase stresses $\langle \sigma_{RD} \rangle_{ph}$ calculated by self-consistent model in the direction of applied load (RD) are presented in Fig. 4.9a. It is clearly seen that the stress in

ferritic phase is higher than that in austenite until about 1350 MPa (below the threshold A). Subsequently, the significant stress relaxation occurring in ferritic phase causes transfer between the loads in each phase leading to a superior stress in austenite and the saturation of macro-stress Σ_{RD} . It should be also underlined that the damage process described in this work is studied only during the saturation (end) of macro-stress Σ_{RD} for which the neutron measurements can be done. This process corresponds to ductile damage at microscopic level and develops gradually in the ferrite for the sample deformation range $0.8 < E_{RD} < 2.4$ (Fig. 4.7a).

4.5.2 Tests of equivalent stress criterion for damage

In spite of successful adjustment of the model with “equivalent strain” damage criterion, other possible definition of the damage parameter as “**equivalent stress**” should be verified. At first the criterion based on the equivalent von Mises stress were checked. In this case the damage parameter \dot{d}^g for a grain g was defined as follows:

$$\dot{d}^g = \xi^{ph} (\sigma_{eq}^g - \sigma_0^{ph})_+^{n^{ph}} (\dot{\sigma}_{eq}^g)_+ \quad \text{Eq. 4.1}$$

where σ_{eq}^g is the equivalent stress threshold for which damage begins and

$$\sigma_{eq}^g = \sqrt{\frac{3}{2} \left(\sigma_{ij}^g - \frac{1}{3} \text{tr}(\sigma_{ij}^g) I_{ij} \right) : \left(\sigma_{ij}^g - \frac{1}{3} \text{tr}(\sigma_{ij}^g) I_{ij} \right)} \quad \text{Eq. 4.2}$$

while n^{ph}, ξ^{ph} parameters have the same meaning as in Eqs. 3.35 and 3.36.

The results of model fitting with equivalent stress criterion are shown in Fig. 4.10, while the adjusted model parameters (according to Eqs. 4.1, 4.2) are given in table 4.4.

| Damage criterion | Phase | Parameters | Values |
|------------------------------------|---------|-----------------|------------|
| Equivalent stress Eqs. 4.1, 4.2 | Ferrite | σ_0^{ph} | 1650 (MPa) |
| | | n^{ph} | 0 |
| | | ξ^{ph} | 150 (MPa) |

Table 4.4 Values of adjustable parameters describing the damage process in ferrite, determined using self-consistent model with **equivalent stress** damage criteria.

Fig. 4.10a shows the linearity of calculated Σ_{RD} vs. E_{RD} curves in the damage range with **equivalent stress** criterions. From the Fig. 4.10b, linearity is obtained by model calculation

until the damage stage, and the slope is not far from the extrapolated experimental data, thus the calibration of experimental data can be performed as proposed in Appendix 11.

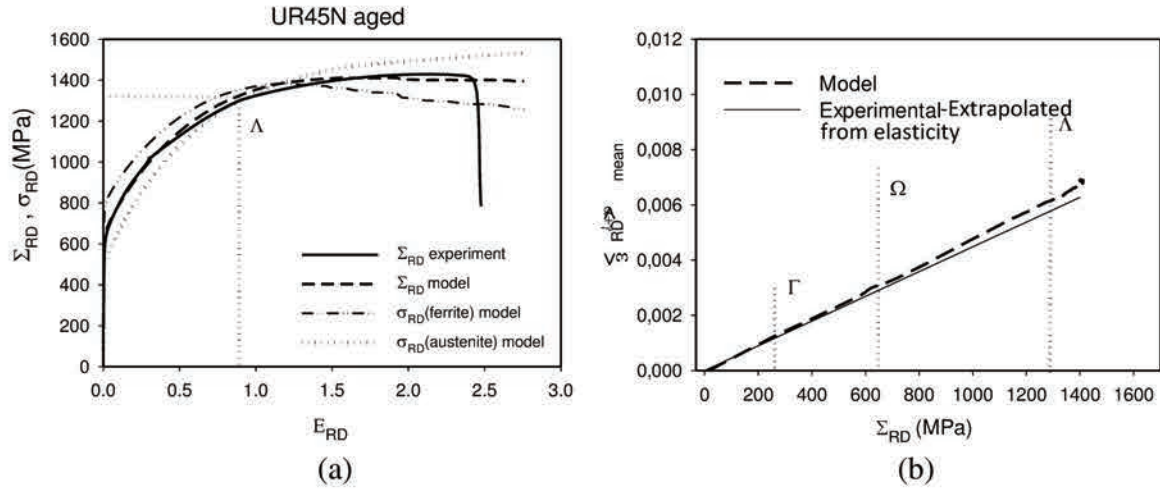


Figure 4.10 The result of mechanical tensile test performed along RD compared with model prediction, and the predicted dependence of total lattice strain $\langle \epsilon_{RD} \rangle_{\text{mean}}^{\text{aus+fer}}$ vs. macro-stress along applied load (RD) for damage **criterion of equivalent stress**.

Analysing the results obtained for damage “equivalent stress criterion” it can be concluded that they are different from those for “equivalent strain criterion”. In the case of “equivalent stress criterion” the damage process is unstable, causing more rapid relaxation of the stresses in part of ferritic grains (see model strains for 211 and 110 reflections in Fig. 4.11). On the other hand, according to the used model, the measured lattice strains (and corresponding stresses) increase with the applied stress for part of grains contributing to the 200, 310 reflections in the ferritic phase. In addition, increase of lattice strain is seen for all reflection measured in the austenite. Comparing the evolution of lattice strains it can be concluded that the model results do not fit as well as with “**equivalent strain criterion**” to experimental results, especially for 200 and 310 reflections in ferritic phase. It means that, the distribution of stresses between grains in ferrite is not appropriately predicted with the “**equivalent stress**” criterion.

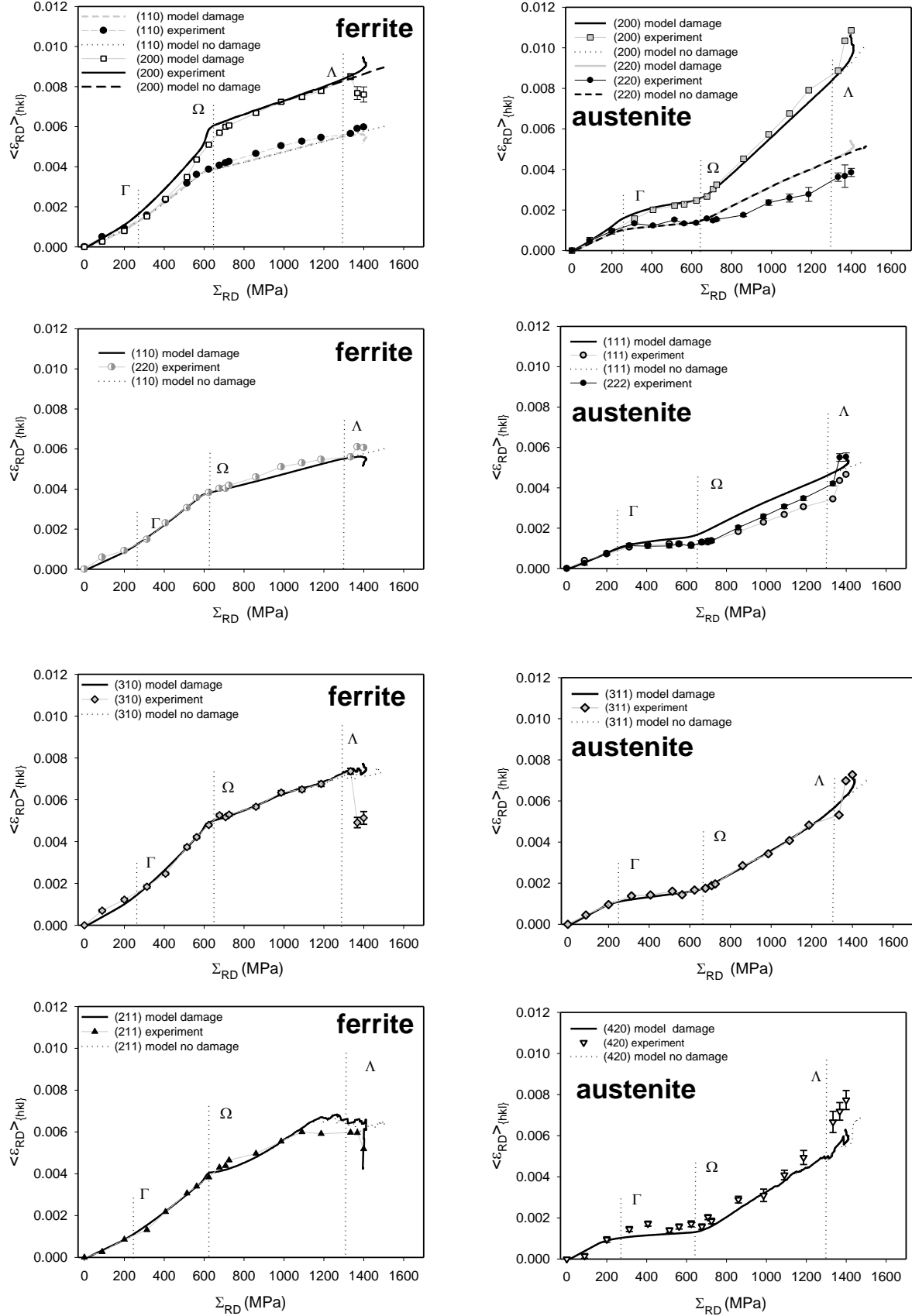


Figure 4.11 The measured elastic lattice strains $\langle \epsilon_{RD} \rangle_{\{hkl\}}$ vs. applied stress Σ_{RD} in the aged UR45N sample fitted by self-consistent model with and without prediction of the damage effect (criterion of **equivalent stress**).

4.5.3 Tests of the total energy criterion for damage

Finally, the criterion based on the **total energy** (elastic and plastic) was considered. The results of model fitting to experimental results with **total energy** criterion (according to Eqs. 4.3, 4.4) are shown in Fig. 4.13. In this case the damage parameter \dot{d}^g for a grain g was defined as follows:

$$\dot{d}^g = \xi^{ph} (w_{tot}^g - w_0^{ph})_+^{n^{ph}} (\dot{w}_{tot}^g)_+ \quad \text{Eq. 4.3}$$

where w_{tot}^g is the specific energy threshold for which damage begins and the total energy is calculated for the whole process:

$$w_{tot}^g = \int \sigma_{ij}^g d\varepsilon_{ij}^g \quad \text{Eq. 4.4}$$

while n^{ph}, ξ^{ph} parameters have the same meaning as in Eqs. 3.35 and 3.36. The adjusted model parameters are given in table 4.5.

| Damage criterion | Phase | Parameters | Values |
|-------------------------------|---------|------------|--------------------------------|
| Total energy Eqs. 4.3, 4.4 | Ferrite | w_0^{ph} | 400.e+06 (J/m ³) |
| | | n^{ph} | 0 |
| | | ξ^{ph} | 5500. e+06 (J/m ³) |

Table 4.5 Values of adjustable parameters describing the damage process in ferrite, determined using self-consistent model with **total energy** damage criteria.

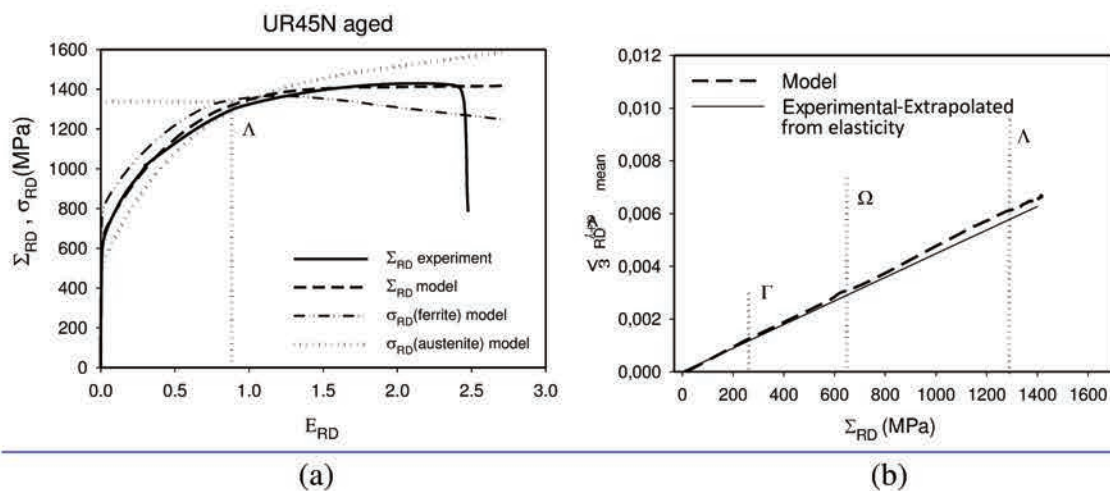


Figure 4.12 The result of mechanical tensile test performed along RD compared with model prediction, and the predicted dependence of total lattice strain $\langle \varepsilon_{RD} \rangle_{mean}^{aus+fer}$ vs. macro-stress along applied load (RD) for damage criterion of **total energy**.

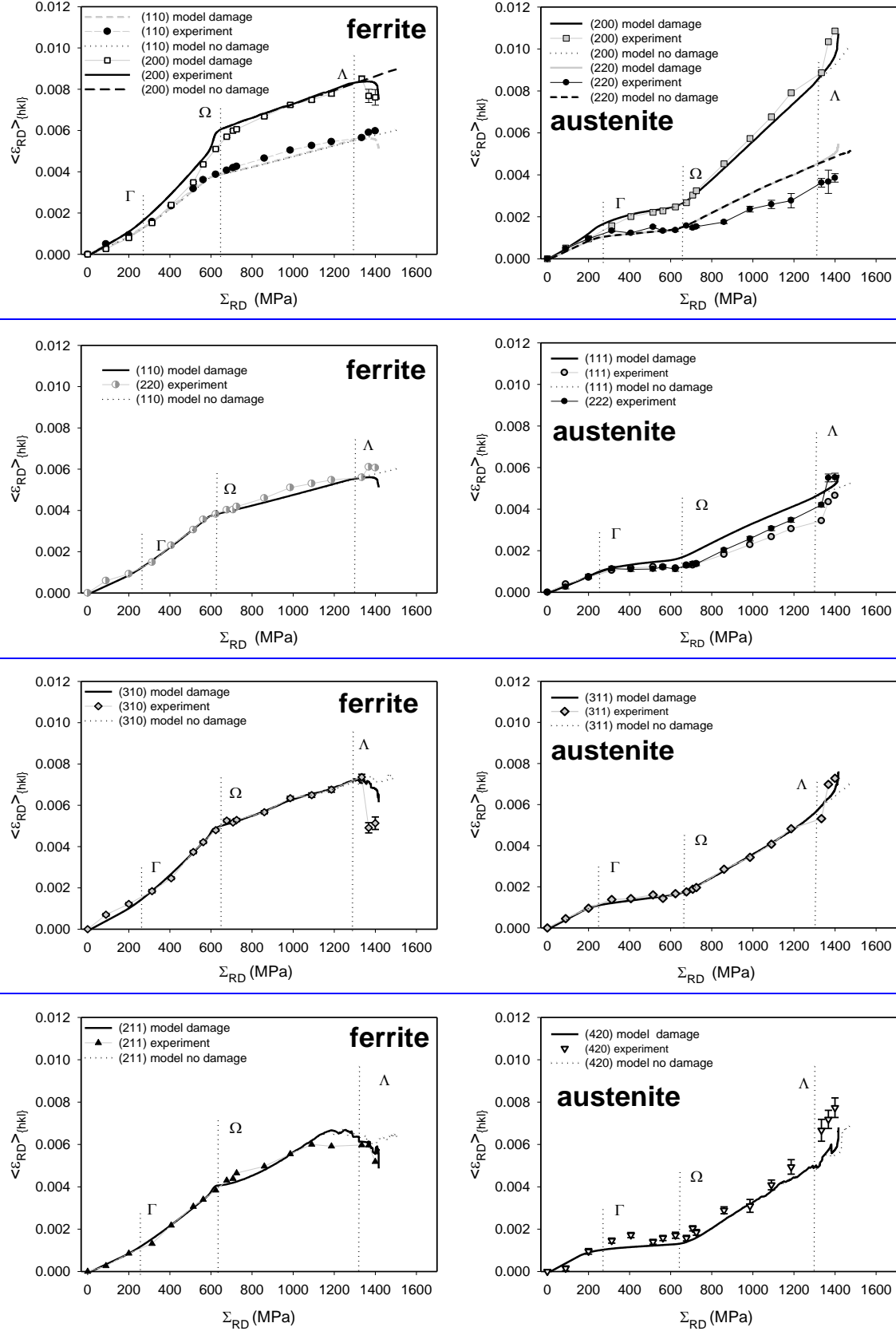


Figure 4.13 The measured elastic lattice strains $\langle \epsilon_{RD} \rangle_{\{hkl\}}$ vs. applied stress Σ_{RD} in the aged UR45N sample fitted by self-consistent model with and without prediction of the damage effect (criterion of **total energy**).

In Fig. 4.12a, the calculated Σ_{RD} vs. E_{RD} curves show again linearity in the damage range for **total energy** criterion. From the Fig. 4.12b, linearity is obtained by model calculation before the threshold Γ , a slight slope changing occurs in the plasticity range (around threshold Ω), but it is not far from the experimental data, thus the calibration of experimental data is available as proposed in Appendix 11.

For the damage criterion based on **total energy** the linear dependence of $\langle \varepsilon_{RD} \rangle_{mean}^{aus+fer}$ vs. Σ_{RD} (Fig. 4.12b) was determined from calculations in the damage range of deformation, hence the calibration of the macro-stress has been confirmed by model. The results of model prediction, compared with experimental data are shown in Fig. 4.13 for lattice strains and in Fig. 4.12 for macroscopic curve. In the case of “**total energy** criterion” the relaxation effect is successfully predicted for ferrite, but the relaxation amplitudes are not calculated such accurately as by “equivalent strain criterion” (compare Fig. 4.8 and Fig. 4.13). Also, increase of lattice strain is seen for all reflection measured in the austenite. Comparing the evolution of lattice strains, it can be concluded that the model results fit fairly well to experimental results.

4.5.4 Conclusion concerning damage criteria

Three damage criteria are tested in this work. For the **equivalent stress** damage criterion the equivalent von Mises stress was chosen as the damage parameter determining threshold of damage activation and then damage evolution. However, the distribution of stresses between grains in the ferrite was not correctly predicted when the “equivalent stress” criterion was used in calculations. The **total energy** damage criterion was based on the specific energy defined as the parameter of damage. In this case prediction of the damage process is fairly good and the relaxation of the stresses in ferrite was correctly predicted, i.e. the theoretical lattice strain evolution after threshold Λ agree with experimental results (Fig. 4.13). Finally, the **equivalent strain** damage criterion was based on the equivalent grain strain, calculated from the elasto-plastic strain tensor of grains during the whole deformation process. The results obtained with the latter criterion are similar to the model prediction with criterion of “equivalent energy” (cf. Fig. 4.7 and Fig. 4.8).

It can be concluded that the best agreement between model predictions and measurements is obtained with criterion of “equivalent strain”. This result suggests that the accumulation of grain strain and the history of grains’ deformation, including the variation of grains’ orientations, dominate the damage initiation. In this case significant load transfer between

both phases can be predicted if damage/softening in the ferritic phase is taken into account. It should be underlined that, a very good agreement between experiment and model is obtained for the lattice strains in both phases, as well as for macro-mechanical curves during the elasto-plastic deformation. Hence, the observed relaxation of stress in the ferrite can be identified as the result of the damage occurring at the grain scale, which is correctly described using a new version of self-consistent model.

4.6 Space depending analysis and necking behaviour study

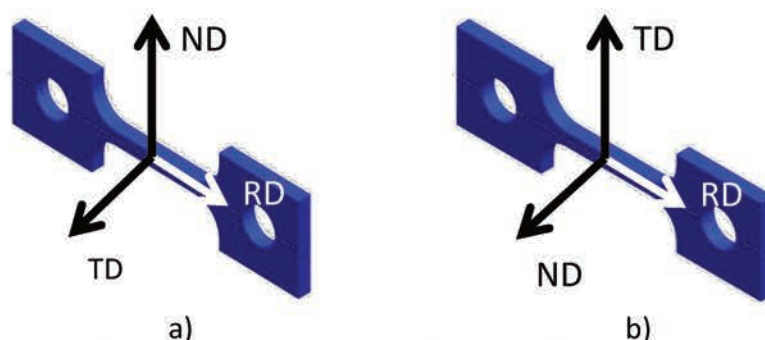


Figure 4.14 Schematic illustration of “Sample TD” (a) and “Sample ND” (b).

For the second part of damage study, synchrotron diffraction was applied to scan the lattice strain along the necking zone, generated during large deformation of the UR45N aged steel. The experimental setup and the shape of the samples used in this work were the same as in the previous study using synchrotron diffraction measurements (cf. section 4.1). Two samples “sample TD” and “sample ND” with their orientations are shown in Fig. 4.14. Both samples were machined from a rolling sheet of UR45N aged steel. Sample TD was manufactured in the way that the transverse direction (TD) was perpendicular to the sample surface, which means that the incident X-ray beam was parallel to the TD direction during the tensile test (see Fig. 4.1 and Fig. 4.14). Sample ND was made with the normal direction (ND) perpendicular to its surface, allowing measurement with the incident X-ray beam parallel to the ND. The load was applied along the RD for both samples.

The loads were applied in the RD direction but the tensile tests in this study were conducted in the strain control mode. The strain rates were defined as $2.8 \times 10^{-4} \text{ s}^{-1}$ and $2.4 \times 10^{-4} \text{ s}^{-1}$ respectively for test of “Sample TD” and “Sample ND” before the appearance of necking, and then the necks were scanned for given constant sample strains. The advantage of strain control mode is that it enables the measurement even during the heterogeneous deformation when the neck occurs. In this case, during a progressively increasing sample

strain, the loading of the sample decreases, preventing a concentration of the large stress in the narrowest section of the neck.

During measurements the position of grip in tensile rig was recorded and the force applied to the sample was determined using a load cell. The true macro-stresses were determined considering the evolution of sample cross section, while the elasticity of rig was taken into account in the calculation of true macro-strain. The plots of true stress (Σ_{RD}) vs. true strain (E_{RD}) are reported respectively for the two studied samples in Fig. 4.15 a and b. It should be underlined that in the case of “Sample TD” the measurement was made only during the pronounced plastic deformation range including the necking process and the Σ_{RD} vs. E_{RD} plot of this sample was completed by our previous results obtained from an identical sample (cf. Fig. 4.18).

The curves obtained in both experiments perfectly overlap in the elasto-plastic deformation range (sample strain $0.015 < E_{RD} < 0.2$). As shown in Fig. 4.15 a and b an important reduction of the applied stress occurred at about $E_{RD} \approx 0.25$ until the end of the test, i.e. up to the sample fracture. This stress reduction indicates the appearance of sample necking which was observed through an optical lunette during measurements. It should be stated that starting from $E_{RD} \approx 0.25$ the true stress as well as the true strain cannot be correctly estimated because of the heterogeneous sample deformation and the important difference between the cross section inside and outside the necking (i.e., from this moment the applied macro-stress was relaxed during the further sample deformation, but the values Σ_{RD} and E_{RD} do not have a correct physical meaning).

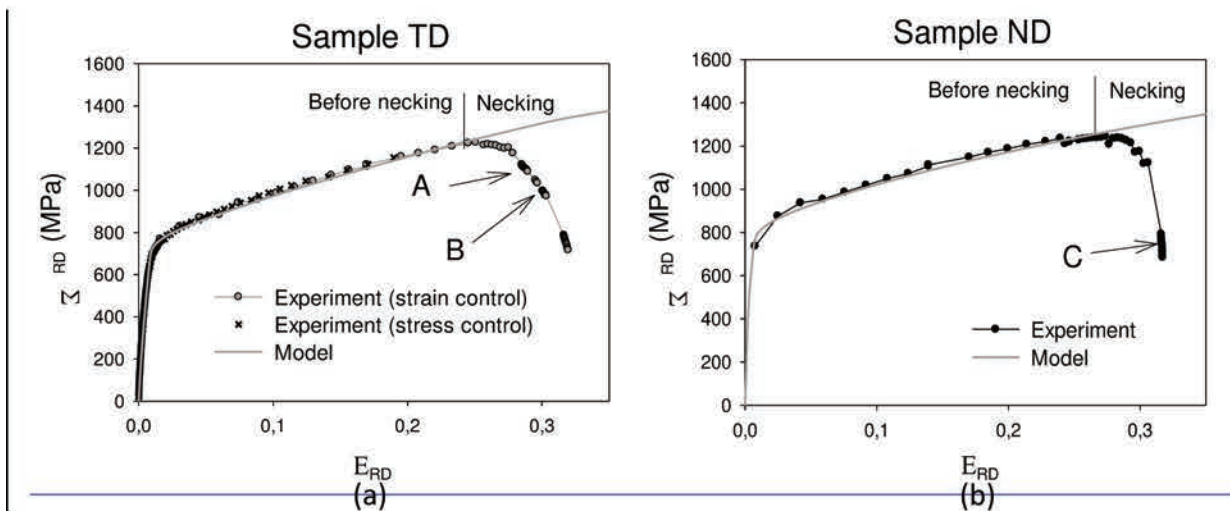


Figure 4.15 The plots of true stress vs. true strain for the measured “Sample TD” and “Sample ND”. The indicated A, B and C points represent the stages for which scanning of necking zone was performed.

Three scans along the neck were carried out at the sequence of three necking stages A, B and C as indicated in Fig. 4.15. These scans were performed at different evolution stage of the ductile damage process for two studied samples. The scan A was carried out at the beginning of necking effect, the scan B is performed during the necking growing, and the scan C is done at the end of tensile test before the sample fracture.

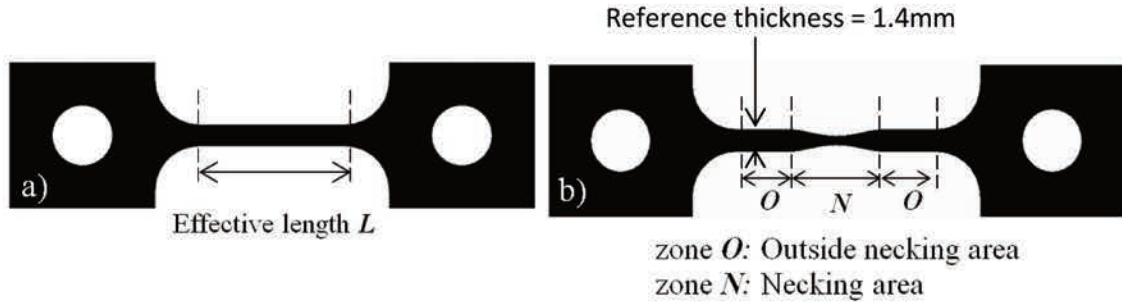


Figure 4.16 Schematic drawing of tensile test sample: the sample before tensile test (a) and the sample after the appearance of necking (b). The studied zones are indicated.

The scans were performed along and outside the necking zone (zones Necking and Outside in Fig. 4.16), and the X-ray beam was parallel to TD in the case of “Sample TD” (stages A and B) and to ND in the case of “Sample ND” (stage C), cf. Fig. 4.15. The estimation of sample thickness along necking was based on the comparison of the outgoing beam intensity received by the detector “Pico1” from the neck and from the known reference thickness, far from the neck. The reference thickness is equal to 1.4 mm (as shown in Fig. 4.16), measured from the outside necking area of fractured sample by vernier calliper after the tensile test. A schematic drawing of the setup used with “Pico1” detector is presented by Fig. 4.17a.

The spatial evolutions of the sample thickness along the necking zone estimated for two samples are presented in Fig. 4. 17b. However, the curves determined for the stages A and B cannot be compared with the one for stage C, because the measurements were performed with different orientations of the sample (TD or ND) with respect to the incident beam. Comparing thickness of the deformed necks in two directions after tensile tests, we found that the reduction of sample thickness in the necking region was more significant in ND than in TD. This phenomenon can be explained by the strong crystallographic texture in both phases of the studied steel (cf. Fig. 1.12 and Fig. 1.13 page 23,24), leading to anisotropy of macroscopic plastic deformation (the elliptical cross section of the neck is shown in [Le Joncour 11] for the round sample). The absorption law was used to evaluate the variation of the sample thickness:

$$I = I_0 e^{-\mu d} \quad \text{Eq. 4.5}$$

where I_0 and I are the measured intensities of incident and outgoing beams, d is the thickness of the sample in the scanned area and $\mu = 2.9 \times 10^{-1} \text{ cm}^{-1}$ is the linear absorption coefficient of iron determined for a synchrotron X-ray energy of 87 KeV [Daniels 09].

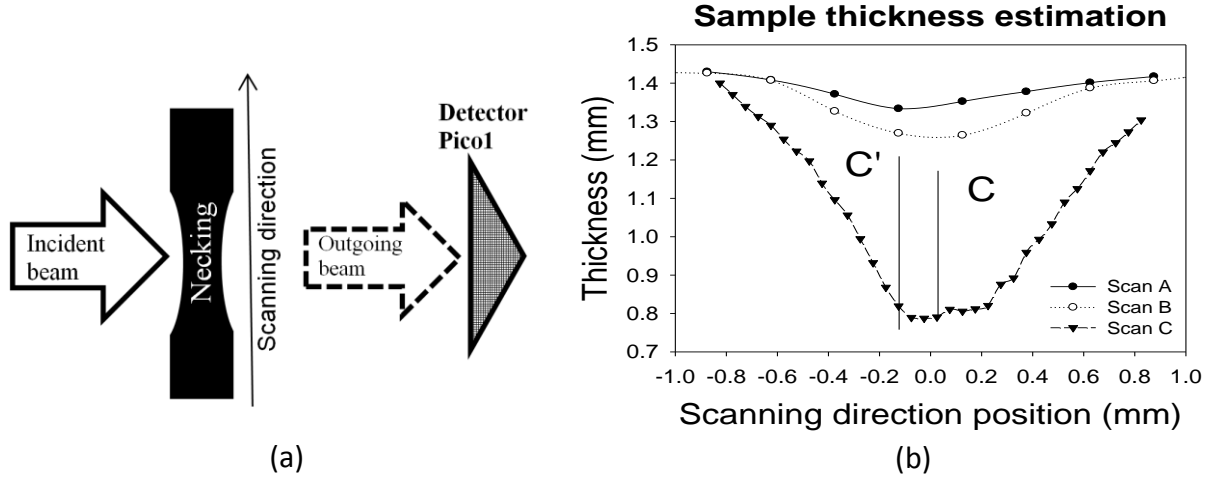


Figure 4.17 (a) Schematic drawing of the setup used for necking scan. (b) The estimated sample thickness along the necking zone determined from scans A, B and C. The abscissa represents positions of measurement along the scanning direction.

4.6.1 Experimental data treatment

The interplanar spacings were determined for the direction along the applied load (RD, $\alpha = 0^\circ$ and 180° , cf. Fig. 4.1b) for both studied samples. Diffraction rings were integrated within “cake shape” sectors defined by $\alpha_n \pm 7.5^\circ$ and the mean $\langle d \rangle_{\{hkl\}}$ spacings were calculated for symmetrically equivalent α_n and $\alpha_n + 180^\circ$ angles. Next, the elastic lattice strains $\langle \varepsilon \rangle_{\{hkl\}}$ corresponding to different hkl reflection were then determined (cf. Eq. 4.3, \vec{n} is parallel to RD).

Finally, the arithmetic averages $\langle \varepsilon_{RD} \rangle_{phase}$ over lattice strains of individual hkl reflections belonging to each phase were determined for both samples. Reflections 111, 200, 220, 311 in the austenite and 110, 200, 211, 220 in the ferrite were available for the calculation of average phase strains (intensity of other reflections was too weak for a reasonable analysis). The plots of mean lattice strains vs. applied true stress are shown in Fig. 4.18a, separately for the ferritic and austenitic phases. In the case of “sample TD” the results of the previous experiment performed until necking (cf. section 4.1) are also included in Fig. 4.18a.

The same reflections as in the case of “Sample TD” were involved into the calculation of average phase strains for “Sample ND”. The plots of mean lattice strains vs. applied true stress for “Sample ND” are shown in Fig. 4.19a. The initial diffraction pattern allowed us to determine only one component of the initial stress tensor (measurement was performed only for one sample orientation).

The initial stresses for each sample are presented in table 4.6. In the case of “Sample TD” the stress tensor is the same as determined from the previous samples (cf. table 4.1).

| | Phase | σ_{RD} (MPa) | σ_{TD} (MPa) | σ_{ND} (MPa) |
|-----------|-----------|---------------------|---------------------|---------------------|
| Sample TD | Austenite | 134 ± 15 | 84 ± 15 | -218 ± 15 |
| | Ferrite | -155 ± 19 | -44 ± 19 | 199 ± 18 |
| Sample ND | Austenite | -34 ± 11 | not measured | not measured |
| | Ferrite | 59 ± 19 | | |

Table 4.6 Initial residual stresses measured in each phase of the studied UR45N aged.

The self-consistent model of elasto-plastic deformation [Lipinski 89, Lipinski 95, Franz 13, Franz 14] was used to interpret the experimental results as well as to determine the parameters of Voce law [Tomé 89, Baczmański 16] in each phase of the studied duplex steels. This allows us to characterize the mechanical behaviour of the phases within polycrystalline material. In these calculations, the initial orientations of crystallites, corresponding to the experimental textures (cf. Fig. 1.13 page 24), single crystal elastic constants given in table 1.6 page 23 (the same as for XEC calculation) and the initial stresses listed in table 4.6 were used as the input data for each phase. Simulations were performed for 2,000 spherical grains belonging either to the ferrite (50%) or to the austenite (50%) phases, as the model calculation in previous study. The elastic lattice strains $\langle \varepsilon_{RD} \rangle_{\text{phase}}$, and the total sample strain Σ_{RD} vs. applied stress E_{RD} were calculated for different tensile loads corresponding to the experimental ones.

4.6.2 Analysis during tensile tests

To adjust the model strains $\langle \varepsilon_{RD} \rangle_{\text{phase}}$ to the experimental data, the values of the critical resolved shear stress were varied for both phases. Thus, the two thresholds Γ and Ω , defined as in section 4.3, can be identified as the yield points for the austenitic phase and for the ferrite phase, respectively. The model results were fitted to the experimental lattice strains

(Fig. 4.18a and 4.19a) and simultaneously to the experimental Σ_{RD} vs. E_{RD} plot (see Appendix 11). The critical resolved shear stresses (CRSS) τ_0^{phase} and parameters τ_1^{phase} , θ_0^{phase} , θ_1^{phase} characterizing work hardening for each phase can be determined. The parameters of Voce law determined for ferrite and austenite are presented in table 4.7.

| | | Sample TD | Sample ND |
|---------------------------------|-----------|-----------|-----------|
| τ_0^{phase} (MPa) | austenite | 150 | 150 |
| | ferrite | 420 | 490 |
| θ_0^{phase} (MPa) | austenite | 380 | 420 |
| | ferrite | 190 | 150 |
| τ_1^{phase} (MPa) | austenite | 280 | 280 |
| | ferrite | 140 | 140 |
| θ_1^{phase} (MPa) | austenite | 80 | 80 |
| | ferrite | 40 | 40 |

Table 4.7 Parameters of plastic deformation determined for the studied samples.

A very good agreement between the macroscopic behaviour (Fig. 4.15) predicted by the model and experimental results were observed in the measuring range of the homogenous deformation, i.e. up to about 0.25 of the sample strain E_{RD} . After that an unstable process caused by the necking phenomenon began.

The stress calibration as described in Appendix 11 and expressed by Eq. A11.1 has been applied for the experimental data collected during scanning of the necking zone of the sample, where the heterogeneous macroscopic deformation occurred. However, before the appearance of necking, samples can be considered as homogeneously deformed. To calibrate the macro-stress value in the necking zone the arithmetic mean over the lattice strains available for both phases $\langle \varepsilon_{RD} \rangle_{\text{mean}}^{\text{Aus+Fer}}$ was calculated according to Eq. A11.1 and Eq. 11.2.

A few measurements have been performed along the necking from outside to its centre, when the neck occurred. Additionally, the difference between the mean lattice strain in the austenite $\langle \varepsilon_{RD} \rangle_{\text{Aus}}$ and the ferrite $\langle \varepsilon_{RD} \rangle_{\text{Fer}}$, defined by the equation Eq. 4.6, are presented separately in Fig. 4.18b for “Samples TD” and in Fig. 4.19b for “Sample ND”. This difference was calculated from formula:

$$\langle \varepsilon_{RD} \rangle_{\text{Aus-Fer}} = \langle \varepsilon_{RD} \rangle_{\text{Aus}} - \langle \varepsilon_{RD} \rangle_{\text{Fer}} \quad \text{Eq. 4.6}$$

4.6.2.1 Analysis on “Sample TD”

A good accordance between theoretical and experimental data is obtained for the measured lattice strains on “Sample TD” (Fig. 4.18a), for both measurements on pre-necking stage and

in the centre of the neck. The results prove that the model correctly predicts the partition of the stresses between both phases, and the calibration method enabled the determination of the macro-stresses in the gauge volume.

It is found that the tendency of the phase strains/stresses evolution slopes determined for pre-necking stages continue in the centre of the neck (points A and B are close to the model calculated curves). It should be noted that either during the pre-necking stages or in the centre of the neck the mean lattice strains in the austenite are larger than the strains in the ferrite (negative value of $\langle \varepsilon_{RD} \rangle_{Aus-Fer}$). This difference is caused by a lower yield stress of the austenitic phase, as explained in [Baczmański 11, Baczmański 16] and in the Appendix 11.

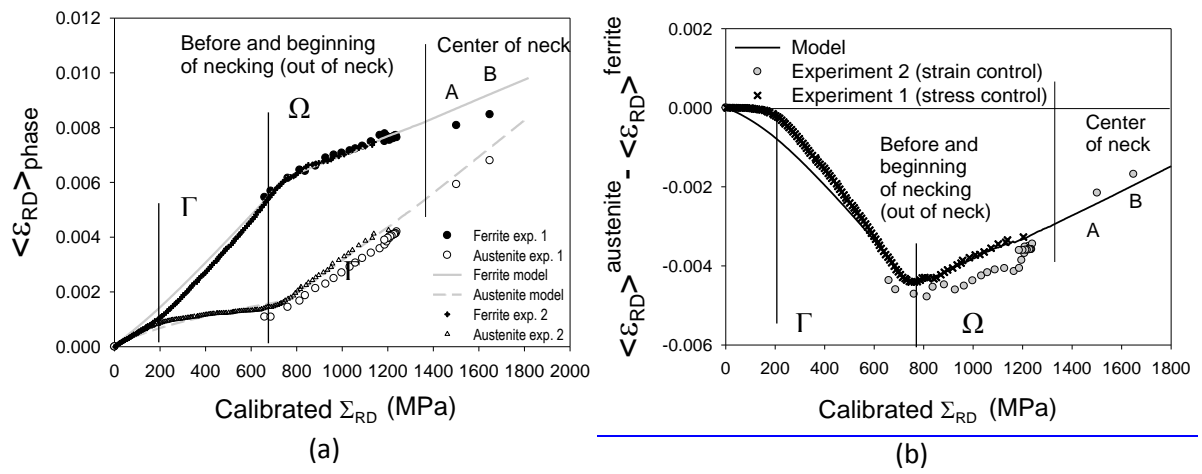


Figure 4.18 (a) The evolution of phase lattice strains vs. calibrated sample stress before beginning of necking and in the centre of the neck for the “samples TD”, deformed in the load control mode and in the strain control mode. (b) The difference between lattice strains in the austenite and the ferrite $\langle \varepsilon_{RD} \rangle_{Aus-Fer}$ is also shown. Experimental results (point) are compared with the model (lines).

The plots of mean lattice strain $\langle \varepsilon_{RD} \rangle_{phase}$ in each phase vs. calibrated stress Σ_{RD}^{cal} are presented in Fig. 4.18a for two “Samples TD” under tensile tests (the first experiment **exp.1** was measured in load control mode until failure, while the second one **exp.2** was measured during a large deformation and the necking process in the strain control mode). The diffraction measurement was carried out during the whole experiment **exp.2**, while the elastic deformation stage is skipped from the diffraction measurement during the experiment **exp.1**. So the experimental data of both experiments are put together to complete the stress-strain evolution curves (Fig. 4.18a). Good accordance was found between the two tests. A slight turn back parallel to the slope of elastic stage can be observed from the end of “out of neck” curves of **exp.1**, which indicates a spring back rather than a relaxation of material in the sample out of necking.

4.6.2.2 Analysis on “Sample ND”

Then, the “Sample ND” was in situ measured during a tensile test, and a very different evolution of phase strains is observed compared with that of “Samples TD” (cf. Fig. 4.18 and 4.19), especially during the elastic stage of both phases. The threshold Γ occurred at 410 MPa while the threshold Ω occurred at 800 MPa. From the measured initial stress presented in table 4.7, we can see that the stress component along RD direction in “Sample ND” is significantly different from that in “Sample TD”, and it has a negative value. This negative initial stress has been taken into account during the model calculation and a very good agreement between the model and the experiment was obtained (Fig. 4.19). The same value of τ_0^{phase} for austenite and a higher value for ferrite than that used in the model calculation of “Samples TD” were applied in the calculation for “Sample ND” (see table 4.7). It can be concluded that the material heterogeneity, especially the difference in initial residual stresses, plays an important role in the elasto-plastic deformation of material (cf. Fig. 4.18 a and Fig. 4.19a).

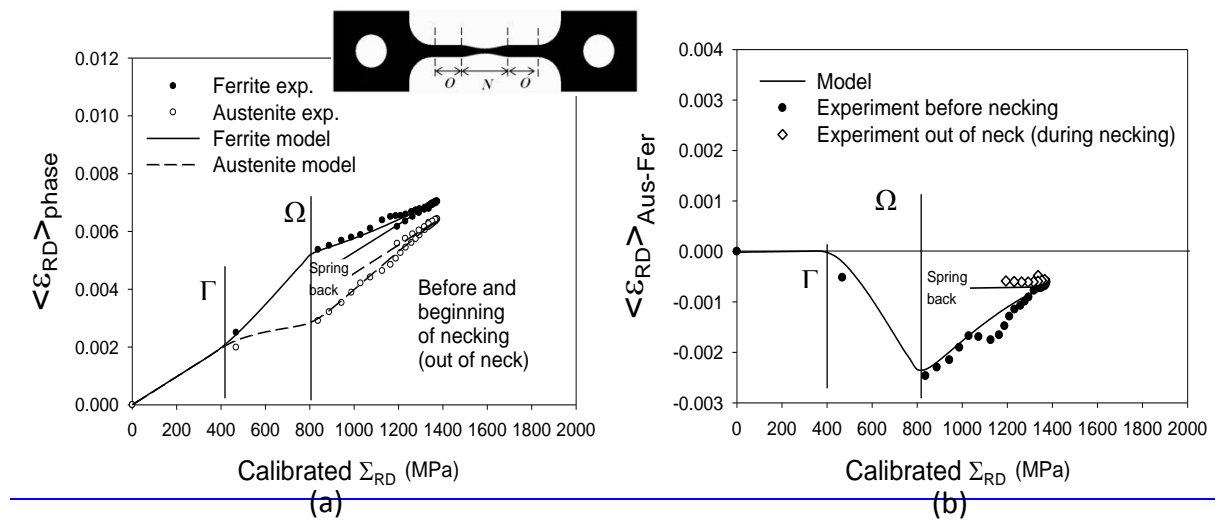


Figure 4.19 Measurements outside necking zone, (a) The evolution of phase lattice strain for “Sample ND” and (b) the difference between the lattice strain $\langle \epsilon_{RD} \rangle_{\text{Aus-Fer}}$ in austenite and in ferrite for “Sample ND”.

If we analyse the phenomenon during the necking stage, a strong spring back of the lattice strain/stress (shown at the end of plots in Fig. 4.19a) can be observed in the zone O, out of neck. At the same time, the difference between phase strains ($\langle \epsilon_{RD} \rangle_{\text{Aus-Fer}}$) stabilized. This phenomenon means that the stress in the material outside neck decreased when the necking occurred, and the plastic deformation was terminated in this part of the sample (zone O). The experimental strains for both phases as well as the difference between them were correctly predicted by the self-consistent model. On the contrary, the stress in the neck does

not decrease due to a narrowing of the sample section, leading to stress concentration in this region (zone N).

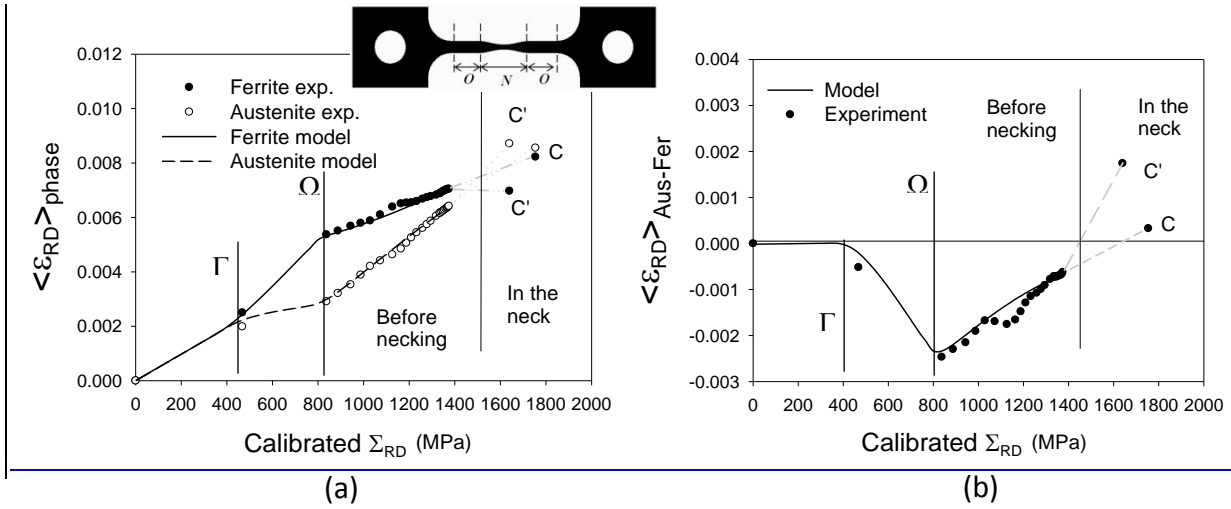


Figure 4.20 Measurements outside necking, (a) The evolution of phase lattice strain of “Sample ND” and (b) the difference between the lattice strain $\langle \epsilon_{RD} \rangle_{\text{Aus-Fer}}$ in austenite and in ferrite for “Sample ND”.

As shown in Fig. 4.20a and b, both materials in the centre of the neck (point C, cf. Fig. 4.17b) or close to the centre (point C') were subjected to a higher loading than in the pre-necking stage. The lattice strains in the neck centre (point C) followed the tendency of evolution before necking (Fig. 4.20a) and the difference between lattice strains in both phases ($\langle \epsilon_{RD} \rangle_{\text{Aus-Fer}}$) approaches to zero value (Fig. 4.20b). In point C', placing close to the centre C and still in N zone, the lattice strain was much smaller in the ferrite in comparison with that in the austenite (Fig. 4.20a). Hence the difference between these strains $\langle \epsilon_{RD} \rangle_{\text{Aus-Fer}}$ was large and positive (Fig. 4.20b). The significant heterogeneity of the stresses in the necking region will be discussed in the next section. These points (C and C') will be discussed in the following text.

4.6.3 Analysis of spatial scanning results in the necking area

Interesting evolutions of lattice strains along the neck were observed from the three scans performed during the stages A, B and C, marked in Fig. 4.21. The lattice strains in the loading direction for each phase, and the difference between strains in austenite and in ferrite ($\langle \epsilon_{RD} \rangle_{\text{Aus-Fer}}$) in the spatial positions along the neck are presented in Fig. 4.21, respectively for the scan A (Fig. 4.21a), the scan B (Fig. 4.21b) and the scan C (Fig. 4.21c).

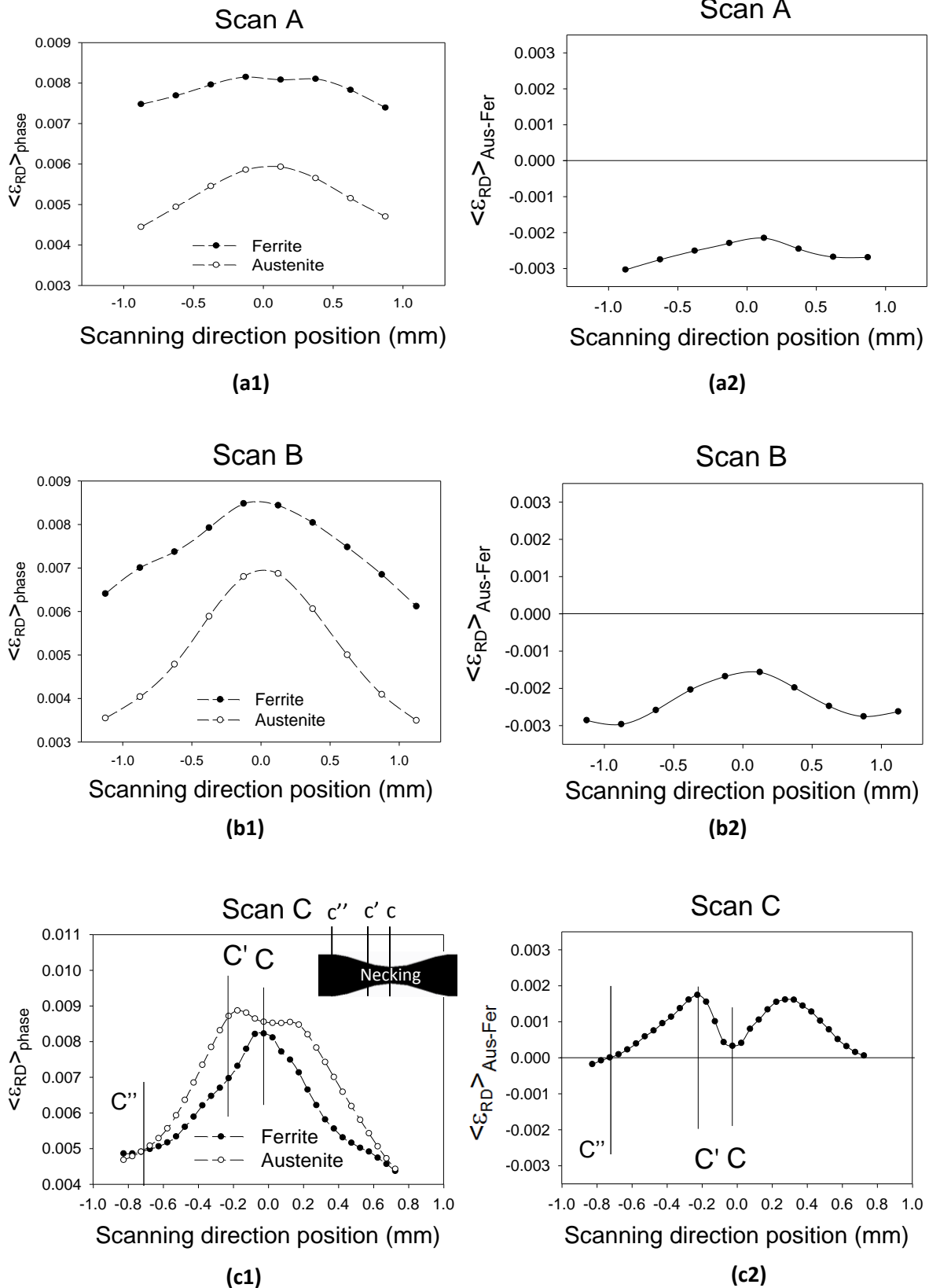


Figure 4.21 The evolution of phase lattice strains (a1, b1, c1) and difference between strains in the austenite and the ferrite $\langle \epsilon_{RD} \rangle_{\text{Aus-Fer}}$ (a2, b2, c2) in function of position in the neck. The results for scans in positions A, B (“sample TD”) and C (“sample ND”) are shown respectively in Figures (a), (b) and (c). The position of threshold C, C’ and C’’ are shown on the small legend of necking are on the top right corner.

In the case of no-advanced necking process (scans A and B), the lattice strains in austenite was lower than that in ferrite along the whole neck (i.e. negative value of $\langle \varepsilon_{RD} \rangle_{Aus-Fer}$ was determined along the neck). In the centre of the neck, the value of difference between phase strains (i.e. the absolute value of $\langle \varepsilon_{RD} \rangle_{Aus-Fer}$) decreased faster than that in other positions in the sample. This phenomenon can be explained as the highest stress concentration through the most pronounced plastic deformation within the neck (i.e. the centre of neck).

On the contrary, an unexpected evolution of the difference $\langle \varepsilon_{RD} \rangle_{Aus-Fer}$ vs. spatial position along the neck is observed on the scan C (Fig. 4.21c2). We can see the lattice strains in the centre of neck (point C) are almost equal for both phases, but in the area next to the centre (i.e. point C'), a significant inversion of strains occurred, where the strain in austenite is much higher than that in ferrite. Consequently, much lower mean lattice strains were measured in the ferrite than in the austenite over the neck, excluding its centre.

The inversion of strains, started at the point C'' (see Fig. 4.22), suggests relaxation effect in ferrite which has been previously observed (cf. section 4.5 time depending analysis, Fig.4.9) using neutron diffraction on a larger gauge volume within the neck. The transition of the load from the ferrite to the austenite can be explained by the damage process potentially initiated in the ferrite, which leads to a loss of mechanical strength of this phase. Hence, the observation from the previously neutron diffraction measurement over a large gauge volume inside the neck, is confirmed using a synchrotron measurement performed with a finer beam resolution along the deformation neck.

Other issue is to find which grains in a given phase are responsible for the load transition between phases observed at the beginning of damage. In this aim, the evolution of lattice strains $\langle \varepsilon \rangle_{\{hkl\}}$ of each hkl reflections measured along the neck is shown in Fig. 4.22. As presented, the evolution of $\langle \varepsilon \rangle_{\{110\}}$ for reflection 110 in ferrite and all lattice strains for the reflections in austenite exhibit a similar variation along the neck. However, for the reflections 211 and 200 in ferrite, the lattice strains $\langle \varepsilon \rangle_{\{211\}}$ and $\langle \varepsilon \rangle_{\{200\}}$ declined sharply with the distance away from the neck centre. This phenomenon agrees with the previous result measured by neutron diffraction (cf. section 4.5), and showing that close to the fracture of the sample the lattice strains decreased significantly for the reflections 211 and 200 and remained stable for the reflection 110 in (cf. Fig. 4.22).

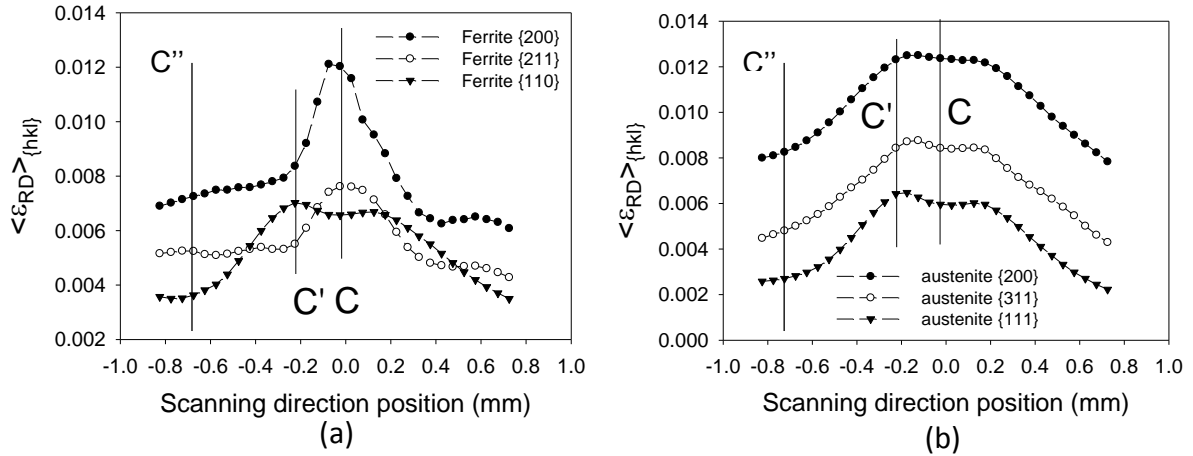


Figure 4.22 The evolution of the lattice strains measured for different reflections in the ferrite (a) and in the austenite (b) along position in the neck (stage C/C' in “sample ND”).

In conclusion, the ferritic grains having particular orientations, which contributed to the reflections 211 and 200, exhibited different behaviour from the other grains in the sample. This phenomenon can be potentially caused by micro-cracks initiated on these mentioned grains in ferrite. And supporting Alvarez–Armas’s observation [Alvarez-Armas 12], that the micro-cracks propagate through planes $\{112\}$. However, it should be emphasised that the link between the evolution of measured lattice strains and cracks orientation is probably more complex and related to grain orientation with respect to the applied load, as well as intergranular interactions. The latter factors are taken into account in the self-consistent model which is used to explain the experimental results. However, such phenomena, for example the role of grains boundaries, are not taken into consideration in the interpretation.

The load transfer seems depending on the spatial position along the neck. Therefore, the sample geometry is important to the stress distribution and to the evolution of phase strains along the neck. The contribution of sample geometry on stress and strain evolution will be investigated in the following section.

4.6.4 Finite Element Method (FEM) simulation

In order to study the contribution of geometry to stress distributions, a simple FEM simulation was carried out with Abaqus CAE 6.13 software. The three-dimensional geometric model was built according to the sample dimensions determined from the deformed sample in which the neck was created. The dimensions of 3D model are given in Fig. 4.23. The elastic deformation of the studied material was simulated using the anisotropic overall elastic

constants previously determined by a self-consistent model. The overall stiffness tensor (given in table 4.8) was calculated from single crystal elastic constants of each phase and accounting for the crystallographic texture.

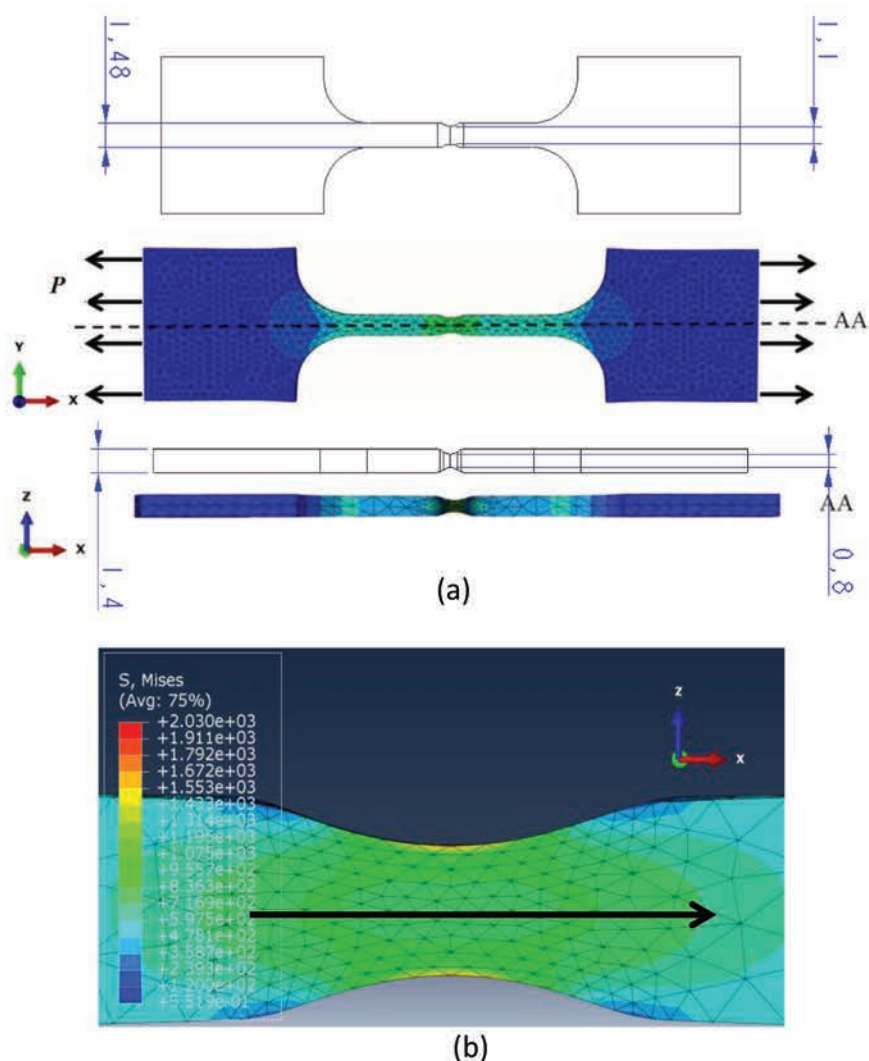


Figure 4.23 Illustration of sample modelling without and with loading (a, length in mm) and the spatial distribution of von Mises stress with indicated scanning path direction (b).

| C_{11} [GPa] | C_{22} [GPa] | C_{33} [GPa] | C_{12} [GPa] | C_{13} [GPa] | C_{23} [GPa] | C_{44} [GPa] | C_{55} [GPa] | C_{66} [GPa] |
|----------------|----------------|----------------|----------------|----------------|----------------|----------------|----------------|----------------|
| 261 | 265 | 252 | 99 | 112 | 108 | 84 | 88 | 74 |

Table 4.8 Anisotropic elastic matrix determined using self-consistent method in consideration of experimental textures and single crystal elastic constants given in table 4.2.

In order to get a preliminary model simulation, dynamic implicit step with a time period of 100 seconds was applied only on the elasticity range. The external load is estimated from the applied force and the cross section of extremity of sample, a homogeneous uniform pressure of $P = -80$ MPa (calculated by imposed force F /sample cross section S was imposed on the

two end sections of sample (shown in Fig. 4.23) to simulate the stress imposed by external loading during tensile test. In order to balance the computation speed and the accuracy of FEM simulation, triangle elements were applied. On the out-necking area, the mesh with free structured tetrahedral element was used, the element seeds were assigned every 0.5 mm along the edge of model. The same type of element was applied for the mesh of in-necking area, but the distance between the element nodes was reduced to 0.05 mm in order to get a more accurate result along the necking. The macroscopic elastic tensor of the studied duplex steel was introduced into the model to account for elastic anisotropy of the sample. In the simulation performed in this work mainly the influence of the neck shape on stress distribution was studied (two-phase structure was not considered in the calculations).

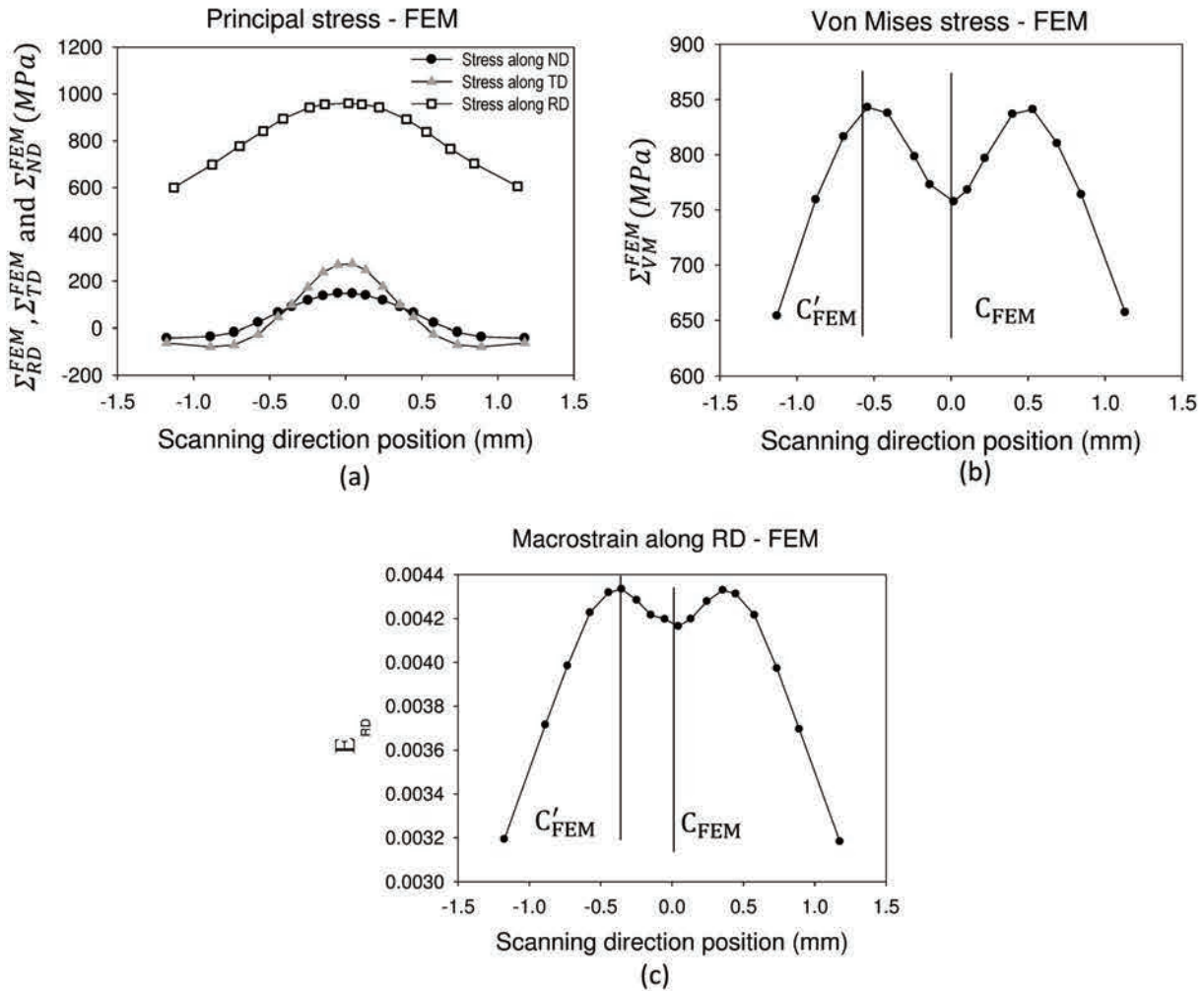


Figure 4.24 Dependence of the principal stresses (a) von Mises stress (b) and longitudinal strain(c) on the position along the neck.

The evolutions of the simulated principal stresses Σ_{RD}^{FEM} , Σ_{TD}^{FEM} and Σ_{ND}^{FEM} (shear stresses are negligible), principal strain E_{RD}^{FEM} and in the direction of the applied load and von Mises stress Σ_{VM}^{FEM} in position function along the neck are plotted in Fig. 4.24. It can be concluded that due to **triaxiality** of the stresses in the necking region the maximum von Mises stress Σ_{VM}^{FEM} and strain ε_{RD}^{FEM} are not concentrated in the narrowest part of the neck, the stress concentration occurs rather in the place at approximately the same distance from the necking centre. Comparing Fig. 4.22 and Fig. 4.24 an interesting qualitative correlation is found between phase strains difference $\langle \varepsilon_{RD} \rangle_{Aus-Fer}$ determined from diffraction measurement and the value of von Mises equivalent stress Σ_{VM}^{FEM} obtained from the FEM simulation. Both quantities decrease significantly in the centre of the neck. The value of the difference between phase strains $\langle \varepsilon_{RD} \rangle_{Aus-Fer}$ increases and reach maximum value at the distance of approximately 0.3mm from the centre and also the value of von Mises equivalent stress Σ_{VM}^{FEM} increases up to maximum but at the distance of about 0.5 mm (C'_{FEM}) from the centre.

In a word, an approximate correlation can be seen between the calculated Σ_{VM}^{FEM} , E_{RD}^{FEM} and the measured lattice strains for all reflections of austenite and the reflection 110 of ferrite (cf. Fig. 4.22 and Fig. 4.24). The grains contributing to the above mentioned reflections probably characterize the deformation along neck under tensile load. However, the lattice strains measured on reflections 211 and 200 of ferrite exhibit different dependence on scanning position comparing with the calculated von Mises stress Σ_{VM}^{FEM} and strain E_{RD}^{FEM} . The highest strain is concentrated in the narrowest part of the neck and significantly decreases away from the centre. This effect can be caused by the damage occurring in the grains contributing to reflection 211 and 200 of ferrite, as it was previously observed using the neutron diffraction (cf. section 4.5).

It should be reminded, both maxima are not perfectly correlated and this disparity can be explained by several factors not accounted in the FEM calculations, such as: heterogeneity of the real material properties caused by plastic deformation in the necking zone, simple elastic stage, and inaccurate neck form of sample model compared with the neck form during tensile test, etc. Despite of this disagreement, the FEM calculation indicates that the stress **triaxiality** seems to play an important role in the stress relaxation in the ferrite and probably leads to the initiation of the damage process in this phase. The value of the von Mises macro-stress increases at some distance from the neck centre due to **triaxiality** of the macro-stress, which probably leads to more advanced damage processes occurring in the whole material.

4.8 Conclusions

In this chapter, the mechanical behaviour of duplex steel UR45N and UR52N during tensile test was studied. The lattice strains of both the austenitic and ferritic phases were in situ measured by neutron and synchrotron diffractions during the tensile test. The self-consistent model predictions were performed in order to compare with the experimental data. In elasto-plastic deformation range, it is confirmed, by comparing the experimental results with the model prediction, that the elasto-plastic properties are different in each phase, the yield stress of austenite is much lower than that of ferrite. Different critical resolved shear stresses as well as the other concerned plastic deformation parameters are identified for both phases in differently manufactured duplex steels. The values of CRSS for both phases are determined by adjusting the predicted results to the experimental data obtained from synchrotron or neutron diffraction measurements. The experimental and theoretical yield points (Γ and Ω , cf. Fig. 4.5) for each phase is compared, allowing to determine the initial CRSS of austenite and of ferrite. The Voce law parameters (τ_1^{ph} , θ_0^{ph} , θ_1^{ph}) related to the plastic behaviours and evolution of work hardening have been determined for each phase. It can be proved that the micro-mechanical behaviour of materials at grain scale was strongly influenced by the chemical composition of material and by the heat treatment process. Comparing the experimental data from UR45N steels subjected to different thermal treatments, considerably lower yield stress for ferrite was observed in the quenched material than in the aged one. Comparing the mechanical properties between steels UR45N and UR52N, which were manufactured by same thermal treatment but with different chemical compositions, higher yield stresses and CRSS can be seen in both phases of quenched UR52N. Besides, it was also found that the yield stress for each phase strongly depends on the initial residual stress remained in the phase (cf. table 4.1). Comparing the results obtained from tensile (Fig. 4.6), asymmetric evolution of lattices strains was found for both phases, due to the initial stress in each phase.

The main original issue of the presented work is the study of the stress and strain partitioning between the phases in duplex stainless steel, correlated with the damage process during the necking phenomenon. To do this, measurements of lattice strains during tensile and compression tests including spatial scanning along the necking were performed. The experimental data were compared with self-consistent model and FEM simulation.

On the basis of the synchrotron and neutron diffraction experiments, it is observed that in the case of the UR45N steel, the stress relaxation responsible for damage initiations seems beginning in ferritic grains, especially the grains which contribute to the 211 and 200 reflections. In both experiments a significant decrease of the lattice strains measured with those reflections were observed. Comparing the results of neutron diffraction obtained for UR45N steel with self-consistent prediction, it was found that the criterion of damage based on the **equivalent strain** gives the best results concerning stress (or lattice strains) partitioning between phases and individual grains. Almost the same but a little worse results were obtained when the **total energy** criterion was used.

Good spatial resolution of the synchrotron diffraction experiment enabled finding out that the maximum decrease of the lattice strains occurred at the distance 0.3 mm from the neck centre. For early stages of necking, the difference between the lattice strains in the austenite and the ferrite evolves more significantly in the neck centre (compared to beyond the centre) leading to an increase of strains in the austenite and a decrease of strains in the ferrite. This tendency agrees with the evolution observed before necking and can be explained by the stress concentration in the narrowest region of the neck. In the case of an advanced necking process, the mean strains in the ferrite decrease more significantly in the positions out of the neck centre, causing a load transfer to the austenite. As the result, the strains in the ferrite become lower than in the austenite for all positions measured along the neck, and the inversion in the strain partitioning between the phases is much more important than that extrapolated from the tendency before necking.

The spatial evolution of the lattice strains along the neck was compared with FEM simulations. A qualitative correlation between the variation of macroscopic von Mises stress and the difference between lattice strains in both phases suggest that the stress **triaxiality** could be responsible for the processes occurring in the phases, especially for the relaxation (or damage) process started in the ferritic phase. On the other hand, according to self-consistent model a good prediction of strain partitioning between grains can be obtained if the damage parameter is related to **total equivalent strain** or **total energy**. Therefore it can be stated that both the stress and the total strain are important factors influencing the damage process. The stress **triaxiality** could be important for damage initiation in the sample. And the history of grain deformation (**total strain** or **total energy**) is responsible for its damage resistance.

Chapter 5. Studies of mechanical properties using Instrumented Indentation Test

Supplementary tests are carried out on fractured samples in order to complete the studies of elasto-plastic deformation and damage processes by diffraction measurements. The investigations of microstructure, mechanical properties during large deformation and the ductile damage process have been conducted for both phases of the aged UR45N duplex steel. To this end, the IIT (Instrumented Indentation Test) measurements on the fractured sample were performed. A correlation between mechanical properties of each phase was observed and discussed.

5.1 Instrumented Indentation Test on initial specimens

After the diffraction measurements, the next investigation was carried out in order to observe the variation of micro-hardness and elastic modulus E in the grains belonging to each phase of the studied steel. To this end an Instrumented Indentation Test (IIT) was performed on one part of the fractured “Sample TD”. The preparation of samples and the estimation of plastified zone size induced by nano-imprint are respectively developed in Appendix 14 and Appendix 15.

The instrumental indentation tests were performed on Nano indenter® XP (MTS systems corporation, Eden Prairie, USA), with a Berkovich indenter (cf. section 2.2). The instrument was calibrated by the manufacturer in order to bring the system in operation conditions [Nano-indentation 02].

Firstly, the IITs were carried out on three initial specimens. A test map consisting 10 x10 points spaced by the distance 100 μm for each x and y directions (see Fig. 5.8) was defined and used in a batch mode to perform the indentation test at different positions on the studied surfaces. The tests were carried out following the standard ASTM E 2546-07 [ASTM 07], with 500 nm of maximum penetration depth h_{max} . The Young’s modulus E and the Vickers hardness H were determined at each test point from the P - h curve (cf. section 2.2) recorded during indentation process. The results are shown in the histograms in Fig. 5.10 together with the values of mean $\langle H \rangle$ and $\langle E \rangle$ ($\langle \rangle$ means the arithmetic average). The Vickers hardness is expressed in GPa.

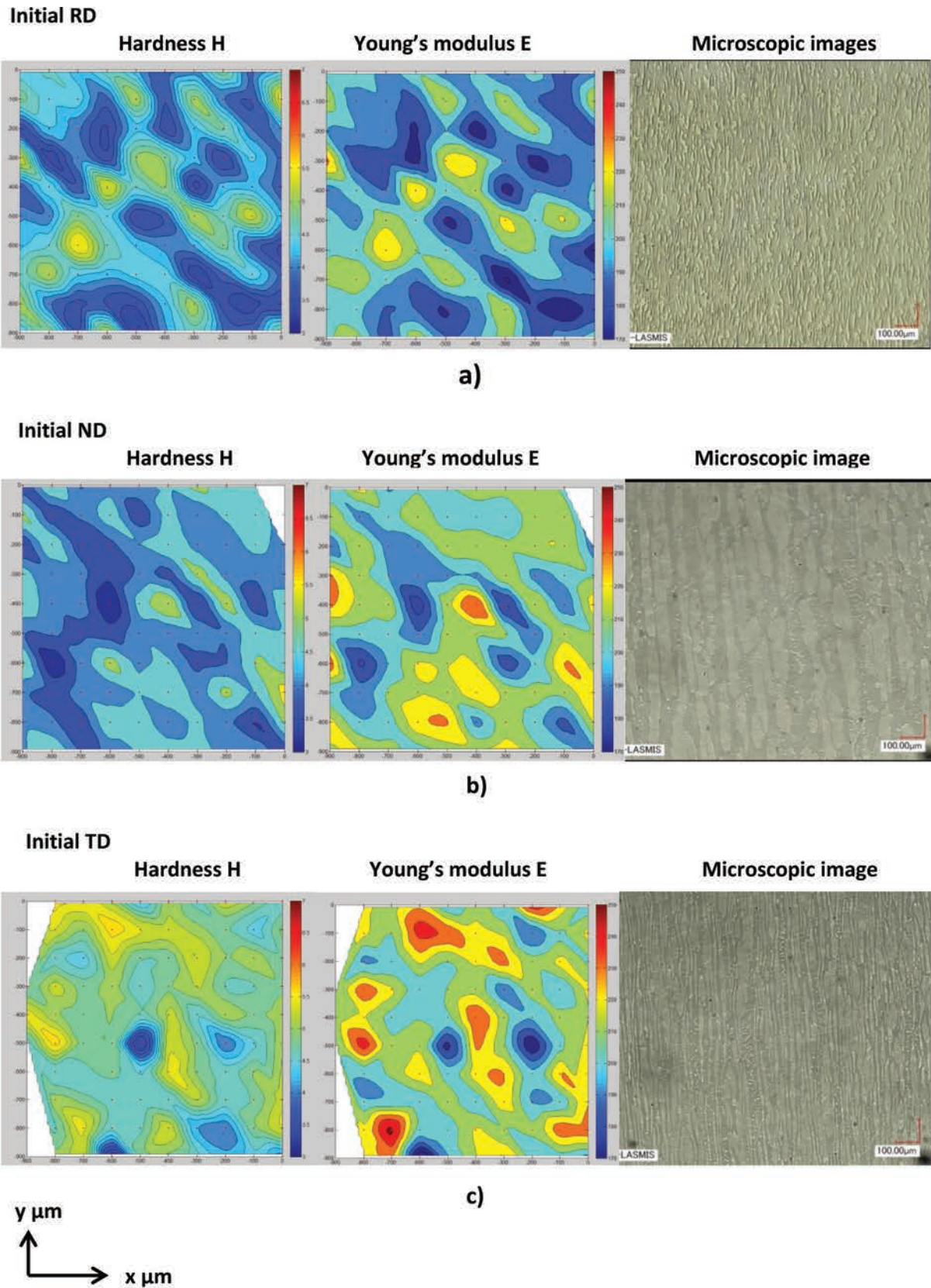


Figure 5.1 The distribution maps of hardness (on the left) and the Young's modulus (on the right) compared with microstructure (magnitude 300 x) of aged UR45N in TD (a), in ND (b) and in RD (c), determined for initial specimens.

The indentation results on the initial samples are presented in Fig. 5.1 by distribution maps. The values of H and E are taken from their average values over the defined range of indenter penetration depth from 250 nm to 480 nm for each test point, in order to avoid the influence of rough sample surface and the work hardening on the surface layer introduced by polishing process, as well as to decrease the uncertainty occurring at the end of penetration process. The distribution maps of both E and H were plotted by a programme coded in Matlab® using the relative coordinates of each test points. Some test points were badly measured and removed from the maps (white space on the map, see Fig. 5.1 A13.2 b and c).

From these maps we can see that the high and low values (red or blue) are spread irregularly on the studied sample surfaces for both Young's modulus and hardness. However, comparing the microscopic images (Fig. 5.2) with the distribution maps, no evident correlation can be found between the values of E modulus or hardness and the phase present at the test points for the initial samples.

The distribution maps of Young's modulus E and hardness H show that both quantities are relatively low for the RD surface (i.e. RD denotes normal to this surface). Then, for the ND surface H is almost the same, while E is higher comparing to the RD surface. We can clearly see that for TD surface the values of both quantities are significantly higher in comparison with the other surfaces.

In order to study quantitatively the variation of H and E on different surfaces, a statistic study was carried out. The statistic results are synthesised in table 5.1. The results are also presented by histograms in Appendix 15, Fig. A15.1. Compared with previous studies on ferrite and austenite using indentation test [Rezakhanlou 93, Wang 07], the obtained values of Young's modulus and hardness from the initial samples are within the normal range, which means the IIT tests are correctly performed.

| Surface | RD (GPa) | ND (GPa) | TD (GPa) | Hot forged | | Aged 2500h 325°C | |
|---------|-----------|-----------|-----------|------------|-----------|------------------|-----------|
| | | | | Ferrite | Austenite | Ferrite | Austenite |
| | | | | [Wang 07] | | [Rezakhanlou 93] | |
| Range E | 170 - 235 | 185 - 250 | 200 - 245 | | | | |
| Range H | 3.6 - 5.6 | 3 - 5.2 | 4.2 - 5.8 | | | | |
| < E > | 200±13 | 213.6±14. | 214.2±15 | 224.8 | 219.4 | 170 | 171 |
| < H > | 4.33±0.53 | 3.95±0.45 | 4.89±0.44 | 4.95 | 4.94 | 4.02 | 3.04 |

Table 5.1 The statistic results of Young's modulus E and hardness H over the surface of RD, ND and TD.

The statistics results show that the hardness and Young's modulus are not homogeneous for the different manufacturing directions. In the case of studied duplex steel UR45N, the ND direction exhibits the lowest hardness, while the hardness in TD direction is the highest one. The mean Young's modulus values are very similar for the ND and TD directions, but the distribution range is larger for ND direction, while the values of Young's modulus in RD direction are relatively low in comparison with the other two directions. The fluctuations of the obtained results are caused by the anisotropy and heterogeneity of the material, the variation of residual stress and work hardening introduced by polishing process at different points, or the impurities remained on the surface after the polishing process. Comparing the mean values of the hardness and the Young's modulus between different surfaces, it can be seen the RD surface has a relatively lower elastic modulus. The differences in hardnesses are more significant and the lowest value was measured for the ND surface. It is probably due to the largest size of the grains (softer) and lower density of boundaries (harder) seen on this plane (see Fig. 5.1b) in comparison with two other sections (see Fig. 5.1 a and c).

5.2 Instrumented Indentation Test on fractured specimen

After the characterisation of initial specimens, another Instrumented Indentation Test (IIT) was performed on the part 1 of the fractured “Sample TD” (Fig. 5.2).

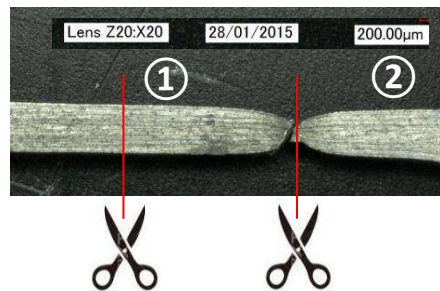


Figure 5.2 Microscopic image of the fractured “Sample TD”. The part 1 on the left was used in the instrumented indentation test.

In this test, the mechanical properties of the material were measured inside the sample, after successive mechanical polishing until the symmetry plane in the centre of the sample (see Appendix 12). Finally, a layer of $675 \pm 10 \mu\text{m}$ was removed by polishing, i.e. almost half of the initial sample thickness ($\approx 1.4 \text{ mm}$).

In this study the distribution maps of hardness H and Young's modulus E are determined for the surface perpendicular to TD. The origin of coordinate x for the fractured specimen was

defined by the red-cross in Fig. 5.3, and different separation distances of test point nets for IIT batch mode were defined, as shown in the same figure.

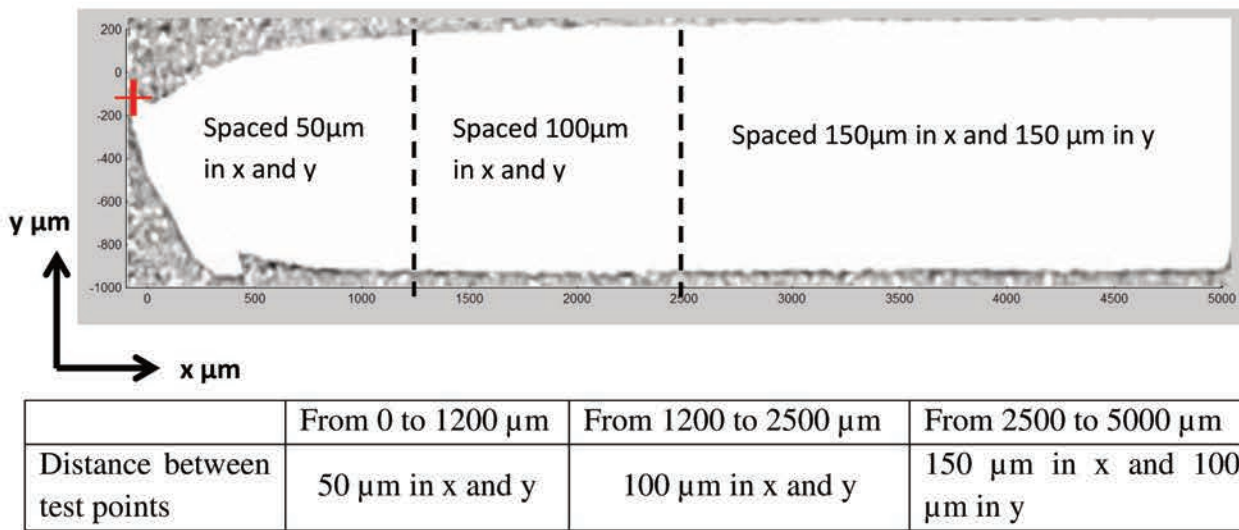


Figure 5.3 The image of the fractured specimen with the definition of test point nets for different regions.

The first point net was made for the necking region, i.e. for x within the range from 0 to 1200 μm . To get maximum information for the neck and near the fracture edge the test points were spaced in a square net with the distance between nodes of 50 μm in x and y directions (the determination of distance between test points please see Appendix 13). Meanwhile, in order to minimize the influence of edge effect, the minimum distance of 50 μm was kept between the fracture edge and the closest test points to the edge. In the second region, close to the neck, for x between 1200 and 2500 μm , the test points were spaced at distances equal to 100 μm in x and y directions. Finally, the third region was defined for x from 2500 to 5000 μm , where the material was homogenously deformed to the smallest extent. The test points were spaced at distances 150 μm in x while 100 μm in y (test points distribution is summarised in the table in Fig. 5.3). The penetration depth was also 500 nm for each test point, and the values of hardness and Young's modulus were also taken from their average over depth range from 250 nm to 480 nm as mentioned above for initial samples.

The IIT on the fractured specimen was also performed using the Nano indenter® XP (MTS systems corporation, Eden Prairie, USA), following the standard ASTM E 2546-07 [ASTM 07], with a Berkovich indenter and the maximum penetration depth h_{max} was 500 nm. The values of each entity were also calculated by the average over depth range from 250 to 480 nm (see Appendix 14).

In the next step of analysis, the hardness and Young's modulus along the specimen are measured separately for the austenite and for the ferrite. Because during the IIT it is not possible to distinguish the phase for which the indentation is performed, the identification of phase was carried out visually after the tests with help of the optical microscope integrated in the IIT machine. The imprints observed on the sample surface were recognized from image contrast and identified with the grains belonging to the phases, as the nano imprint shown on Fig. 5.4. On the same figure, the red and blue triangles give an example for nano-imprints on austenite and on ferrite. The red circle gives an approximate range for plastified zone introduced by nano-imprint (estimation process see Appendix 13). However, the condition of vicinity around indentation imprint is unknown. For example, on the image 5.4, the thickness of austenite is unknown, the imprint may cross through the austenite phase and presses on the ferrite behind it, this effect will influence the accuracy of measurement. The coordinate of each imprint was recorded by the position of specimen holder and related to the indentation results according to the coordinates of test points recorded during IIT test.

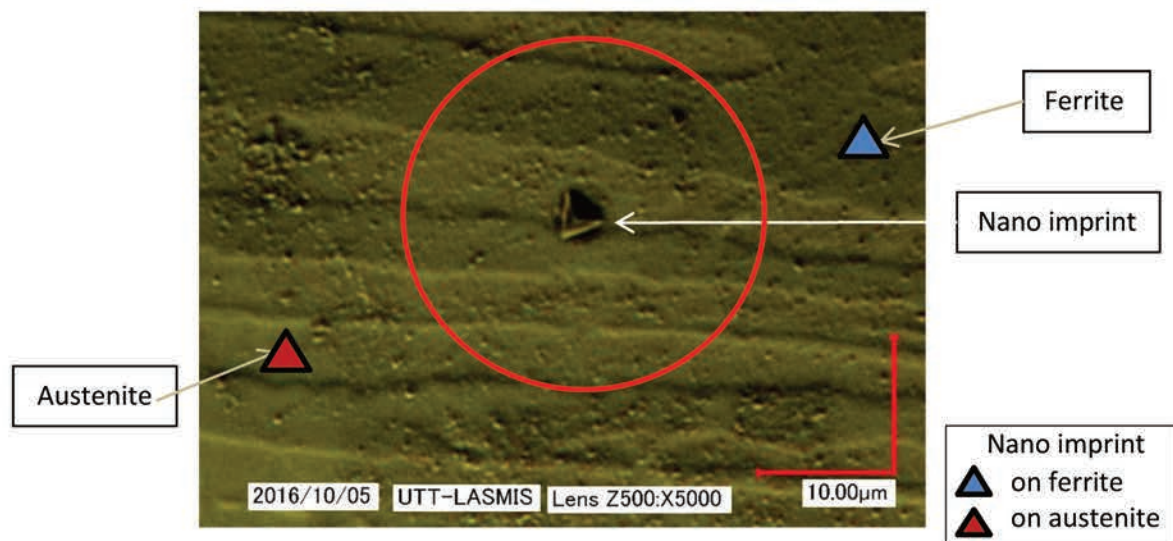


Figure 5.4 Optical microscope image used for identification of the phase for which the imprint is visible. The red circle indicates approximately the range of plastified zone introduced by nano-imprint.

5.2.1 Evolution of mean hardness and mean Young's modulus along specimen

The statistical analysis is carried out for each phase along the specimen for seven zones, one by one along the direction of x axis, as defined in Fig. 5.5. In order to describe the material behaviour around fracture, the zone Fracture 1 is defined for an area having width of

about 200 μm , starting from fracture edge. The zone Fracture 2 is defined as the following area behind the zone Fracture 1, with also a width of about 200 μm , considered as the transit area between fracture and neck of the sample. The next zone Necking 1, defined as a triangle zone after the zone Fracture 2, contains the pronounced necking region close to the fracture surface. The zone Necking 2 is defined by the less pronounced necking area. The zone Necking 3 is from 1200 to 2500 μm , before the end of neck, considered as the initiation of necking effect. Other zones are defined for the material out of the neck, i.e. the zone Out neck 1 is from 2500 μm to 3500 μm , and the zone Out neck 2 is from 3500 to 5000 μm along the x axis (as shown in Fig. 5.5).

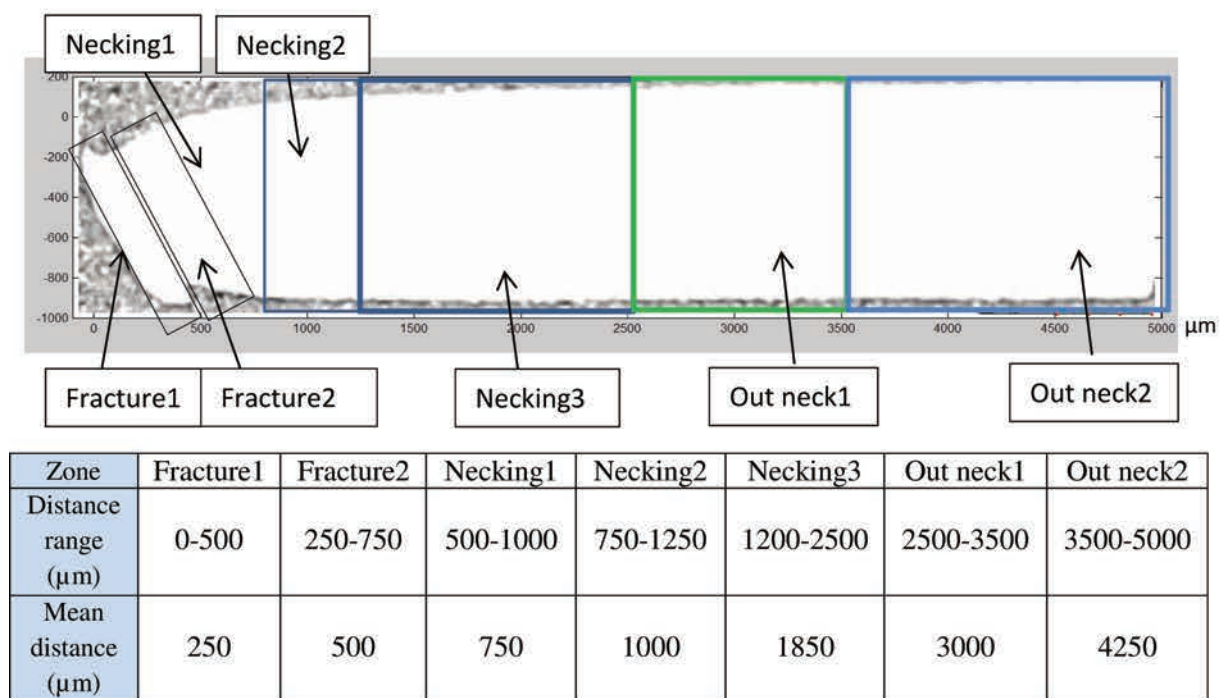


Figure 5.5 Illustration of the division on seven zones along specimen for statistical analysis.

The distribution maps are respectively drawn for **Young's modulus E** and **Hardness H** (Fig. 5.6 a and c). In order to avoid the influence of the number of test points on the distribution maps and to observe the heterogeneity of real physical properties (i.e. hardness or Young's modulus) in the fractured specimen, another version of maps were made by removing half of the test points from 0 to 1200 μm in x axis, i.e. the distance between each two points became 100 μm instead of 50 μm (please see appdenix 16). Although after reduction of points number the variation of hardness and Young's modulus occurs at larger distances, the same phenomena as before can be noticed, i.e. the fluctuations of these quantities are still more intense in the necking region in comparison with the part outside of the neck, even for the same density of points.

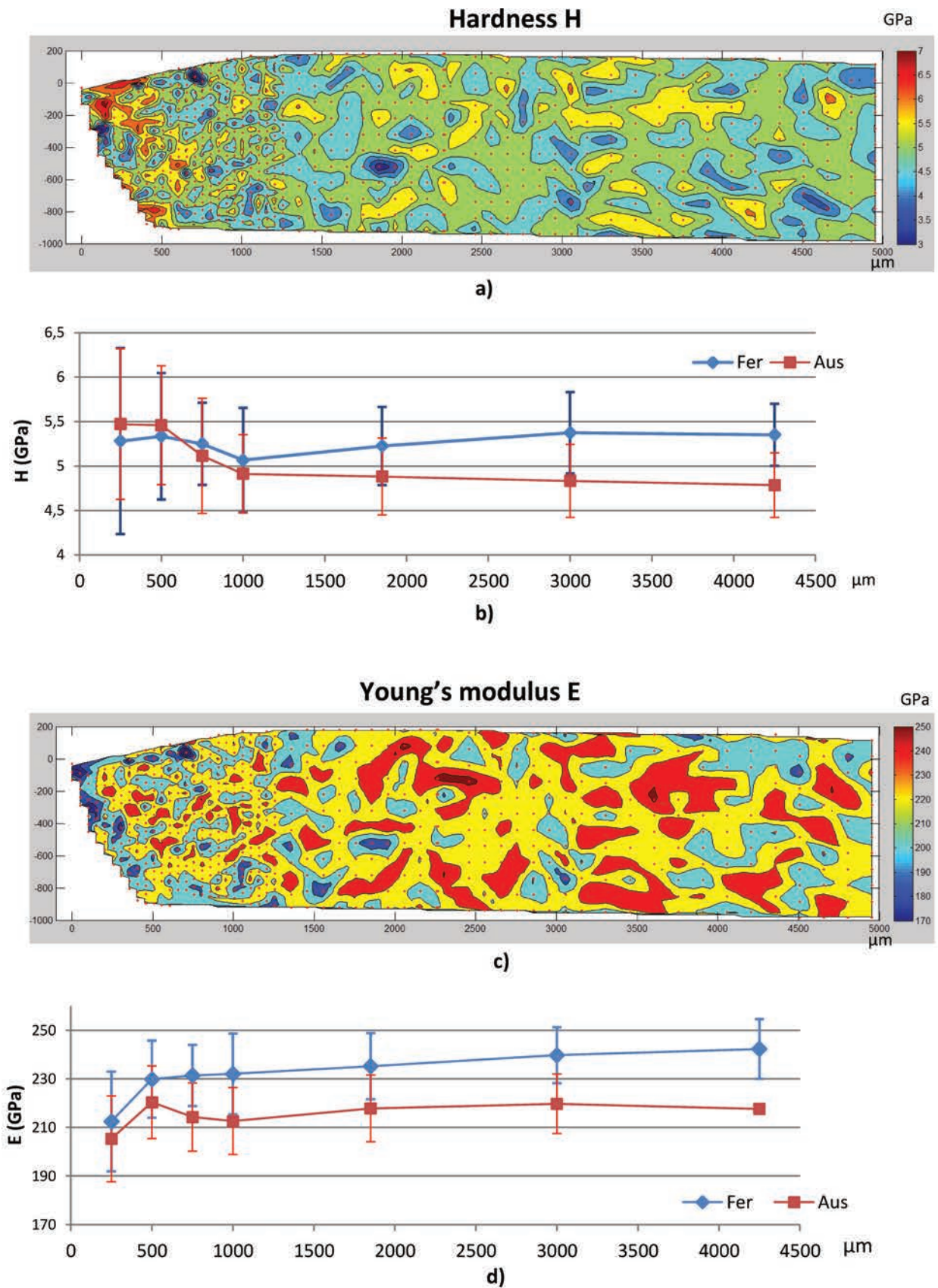


Figure 5.6 The distribution maps of Hardness (a) and Young's modulus (c) with reduced density of test points within the neck. Evolutions of mean values for Hardness (b) and Young's modulus (d) of ferrite and austenite along specimen.

Statistical analyses of hardness and Young's modulus have been performed along the specimen in different zones, the results are presented by histogrammes in Appendix 17. In order to present directly the evolution of hardness H and Young's modulus E in different zones, plots based on the mean values calculated from statistic data of hardness and Young's modulus in each zone are drawn vs. position along the specimen, respectively for test points in ferrite and for test points in austenite. The bars show the standard deviation over the values of test points, which are correctly measured (the incorrectly measured points have been removed from the data, example of correct indentation test curves see Appendix 14), inside each zone. These bars represent the fluctuation of hardness but not the experimental uncertainty.

Greater fluctuations of the physical properties within the neck can be explained by severe plastic deformation, leading to the grains fragments and other material heterogeneities occurring at small distances. The possible answer is the plastic deformation continues only in the necking zone due to the stress concentration (deformation is much more than 100 %, determined by Digital image correlation, cf. [Le Joncour 11]). The unloading of material outside necking zone prevents the further plastic deformation process (total deformation is about 25-30 %, cf. Fig. 4.15). Therefore, in necking zone the phenomena related to the severe large deformation (such as activation of slip systems, twinning, grains fragment, work hardening, softening and relaxation of material or initiation of micro-cracks) occurred much more intensively. All the above mentioned mechanism combined with material heterogeneities leads to a more significant variation of hardness and Young's modulus occurring at small distances within the necking zone.

5.2.1.1 Hardness evolution

The hardness evolution is presented in Fig. 5.6b, where the mean hardness values in function of the distance from fracture edge are shown (the mean distance is defined by the middle of each zone to the fracture edge).

From Fig. 5.6b, we can see that the hardness of both phases is stable at the end of specimen far from the fracture edge (Out neck2). Then, the hardness of ferrite decreases while that of austenite keeps stable (slightly increases) from 3000 μm until 1000 μm , where the necking effect began occurring on the sample. This decreasing of ferrite's hardness is probably due to the residual stress or potentially to the softening occurring after plastic deformation.

Along the neck, the hardness of both phases quickly increased, but the hardness of austenite increased more significantly than that of ferrite. This phenomenon is caused by the increase of dislocation density, which leads to the increasing of work hardening in both phases during large deformation [Tompson 73, Hutchinson 06]. It is also seen that work hardening of austenite was slightly greater than that of ferrite. Finally, in area close to the fracture edge, hardness of austenite exceeded this of ferrite and work hardening decreased for both phases leading to saturation of the hardness values.

It is interesting to compare the results of IIT with diffraction data, in order to clarify the dependence between hardness and stress concentration in each phase.

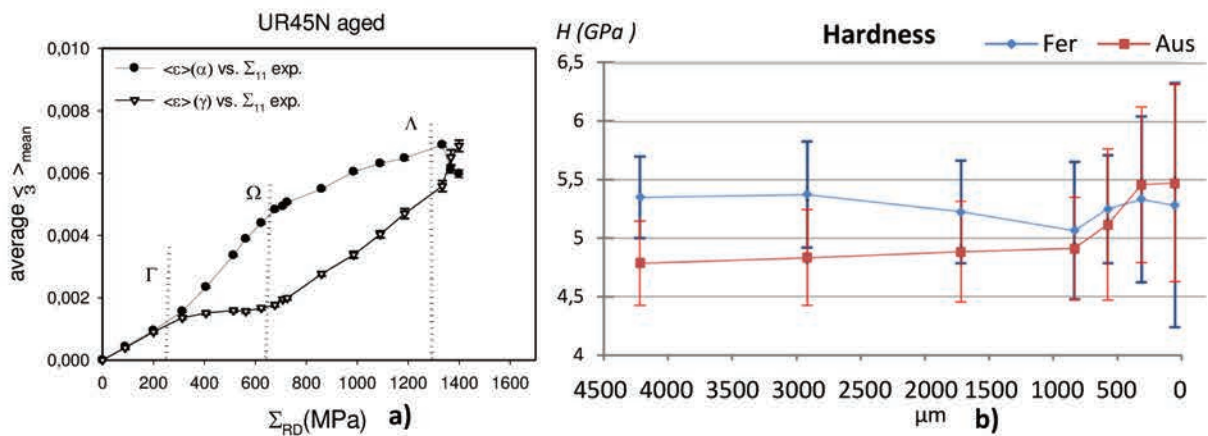


Figure 5.7 Comparison between temporal evolution of strains (a) and evolution of hardness along specimen (b) for both phases.

Fig 5.7 shows comparison between lattice strains measured by diffraction and hardness determined using IIT. The diffraction data were measured in situ during sample loading, while the IIT data are obtained on the fractured specimen. However, some interesting correlation between these experiments can be found.

From Fig. 5.7b, we can see that between the range from 4500 to 3000 μm both phases exhibit stable hardness corresponding to the area of homogenously deformed material (macrostrain is constant within this range). Considering the large deformation suffered by tensile test sample, this range can be compared with the lattice strain evolution after threshold Ω , where both phases are already plastified.

Then, for the zone between 3000 to 1000 μm , the hardness of austenite remained practically constant, while the hardness of ferrite decreased very smoothly and slightly in this range. It is very hard to draw out information from these slight changes.

In the range between 0 and 1000 μm , heterogeneous sample deformation is caused by necking phenomenon. The hardness of both phases rises up promptly in the range between 1000 and 500 μm (Fig. 5.7b), and the hardness of austenite finally surpassed that of ferrite. This effect can be explained by the heterogeneity of sample deformation which increases with narrowing of the neck towards to the fraction zone. This evolution corresponds directly to the range around threshold A during sample loading (Fig. 5.7a). In this stage, strong plastic deformation occurred in both phases, leading to an important dislocation accumulation and a great dislocation density inside the grains, the grain fragmentation is also very pronounced during this stage. All of above mentioned phenomenon could cause the rapid increase of hardness of both phases. Besides, during this period, the plastic deformation rate of austenite is greater than that of ferrite, which means more important dislocation density and more dislocations are accumulated in austenite.

Finally, along the fracture edge (Fig. 5.7b) from 500 to 0 μm , austenite's hardness keeps stable and a slight decline occurred in ferrite, which can be referred to the ductile damage process after threshold A . This phenomenon will be explained in the following analysis.

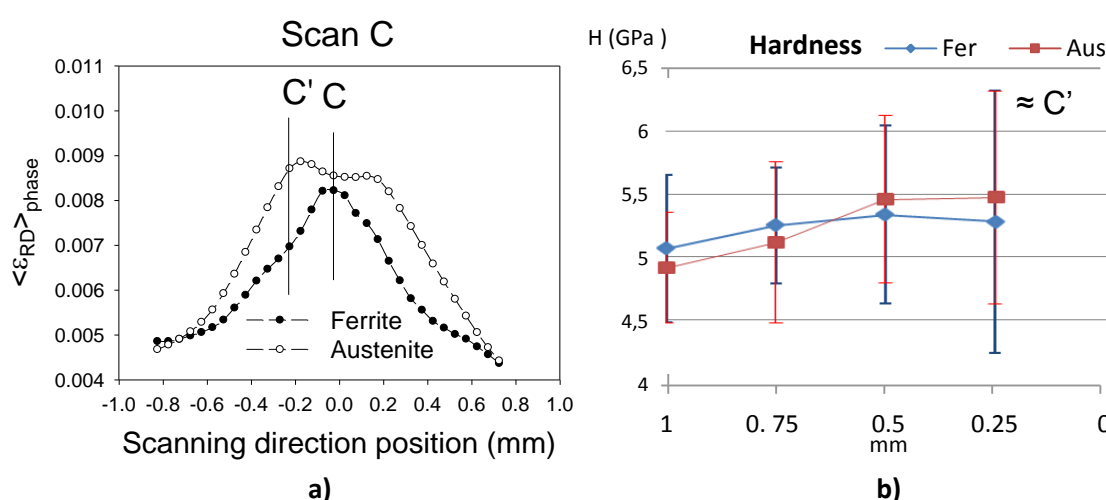


Figure 5.8 Comparison between (a) spatial evolution of strains and (b) evolution of hardness along specimen zoomed between 250 μm (around position C) and 500 μm (around position C') for both phases.

Another interesting correlation can be found comparing the hardness measured by IIT with the lattice strains scanned along the neck, using synchrotron diffraction (Fig. 5.8). These measurements can be correlated for given positions along x axis, however, it should be underlined that the diffraction measurements were done for “in situ” loaded undamaged sample, while the nano-indentation tests were performed for fractured sample.

A decrease in ferrite's hardness can be noticed (Fig. 5.8b) between 500 and 250 μm , close to the fracture edge. This effect may correspond to the lattice strain relaxation occurred in the ferrite from about 0.3 mm (C') to the neck centre (C) (Fig. 5.6a). The decrease of lattice strain means a reduction of stress localised in ferrite (comparing to austenite), which could be caused by material softening in ferrite. It should be however emphasised, that the effect of hardness evolution is very slight compared with large heterogeneity between different test points (their dispersity is shown by bars in Fig. 5.8b), the accuracy of correlation between softening and hardness is interesting and need to be further studied.

5.2.1.2 Young's modulus evolution

The evolutions of Young's modulus along fractured specimen for ferrite and austenite are shown in Fig. 5.6d. From 4500 μm to 1000 μm , the values of Young's modulus slowly decrease for both phases, and the difference between them is stable (Fig. 5.6b). This decrease is probably caused by the progressively increased plastic deformation. On one hand, [Hordon 58, Lemaitre 94] have indicated that for cubic-lattice metals the elastic modulus E can be reduced by plastic deformation. On other hand, the fragmentation of grains during plastic deformation causes also a reduction of the elastic modulus [Kim 99].

Then, in the range between 0 and 500 μm , the elastic modulus E of both phases fell down sharply. This effect is possibly associated with lattice defects evolution, such as dislocations accumulation and vacancies [Hordon 58], but according to the literature, the reduction of E should be much less great than what we measured. Besides, the sharp reduction in Young's modulus E of ferrite and austenite on the fracture edge is likely to suggest that damage was initiated within this area. This decrease of E is probably due to the micro-cracks occurring during the damage process. As reported by [Kim 99], the elastic modulus depends not only on the grains size, but also on the material porosity. The micro-cracks engendered during ductile damage process increase the material porosity along fracture edge, inducing a reduction in elastic modulus on this area. This decreasing may also be simply caused by the insufficient material thickness on the sample edge, which makes the embedding matrix (resin, exhibiting a much lower Young's modulus than steel) having an important influence on the measured values. In a word, the mechanism for the reduction of Young's modulus is not very clear here, further study is needed for a more convincing explanation.

Along the neck between 500 μm and 1000 μm , the mean modulus E of ferrite stabilises. However, the austenite's modulus E increases in this range. The reason of this phenomenon is unclear, maybe simply due to the rough estimation for the mean value of austenite's E caused by insufficient test points. There is no evidence to prove the correlation between Young's modulus and the plastic deformation up to now, therefore more accurate measurement is necessary for the further investigation.

Summarising the results obtained using the IIT method, it confirms the main tendency of mechanical behaviour determined previously by diffraction method for both phases of duplex steel. Unfortunately, the IIT and diffraction measurements were done in different conditions, i.e. lattice strains were measured in situ on the sample loaded during tensile test, while IIT was carried out after unloading, for fractured sample. Moreover, fracture can influence the properties measured close to the edge. So all these above results are qualitatively analysed and only relative evolution tendency are compared between experiments.

Finally it should be emphasised that the study of relative evolution of hardness in both phases brought information independent on the macroscopic effects such as the influence of sample edge during nano-indentation test. Thus, comparison of such data with diffraction experiment is reasonable. However, in the case of determined Young's modulus, similar evolution is found in both phases. Although, different explanations for the observed Young's model decrease are above presented, it should be also taken into account that this effect can also be caused by the fact that the measurements were performed near the edge of the samples.

5.2.2 Evolution of hardness vs. Young's modulus

In order to complete the previous analysis on the evolution of hardness and elastic modulus during large deformation process, scatter plots of the H vs. E for in each zone are drawn (Fig. 5.9 a to g).

The scatter plots for different zones show that the point cloud exhibits a separation tendency for each phase with increasing distance from the fracture edge. In the zone Fracture 1, the point clouds of both phases are mixed together and no evident difference between them can be seen. But it should be noted, the Young's modulus measured near the fracture edge is not very accurate due to the edge effect (influence of embedding matrix resin), the other scatter plots are more meaningful.

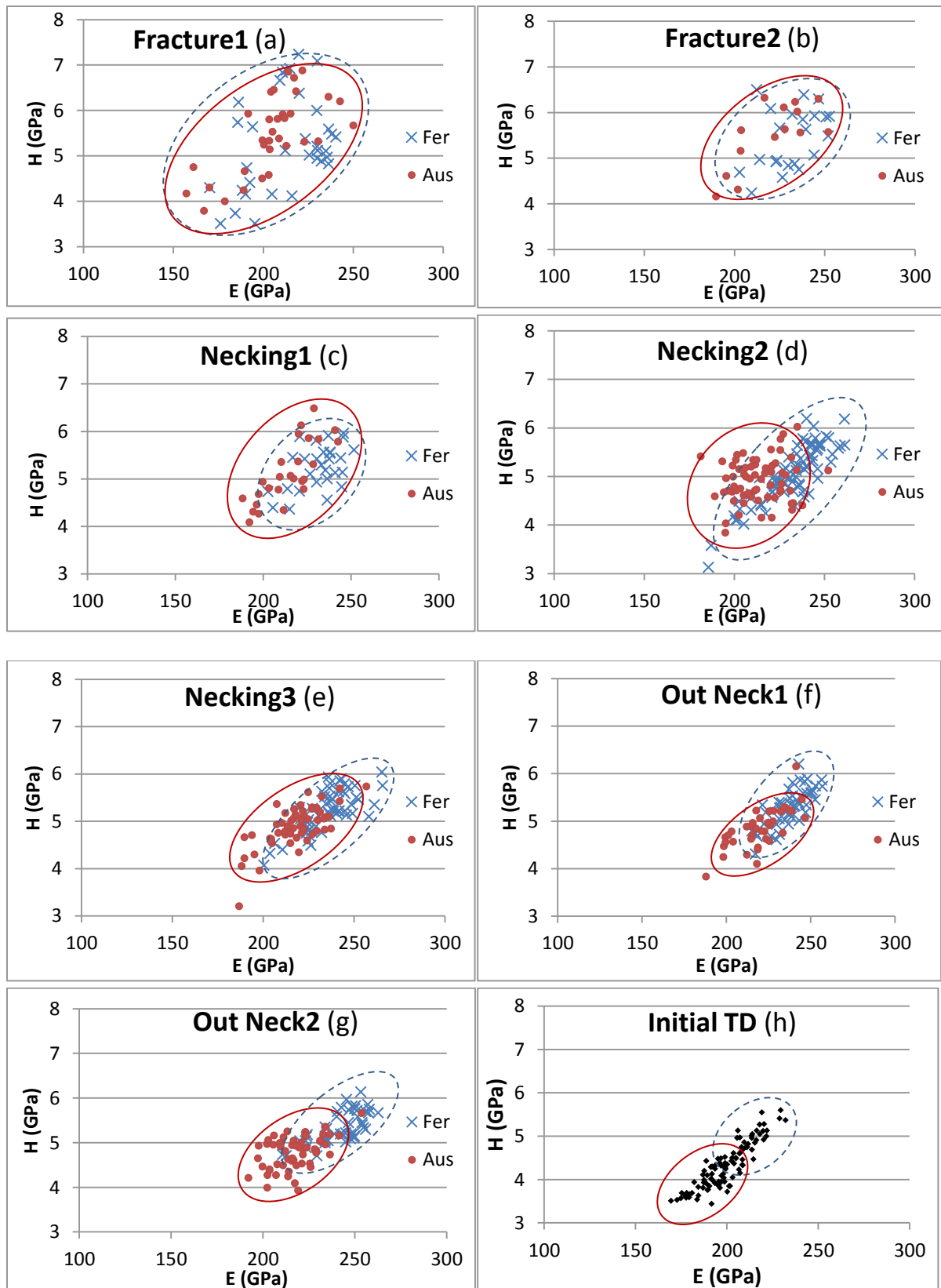


Figure 5.9 The scatter plots of hardness H in function of Young's modulus E for different zones on fractured TD specimen (a to g). And for initial TD specimen (h), the phases are not identified on the initial specimen.

○ Ferrite group ○ Austenite group

In zone Fracture 2 and Necking 1, a slight separation appears between the two clouds, i.e. the points corresponding to ferrite shifts to higher Young's modulus. For zones from Necking 2 to Out neck2, it can be seen that farther the zone away from the fracture, the more evident is the separation between the clouds of two phases. Finally, for the zone Out neck2 the point clouds of two phases are separated, and both the hardness and the Young's modulus of ferrite are higher than those of austenite.

In addition, the scatter points spread significantly in the zone Fracture 1 for both phases, but the points of each phase tend to gather together in the less deformed zones. This effect corresponds to the fluctuation of H and E observed in the area close to fracture surface (cf. Fig. A16.1).

The distributions of H vs. E on initial specimen determined in TD directions surface is presented in Fig. 5.9h. Unfortunately, the phases are not identified on the initial specimens, but a separation tendency can be also observed.

Comparing measurements on the initial and fractured specimens (Fig. 5.9 a to g and Fig. 5.9h), we can infer some reasons for the convergence of point clouds for both phases. Through the analysis above presented, this effect may be due to the decrease in ferrite hardness and increase in austenite hardness after plastic deformation. At the beginning, the ferritic phase was harder than austenite in the initial sample. And then, referring to Fig. 5.7a, we can see the austenite is much more plastically deformed during tensile test, leading to an increasing in hardness of austenite, which makes the hardness ranges of austenite overlap with that of ferrite. Meanwhile, the Young's modulus kept relatively stable for both phases in the along the plastically deformed part. This evolution tendency between H and E shows the mechanical behaviour of grains belonging to each phase is complex and significantly differs within a given phase, but a further more accurate measurement have to be performed to verify the relationship between H and E during large deformation process.

5.3 Conclusion

This chapter reports the results of instrumented indentation test performed for the initial sample and next along the fractured specimen. It was found that much more significant fluctuations on the Young's modulus values and hardness occurred in the necking zone comparing with the region outside of neck as well as for the initial samples. This effect can be

explained by heterogeneity of material engendered during plastic deformation at grain scale. The grains fragmentation in severely deformed duplex steel along the neck leads to variation of mechanical properties for both phases. It is also found that the hardness and Young's modulus significantly varied in the neck, comparing with the data obtained outside necking zone and for the initial specimens. This effect is observed for both phases of the studied steel.

The average hardness of austenite is lower in comparison with ferrite for an intermediate plastic deformation (outside neck). The hardness measured for both phases gradually evolved with position in the neck, and the austenite's hardness finally surpassed that of ferrite at the fracture edge. This observation qualitatively agrees with the results of diffraction measurements and self-consistent model, showing initially lower yield stress as well as smaller load localized in the austenite comparing with the ferrite. The plastic deformation plays an important role for the hardness evolution, because of the work hardening process. Finally, the decrease of ferrite's hardness at fracture edge is probably caused by the softening of this phase during ductile damage as measured by diffraction method. It was also found that the decrease of Young's modulus occurred for both phases of the studied duplex steel. The reduction of E value is more significant in the case of the ferrite, especially on the edge of sample fracture. This reduction of elastic modulus is probably caused by several effects, such as the micro-cracks engendered around the fracture edge, or simply caused by the edge effect due to the insufficient specimen thickness.

The results of IIT performed for the fractured sample, it should emphasise that the hardness of both phases significantly increased near the fracture, this increasing is caused by the severe plastic deformation in this area. However, the hardness of ferrite declined along the fracture edge. This reduction of ferrite's hardness is presumed possibly being caused by the relaxation in ferrite occurred at the end of tensile test, which has been observed by diffraction measurement. Although the IIT provided only qualitative analysis results, this reduction in ferrite's hardness can be still related to the relaxation in ferrite, suggesting the ferrite is firstly damaged at the end of large deformation process. Softening and reduction in Young's modulus for the ferritic phase combined with the results of diffraction measurements during tensile test (relaxation of the load in the ferritic phase) indicates the damage process possibly initiated in the ferrite. It is worthwhile to note that the geometrical effect of fracture edge could influence the measured IIT values. The impact of plastified zone created by imprint is another important influencing factor for the IIT results. Much larger specimen is necessary for the further investigation in order to avoid the overlap of plastified zone and to test more points.

Chapter 6. Studies on α - β titanium alloy Ti-18

The elasto-plastic behavior of a hexagonal material, as well as the interaction between hexagonal and cubic lattice are one of the objectives of this thesis. To study the processes occurring in the material which consists of hexagonal and cubic phases, the two-phase titanium alloys were selected. As most of hcp metals, the hexagonal crystal lattice causes a distinctive anisotropy of plastic deformation in α -phase of titanium due to a large variety of possible slip systems (cf. section 1.2).

In the present thesis, titanium alloy Ti-18 is used to perform the investigation using X-ray diffraction and neutron diffraction measurements. The experimental results are obtained in this work and then compared with predictions of **Elasto-Plastic Self-Consistent** (EPSC) model (cf. chapter 3), in order to determine physical parameters related to the activation of slip systems. The distinction in mechanical properties between hcp and cubic lattices, such as the lattice parameters and the slip systems, is taken into account.

6.1 Tensile test coupled with X-ray diffraction measurements

In this section the results of an in-situ X-ray diffraction measurements during tensile test carried out on TIMETAL-18 alloy are analyzed. The experimental results are compared with EPSC model (cf. chapter 3), and as the results several meaningful parameters related to the elasto-plastic deformation of each titanium phase were determined.

6.1.1 Experimental methodology

In-situ X-ray diffraction measurements were carried out in the Faculty of physics and applied computer science of AGH University, to measure the lattice strain during the uniaxial tensile test. The PANalytical X'Pert diffractometer using Cu radiation ($\lambda_{K\alpha 1} = 1.540562 \text{ \AA}$ and $\lambda_{K\alpha 2} = 1.544398 \text{ \AA}$) was employed to perform the measurement of interplanar spacing. A Göbel mirror was used to collimate the incident beam and a parallel collimator with Soller slits was placed in front of the scintillation detector.

A dog-bone shape sample was machined from the received Ti-18 ingot with an initial effective length of 15 mm, width of 4.9 mm and thickness of 0.6 mm (see Fig. 6.1). The

sample was mechanically polished before the tensile test to get a very high smoothness for the surface.

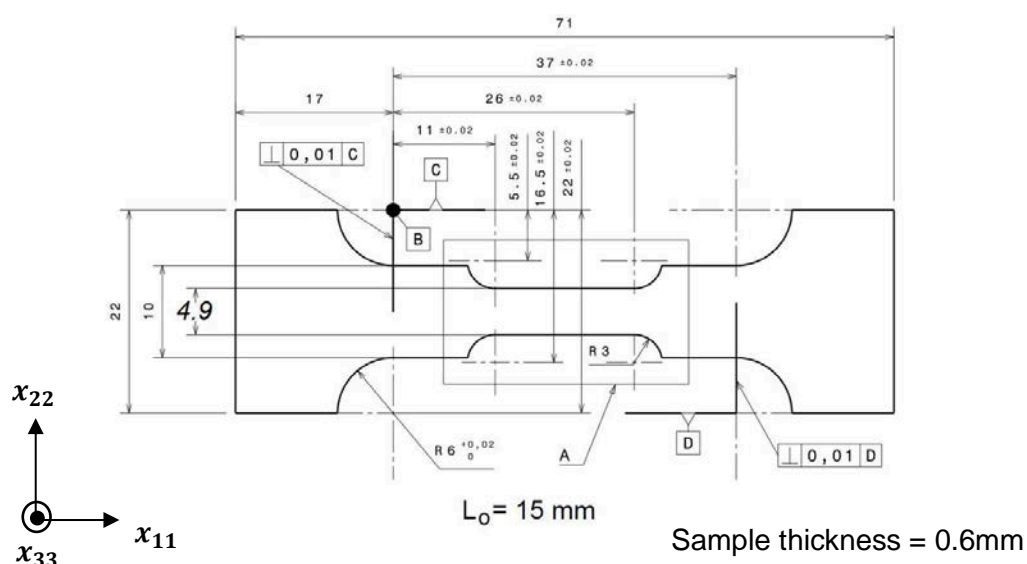


Figure 6.1 Technique drawing of dog-bone shape sample for tensile test on Ti-18.

The longitudinal axis of sample \mathbf{x}_{11} is parallel to the axial direction of ingot, and the load was applied along longitudinal axis until fracture. The macroscopic displacement was recorded by controlling grip position. The tensile test was controlled by applied force, the applied force were recorded by sensor integrated in tensile rig. All in-situ X-rays diffraction measurements were performed after the stabilization of applied load in order to avoid viscosity effect during the elasto-plastic deformation. The mechanical behavior of α and β titanium during elasto-plastic deformation were studied in both parallel and perpendicular directions to the loading axis. The longitudinal stresses in both phases were measured using MGIXD method (cf. section 2.3.3) [Skrzypek 01, Baczmański 01, Baczmański 03, Welzel 04], while the lattice strains in the direction perpendicular to the applied load were determined from the θ -2 θ scans, for which the scattering vector was perpendicular to the sample surface (i.e. parallel to \mathbf{x}_{33} shown in Fig. 6.1).

6.1.1.1 Determination of elastic lattice strains in normal direction

The interplanar spacings $\langle d_{33} \rangle_{\{hkl\}}$ in normal direction (x_{33}) were measured for each available hkl reflection by using conventional θ - 2θ Bragg-Bretano method [Zevin 12]. The relative elastic lattice strains $\langle \varepsilon \rangle_{\{hkl\}}$ are determined with respect to the initial interplanar spacings (cf. Eq. 2.2, page 45, x_{33} is parallel to the scattering vector \vec{n}).

Moreover, the arithmetic mean elastic lattice strains in each phase $\langle \varepsilon_{33} \rangle^{ph}$ were calculated using Eq. 6.1:

$$\langle \varepsilon_{33} \rangle^{ph} = \frac{\sum_{N_{\{hkl\}}^{ph}} \langle \varepsilon_{33} \rangle_{\{hkl\}}^{ph}}{N_{\{hkl\}}^{ph}} \quad \text{Eq. 6.1}$$

where $\langle \varepsilon_{33} \rangle_{\{hkl\}}^{ph}$ denotes the elastic strains determined using hkl reflections, which belong to the concerned phase, $N_{\{hkl\}}^{ph}$ means the number of hkl reflections available for phase ph.

6.1.1.2 Determination of phase stress in loading direction

To determine the mean stresses in the α and β phases during tensile test, the interplanar spacings $\langle d(\phi, \psi) \rangle_{\{hkl\}}$ were measured for all possible reflections hkl (corresponding to different tilts ψ), and for two angles $\phi = 0^\circ$ and $\phi = 90^\circ$ [Dolle 79, Baczmański 93], defined in Fig. 2.4 page 44. During measurements the incident angle $\alpha = 10^\circ$ was kept constants, thus the stress state at penetration depth of about $1.6 \mu\text{m}$ (cf. Eq. 2.8) was studied by the MGIXD method (cf. section 2.3.3). The measurement has been done for the initial sample and next for each loading step during “in-situ” tensile test, as well as after unloading (sample was fractured).

For very shallow penetration depth we can assume that the stress was relaxed in the normal direction (ND) to the surface, leading to the assumption of biaxial stress state (i.e. $\sigma_{33} = \sigma_{13} = \sigma_{23} = 0$) [Cullity 78, Brakman 88]. Therefore the phase stresses σ_{11}^{ph} and σ_{22}^{ph} in α and β titanium can be independently determined using the least square method (cf. Eq. 2.9). For the cubic crystal structure (β titanium), the lattice parameters $\langle a(\phi, \psi) \rangle_{\{hkl\}}$ were calculated from Eq. 6.2:

$$\langle a(\phi, \psi) \rangle_{\{hkl\}} = \langle d(\phi, \psi) \rangle_{\{hkl\}} \sqrt{h^2 + k^2 + l^2} \quad \text{Eq. 6.2}$$

And for the hexagonal structure (α titanium), the lattice parameters $\langle a(\phi, \psi) \rangle_{\{hkl\}}$ were calculated from Eq. 6.3:

$$\langle a(\phi, \psi) \rangle_{\{hkl\}} = \langle d(\phi, \psi) \rangle_{\{hkl\}} \left\{ \left[\frac{4}{3} (h^2 + hk + k^2) \right] + \frac{l^2}{(c/a)^2} \right\}^{1/2} \quad \text{Eq. 6.3}$$

The Reuss, Voigt and Eshelby-Kröner grains-interaction models (cf. Appendix 8) are separately used to calculate the X-ray Stress Factors (XSF), and then the components σ_{11} and σ_{22} of the stress tensor in each phase are determined. The hkl-dependent XSF F_{ij} are calculated for each hkl reflection, using single crystal elastic constants of α and β titanium and accounting for crystallographic texture (cf. table 1.13 and Fig. 1.24 page 37).

6.1.2 Determination of initial stress

The MGIXD method (cf. section 2.3.3) was used to determine the residual stresses in each phase of the initial sample (without tensile load). The $\langle a(\phi, \psi) \rangle_{\{hkl\}}$ vs. $\sin^2 \psi$ plots for stress determination are shown in Appendix 19, where the results for three considered models of XSF are compared. The initial stresses determined by three grains-interaction models for each phase are shown in table 6.1, the mean stress over both phases is also presented.

According to table 6.1, we can see the values of initial stresses in both phases are nearly the same for the three fitting models. It is found that the stresses in α titanium are smaller than experimental uncertainty, while the stresses in β titanium are more significant. Finally, the overall stresses calculated over the two phases (weighted by volume fraction, that of α is assumed equal to 45%) are positive but smaller than their uncertainties. The residual stresses occurred in the initial sample were probably produced due to the heat treatment and phase transition during the manufacturing process of the material.

| Phase | Models | σ_{11} (MPa) $\phi = 0^\circ$ | σ_{22} (MPa) $\phi = 90^\circ$ |
|--|----------------|---|--|
| α titanium | Voigt | -33±66 | -28±67 |
| | Reuss | -41±61 | -42±62 |
| | Eshelby-Kröner | -37±63 | -38±66 |
| β titanium | Voigt | 117±57 | 90±57 |
| | Reuss | 117±54 | 85±54 |
| | Eshelby-Kröner | 118±56 | 89±56 |
| volume weighted average: $0.45\sigma_{ii}^\alpha + 0.55\sigma_{ii}^\beta$ | Voigt | 48±61 | 37±80 |
| | Reuss | 46±57 | 28±58 |
| | Eshelby-Kröner | 48±59 | 31±60 |

Table 6.1 Initial phase stresses measured in α and β phases in the studied sample.

6.1.3 Evolution of stresses in each phase during the tensile test

Fig. 6.2 shows the evolution of phase stress σ_{11}^{ph} vs. macro-strain E_{11} in loading direction (x_{11}) measured during tensile test. So in this figure, only the stresses along the loading direction (x_{11}) are shown, because the values of transverse stresses σ_{22}^{ph} are negligible in comparison with the experimental uncertainty range. In order to reduce the influence of elasticity of tensile rig, a correction has been performed after the tensile test. The below mentioned macro-strain E_{11} in loading direction is the true macrostrain of sample after deduction of the elasticity of tensile machine.

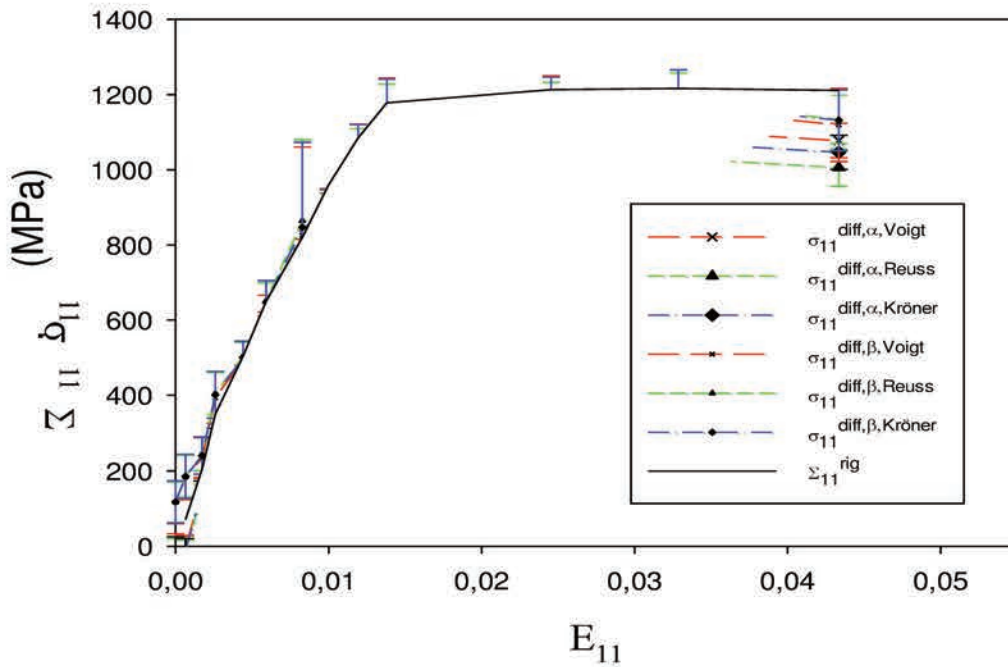


Figure 6.2 Phase stress σ_{11}^{ph} vs. macrostrain E_{11} of sample during tensile test. The phase stress for α titanium $\sigma_{11}^{diff,\alpha}$ and for β titanium $\sigma_{11}^{diff,\beta}$ measured by MGIXD method are calculated respectively using Voigt, Reuss and Eshelby-Kröner models.

Because it's not possible to measure the lattice strain in loading direction by MGIXD method, the stress plots are drawn in function of macro-strain E_{11} . The plots $\sigma_{11}^{diff,ph,Voigt}$, $\sigma_{11}^{diff,ph,Reuss}$, $\sigma_{11}^{diff,ph,Kr\ddot{o}ner}$ vs. E_{11} represent the phase stresses determined using XSF calculated respectively by Voigt, Reuss and Eshelby-Kröner model in which the crystallographic initial texture was taken into account (cf. Fig. 1.24 page 37). As seen in Fig. 6.2, the rig macro-stress is higher than other model fitted stress. One possible explanation is that the macro-stress measured on the sample surface is slightly lower than the applied stress over the whole sample cross section. The Voigt model is considered as the upper limit for determined stress and the Reuss model can be considered as the lower stress limit, while the results obtained using Eshelby-Kröner model are intermediate. Using the three models of XSF

only small differences appeared in the stress values calculated for each phase. Therefore in all further analysis only the intermediate Eshelby-Kröner model will be used.

The plots of phase stress evolution for α and β titanium, calculated using Eshelby-Kröner model until the sample fracture are drawn in Fig. 6.3. The macro-stress is Σ_{11}^{diff} determined as the volume weighted mean value ($\Sigma_{11}^{diff} = 0.45 \cdot \sigma_{11}^{\alpha} + 0.55 \cdot \sigma_{11}^{\beta}$) according to the phase stresses in α and β titanium.

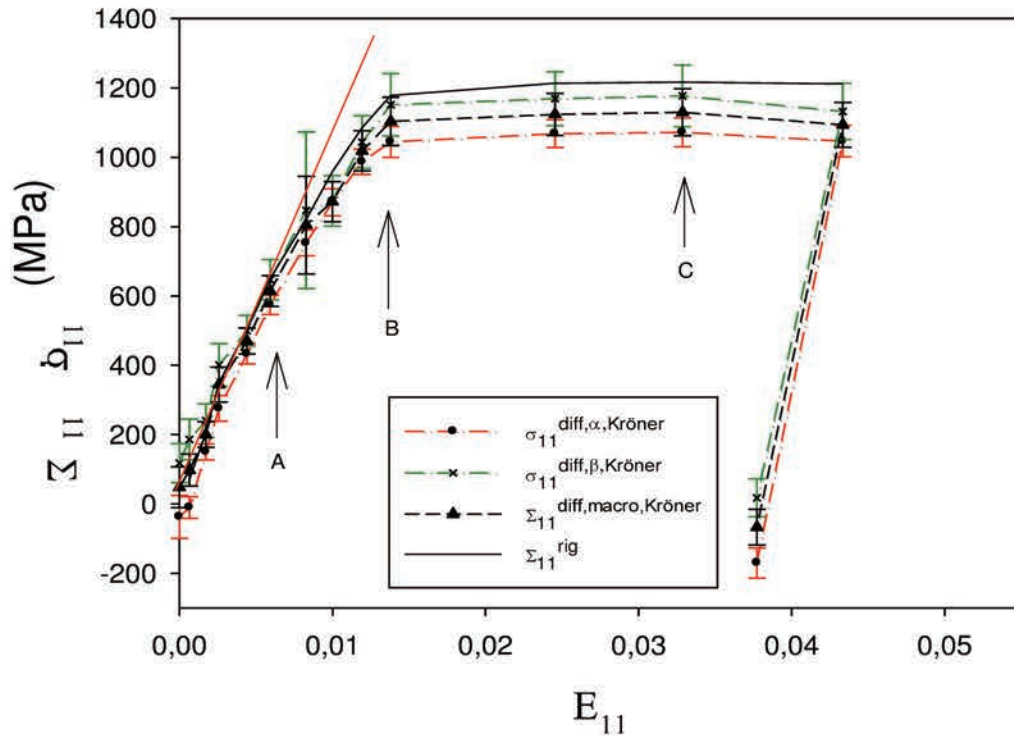


Figure 6.3 Phase stress σ_{11}^{ph} vs. macrostrain E_{11} of sample during tensile test. The phase stress for α titanium $\Sigma_{11}^{diff,\alpha}$ and for β titanium $\Sigma_{11}^{diff,\beta}$ measured by MGIXD method are calculated by Eshelby-Kröner models. Red line was drawn to visualize the change of slope found for experimental plots.

A linear behavior (red straight line) can be observed from both curves of Σ_{11}^{rig} and Σ_{11}^{diff} at the beginning of tensile test, indicating that the material was elastically deformed in this range. The first noticeable change in the slope of Σ_{11}^{diff} plot was found for stress around 600 MPa ($E_{11} \approx 0.008$, threshold A in Fig. 6.3), where small decreasing in slope of stresses Σ_{11}^{diff} compared to linear initial dependence (red line) was observed. At threshold B, where $E_{11} \approx 0.012$, the curves for both phases change significantly their slopes and start to saturate, indicating that both phases entered into plastic deformation range. At threshold C, where $E_{11} \approx 0.033$, the stresses of α titanium ($\Sigma_{11}^{diff,\alpha} \approx 1040 \text{ MPa}$) and β titanium ($\Sigma_{11}^{diff,\beta} \approx 1150 \text{ MPa}$) reached their highest value. After threshold C, the stress in α titanium remained almost

constant, while the stress in β titanium slightly relaxed. Please see Appendix 20 for the fitting of $\langle a(\phi, \psi) \rangle_{\{hkl\}}$ vs. $\sin^2 \psi$ plots for two angles ϕ (0° and 90°) at thresholds A, B, C and for the sample after fracture (unload).

6.1.4 Evolution of lattice strain in each phase during the tensile test

The interplanar spacings of all available hkl reflections were measured for each phase during the tensile test in the direction normal to the surface (ND). The relative elastic lattice strains were then calculated for each hkl reflection (cf. Eq. 2.2, page 45) for α titanium and β titanium. Because of the hcp lattice structure, much more hkl reflections can be observed for α phase comparing with phase β having bcc lattice (see Appendix 21). Then the arithmetic mean elastic lattice strains $\langle \varepsilon_{33} \rangle^{ph}$ in ND were calculated for each phase over all available hkl reflections. The evolution curves of the mean lattice strains vs. E_{11} were plotted for each phase in Fig. 6.4. The analysis of lattice strain will be presented in section 6.1.5.2.

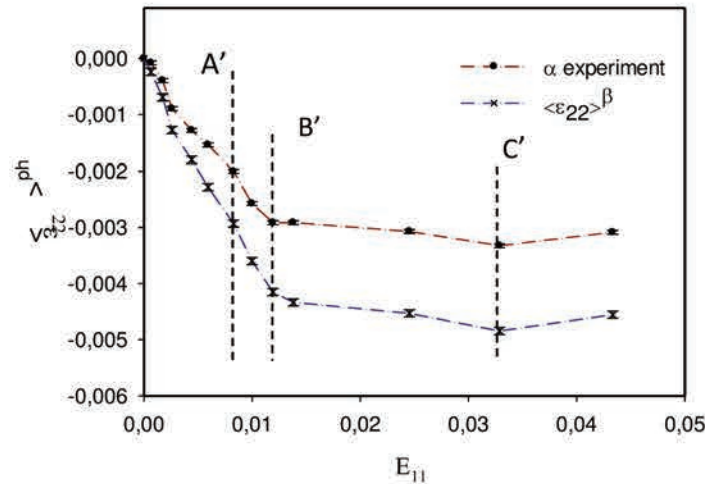


Figure 6.4 Evolution of mean lattice strains $\langle \varepsilon_{33} \rangle^{ph}$ in the normal direction for each phase during tensile test, plotted as a function of macro-strain E_{11} .

6.2 Confrontation of model prediction with experimental results

The prediction of elasto-plastic behaviour has been performed with 2000 spherical inclusions (assuming $a/c=1$ and $b/c=1$ for all grains), among which 900 inclusions represent α phase (45%) and 1100 inclusions represent β phase (55%). The virtual tensile loading was applied in the same direction of the real experimental loading. The initial crystallographic textures (cf. Fig. 1.24 page 37) of each phase have been used to determine the input crystallites orientations. The different crystalline lattice structures of each phase and their anisotropic single crystal elastic tensors (table 1.13 page 37) have been taken into account, but the twinning effect was not taken into consideration. It should be emphasised that twinning is

rare and occurs at strains above 4% in two-phase Ti alloys due to the high aluminium content [Prakash 10].

6.2.1 CRSS determined for slip systems

Model calculations were performed to determine the parameters related to the plastic properties of α and β titanium. The parameters characterising slip systems (τ_0^{ph} and θ_0^{ph} in table 6.2) are adjusted in order to get the optimal fitting between the theoretical and experimental results.

| Parameters | Phases | Slip systems | Values (MPa) | Values (MPa) [Gloaguen 16] | Values (MPa) [Barkia 15] |
|-----------------|----------|---|-------------------|----------------------------|--------------------------|
| τ_0^{ph} | α | (1 α) Prismatic P <a> {0110}<1120> | 400 | 220 | 36 |
| | | (2 α) Basal B <a> {0001}<1120> | 500 | 250 | 252 |
| | | (3 α) Pyramidal III <a> {0111}<1120> | 500 | 350 | 144 |
| | | (4 α) Pyramidal III <c+a> {0111}<1123> | 500 | 400 | 288 |
| | β | (1 β) {110}<111> (2 β) {112}<111> (3 β) {123}<111> | From 510 to 520 * | 310 and 330 | - |
| θ_0^{ph} | α | all systems | 20 | - | - |
| | β | all systems | 20 | - | - |

Table 6.2 Parameters of Voce model determined during tensile test. (* higher value is obtained if the initial stresses are taken into account).

It should be emphasised that the comparison was done simultaneously for wide range of evaluable data, i.e. in situ measured: lattice strains (Fig. 6.5 and 6.6), phase stress (Fig. 6.7) as well as macroscopic stress-strain tensile curve. The initial stresses existing in both phases influence the plastic deformation of studied sample. However, their role on the slip activation can be complex. They can relax in the beginning of plasticity or superpose with the applied stress during elasto-plastic deformation. Therefore the model prediction of plastic deformation was performed twice, i.e. neglecting or taking into account these stresses. In the latter case, the stress measured in a given phase was assigned to each grain belonging to this phase. The optimal fitting parameters obtained for best fitting of all results are given in table 6.2.

Compared with previous studies [Barkia 15, Gloaguen 15], the CRSS determined for α phase are considerably higher. However it is proved that this solution is neither unique for α

phase, nor for β phase, especially in the presence of potentially twinning phenomenon. It should be also mentioned that we have checked with model that in the case of β phase the crystallographic texture play an important role in the activation of slip systems and the simulation does not agree with experiment if the texture is not taken into account.

6.2.2 Evolution of phase strains in transverse direction

The lattice strains are firstly analysed. Fig. 6.5 and 6.6 present respectively the confrontation between model predictions and the experimental results for individual hkl reflections and the comparison of calculated average lattice strains between each phase. The calculations were performed respectively neglecting or taking into account the initial stresses.

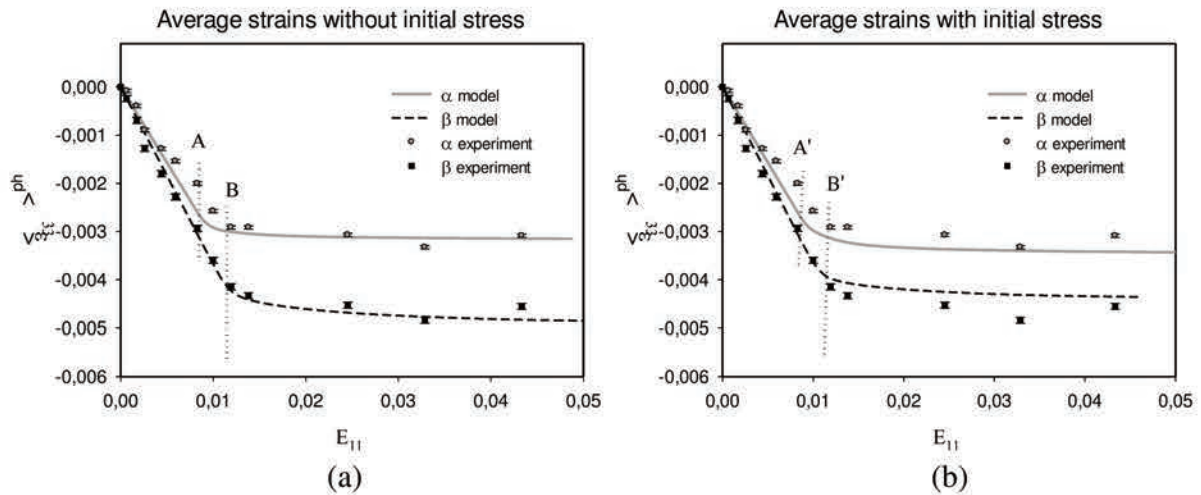


Figure 6.5 The arithmetical mean lattice strains in both phases for tensile test vs. sample strain E_{11} . Experimental points are compared with model functions (lines) with two different assumptions: initial stresses are neglected (a) or taken into account (b).

As shown in Fig. 6.5, a good agreement is obtained between the calculated and measured lattices strains both for α and β titanium. No significant difference is observed by applying the two assumptions concerning initial stresses with the same set of Voce parameters given in table 6.2. However, a better convergence between experimental and theoretical data is obtained when the initial stresses are neglected, which suggests that the initial stresses relaxes early and do not influence significantly the obtained results.

In Fig. 6.6 the lattice strains measured for different hkl reflections are compared with model prediction performed with the set of CRSS values presented in table 6.2, neglecting initial stresses. Due to the complex correspondence between slip systems and the lattice planes it is difficult to get a perfect prediction for all hkl reflections. Some disagreements are

observed for hexagonal lattice (α phase). However, for β titanium (bcc) the lattice strains are well predicted for almost all hkl reflections.

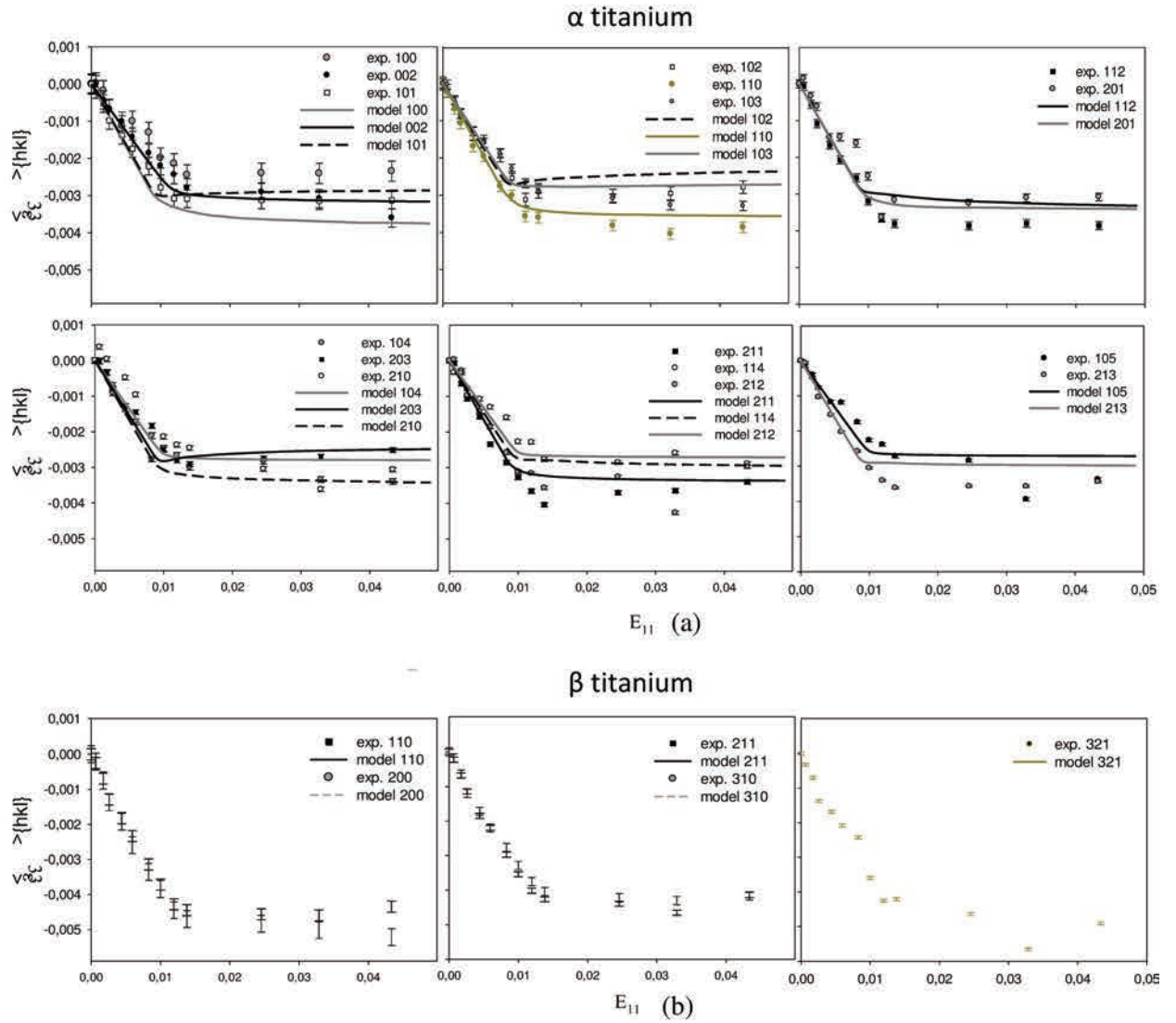


Figure 6.6 The relative lattice strains measured in the direction normal (ND) to the sample during tensile test vs. sample strain E_{11} . Experimental points together with fitted model functions (lines) for different hkl reflections in α phase (a) and β titanium are shown. The convention with three Miller indices was used to denote hexagonal reflections. The initial stresses are neglected in calculations.

The elasto-plastic strain of titanium material at macroscopic scale is determined by the combination of the slip system activated in each phase and the intergranular or interphase behavior at grain scale. The existence of two different phases and the anisotropic properties of α -phase titanium, leads an important influence on the overall mechanical performances of the material. This is why the studies of plastic deformation occurring in both phases, as well as the interaction between phases are of central importance.

6.2.3 Order of slip activation

For bcc β titanium, the same value of CRSS is adjusted for three operating slip systems (so called pencil glides [Taylor 26, Lütering 07]) $\{110\}\langle 111\rangle$, $\{112\}\langle 111\rangle$ and $\{123\}\langle 111\rangle$.

In the case of α titanium, the activation of slip system is more complex due to the different CRSS for different slip systems (cf. section 1.2.1). The stresses inhomogeneously localized on the grains have also important influence on the activation of slip systems. Currently, the present set of parameters (table 6.2) allows to get the best fitting results for evolution curves of all hkl reflections of both α and β titanium (Fig. 6.6). However, this solution is not proved unique for the combination of CRSS within each phase.

According to several studies [Partridge 67, Akahtar 75, Pochettino 92, Tan 94, Zaefferer 03, Glavicic 04, Fréour 06, Gloaguen 13], the prismatic $\{0110\}\langle 1120\rangle$ system is considered as the main active slip system, Pyramidal $\langle c+a\rangle$ $\{0111\}\langle 1123\rangle$, Pyramidal $\langle a\rangle$ $\{0111\}\langle 1120\rangle$ and basal $\{0001\}\langle 1120\rangle$ systems are considered as the secondary slip systems in the 1st order hcp lattice (cf. table 1.9 page 30).

Comparing the results of model prediction with experimental data for different sets of CRSS in α phase, we can conclude that the P $\langle a\rangle$ slip has the lowest CRSS, while the other slip systems have higher and approximate values between each other. In spite of the complex combination of CRSS for slip system of each phase, the performed analysis satisfactorily determines one of the possible CRSS combinations for slip systems in different phases. It is found that the CRSS in both phases are similar but the values in α phase are slightly lower than in β phase. It should be also mentioned that it is checked with model simulation that the crystallographic texture plays an important role in the activation of slip systems and the simulation does not fit well with experimental results if the texture is not taken into account.

6.2.4 Accumulation of shear strains

Fig. 6.7a and b show the model calculated mean values of accumulated shear strain for slip systems operating in one grain:

$$\text{accumulated shear strain} = \frac{1}{N} \sum_{\{hkl\}\langle uvw\rangle} \gamma^g \quad \text{Eq. 6.4}$$

where the sum of slip amplitudes (i.e. γ^g shear strains in one grain g) $\sum_{\{hkl\} \langle uvw \rangle} \gamma^g$ is calculated for a given slip system $\{hkl\} \langle uvw \rangle$ (in the case of hcp lattice $\{hkil\} \langle uviw \rangle$) for all polycrystalline grains and N is a number of grains. Additionally, the sum of accumulated shear strain for all systems and systems in each phase is presented in Fig. 6.7 c and d.

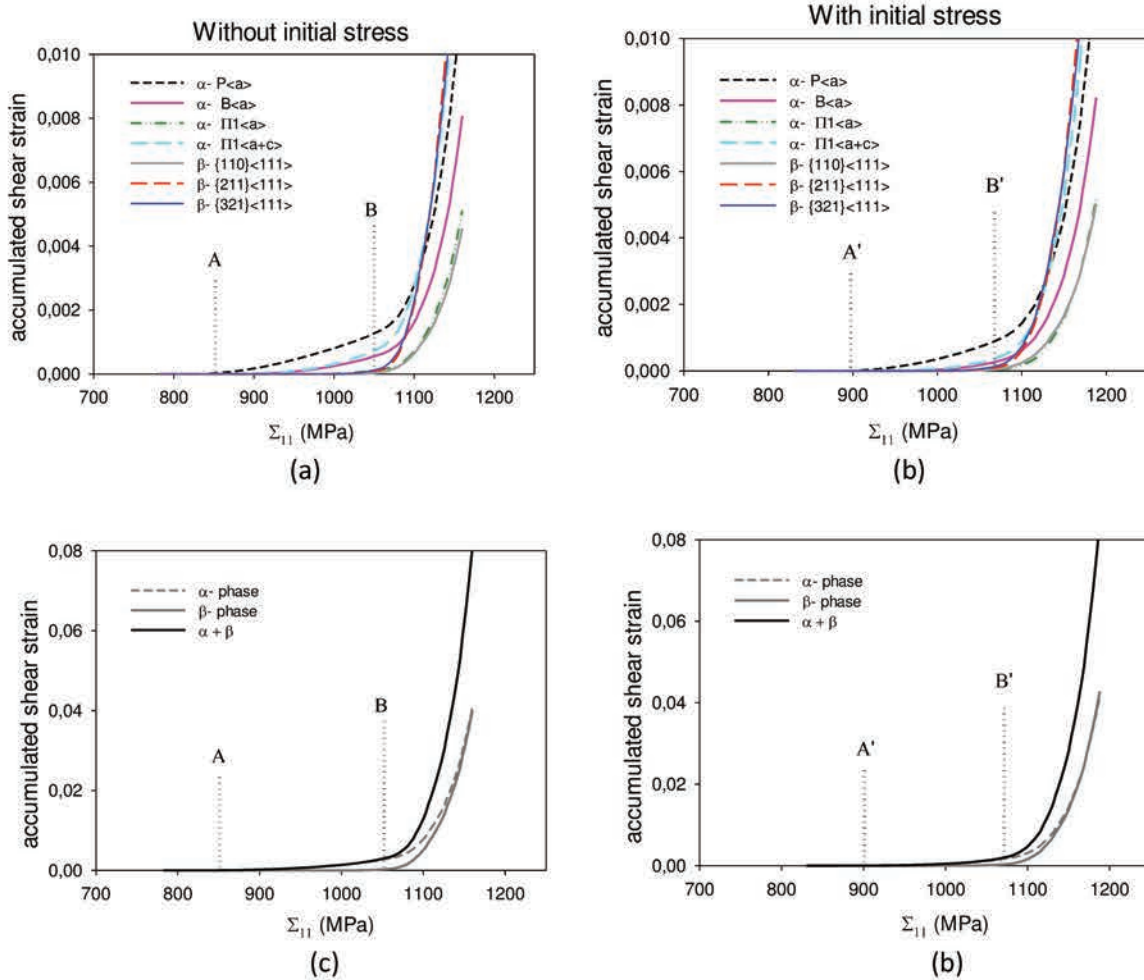


Figure 6.7 Mean accumulated shear strain (per one grain): for each slip system (a,b), for all systems and for the systems in each phase (c,d) as a function of the applied stress Σ_{11} . The initial stresses are neglected (a,c) or taken into account in calculations (b,d).

6.2.4.1 Without initial stress

By analysing Fig. 6.7 a and c, the history of slip system activation can be described. When the initial stresses are neglected, the first activated system is the prismatic system $P \langle a \rangle$ (see table 6.2 and threshold A at about 670 MPa in Fig. 7), as usually happens in α titanium. Next, around $\Sigma_{11} = 900$ MPa, pyramidal $\Pi I \langle c+a \rangle$ slip begins to be activated. In the range from A to B a small macroscopic plastic deformation occurs because only the slips in α titanium are

activated, while the β titanium remains elastic. The successive three slip systems in bcc β titanium (pencil glides) and the slip system B<a> in hcp α titanium are activated at the macroscopic stress around $\Sigma_{11} = 1050$ MPa, leading to significant plasticity of the material above the B threshold (cf. Fig. 6.7a). The activation of slip systems in each phase within the three ranges defined by thresholds A and B is shown in Fig. 6.7c (without initial stresses, the evolution of phase strains is presented in Fig. 6.5a). In both figures different phase behaviours is well illustrated for the following ranges: before threshold A, both phases are elastically deformed; between thresholds A and B, only α titanium is plastically deformed; after threshold B, both phases are plastified.

6.2.4.2 With initial stress

In Fig. 6.5b and 6.7b, d, the results of model calculation results with initial stresses are presented. It can be concluded that the results are similar to those without initial stresses, only the threshold A' ($\Sigma_{11} \approx 900$ MPa) and B' ($\Sigma_{11} \approx 1080$ MPa) are slightly shifted towards higher macro-stress.

6.2.5 Evolution of phase stresses in loading direction

Once the activation of slip systems in titanium is found out, the evolution of phase stress in loading direction can be explained. Fig. 6.8a and b present the prediction results of phase stresses for α and β titanium in function of macro-strain E_{11} , compared with the experimental ones. Fig. 6.8c and d show the correlation between the phase stresses in α and β titanium and the stress Σ_{11} applied in loading direction. This prediction is also performed with the set of parameters in table 6.2.

In Fig. 6.8, only the stresses σ_{11}^{ph} along the loading direction (x_{11}) are shown, because the values of the transverse stresses σ_{22}^{ph} are nearly equal to zero within the experimental uncertainty range. Taking into account the uncertainties of the measurements, it can be stated that good agreement between measured and predicted phase stresses σ_{11}^{ph} is obtained both for the calculations neglecting (Fig. 6.8 a, c) or taking into account (Fig. 6.8 b, d) initial stresses.

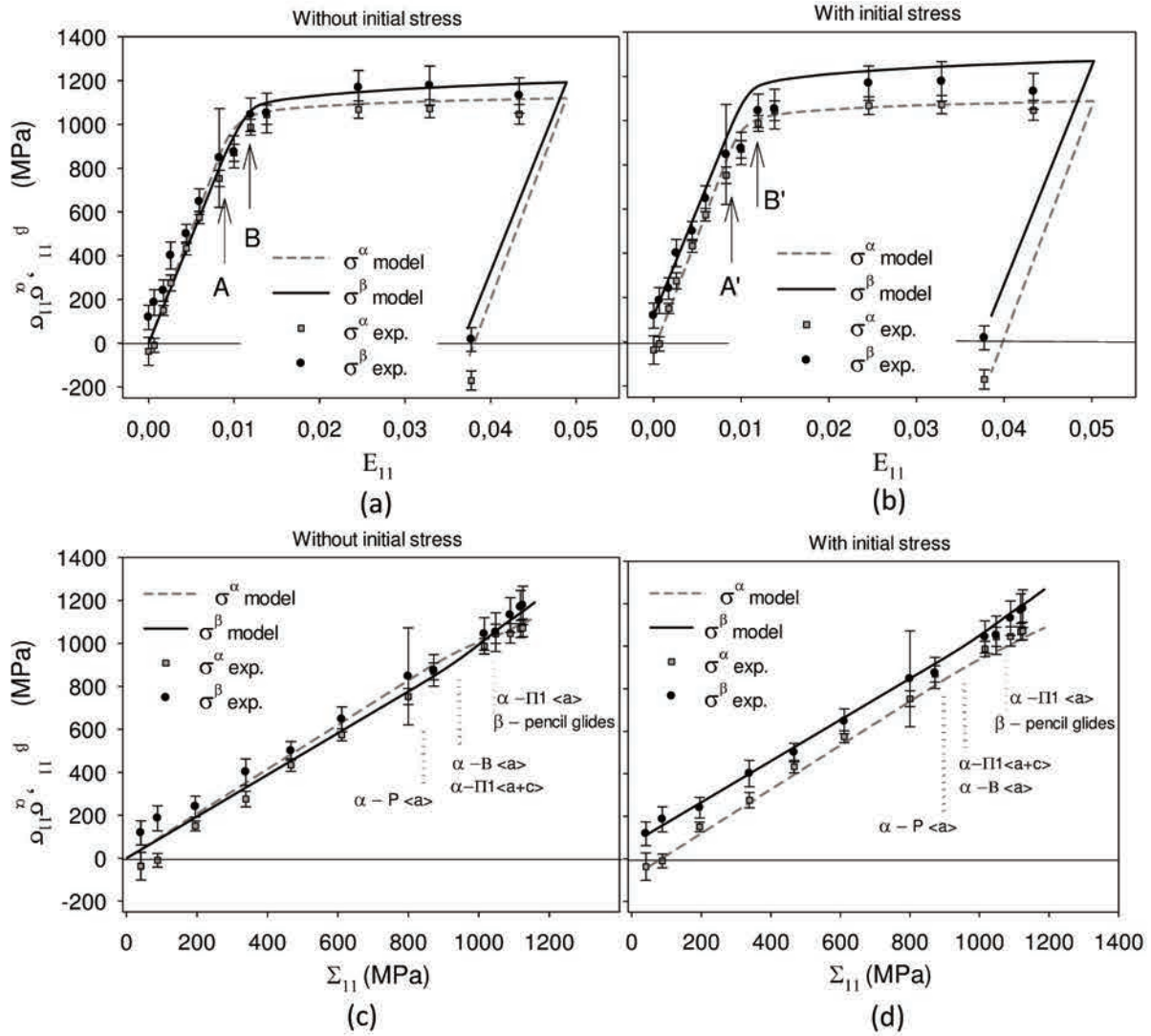


Figure 6.8 Evolution of phases stresses vs. total sample deformation E_{11} (a,b) and applied macrostress Σ_{11} (c,d) with thresholds corresponding to activation of slip systems (cf. table 6.2). The stresses measured using MGIXD are compared with model prediction in which the initial stresses are neglected (a,c) or taken into account in calculations (b,d).

In Fig. 6.8a and b, the yield point of each phase is indicated by thresholds A and B (or A' and B'), referring to the activation of slip systems (cf. Fig. 6.7). Some analysis can be figured out:

- Initially both phases exhibit linear behaviour (vs sample strain E_{11}) during elastic deformation.
- Within the range between A and B (or A' and B'), three slips are activated successively in α titanium, which does not lead to significant softening of any phase (Fig. 6.8a), i.e. these glides are not sufficient to induce macroscopic plasticity of the material.

- It should be pointed out, significant uncertainty of the determined stress in β phase was observed when $P\langle a \rangle$ system started to operate in α titanium ($\Sigma_{11} \approx 850\text{MPa}$ in Fig. 6.8c and $\Sigma_{11} \approx 900\text{MPa}$ in Fig. 6.8d).
- Although the glides in α are not so great as to initiate macroscopic plastic deformation, $P\langle a \rangle$ system are probably capable of leading to a relaxation of intergranular/interphase stresses during measurement of the $\langle a(\phi, \psi) \rangle_{\{hkl\}}$ vs $\sin^2 \psi$ plot.
- Finally, the activation of all slips in β titanium and $\Pi 1 \langle a \rangle$ in α titanium occur over point B or B' ($\Sigma_{11} \approx 1050 - 1100\text{MPa}$ in Fig. 17 c,d) and led to the initiation of plastic deformation in both phases. Then, evolution curves of both phases are going to saturation with small hardening described by parameters θ_0^{ph} parameters given in table 6.2.
- The parameters τ_1^{ph} and θ_1^{ph} characterising hardening for large deformation cannot be identified because of the sample fracture at about 4.5% of sample strain.

Finally, the last measurement was done after sample fracture and small phase stresses with opposite signs are found (cf. Fig. 6.8a, b). This stress state of material is correctly predicted by self-consistent model (especially, when the initial stresses are taken into account).

6.2.6 Evolution of macro-stress in loading direction

The evolution of overall mechanical stress vs strain, determined using three independent approaches, is presented in Fig. 6.9. The first plots $\Sigma_{11}^{\text{diff}}$ vs. E_{11} show the stress determined as the volume-weighted mean value from the phase stresses measured using MGIXD ($\Sigma_{11}^{\text{diff}} = 0.45 \cdot \sigma_{11}^{\alpha} + 0.55 \cdot \sigma_{11}^{\beta}$); the second plots Σ_{11}^{mod} vs. E_{11} are obtained using the self-consistent model for the parameters given in table 6.2; and the third plots $\Sigma_{11}^{\text{mech}}$ vs. E_{11} show the mechanical true macroscopic stress determined from the force recorded by the load cell. Several observations can be pointed out:

- As seen before, linear behaviour can be observed in all of the presented plots during the elasticity stage up to threshold B (or B'). Within this range, the results obtained using the diffraction method and recorded by the tensile rig are in good agreement (Fig. 6.9a, b).
- A small decrease in overall stress was determined for $\Sigma_{11}^{\text{diff}}$ using MGIXD, when the $P\langle a \rangle$ slip system was activated. This phenomenon is caused by phase stresses relaxation around threshold A (or A'), as seen previously. This kind of fast step relaxation occurs only in the gauge volume measured by diffraction but is not observed in the macroscopic

response Σ_{11}^{mech} vs. E_{11} . Thus, the reason for the latter evolution could be explained by the effect of sample heterogeneity, such as micro-damage or cracking in the near-surface region of the sample.

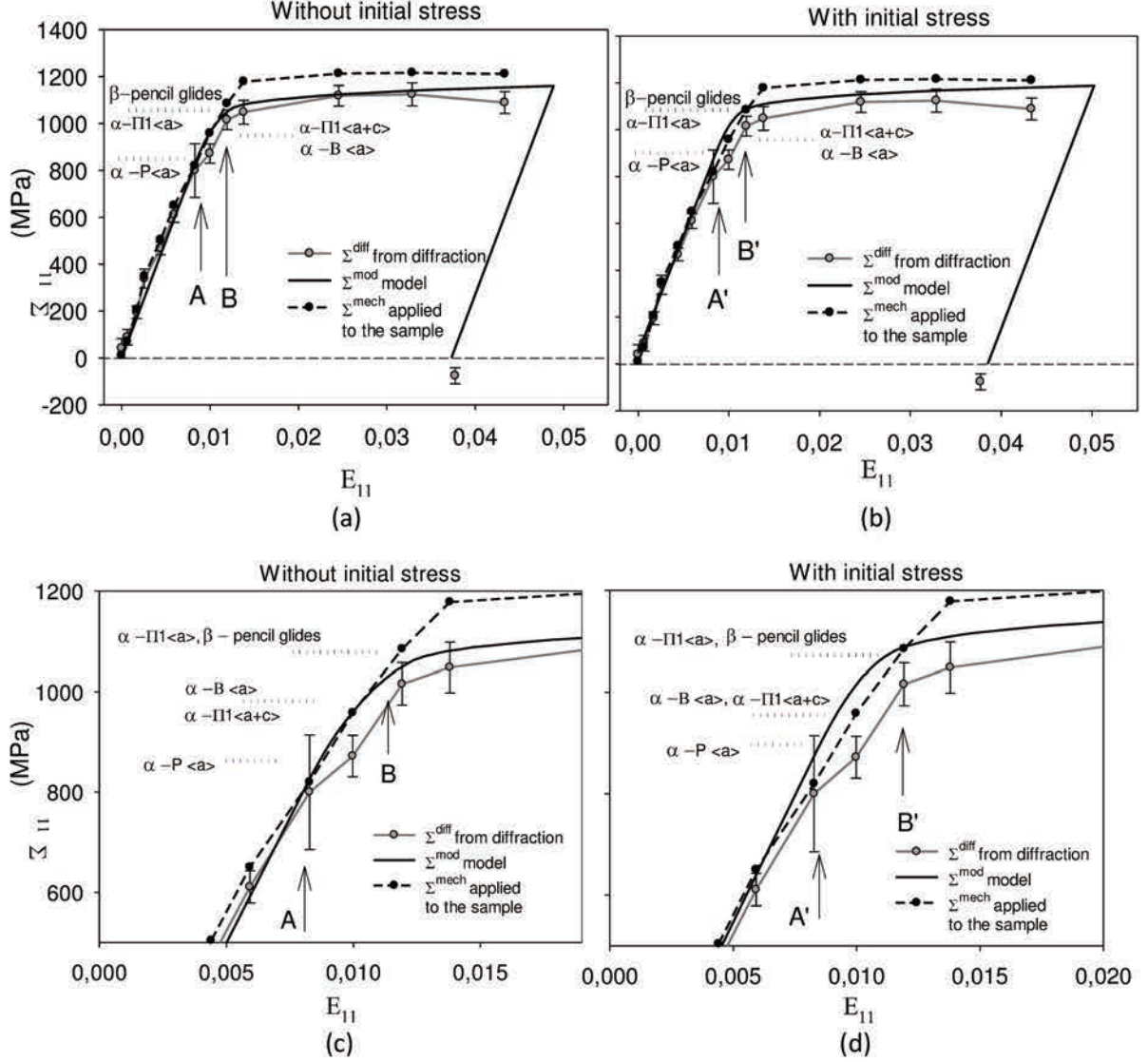


Figure 6.9 Evolution of overall macro-stresses Σ_{11} vs. total sample deformation E_{11} (a,b) and magnification of this plot for the elastic-plastic transition (c,d). The results determined from diffraction ($\Sigma_{11}^{diff} = 0.45 \cdot \sigma_{11}^{\alpha} + 0.55 \cdot \sigma_{11}^{\beta}$), determined from loading cell (Σ_{11}^{mech}) and computed for parameters given in table 7.7 (Σ_{11}^{mod}). The thresholds corresponding to activation of slip systems are shown (table 7.7). The initial stresses are neglected (a,c) or taken into account in calculations (b,d).

- It is observed that during the subsequent deformation process, the stress measured using MGIXD (Σ_{11}^{diff}) was slightly lower than predicted (Σ_{11}^{mod}), but the agreement between model and experiment results still remained within the uncertainty range (Fig. 6.9). It was also observed that the surface stress (i.e. Σ_{11}^{diff}) was significantly smaller than the mean

stress in the bulk volume (Σ_{11}^{mech}), which means that the deformation was not homogenous over the cross section of the sample. However, such heterogeneity is not very significant because the difference between Σ_{11}^{diff} and Σ_{11}^{mech} did not exceed 10%.

- Despite the small step relaxation, the macroscopic stress Σ_{11}^{diff} rises again between A and B with an increasing rate (slope) almost equal to that during elastic deformation (Fig. 6.9c, d). Thus, as already concluded, the activated slip systems in α titanium do not cause significant macroscopic plastic deformation. Macroscopic plastic deformation was initiated about 1050 MPa (B or B' thresholds) along with the activation of the slip systems in β phase. The latter phenomenon is clearly confirmed by the evolution of the model-predicted overall stress Σ_{11}^{mod} .
- Finally, we can see that after sample fracture, i.e. after sample unloading (i.e. $\Sigma_{11}^{mech} = 0$), a small non-zero compressive residual stress (i.e. $\Sigma_{11}^{diff} < 0$) remained on the sample's surface.

In conclusion, it should be emphasised that in the above presented analysis the plastic properties of both phases in the studied Ti alloy were characterised. The advantage of using experimental methodology is that the measured and model calculated lattice strains and stresses can be simultaneously compared. It is well seen that during plastic deformation higher stress is localised in β phase comparing with that in α phase, but the difference is not so important, which can be also caused by initial stresses. The crystallographic slips are firstly activated in α phase, just before glides in β phase. It should be also emphasised that the new methodology (MGIXD) enables to estimate level of second order stresses causing usually deviation of the $\langle a(\phi, \psi) \rangle_{\{hkl\}}$ vs $\sin^2 \psi$ plot. For studied samples the deviations are not significant, i.e. the second order stresses in both phases are negligible.

6.3 TKD measurement for Ti-18 microstructure

The Transmission Kikuchi Diffraction (TKD) method [Trimby 12, Tokarski 16] is employed to determine the microstructures of initial and fractured (deformed) samples. TKD methodology offers much better spatial resolution in comparison with standard EBSD technique, therefore the orientation maps acquired with a step of 20 nm allowed us to determine reasonable images for α_s lamellas (acquisition parameters were set according to [Tokarski 16]). The results of TKD analysis, in the form of raw data without any map

cleaning procedures, are shown in Fig. 6.10a. As expected for 4.5% small sample strain (Fig. 6.10b), no significant differences between the initial and deformed samples are observed and no twins were found in both phases of the studied Ti-18 alloy.

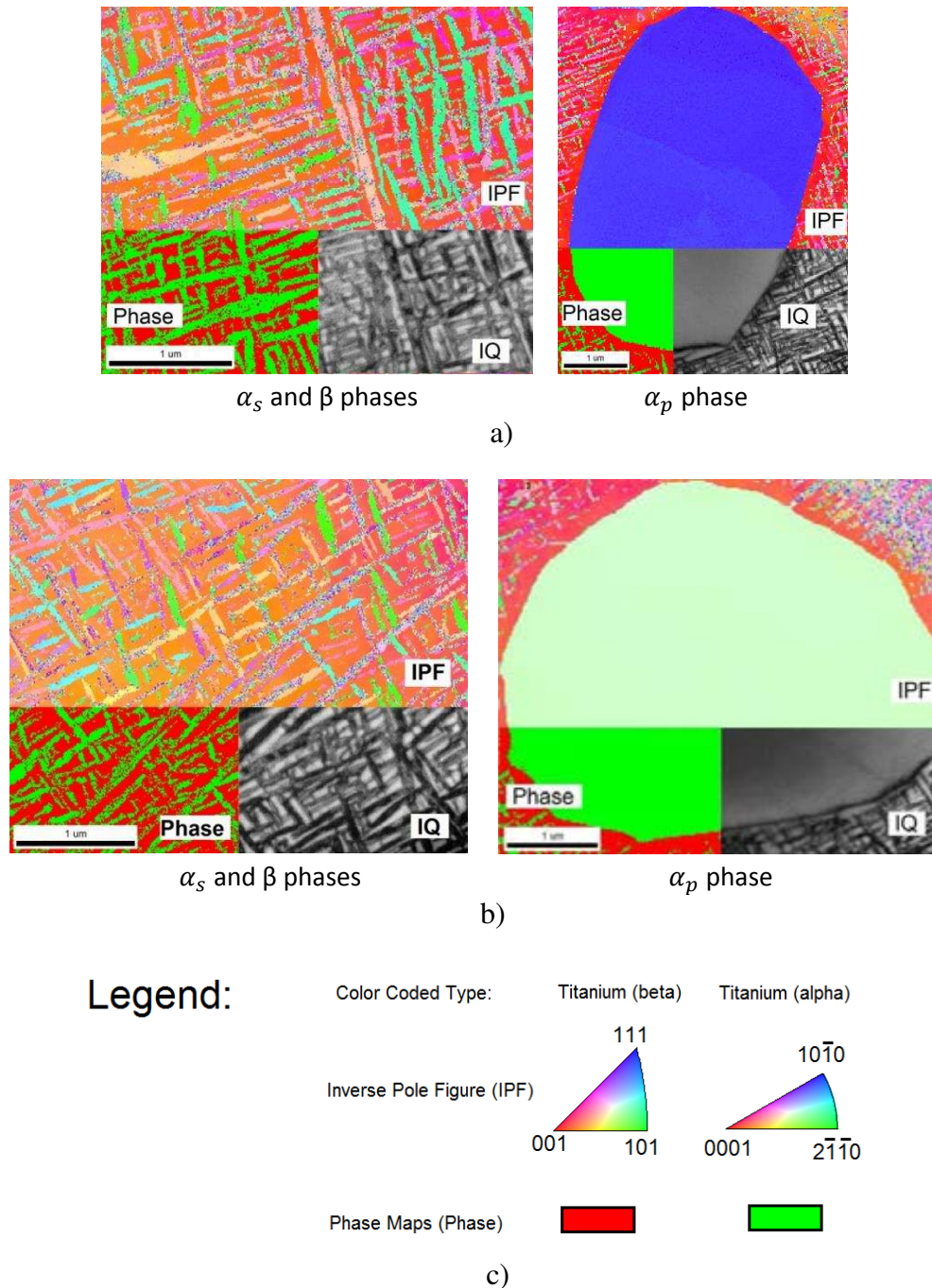


Fig. 6.10 Results of TKD measurement for initial (a) and deformed (b) samples: lamellar structure of α_s phase embedded in β phase (on the left) and α_p precipitate (on the right) are shown (IPF – inverse pole figure, IQ – image quality index and Phase map).

The inverse pole figures (IPF) maps (Fig. 6.10c) show homogenous lattice orientation in β titanium as well as within α_p precipitates. Analysis of the image quality (IQ) maps [Wright 06] (Fig. 6.10 a and b) shows that the worse quality of Kikuchi patterns (dark shade of gray) were obtained for α_p precipitates, this can be due to their small grain size or to higher density of defects.

The TKD and X-ray diffraction measurements showed that lattice orientation in both α_p and α_s precipitates fulfils or approximates to the Burgers relation $\{110\}_\beta \parallel \{0001\}_\alpha$ [Newkirk 53] (cf. pole figures in Fig. 1.24a, page 37). And no evident twinning effect is observed.

6.4 Conclusions

In the present chapter, “in situ” X-ray diffraction measurement (MGIXD method) is combined with the prediction by EPSC model in order to study mechanical behaviour of two-phase titanium alloy. The presented EPSC model provides a possibility to compare with the elasto-plastic behaviour of each phase, groups of grains or macroscopic sample using a small number of adjustable physical parameters.

The X-ray diffraction measurement is done in the near-surface volume in which we can assume relaxation of normal stresses. This enables direct measurement of other stress components in the initial sample as well as during sample loading and finally for unloaded sample. The measured stresses bring new information because the elasto-plastic transition can be directly observed for each phase.

As the result of analysis, the initial CRSS for different slip systems (basal, prismatic and pyramidal) in α titanium and for pencil glides in β titanium [Taylor 26] have been determined by comparing the lattice strains' evolution during tensile test with predictions of the EPSC model. Very good agreement between measured and predicted data confirms the reliability of determined initial CRSS for all considered slip systems. It is found that the slip systems are firstly activated in α titanium. The initial hardening parameters θ_0^{ph} are also determined assuming similar value for all systems. Subsequently, the measured phase stresses and macrostresses were compared with theoretical values and a good accordance in the range of uncertainty was obtained. Analysis of the latter results showed that in spite of early activated slips in α titanium, both phases remains almost elastic until activation of slips in β phase. During the range of small plasticity (when slips operate in α phase, between thresholds A and

B) some small relaxation of interphase stresses occurred, but the significant plastic deformation process will start together with crystallographic glides in β phase. The image quality (IQ) maps show smaller grain size or greater defect density present in the primary α_p . And The TKD results lattice orientation in both α_p and α_s precipitates fulfils or approximates to the Burgers relation $\{110\}_\beta \parallel \{0001\}_\alpha$ with β titanium. Finally, because the sample was fractured at about 4.5% of sample strain, the parameters τ_1^{ph} and θ_1^{ph} describing hardening for large deformation couldn't be identified.

Although fruitful results have been obtained, some issues remain to be solved:

- In this test, the tensile test isn't successfully performed until large deformation. For the further test, a more ductile titanium alloy can be proposed, in order to collect information on the large deformation, e.g. non-linear hardening or/and the ductile damage process.
- The mechanical behaviours observed on near-surface volume aren't completely coherent with what happens inside the material during tensile test, thus high energy diffraction measurement is proposed for the further investigations.
- The neutron diffraction has been proved not suitable for measurement of titanium (see Appendix 24), probably due to its inelastic scattering with titanium atoms [Chun 08, Willis 09, Petit 10]. In this case, high energy synchrotron X-ray diffraction is proposed for the next studied on titanium alloys, in order to get the information under near-surface layer of sample.
- Because of the lattice structures, the number of reflections is considerably different between hcp (α titanium) and bcc (β titanium). In this case, weighted calculation based on the number of reflections could be proposed to the determination of phase strain/stress for the further studies.

General conclusion

The purpose of this thesis is to develop experimental techniques, mostly the diffraction method, as well as self-consistent modelling in order to deeply understand and to better predict mechanical behaviours of two-phase polycrystalline materials exhibiting different crystalline structures. To this end, investigations on mechanical behavior have been carried out at micro, meso and macroscopic scales. On one hand, the in-situ diffraction measurements were applied during monotonic tensile tests until sample fracture. The damage process was of particular interest for this work. Supplementary experiments, such as instrumented indentation test and TKD observations were also performed, in order to collect experimental data at different scales. These experiments allowed investigating the elasto-plastic properties, and the mechanism of ductile damage in the selected materials. On another hand, model simulations were carried out to quantitatively determine the parameters related to the elasto-plastic behaviour as well as initiation of damage. Self-consistent model was used to study the activation of slip systems and the evolution of work hardening during elasto-plastic deformation of desired materials. The local behaviour during necking process was also studied using synchrotron diffraction in order to see the influence of ductile damage. In this case both self-consistent model and FEM simulation were performed to analysis the experimental results.

In this manuscript, important progress has been obtained for our current knowledge, and original conclusions have been drawn for the issues raised at the beginning of thesis. The main achievements can be summarized as follow:

1. The mechanical behavior of duplex steels was studied during monotonic tensile test. This study is directly related to that reported by [Le Joncour 11]. It was confirmed that the elasto-plastic properties are different between austenite and ferrite, the yield stress of austenite is lower than that of ferrite in the studied steels. By comparing the experimental results of neutron diffraction with the predictions of elasto-plastic self-consistent model, the values of CRSS were determined for the austenite and the ferrite in different types of duplex steels. It was proved that the micro-mechanical behaviour of materials at grain scale is strongly influenced by their chemical compositions and the heat treatments. Besides, it was found that the yield stress of each phase is also strongly influenced by the residual stresses remained in the material after its processing.

2. Using neutron and synchrotron diffraction, temporal studies of ductile damage have been carried out for aged UR45N. Stress relaxation in ferrite was observed at the end of large deformation process. This effect is probably caused by the initiation of ductile damage. With help of synchrotron diffraction measurement, the spatial scans along neck were performed and stress relaxation in ferrite was confirmed. The stress relaxation in ferritic grains contributing to the reflections 200 and 211 was observed. Decrease of lattice strains was measured for these reflections in the centre of neck and even more significant effect was found in a small distance apart from the centre. The synchrotron measurement along the neck confirmed the previous neutron diffraction measurement, for both measurements lattice strains in a large volume inside neck was determined. The spatial evolution of lattice strains along the neck was simulated with the help of FEM approach. A qualitative correlation between the macroscopic von Mises stress and the lattice strains, measured in both phases using synchrotron radiation, suggests that the stress triaxiality is probably associated with damage process. This can be implemented into future numeric modelling, allowing to give a more accurate simulation results in the case of large deformation.

3. The self-consistent model was developed in order to predict the damage initiation process, different damage criteria have been tested. Comparing the results from neutron diffraction measurement with that from calculations, it is found that the damage criteria based on the total energy or on equivalent strain give the best prediction of the stress partitioning between phases. However, as shown by self-consistent model, the grain evolution history, which is presented by the total strain or total energy criteria, is also important and probably it is responsible for damage resistance of the grain. Therefore, the damage begins in the more deformed grain, due to the accumulation of lattice defects. It can be concluded, that both the stress and the total strain play an important in initiation of the damage process.

4. Instrumented indentation tests performed for fractured sample shows that much greater fluctuations of both Young's modulus and hardness occurred in the neck comparing with other parts of sample out of the neck. This effect can be explained by a large heterogeneity of material occurred at grain scale for each phase during severe plastic deformation. It was also found that the mean hardness of ferrite exceeded that of austenite during intermediate deformation process. However for large deformation (close to the fracture surface in the studied sample) the inversion of the phases' hardness values occurred. Before the fracture, when damage process is initiated in ferrite, the hardness of ferrite decreased and became smaller than for austenite. This variation of hardness in ferrite can be considered to be

relevant to the local behaviour of ferrite. The same tendency was observed in the softening of ferrite (on point C', cf. section 4.6.3) by diffraction experiment, where relaxation of the stress in ferrite was also interpreted as a result of damage initiation in this phase.

5. The study of elasto-plastic deformation of two-phase titanium alloy was done, in order to study the mechanical behavior of a hexagonal structure material. To do this, the multireflection grazing incident X-ray diffraction (MGIXD) was used in-situ during tensile test. This method enabled to measure not only the lattice strains but also the stresses in both phases of titanium Ti-18 alloy. As a result the parameters characterizing the activation (CRSS) and hardening (H) of slip systems were determined for both α (hcp) and β (bcc) phases. It was confirmed as in literatures, that the slip systems are firstly activated in α titanium, especially the prismatic system $P_{\langle a \rangle} \{1100\} \langle 1120 \rangle$, which exhibits the lowest CRSS [Zambaldi 12, Benmhenni 13, Barkia 15, Gloaguen 15,]. Then, both phases entered into plastic deformation almost at the same macro-strain level, leading to the complete plastic deformation of the material. It was also found, that the yield stress of β titanium is slightly higher than that of α titanium.

Although fruitful results have been taken through this work, the experimental measurement of damage still remains difficult. Nevertheless, some meaningful progresses concerning the mechanism of ductile damage have been gradually obtained. The time and spatial depended study let us observe the mechanical behaviour of different phases through their hkl reflections at the initiation of damage process. The finite elements simulation showed us the importance of stress triaxiality on the damage distribution. The IIT measurements revealed the influence of damage on the mechanical properties of material.

Perspectives

Most of the issues raised at the beginning have been deeply studied by achievements of this manuscript. The scientific research has never a final end, every new discover will enlighten a new way for the future. Thanks to this work, several meaningful research fields have been opened and some issues show new tracks for the further work.

It was confirmed, that the diffraction method is a powerful tool for the measurements of mechanical behaviours of two phase materials at micro/mesoscopic scales. However, in the case of the titanium alloys, using laboratory X-ray diffraction, the measurements are limited only in the near-surface volume of sample, the information is not available for the material interior.

Through the diffraction measurement on titanium alloy, the neutron diffraction seems not suitable for the measurements on titanium due to the low coherent scattering of neutrons. Additionally, the texture of specimen led to a weak signal on certain reflection peaks. Therefore, the high energy synchrotron X-ray diffraction can be suggested for the further in situ measurements on titanium alloys. A suitable material should also be well chosen for the following study, with weaker crystallographic texture, no diffraction peak overlaps, the number of reflections of each phase should be enough to calculate reasonably the average phase strain, etc.

In the current work, the two phase Ti sample is broken at a relatively small deformation level and the mechanical behaviour of different phases (including damage) was not observed during large deformation. In the further work, more ductile titanium alloys should be studied to collect experimental data during large sample deformation, as well as during ductile damage. This range of experimental data can be then interpreted by EPSC model enabling prediction of damage process. Of course, the diffraction measurement can be applied for a larger range of materials. For example, the neutron diffraction has been carried out on magnesium with purely hexagonal structure, the experimental data is waiting to be processed. The following studies could be carried out on ductile metals, such as two-phase brass, aluminium alloy or pure zinc under 100°C-150°C to increase its ductility. This study can be also continued on titanium alloys, such as high ductile β -type titanium Ti-24Nb-4Zr-7.9Sn [Hao 07], continuously on two-phase Ti-17, Ti-18, giving possibility of measurement during ductile damage range. Or even we can performe studies on ferrite-martensite duplex steel to

see the difference with austenite-ferrite duplex steel. In a word, the ultimate aim with these materials is to have a clear observation of damage mechanism between the phases at the end.

In this thesis it is shown that the IIT method can also be applied to investigate properties evolution for two phase titanium, but attention should be paid to avoid the edge effect. Due to the limited sample size, the distance between test points is not enough to avoid completely the overlap of plastified zone introduced by indentation imprints. The relationship between ductile damage and hardness or Young's modulus could be a study issue. Additionally, increasing the number of test points can efficiently reduce the measurement errors. So larger specimen and more test points are proposed for the further IIT measurements. One of the most important issues is the identification of phases on which the indentation data are collected. This identification is currently carried out by eyes on the SEM image of ex situ sample. In the future we could propose an in situ identification method during sample deformation step by step (for example an automatic identification by contrast on SEM images or optical microscope images during tensile test), until the final fracture.

In this work, the EPSC model has been developed in order to predict damage at the grain scale, but the assumption of homogenous macroscopic deformation is still applied in calculations. Certainly, large heterogeneity occurs in the neck, to completely predict this process the model should be extended. Therefore, an important further goal is to incorporate the EPSC damage model into FEM approach, in order to predict not only the materials' mechanical behaviour at different levels but also to realize the structural calculation for large heterogeneous deformation.

Finally, the tomography and TKD technique have shown their ability for microstructure observation. For the next step, we can use the high energy tomography to detect the initiation and propagation of micro-cracks inside materials [Qi 14, Marrow 14], the first test can be performed on a single phase material. If possible, the multi-phase material with great difference in their absorption properties could be used to identify the order of damage between phases. The TKD technique is also a powerful tool to observe the variation of microstructure at grain level during the damage range, which can be used to observe the damage procedure and the propagation of cracks.

Résumé de la thèse en français

Table des matières

| | |
|---|------------|
| Introduction | 164 |
| Objectifs de recherche | 165 |
| I. Contexte de la recherche et état de l'art | 165 |
| 1.1 Description des aciers duplex | 166 |
| 1.1.1 Déformation élasto-plastique et initiation de l'endommagement dans les aciers duplex .. | 166 |
| 1.1.2 Caractérisation des aciers duplex étudiés | 167 |
| 1.2 Description des alliages de titane biphasé | 168 |
| 1.2.1 Déformation élasto-plastique et endommagement ductile dans les titanes biphasés..... | 169 |
| 1.2.2 Caractérisation du TIMETAL-18..... | 170 |
| II. Mesure expérimentales et techniques | 171 |
| 2.1 Mesure par diffraction | 171 |
| 2.1.1 Détermination des déformations cristallines par méthode de diffraction..... | 171 |
| 2.1.2 Détermination de l'état de contrainte par méthode de diffraction..... | 172 |
| 2.2 Essais de l'indentation instrumentée | 172 |
| 2.3 Diffraction d'électrons rétrodiffusés (EBSD)..... | 172 |
| 2.3.1 Microscope électronique à balayage (MEB) | 173 |
| 2.3.2 Transmission Kikuchi Diffraction (TKD)..... | 173 |
| III. Modèle auto-cohérent et modélisation d'endommagement | 174 |
| 3.1 Volume Élémentaire Représentatif (VER)..... | 174 |
| 3.2 Transition d'échelles et les équations constitutives | 174 |
| 3.2.1 Echelles de l'étude..... | 174 |
| 3.2.2 Transition d'échelles..... | 174 |
| 3.3 Modélisation de l'endommagement ductile..... | 175 |
| 3.4 Paramètres déterminés..... | 175 |
| IV. Etude des aciers duplex par diffraction et confrontation au modèle | 176 |
| 4.1 Montages expérimentaux | 176 |
| 4.1.1 Mesures in situ par la diffraction des neutrons | 176 |
| 4.1.2 Mesures in situ par diffraction de rayons X (synchrotron)..... | 176 |
| 4.2 Traitement des données..... | 177 |
| 4.3 Détermination des contraintes initiales | 177 |
| 4.4 Evolution des micro-déformations dans la plage élasto-plastique | 178 |
| 4.4.1 Mesures in situ par la diffraction des neutrons | 178 |
| 4.4.2 Mesures in situ par la diffraction de rayons X (synchrotron) | 178 |
| 4.4.3 Interprétation des résultats expérimentaux et confrontation au modèle..... | 179 |
| 4.5 Etude de l'endommagement ductile..... | 180 |
| 4.5.1 Analyse temporelle de l'endommagement et test des critères de l'endommagement | 180 |
| 4.5.2 Analyse spatiale de l'endommagement..... | 182 |
| V. Test d'Indentation Instrumenté (TII) | 184 |
| 5.1 TII sur les surfaces des échantillons initiaux | 184 |

| | |
|---|------------|
| 5.2 TII sur la surface de l'échantillon après la rupture | 185 |
| 5.2.1 Répartition de la dureté et du module d'Young | 185 |
| 5.2.2 Evolution de la dureté et du module d'Young moyens le long de l'échantillon | 186 |
| 5.2.3 Evolution de la dureté vs. le module d'Young..... | 187 |
| VI. Etudes de l'alliage de titane biphasé..... | 188 |
| 6.1 Essai de traction couplé avec mesure in situ par diffraction des rayons X..... | 188 |
| 6.1.1 Méthodologies expérimentales | 188 |
| 6.1.2 Evolution des contraintes et des déformations dans chaque phase | 188 |
| 6.2 Prédiction du modèle et confrontation aux résultats expérimentaux | 189 |
| 6.3 Mesure de TKD sur la microstructure de Ti-18 | 191 |
| Conclusions générales et perspectives | 191 |

Introduction

La présente thèse est réalisée dans le but de mieux comprendre le comportement mécanique des matériaux métalliques polycristallins en grandes déformations, ainsi que le mécanisme de l'endommagement ductile. En effet, la réponse mécanique macroscopique des matériaux n'est pas seulement déterminée par le chargement appliqué à ces derniers, mais dépend aussi des propriétés et hétérogénéités mécaniques internes associés à leurs microstructures. La texture cristallographique, les contraintes résiduelles, les incompatibilités inter-grains ou inter-phases, et les propriétés mécaniques à l'échelle du réseau cristallin influencent considérablement le comportement mécanique global des matériaux à l'échelle macroscopique. De ce fait, les problématiques concernées peuvent être résumé comme suit :

1. L'influence de l'hétérogénéité des matériaux à l'échelle microscopique sur la représentation macroscopique des matériaux.
2. L'activation des systèmes de glissement lors des déformations élasto-plastiques.
3. L'interaction entre grains et phases sous sollicitation externe.
4. L'évolution du comportement mécanique aux différentes échelles au cours des grandes déformations et de l'endommagement ductile.
5. La modélisation de l'initiation d'endommagement ductile des matériaux, ainsi que la détermination des paramètres physiques liés à ce dernier.

Dans cette thèse, afin d'étudier ces questions, des aciers duplex et un alliage de titane biphasé sont sélectionnés pour leurs structures cristallines.

La méthode de diffraction a été appliquée pour sa sélectivité et la possibilité de mesure non-destructive. Cette méthode nous permet de mesurer l'évolution des propriétés mécaniques des matériaux dans le volume diffractant à l'échelle microscopique et mésoscopique au cours de la sollicitation.

En termes d'étude quantitative, le modèle numérique basé sur un algorithme auto-cohérent est employé pour comparer les données expérimentales. Les paramètres associés à la déformation élasto-plastique sont ainsi déterminés. De plus, la modélisation de l'endommagement ductile est implémentée dans le modèle auto-cohérent pour explorer le mécanisme d'initiation de l'endommagement ductile dans l'acier duplex.

Objectifs de recherche

- Détermination des contraintes de cisaillement critiques résolues (CRSS) et des paramètres d'écrouissage des systèmes de glissements des aciers duplex et de l'alliage de titane biphasé.
- Vérification du critère d'initiation d'endommagement nouvellement introduit dans le modèle auto-cohérent par comparaison aux expériences.
- Etudes temporelles et spatiales de la répartition des contraintes de phase dans la striction lors des grandes déformations, afin d'observer l'initiation d'endommagement ductile.
- Observation de l'évolution de l'hétérogénéité de la dureté et du module d'Young dans la striction.

I. Contexte de la recherche et état de l'art

Les aciers duplex et les alliages de titane biphasé sont sélectionnés comme matériaux d'étude. Le choix de ces matériaux est basé tout d'abord sur leurs vastes applications industrielles. Leurs structures cristallines variées (cc, cfc, hexagonal) sont également un critère de choix. Leurs mécanismes de déformation élasto-plastique, et d'endommagement seront ainsi étudiés.

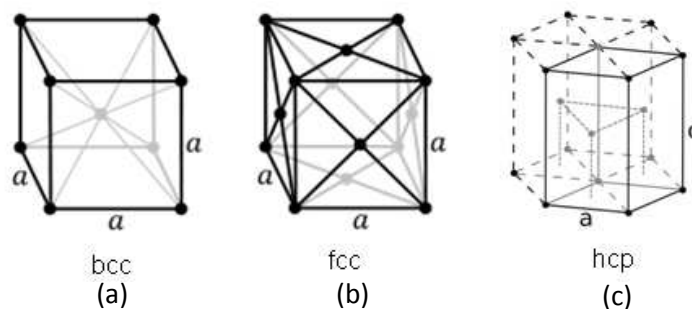


Figure F1.1. Mailles cristallines : (a) Cubique centrée ; (b) Cubique face centrée ; (c) Hexagonale.

- Dans les aciers duplex, l'austénite et la ferrite présentent une structure cristalline cubique. La ferrite (phase α) possède une maille cubique centrée **cc** (Fig. F1.1a), tandis que l'austénite (phase γ) a une maille cubique face centrée **cfc** (Fig. F1.1b). La structure de ces deux phases nous permet de comprendre le comportement mécanique des cristaux cubique, et d'observer l'interaction entre les mailles **cc** et **cfc** sous chargement externe.

- L'alliage de titane biphasé étudié consiste en une phase α ayant une maille hexagonale (Fig. F1.1c) et en une phase β qui présente une structure cc. Au travers de l'étude du titane biphasé, on peut observer l'évolution des propriétés mécaniques des mailles hexagonales ainsi que l'interaction entre la structure hexagonale et la structure cubique.

1.1 Description des aciers duplex

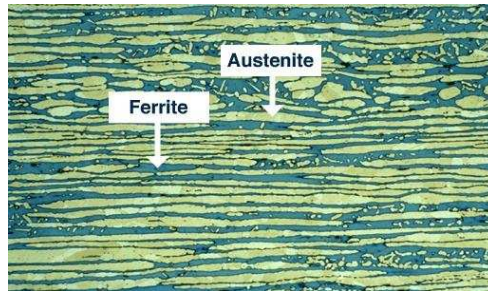


Figure F1.2 Image microscopique de l'acier duplex [DeBold 89].

Les aciers austéno-ferritiques, peuvent être appelés aciers duplex lorsque la proportion de phase entre l'austénite et la ferrite est proche de 50% - 50%. La Fig. F1.2 montre la microstructure typique des aciers duplex, la phase austénitique est présente dans la matrice de ferrite sous forme d'« îlots ». Généralement, l'acier duplex a de meilleures propriétés mécaniques que l'acier ferritique ou austénitique seul (tableau 1.1).

1.1.1 Déformation élasto-plastique et initiation de l'endommagement dans les aciers duplex

Le comportement mécanique sous traction des deux phases dans l'acier duplex a été étudié par Le Joncour et al. [Le Joncour 11] utilisant la mesure par diffraction de neutron. D'après la Fig. F1.3, quatre étapes de déformation élasto-plastique et l'initiation du processus d'endommagement peuvent être identifiées. Au cours de l'étape $E_{\alpha,\gamma}$, la ferrite et l'austénite sont déformées élastiquement. L'étape $E_{\alpha}P_{\gamma}$ correspond au début de la déformation plastique de l'austénite tandis que la ferrite continue sa déformation élastique. Les courbes d'évolution des deux phases montrent que la contrainte s'équilibre entre elles, i.e. la ferrite récupère une partie de la charge de l'austénite. Au cours de la troisième étape $P_{\alpha}P_{\gamma}$, les deux phases ont plastifiées, l'austénite a repris une partie de contrainte relâchée par la ferrite.

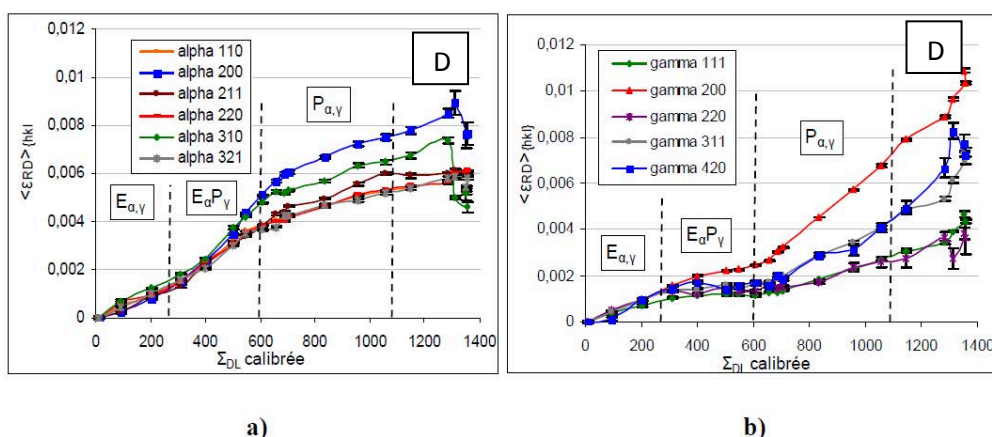


Figure F1.3 Evolution des micro-déformations des réflexions hkl au cours de la déformation élasto-plastique et de l'initiation de l'endommagement pour la ferrite (a) et pour l'austénite (b) [Le Joncour 11].

La dernière étape D indique l'initiation de l'endommagement du matériau. Une décroissance importante des micro-déformations peut être observée dans les réflexions hkl de la ferrite. Ce phénomène est associé à l'adoucissement de matériau dans la ferrite. Il semble indiquer que l'endommagement est initié dans la ferrite.

La déformation plastique se propage d'une manière plus homogène dans l'austénite et un grand nombre de lignes de glissement peuvent être observées [Joly 92], mais plus localisées dans la ferrite. Des lignes de glissement sont fréquemment trouvées à côté des joints de grain, considérés comme la source de dislocations [El Bartali 07].

A la fin de la déformation plastique, une décohésion interfaciale s'initie, puis des clivages se forment dans la ferrite le long des lignes de glissement, ce qui conduit à l'adoucissement de cette dernière. Les défauts vont ensuite coalescer entre eux. Finalement, la rupture ductile se produit à cause de la coalescence de toutes les micro-fissures au sein du matériau. Veuillez reporter à la section 1.1.3 de la thèse l'explication plus précise.

1.1.2 Caractérisation des aciers duplex étudiés

Deux types d'aciers duplex, l'UR45N et l'UR52N, ont été étudiés lors d'essais de traction. Les deux alliages bruts ont été coulés en continu puis laminés à chaud. Les échantillons ont été préparés à partir des deux aciers duplex ayant subis différents traitements thermiques.

Des cartographies EBSD ont été réalisées pour identifier les dans l'UR45N. Comme montré par Fig. F1.4, les « îlots » de l'austénite se divisent en cristallites plus fines avec différentes orientations, tandis que les grains de la phase ferritique possèdent presque la même orientation cristalline, due aux processus de laminage.

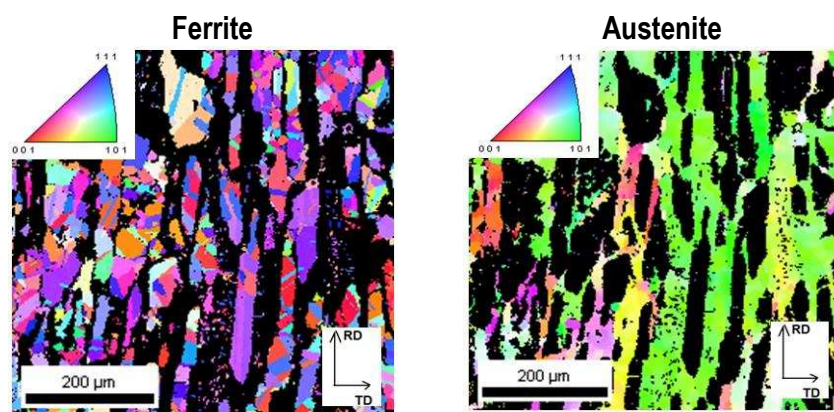


Figure F1.4 Microstructure de l'acier UR45N déterminée par la cartographie EBSD. Les orientations des grains dans la phase sélectionnée sont en couleur, tandis que les phases non sélectionnées sont en noir [Le Joncour 10].

Ensuite, les fonctions de distributions des orientations [Bunge 82] ont été déterminées pour chaque phase dans les deux aciers. Une anisotropie des orientations a été trouvée pour les deux phases dans les deux matériaux, et la texture est particulièrement prononcée dans la ferrite, comme montré par les Fig. F1.5 a, b, c et d.

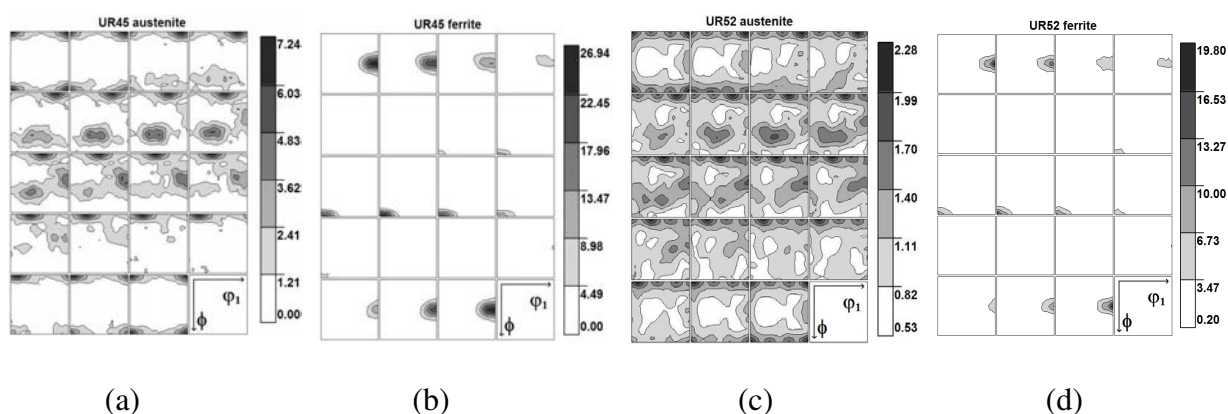


Figure F1.5 Fonction de distribution des orientations pour la phase ferritique et austénitique dans l'acier UR45N (a et b) ainsi que celles dans UR52N (c et d).

1.2 Description des alliages de titane biphasé

Les alliages de titane sont largement utilisés dans l'industrie aéronautique et aérospatiale grâce à leurs bonnes résistances mécaniques, leur ductilité et leur masse volumique relativement faible. Les alliages de titane biphasé présentent deux microstructures typiques: la microstructure lamellaire et bimodale (Fig. F1.6a et b). Pour la microstructure lamellaire, la phase α est enrobée dans une matrice de phase β . Pour la microstructure bimodale, deux

morphologies peuvent être identifiées pour la phase α : la primaire α_p , sous forme globulaire, et la aciculaire α_s secondaire.

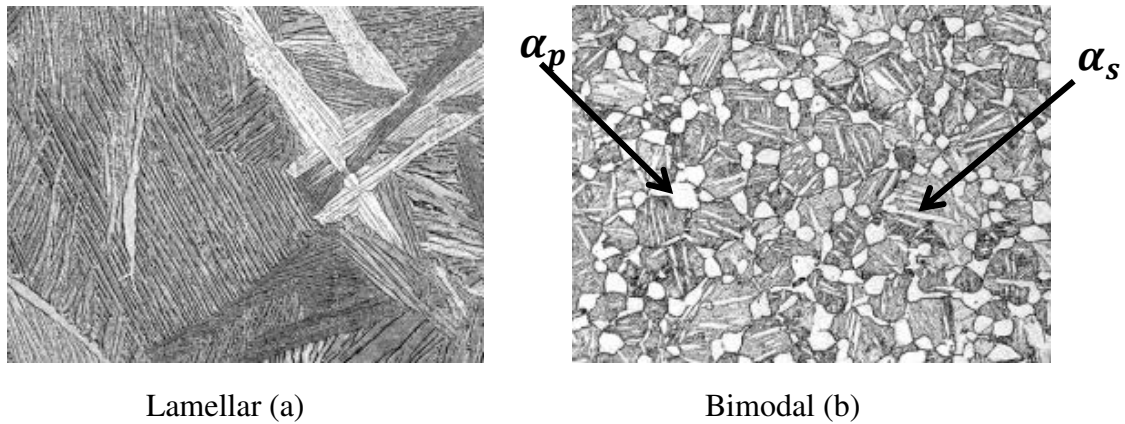


Figure F1.6 Microstructures typiques des alliages de titane biphasés : (a) lamellaire phase α enrobée dans la matrice de phase β ; (b) bimodale microstructure la primaire α_p sous forme globulaire et la aciculaire α_s secondaire enrobées dans la matrice de phase β .

1.2.1 Déformation élasto-plastique et endommagement ductile dans les titanes biphasés

La déformation plastique et sa propagation dans le titane biphasé sont fortement liées à sa structure cristalline. [Greenfield 72] a montré que les lignes de glissement peuvent passer de la phase α à la phase β . D'après les études précédentes [Patridge 67, Bridier 05, Raabe 07, Wang 10, Beyerlein 10], le système de glissement basal et prismatique ont été identifiés comme les modes de glissement principaux dans la phase α_p primaire. Le système prismatique $\langle a \rangle$ est probablement le plus activé à température ambiante. De plus, dans le titane biphasé, les phases α_s et β obéissent généralement à la relation d'orientation de Burgers [Burgers 34], i.e. le plan et la direction de glissement $\{0001\}$ et $\langle 1120 \rangle$ de phase α sont respectivement parallèles à $\{110\}$ et $\langle 111 \rangle$ de phase β ($\{0001\}_\alpha \parallel \{110\}_\beta$ and $\langle 1120 \rangle_\alpha \parallel \langle 111 \rangle_\beta$) [Bhattacharyya 03, Jun 16]. Et une interface semi-cohérent à faible énergie existe entre les phases [Furuhara 95]. Au début de la déformation plastic, les dislocations ont tendance à pénétrer par la frontière inter-phase semi-cohérente.

Lors de l'endommagement ductile du titane biphasé, il est observé que les micro-fissures ont été nucléées aux interfaces des phases [Greenfield 72]. Dans les alliages de titane, il est constaté que le nombre de micro-fissures s'accroît avec l'augmentation de la triaxialité de contrainte. Comparé aux mailles cubiques, les contraintes locales peuvent être plus élevées pour la structure hexagonale. Cette augmentation de contrainte pourrait aboutir à la coalescence de dislocation [Stroh 57], qui à son tour conduit à l'initiation de micro-fissures.

1.2.2 Caractérisation du TIMETAL-18

Des essais de traction ont été effectués sur des éprouvettes de TIMETAL-18 (Ti-18), et mesurés in situ par diffraction de rayon X. Les données expérimentales ont ensuite été confrontées à un modèle auto-cohérent élasto-plastique, plusieurs paramètres liés à la déformation élasto-plastique ont ainsi déterminés pour les deux phases α et β .

D'après l'observation microscopique, une microstructure typique bimodale a été constatée sur Ti-18. L'estimation de la fraction volumique des deux phases a été réalisée pour déterminer la proportion des phases. Les estimations se sont effectuées sur des images microscopiques des sections dans les directions radiales et axiales. Les fractions volumiques de la phase α et de la phase β sont montrés dans le tableau F1.1.

| Section | Fraction surfacique α_p | Fraction surfacique α_s dans la matrice de β | Fraction surfacique totale de phase α |
|---------|--------------------------------|--|---|
| Radiale | 18.61% | 34.96% | 47.06% |
| Axiale | 24.49% | 23.86% | 42.5% |

Tableau F1.1 Les fractions surfaciques de phase α dans la matrice de phase β .

D'après les fonctions de distribution des orientations de la phase α (Fig. F1.8a) et de la phase β (Fig. F1.8b), il existe des orientations préférentielles importantes pour toutes les deux phases, surtout pour la phase β .

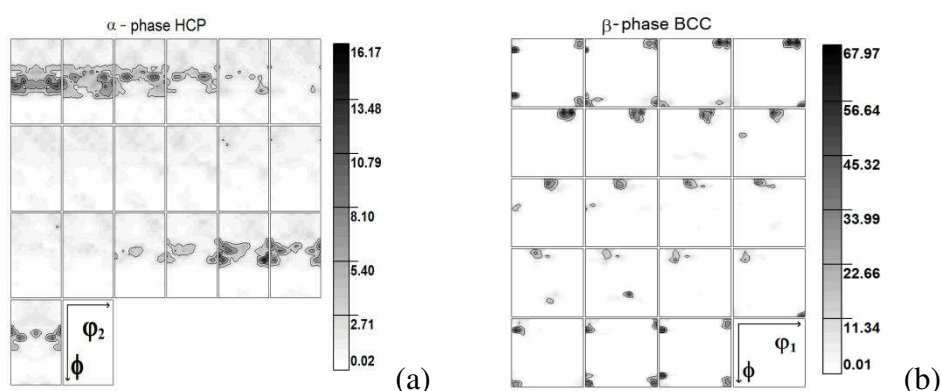


Figure F1.7 Les fonctions de distribution des orientations de la phase α (a) et de la phase β (b).

II. Mesure expérimentales et techniques

Plusieurs techniques expérimentales traditionnelles ou avancées ont été impliquées dans le travail de recherche présenté par cette thèse. Le but est de découvrir les mécanismes de déformation élasto-plastique et d'endommagement ductile au sein des matériaux polycristallins et polyphasés.

2.1 Mesure par diffraction

La méthode de diffraction est considérée comme un outil puissant pour l'inspection non-destructive. Cette méthode est fréquemment utilisée pour analyser le comportement mécanique des matériaux polycristallins à l'échelle des grains et des phases grâce à sa sélectivité. La méthode de diffraction est basée sur la loi de Bragg (Eq. F2.1), qui permet d'établir un lien entre la longueur d'onde λ , l'angle d'incident θ et la distance interréticulaire d_{hkl} .

$$2d_{hkl}\sin\theta = n\lambda \quad \text{Eq. F2.1}$$

Cette relation permet de mesurer la déformation élastique au niveau des mailles cristallines à l'intérieur du volume irradié. Elle permet aussi de déterminer la contrainte localisée dans chaque phase [Gloaguen 02, Baczmański04a, Le Joncour 10].

Les mesures par diffraction peuvent être effectuées en mode de « réflexion » et de « transmission » (l'explication des deux modes dans la section 2.1.3 de thèse). En mode « réflexion », le faisceau incident et le faisceau diffracté sont localisés du même côté de la surface de l'échantillon. Dans le cas de mode « réflexion », le faisceau incident ne peut pénétrer qu'une courte profondeur dans l'échantillon. Le mode « réflexion » est souvent utilisée avec un rayonnement X de faible énergie aux diffractomètre de laboratoire.

Dans le cas du mode « transmission », le faisceau incident traverse l'échantillon et le signal du faisceau diffracté est capturé de l'autre côté de ce dernier. L'avantage du mode de « transmission » est de permettre d'obtenir des informations en volume plutôt qu'en surface, mais ce mode exige un rayonnement d'énergie extrêmement élevée.

2.1.1 Détermination des déformations cristallines par méthode de diffraction

Le principe de la détermination des déformations cristallines se base sur la mesure des distances interréticulaires $\langle d_{\vec{n}}(\phi, \psi) \rangle_{\{hkl\}}$ des plans hkl le long du vecteur de diffraction \vec{n} .

La déformations cristalline $\langle \varepsilon_{\bar{n}}(\phi, \psi) \rangle_{\{hkl\}}$ d'un plan hkl est ensuite calculée par l'équation Eq. F2.2 :

$$\langle \varepsilon_{\bar{n}}(\phi, \psi) \rangle_{\{hkl\}} = \frac{\langle d_{\bar{n}}(\phi, \psi) \rangle_{\{hkl\}} - \langle d_{\bar{n}}^0(\phi, \psi) \rangle_{\{hkl\}}}{\langle d_{\bar{n}}^0(\phi, \psi) \rangle_{\{hkl\}}} \quad \text{Eq. F2. 2}$$

d'où $\langle d_{\bar{n}}^0(\phi, \psi) \rangle_{\{hkl\}}$ est la distance interréticulaire d'un plan hkl sans déformation, les crochets $\langle \rangle_{\{hkl\}}$ représente la valeur moyenne sur le volume mesuré.

2.1.2 Détermination de l'état de contrainte par méthode de diffraction

A cause de la forte dissipation d'énergie et de l'absorption élevée du rayon X, les mesures de contraintes sont normalement effectuées en mode « réflexion » sur des diffractomètres de laboratoire. Trois référentiels sont ainsi établit, il s'agit du référentiel de l'échantillon, du référentiel du laboratoire et du référentiel du goniomètre. L'analyse de l'état de contrainte est basée sur la mesure des distances interréticulaires en prenant différentes directions des vecteurs de diffraction [Noyan 87, Hauk 97, Inal 99, Welzel 05, Baczmański 05]. La méthode standard $\sin^2\psi$, la méthode multi-réflexion grazing incidence et trois modèles d'interaction grains-milieu (Voigt, Reuss, Eshelby-Kröner) sont appliqués dans ce travail (Veuillez voir la section 2.1.4 de la thèse complète les informations détaillées).

2.2 Essais de l'indentation instrumentée

Des essais d'indentation instrumenté (ITT) ont été réalisés comme méthode complémentaire aux mesures de diffraction, afin d'étudier les propriétés mécaniques des matériaux, telles que le module d'Young et la dureté [Olivier 92] dans ce travail. Une pointe de type Berkovich a été utilisé. Le chargement imposé et le déplacement de la pointe sont enregistrés pendant tout le processus d'indentation. A chaque indentation, une courbe de charge-déplacement de la pointe (appelé courbe P-h) est tracée, ensuite les propriétés en sont déduites. L'indentation instrumentée est employée ici pour observer l'évolution de la dureté et le module d'élasticité de l'acier duplex le long de la striction.

2.3 Diffraction d'électrons rétrodiffusés (EBSD)

La diffraction d'électrons rétrodiffusés, en anglais Electron BackScatter Diffraction (EBSD), est une technique cristallographique permettant de mesurer la microstructure et l'orientation cristallographique des matériaux cristallins. La technique EBSD peut être utilisée

pour déterminer la texture cristallographique (ou l'orientation préférentielle) des matériaux cristallins et appliquée à la cartographie d'orientation cristalline [Randle 00].

Expérimentalement, un système EBSD consiste en un Microscope Electronique à Balayage (MEB) équipé d'un détecteur d'EBSD. Le détecteur d'EBSD comporte au moins un écran phosphorescent, un objectif compact, et une caméra CCD à faible luminosité [Winkelmann 07].

Lorsque le faisceau primaire interagit avec la maille cristalline, les faisceaux des électrons rétrodiffusés s'accroissent ou s'atténuent dans les directions qui induisent les interférences constructives ou destructives. Un diagramme de diffraction d'électrons rétrodiffusés (Electron BackScatter diffraction Pattern EBSP) se forme lorsque plusieurs différents plans cristallins diffractent les électrons et forment les lignes (bandes) de Kikuchi. Chaque bande de Kikuchi peut être indexée individuellement par les indices de Miller $\{hkl\}$ aux plans cristallins qui l'ont formé.

2.3.1 Microscope électronique à balayage (MEB)

Le microscope électronique à balayage (MEB) est un type de microscope électronique qui produit des images microscopiques de l'échantillon en appliquant un faisceau d'électron focalisé. L'avantage principal de cette technique est la possibilité d'obtenir des images microscopiques à haute résolution, ce qui nous permet d'observer très précisément la morphologie de la surface de l'échantillon. Cette technique a été utilisée dans cette thèse dans le but d'identifier les échantillons initiaux et d'observer la surface de rupture.

2.3.2 Transmission Kikuchi Diffraction (TKD)

La Transmission Kikuchi Diffraction (TKD) est une technique récemment développée [Trimby 12]. Cette technique est basée sur du matériel et des logiciels actuels de l'EBSD, et permet d'avoir une résolution spatiale plus élevée. La technique TKD présente des avantages par rapport à la technique d'EBSD conventionnelle :

- Résolution spatiale élevée (5-10nm).
- L'échantillon est placé horizontalement, évitant ainsi la correction d'inclinaison.
- Bon contraste d'image.
- Acquisition des données à grande vitesse.

La TKD a été utilisée à fin de mémoire pour étudier la variation de microstructure des phases dans Ti-18.

III. Modèle auto-cohérent et modélisation d'endommagement

Les modèles numériques sont largement utilisés dans l'analyse du comportement mécanique de matériaux polycristallins hétérogènes. Ils permettent de déterminer quantitativement les propriétés des matériaux de manière plus efficace et permettent d'obtenir les résultats plus précis.

3.1 Volume Élémentaire Représentatif (VER)

Un VER est défini comme le sous-volume d'un matériau homogène le plus petit ayant une taille suffisante pour représenter toutes les informations statistiques nécessaires de la microstructure du matériau. Le VER devrait pouvoir caractériser la distribution et la morphologie des propriétés hétérogènes des matériaux étudiés [Besson 01]. Pour définir une représentation élémentaire du milieu continu, les équations constructives doivent satisfaire les exigences des structures de matériaux à tous les niveaux.

3.2 Transition d'échelles et les équations constitutives

3.2.1 Echelles de l'étude

L'échelle macroscopique est l'échelle du VER, elle correspond physiquement à l'agrégat de grains ou polycristal. Le comportement global des matériaux est modélisé à ce niveau d'échelle.

L'échelle mésoscopique est l'échelle intermédiaire correspondant au comportement des grains ou des monocristaux. A cette échelle, l'évolution des contraintes et des micro-déformations des polycristaux liées à l'interaction inter-cristal est calculée. Les calculs sont effectués en tenant compte de l'anisotropie du grain et du milieu. Les rotations des mailles cristallines menant à la variation de texture sont également prises en compte.

L'échelle microscopique est l'échelle la plus fine étudiée ici, c'est à cette dernière que les mécanismes de plasticité, y compris l'activation des systèmes de glissement, l'interaction entre les systèmes et l'écrouissage, sont modélisés.

3.2.2 Transition d'échelles

Le processus de transition d'échelles est essentiel pour les modèles multi-échelles auto-cohérents. Il est divisée en trois étapes principales, que sont respectivement : la localisation, la modélisation du comportement local et l'homogénéisation.

La localisation est appliquée pour transformer les grandeurs physiques à partir de l'échelle macroscopique (VER) à l'échelle mésoscopique (grains) puis à l'échelle microscopique (système de glissement). Les comportements et l'interaction entre les grains ainsi que entre les systèmes de glissement sont calculés successivement aux échelles mésoscopique et microscopique.

L'homogénéisation est un processus de calcul du comportement macroscopique à partir de résultats des échelles plus fines. Cette étape est souvent réalisée par le calcul des moyennes arithmétique pondérées des grandeurs physiques sur les échelles inférieures, jusqu'à l'obtention des grandeurs physiques macroscopiques correspondantes.

Les équations constructives sont présentées dans la section 3.4 de la thèse.

3.3 Modélisation de l'endommagement ductile

La modélisation de l'endommagement ductile a été proposée dans le modèle auto-cohérent utilisé dans le travail présent par Panicaud et al. [Panicaud 11]. Le processus d'endommagement ductile est modélisé en se basant sur l'hypothèse d'équivalence en l'énergie totale [Saanouni 96] à l'échelle des grains.

Si l'endommagement ductile est pris en compte, le critère de plasticité doit également être modifié pour intégrer son effet. La modélisation d'écrouissage non linéaire est également nécessaire dans le cas des grandes déformations. La loi de Voce [Tomé 84] est employée dans le calcul. Les équations constructives et les critères d'endommagement sont montrés dans la section 3.5 de la thèse.

3.4 Paramètres déterminés

Le modèle présenté est proposé pour la prédiction de l'évolution du comportement mécanique des matériaux sous traction à trois échelles différentes. Les valeurs des paramètres liés à la déformation plastique et au processus de l'endommagement peuvent être déterminer, tels que τ_{c0}^s , τ_{c0}^{ph} , τ_1^{ph} , θ_0^{ph} , θ_1^{ph} pour la déformation plastique et ε_0^{ph} , n^{ph} , ξ^{ph} pour l'endommagement ductile. Veuillez voir la section Les paramètres des autres critères d'endommagement dans la section 4.5 de la thèse.

IV. Etude des aciers duplex par diffraction et confrontation au modèle

L'acier duplex est le matériau principal étudié dans cette thèse. Les essais de traction couplés avec la mesure in situ de diffraction des neutrons ou des rayons X (synchrotron) ont été réalisés afin d'observer le comportement élasto-plastique des phases et leurs réponses mécaniques lors de l'initiation de l'endommagement ductile.

Les résultats des simulations par le modèle auto-cohérent ont été confrontés aux résultats expérimentaux en ajustant la valeur des paramètres physiques. Ces paramètres sont associés aux propriétés intrinsèques des phases. Il s'agit de la contrainte critique de cisaillement (CRSS) et les paramètres liés à l'écrouissage et au processus d'endommagement.

4.1 Montages expérimentaux

4.1.1 Mesures in situ par la diffraction des neutrons

La mesure des micro-déformations par diffraction des neutrons a été effectuée par Le Joncour et al. [Le Joncour 10, Le Joncour 11, Baczmański 16]. Elle se base sur le principe de « Temps de vol » et a été réalisée sur ENGIN-X à la source de neutrons, du laboratoire ISIS spallation, Oxford, Royaume-Uni. L'installation expérimentale consiste en une source de neutrons et deux détecteurs. Les deux détecteurs sont centrés sur l'angle de diffraction horizontal ($2\theta = \pm 90^\circ$), comme montré par Fig. F4.1.

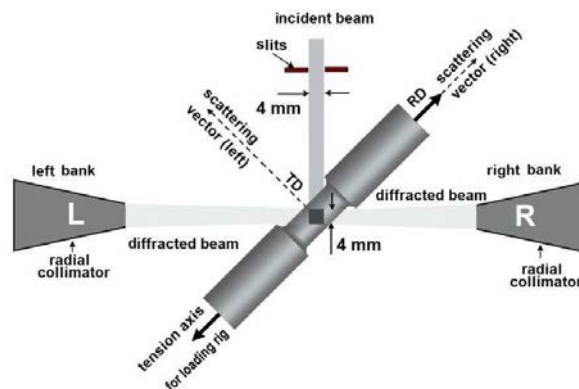


Figure F4.1 Illustration de l'installation expérimentale et l'orientation de l'échantillon par rapport aux détecteurs.

4.1.2 Mesures in situ par diffraction de rayons X (synchrotron)

Les mesures in situ par la diffraction de rayons X ont été réalisées à l'installation européenne de rayonnement synchrotron (ESRF) à Grenoble. La ligne de faisceau ID15B a été utilisée pour effectuer les mesures de diffraction en mode de transmission (Fig. F4.2a). Un

rayonnement synchrotron monochromatique (longueur d'onde $\lambda = 0.14256 \text{ \AA}$, l'énergie de faisceau incident 87KeV) a été appliqué comme le faisceau incident.

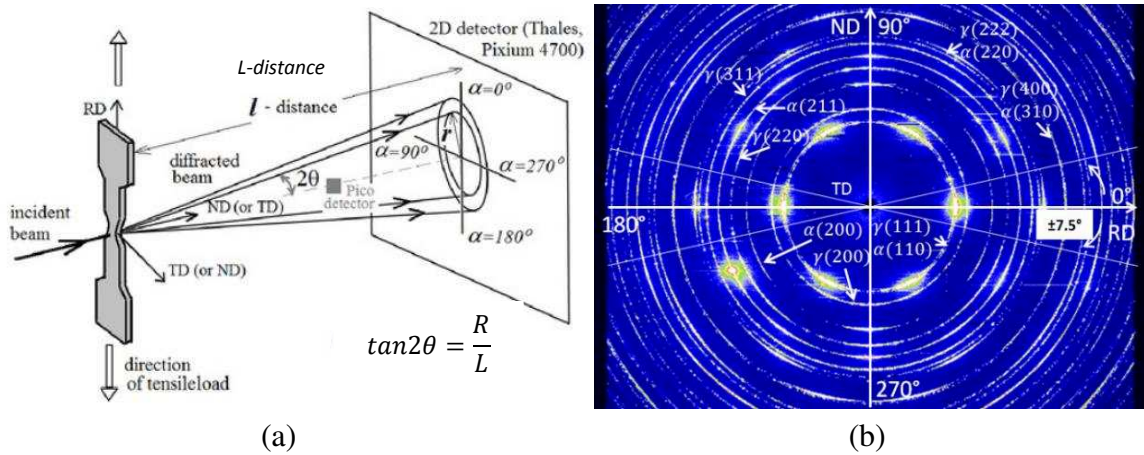


Figure F4.2 (a) La mesure de diffraction de rayonnement synchrotron en mode de transmission sur la ligne de faisceau ID15B. (b) Exemple du diagramme de diffraction en 2D obtenu par le détecteur.

4.2 Traitement des données

Les données mesurées par diffraction de neutron sont traitées par un programme codé par Le Joncour [Le Joncour 11] sous Mathematica®. Ce programme effectue une régression à base de fonction de Pseudo-Voigt.

Les diagrammes de diffraction bidimensionnels obtenus par la diffraction de rayon X sont traités premièrement par le logiciel FIT2D, qui permet de convertir les diagrammes de diffraction 2D aux spectres de diffraction unidimensionnel. Ensuite, les spectres 1D ont été fittés par le logiciel MULTIFIT en utilisant également une fonction Pseudo-Voigt.

4.3 Détermination des contraintes initiales

Les contraintes initiales, dues au processus de fabrication et/ou au traitement thermique, peuvent être déterminée avant les essais de traction. Pour la détermination des contraintes initiales, les distances interréticulaires $\langle d \rangle_{\{hkl\}}$ des plans hkl ont été mesurées dans différentes orientations, puis le modèle de Kröner-Eshelby a été utilisé pour modéliser l'interaction entre les grains. Les contraintes initiales sont ainsi déterminées dans différentes directions (RD, ND et TD) pour les différents échantillons et sont présentées dans le tableau F4.1.

| | | Neutron diffraction (ISIS) | | | Synchrotron (ESRF) |
|---------------------|-----------|----------------------------|-----------------|------------------|--------------------|
| | | UR45N (Trempe) | UR45N (Vieilli) | UR52N (Trempe) | UR45N (Vieilli) |
| σ_{RD} (MPa) | austénite | 61 ± 12 | 87 ± 9 | 85 ± 10 | 134 ± 15 |
| | ferrite | -50 ± 15 | -57 ± 11 | -24 ± 15 | -155 ± 19 |
| σ_{TD} (MPa) | austénite | 59 ± 12 | -7 ± 9 | 50 ± 10 | 84 ± 15 |
| | ferrite | -29 ± 15 | -19 ± 12 | -122 ± 15 | -44 ± 19 |
| σ_{ND} (MPa) | austénite | -120 ± 12 | -80 ± 9 | -135 ± 10 | -218 ± 15 |
| | ferrite | 79 ± 15 | 76 ± 9 | 144 ± 15 | 199 ± 18 |

Tableau F4.1 Contraintes initiales déterminées pour différents échantillons et dans différentes directions (RD, ND et TD).

4.4 Evolution des micro-déformations dans la plage élasto-plastique

Des mesures in situ par diffraction (neutrons ou synchrotron) ont été effectuées au cours des essais de traction jusqu'à la rupture des échantillons. Afin d'observer l'évolution des micro-déformations dans une direction donnée, les distances interréticulaires ont été déterminé pour différentes réflexions hkl appartenant à chaque phase, suivant le vecteur de diffraction parallèle à la direction désirée.

4.4.1 Mesures in situ par la diffraction des neutrons

Les mesures de diffraction de neutrons ont été effectuées pour l'acier UR45N, UR45N vieilli et UR52Ntrempé. Les échantillons ont été soumis à des essais de traction, les échantillons d'UR45N vieilli ont également été utilisés pour un essai de traction et un essai de compression.

D'après les résultats expérimentaux, trois seuils Γ , Ω and Λ peuvent d'être identifié sur les courbes d'évolution des déformations élastiques mésoscopique. Elles correspondent respectivement à la limite d'élasticité de l'austénite, à la limite d'élasticité de la ferrite et à l'initiation de l'endommagement ductile (Fig. F4.3).

4.4.2 Mesures in situ par la diffraction de rayons X (synchrotron)

Pour les mesures par diffraction de rayons X, les essais de traction ont été effectués sur l'UR45N vieilli. Des comportements similaires à ceux mesurés par la diffraction de neutrons ont été constatés. Les résultats expérimentaux plus précis sont présentés dans la section 4.4 de la thèse.

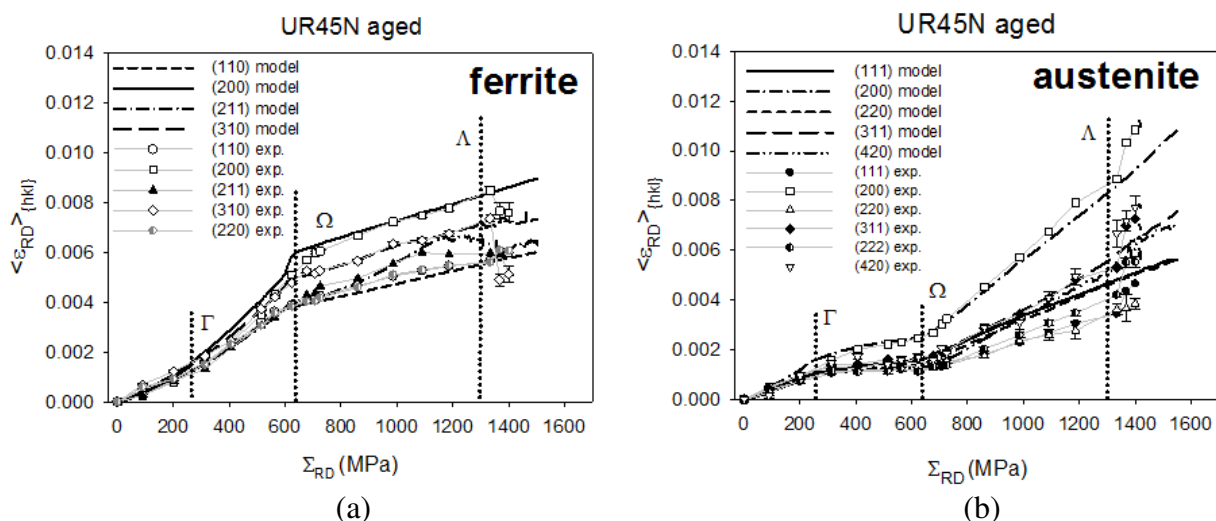


Figure F4.3 Les résultats expérimentaux des micro-déformations de maille de différentes réflexions hkl de la ferrite (a) et de l'austénite (b) dans la direction de traction confrontés à la prédiction du modèle auto-cohérent.

4.4.3 Interprétation des résultats expérimentaux et confrontation au modèle

Le modèle auto-cohérent a été utilisé pour comparer aux résultats expérimentaux dans la plage des déformations élasto-plastique, ainsi que pour déterminer les paramètres physiques associés. Pour effectuer le calcul du modèle, les orientations initiales des cristallites ont été définies en fonction de la texture du matériau, les constantes élastiques monocristallines et les contraintes initiales prises comme les données d'entrée. La simulation a été réalisée avec 20.000 inclusions sphériques représentant les grains appartenant à la ferrite (10.000) et à l'austénite (10.000).

| | | Diffraction de neutron (ISIS) | | | Synchrotron (ESRF) |
|-----------------------|-----------|-------------------------------|-----------------|----------------|--------------------|
| Materiaux | | UR45N (Trempe) | UR45N (Vieilli) | | UR45N (Vieilli) |
| Mode de déformation | | traction | traction | compression | traction |
| τ_0^{ph} (MPa) | austénite | 140 | 140 | 120 | 180 |
| | ferrite | 220 | 350 | 360 | 290 |
| θ_0^{ph} (MPa) | austénite | 225 | 225 | 225 | 225 |
| | ferrite | 110 | 110 | 110 | 110 |
| τ_1^{ph} (MPa) | austénite | Non déterminée | 280 | Non déterminée | 280 |
| | ferrite | | 150 | | 140 |
| θ_1^{ph} (MPa) | austénite | Non déterminée | 6 | Non déterminée | 6 |
| | ferrite | | 5 | | 3 |

Tableau F4.2 Paramètres liés à la déformation plastique des aciers duplex déterminés au cours des essais de traction et de compression.

Comme mentionné précédemment, le seuil Γ correspond à la limite élastique de l'austénite, cela permet de déterminer sa contrainte de cisaillement critique initiale (CRSS) τ_0^{ph} liée au

début de la plasticité de l'austénite. Le deuxième seuil Ω permet de déterminer le CRSS initiale de la ferrite. Les courbes de contrainte vs. déplacement macroscopiques expérimentales ont également été confrontées au modèle, permettant de déterminer les paramètres de loi de Voce τ_1^{ph} , θ_0^{ph} and θ_1^{ph} , liées à l'écrouissage des matériaux. Les valeurs des paramètres déterminés sont présentées dans le tableau F4.2.

4.5 Etude de l'endommagement ductile

Le processus de l'endommagement ductile est étudié au cours des grandes déformations.

Une analyse temporelle est effectuée à partir des données mesurées par diffraction de neutrons. Pour la première fois, des balayages par rayonnement synchrotron en mode de transmission sont réalisés le long de la striction des échantillons de l'UR45N vieilli, dans le but d'examiner le comportement mécanique des phases lors de l'initiation de l'endommagement ductile.

4.5.1 Analyse temporelle de l'endommagement et test des critères de l'endommagement

Une diminution significative des micro-déformations est trouvée pour les réflexions hkl de la phase ferritique à la fin de l'essai pour l'échantillon UR45N (cf. Fig. F4.5a). En parallèle, une augmentation des micro-déformations se produit dans l'austénite (cf. Fig. F4.3b). Ce phénomène indique une relaxation de contrainte dans la ferrite, et cette relaxation est compensée simultanément par l'augmentation de la contrainte dans la phase austénitique. Cette évolution de contrainte dans les deux phases sera comparée à une nouvelle version du modèle auto-cohérent, incluant la modélisation de l'emmagement ductile.

La modélisation d'évolution d'endommagement implémentée dans le modèle auto-cohérent a été appliquée pour expliquer le comportement mécanique au niveau des mailles des deux phases dans l'acier duplex après le seuil A (cf. Fig. F4.3). La phase ferritique est considérée comme la première à s'endommager.

Trois différents critères d'endommagement sont testés. Le critère d'équivalence en déformation est basé sur la déformation granulaire équivalente, calculée à partir du tenseur de déformation élasto-plastique des grains tout au long du processus de déformation (cf. Eq. F4.1).

$$\dot{d}^g = \xi^{ph} (\varepsilon_{eq}^g - \varepsilon_0^{ph})_+^{n^{ph}} (\dot{\varepsilon}_{eq}^g)_+ \quad \text{Eq. F4.1}$$

d'où ε_0^{ph} , n^{ph} , ξ^{ph} sont les paramètres dépendant de la phase, et ε_{eq}^g est la seconde invariant du tenseur de déformation d'un grain g (Veuillez voir la section 3.5.2.2 l'expression complète du critère).

Le critère de contrainte équivalente est paramétré par la contrainte équivalente de Von Mises. L'expression du critère est montrée par Eq. F4.2.

$$\dot{d}^g = \xi^{ph} (\sigma_{eq}^g - \sigma_0^{ph})_+^{n^{ph}} (\dot{\sigma}_{eq}^g)_+ \quad \text{Eq. F4.2}$$

Mais par ce critère, la distribution des contraintes entre grains de la ferrite n'est pas bien prédite (cf. section 4.5.2 de la thèse).

Pour le critère d'endommagement basé sur l'énergie totale (Eq. F4.3), la dépendance linéaire entre la déformation moyenne sur les phases $\langle \varepsilon_{RD} \rangle_{\text{mean}}^{\text{aus+fer}}$ et la contrainte macroscopique imposée Σ_{RD} a été déterminée (cf. section 4.5.3 de la thèse).

$$\dot{d}^g = \xi^{ph} (w_{tot}^g - w_0^{ph})_+^{n^{ph}} (\dot{w}_{tot}^g)_+ \quad \text{Eq. F4.3}$$

Les résultats de l'identification des paramètres de prédiction avec différents critères d'endommagement sont montrés dans le tableau F4.3.

| Critère d'endommagement | Phase | Paramètres | Valeurs |
|----------------------------|---------|----------------------|-------------------|
| Déformation équivalente | Ferrite | ε_0^{ph} | 0.8 |
| | | n^{ph} | 0 |
| | | ξ^{ph} | 0.2 |
| Contrainte équivalente | | σ_0^{ph} | 1650 (MPa) |
| | | n^{ph} | 0 |
| | | ξ^{ph} | 150 (MPa) |
| Energie totale | | w_0^{ph} | 400.e+06 (J/m³) |
| | | n^{ph} | 0 |
| | | ξ^{ph} | 5500. e+06 (J/m³) |

Tableau F4.3 Valeurs des paramètres réglables liés au processus de l'endommagement de ferrite en utilisant différents critère d'endommagement.

Parmi les 3 critères, le critère d'équivalence en déformation est celui pour lequel les meilleures prédictions d'endommagement sont obtenues. Les résultats de prédiction du critère de l'énergie totale sont moins coïncidents avec ceux expérimentaux, mais la tendance d'évolution est également bien prédite. Les résultats de prédiction des deux critères indiquent que l'accumulation des déformations des grains et l'histoire des déformations des grains, y

compris la variation de leurs orientations, sont très importantes pour l'initiation d'endommagement.

4.5.2 Analyse spatiale de l'endommagement

Des mesures de diffraction par synchrotron ont été appliquées pour balayer les micro-déformations dans la zone de striction lors des grandes déformations des échantillons de l'UR45N vieilli. Trois mesures de balayage (A, B et C) ont été effectuées successivement en fonction du niveau de striction (voir la figure F4.4, A : initiation de striction, B : évolution de striction, C : striction prononcée avant la rupture)

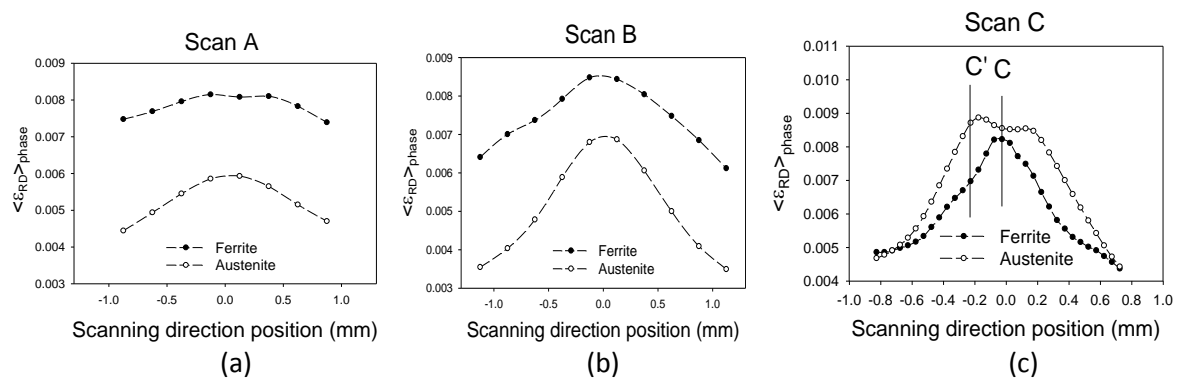


Figure F4.4 Evolutions des déformations des phases le long des balayages A (a), B (b) et C (c) en fonction de la position sur les strictions.

Les évolutions des déformations des phases le long des trois balayages sont présentées par la Fig. F4.4. Dans le cas des strictions non prononcée (Scan A et Scan B), les déformations de la ferrite sont plus importantes que celles de l'austénite. Au centre de la striction, les déformations des deux phases s'augmentent plus rapidement. Ce phénomène peut être expliqué par la concentration de contrainte élevée au centre de la striction, et on peut observer que les déformations de la ferrite augmentent plus rapidement que celle de l'austénite.

Un phénomène intéressant se produit en fin d'essai (scan C, Fig. F4.4c). Les déformations des deux phases se rapprochent au centre de la striction (position C), mais dans ses zones adjacentes (position C'), une inversion significative des déformations des phases se produit, la déformation de l'austénite est plus élevée que celle de ferrite. Ce phénomène implique probablement la transition de charge que l'on a observée précédemment par la diffraction de neutrons (cf. section 4.5 de la thèse). Cette transition de charge peut être expliquée par le processus d'endommagement, qui provoquerait une perte de résistance de la ferrite.

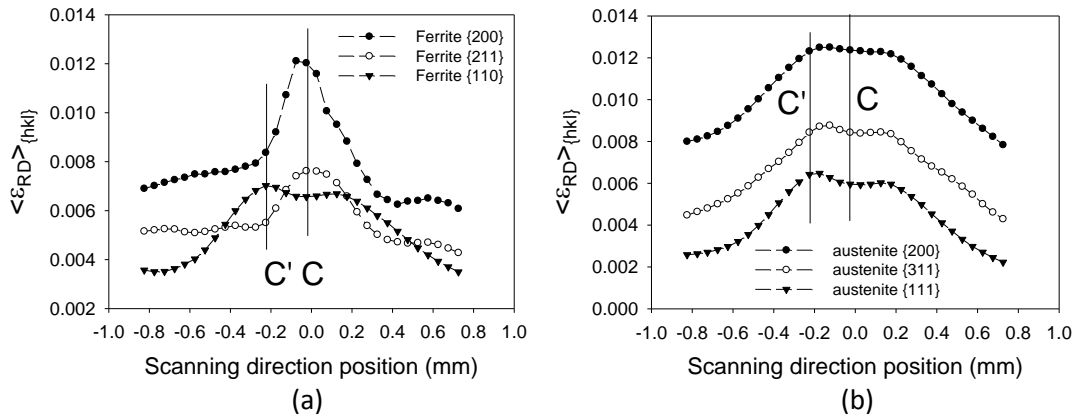


Figure F4.5 Evolutions des micro-deformations de maille des différentes réflexions hkl appartenant à la ferrite (a) et à l'austénite (b) le long de la striction C.

La Fig. F4.5 montre les évolutions des micro-deformations de maille des différentes réflexions hkl. Ces évolutions confirment l'observation précédente que les grains de ferrite qui contribuent aux réflexions 211 et 200 ont un comportement différent des autres. Ceci pourrait à nouveau être expliqué par l'endommagement dans ces groupes de grains. La relaxation de contrainte est localisée dans les grains endommagés, et entraîne une transition de charge vers les autres grains des deux phases. Notons également que, la transition de charge dépend de la position spatiale le long de la striction.

Afin d'étudier la contribution de la géométrie de striction à l'évolution de la contrainte, une simulation MEF simple est réalisée en utilisant le logiciel Abaqus 6.13. Un pas implicite dynamique avec une période de 100 secondes est appliqué. Une pression homogène uniforme de $P = 80\text{MPa}$ est imposée sur les deux extrémités de l'échantillon. Les constantes élastiques du matériau utilisées pour la prédiction du modèle auto-cohérent sont affectées au modèle 3D. La géométrie du modèle 3D a été estimée à partir de la mesure des échantillons réels. Notons que la simulation de MEF s'est effectuée uniquement pour un comportement élastique du matériau.

Les Fig. F4.6 montrent la distribution et l'évolution de la contrainte équivalente de von Mises dans la zone de striction sous traction. La Fig. F4.6b montre que la contrainte équivalente de von Mises est distribuée qualitativement de la même manière que l'évolution des déformations des phases mesurées expérimentalement dans la striction. Ce résultat de simulation semble indiquer que la contrainte équivalente de von Mises joue un rôle important dans la relaxation des contraintes dans la ferrite et conduit probablement à l'initiation du processus de l'endommagement dans la ferrite. La valeur de la contrainte de von Mises

augmente à une certaine distance du centre de la striction en raison de la triaxialité de la contrainte, menant à l'évolution prononcée de l'endommagement dans les phases.

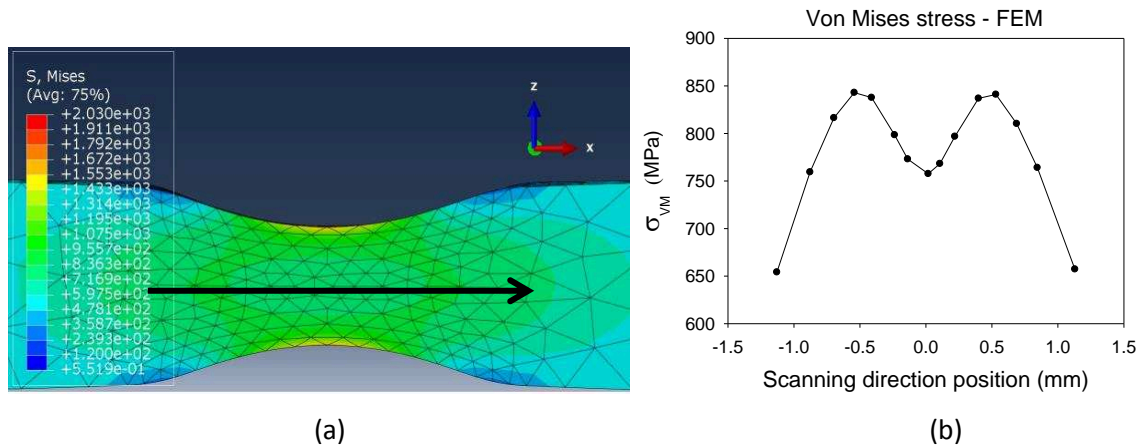


Figure F4.6 (a) La distribution simulée de la contrainte équivalente de von Mises dans la zone de striction. (b) L'évolution simulée de la contrainte équivalente de von Mises le long de la striction suivant la flèche noire sur (a).

V. Test d'Indentation Instrumenté (TII)

Afin de compléter les études de comportement élasto-plastique et d'endommagement par diffraction, le Test d'Indentation Instrumenté (TII) a été effectué afin d'observer la variation de la dureté H et du module d'Young E des deux phases. Avant d'effectuer le TII sur l'échantillon, la taille de la zone plastifiée par l'empreinte est estimée pour éviter l'interférence des empreintes entre les points de test (cf. annexe 13 de la thèse).

5.1 TII sur les surfaces des échantillons initiaux

Tout d'abord, le TII ont effectués sur les échantillons non déformés ayant trois directions (TD, ND, RD) normal à la surface. Les cartes de distribution de la dureté et du module d'Young sont tracées en fonction des résultats de TII en trois échantillons (par exemple, celle de RD Fig. F5.1a et b). En comparant avec l'image microscopique (Fig. F5.1c), aucune corrélation évidente ne peut être trouvée entre la distribution de E ou H et la distribution des phases pour les échantillons initiaux.

Afin d'étudier quantitativement la variation de H et E sur différentes surface, une analyse statistique a été réalisée. Comme montré par le tableau F5.1, la dureté et le module d'Young ne sont pas homogènes dans les directions différentes.

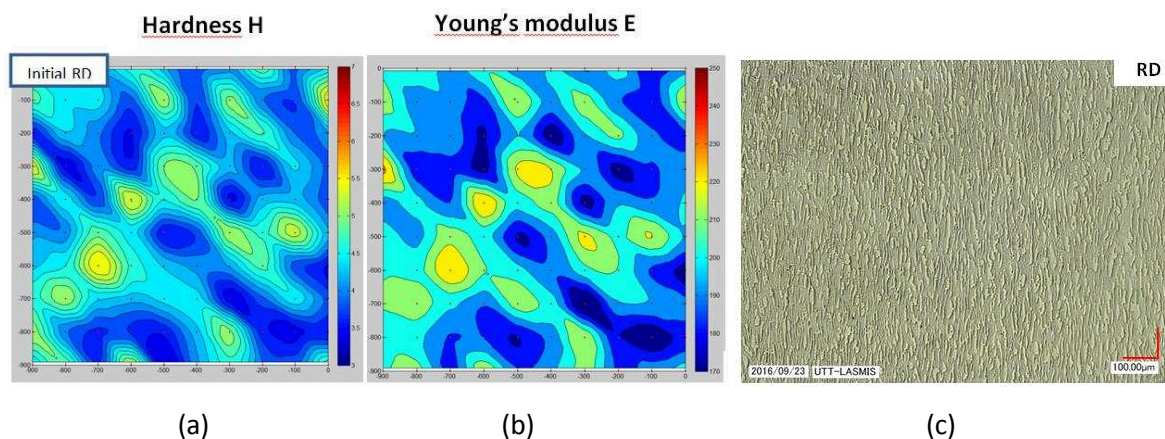


Figure F5.1 Les cartes de distribution de la dureté H (a) et du module d'Young E (b) sur la surface RD. L'image microscopique de la surface RD (c).

| Surface | RD (GPa) | ND (GPa) | TD (GPa) |
|---------|-----------------|-------------------|-------------------|
| Plage E | 170 - 235 | 185 - 250 | 200 - 245 |
| Plage H | 3.6 - 5.6 | 3 - 5.2 | 4.2 - 5.8 |
| < E > | 200 ± 13 | 213.6 ± 14.34 | 214.2 ± 15.23 |
| < H > | 4.33 ± 0.53 | 3.95 ± 0.45 | 4.89 ± 0.44 |

Tableau F5.1 Le résultat statistique de H et E sur les surfaces des trois échantillons.

5.2 TII sur la surface de l'échantillon après la rupture

5.2.1 Répartition de la dureté et du module d'Young

Dans cette étude les cartes de distribution de la dureté H et du module d'Young E ont été réalisées sur la surface de normale TD de l'échantillon fracturé (Fig. F5.2). A partir de ces cartes, on peut voir que la déviation de la dureté ou du module d'Young est plus significative dans la zone proche de la surface de rupture (proche du point d'origine des coordonnées). Les fluctuations intensives des propriétés mécaniques dans la striction peuvent être expliquées par la déformation plastique sévère, qui entraîne une diminution de la taille des grains, et l'hétérogénéité, associée aux grandes déformations, tels que l'activation des systèmes de glissement, le maclage, l'écrouissage, la relaxation ou l'initiation des micro-fissures.

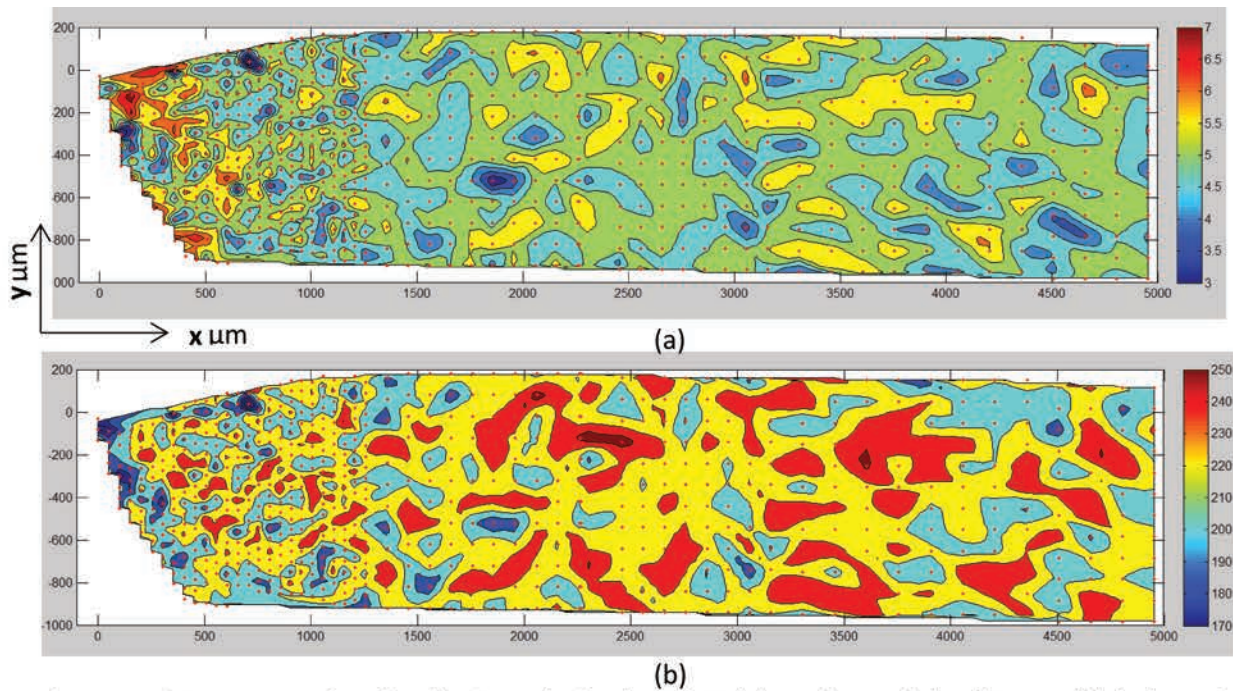


Figure F5.2 Les cartes des distributions de la dureté H (a) et du module d'Young (b) le long de l'échantillon fracturé.

5.2.2 Evolution de la dureté et du module d'Young moyens le long de l'échantillon

L'évolution de la dureté le long de la striction est comparée séparément avec l'évolution temporelle et spatiale des déformations des deux phases, mais il faut prendre en compte que les données d'indentation sont mesurées sur une éprouvette post-mortem.

Les Fig. F5.3 et Fig. F5.4 montrent que la variation de la dureté des phases est liée à l'évolution de la déformation et de la plasticité des phases. Ces effets peuvent s'expliquer par l'hétérogénéité du matériau engendrée au niveau des grains pendant la déformation plastique. La fragmentation des grains le long de la striction gravement déformée entraîne la variation des propriétés mécaniques des phases. En outre, la relaxation du matériau pourrait diminuer la dureté de la phase ferritique (Fig. F5.4b). Par contre, pour l'évolution du module d'Young, une chute importante est observée proche de la borne de rupture, ce qui est éventuellement induite par l'effet de bord (l'effet de résine en-dessous de l'échantillon).

Pour conclure, la déformation plastique joue évidemment un rôle important dans l'évolution de la dureté en raison du processus d'écrouissage. La réduction de dureté près de la zone de rupture est probablement entraînée par la relaxation de ferrite dans cette zone gravement déformée. La réduction du module d'Young peut donc être provoquée par des micro-fissures au voisinage de la rupture, ou simplement due à l'effet de bord causé par une épaisseur insuffisante de l'échantillon.

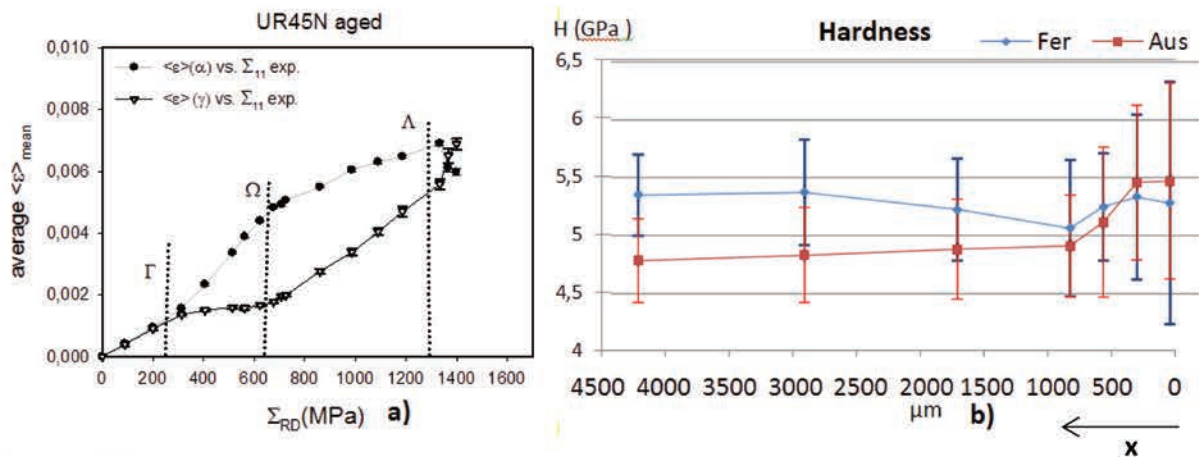


Figure F5.3 Comparaison entre l'évolution temporelle des déformations (a) et l'évolution de la dureté des phases.

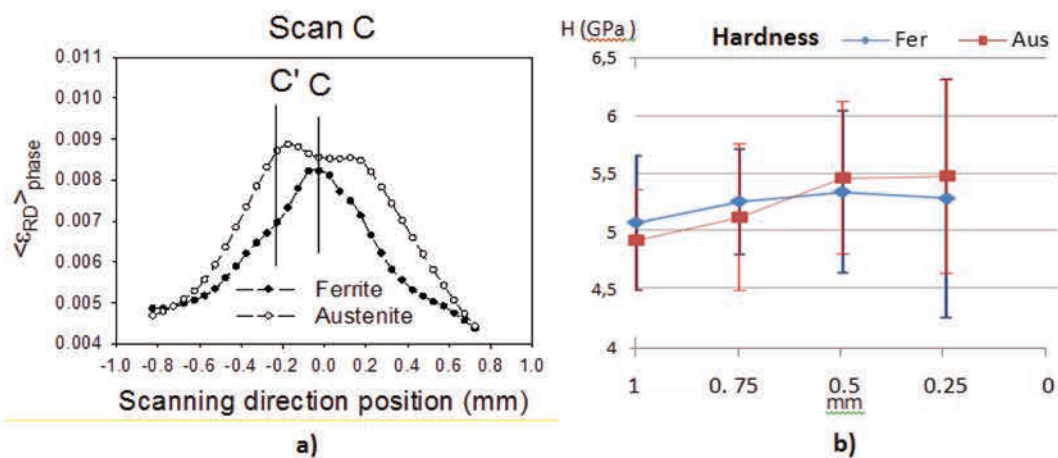


Figure F5.4 Comparaison entre l'évolution spatiale des déformations (a) et l'évolution de la dureté des phases.

5.2.3 Evolution de la dureté vs. le module d'Young

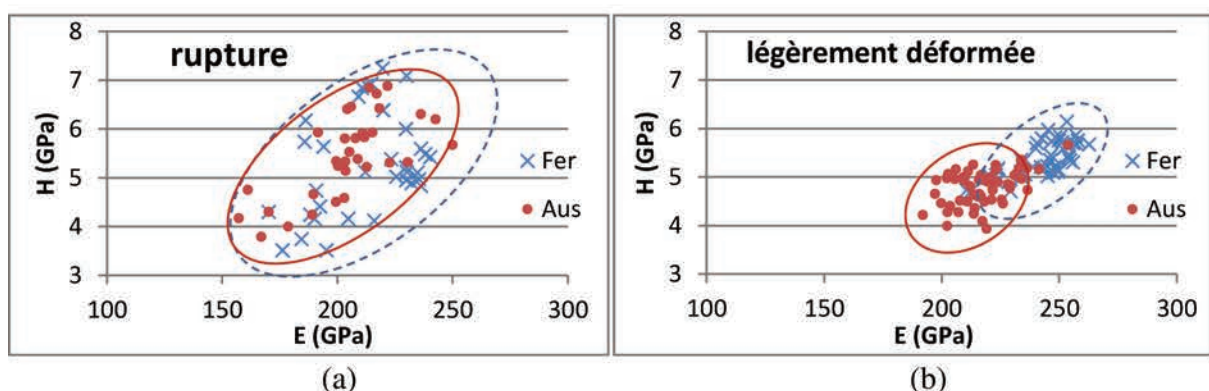


Figure F5.5 Evolution de la dureté vs. le module d'Young de la borne de rupture à la zone légèrement déformée.

Une autre tendance a aussi été constatée pour l'évolution de la dureté (H) vs. le module d'Young (E). On peut voir du diagramme de dispersion (Fig. F5.5) que, la différence entre les point H vs. E (chaque point de dispersion représente un couple de H et E d'une empreinte

d'indentation) des phases mesurées sur la rupture (Fig. F5.5a) n'est pas évidente. Mais une tendance de séparation des couple H vs. E se produit lors que les empreintes s'éloignent de la rupture, notamment dans la zone légèrement déformée (Fig. F5.5b). Ce phénomène indique un rapprochement de comportement des deux phases mené par l'endommagement.

VI. Etudes de l'alliage de titane biphasé

Le comportement élasto-plastique d'un matériau de structure cristalline hexagonale, ainsi que l'interaction entre les mailles hexagonales et les mailles cubiques, sont l'un des objectifs de cette thèse. L'alliage de titane biphasé TIMETAL-18 (Ti-18) a été sélectionné dans ce but.

6.1 Essai de traction couplé avec mesure in situ par diffraction des rayons X

6.1.1 Méthodologies expérimentales

Les mesures de diffraction des rayons X ont été réalisées pour déterminer les micro-déformations de la maille au cours d'un essai de traction. Le comportement mécanique des deux phases au cours de la déformation élasto-plastique a été étudié dans les directions parallèle et perpendiculaire au chargement. Les contraintes subies par les deux phases dans la direction de chargement ont été mesurées et calculées en utilisant la méthode MGIXD (Multi-reflection Grazing Incidence X-Ray Diffraction, cf. section 2.1.4.4 de la thèse). L'hypothèse des contraintes biaxiales est appliquée (i.e. $\sigma_{33} = \sigma_{13} = \sigma_{23} = 0$), en raison de la pénétration très faible du rayon X [Cullity 78, Brakman 88]. Les distances interréticulaires dans la direction transversale ont été mesurées pour différentes réflexions hkl en utilisant la méthode de Bragg-Bretano θ - 2θ [Zevin 12].

6.1.2 Evolution des contraintes et des déformations dans chaque phase

Un comportement linéaire (ligne rouge droite) peut être observé sur les courbes d'évolution de contraintes des deux phases au début de l'essai de traction. Ceci indique que les deux phases se déforment élastiquement dans cette période. Le premier changement notable est trouvé pour une contrainte macroscopique Σ_{11}^{diff} autour de 600MPa (au seuil A) (Fig. F6.1), une faible diminution de la pente de contrainte Σ_{11}^{diff} se produit. Au seuil B, les deux phases commencent la déformation plastique complète. Au seuil C, les contraintes des deux phases ont atteint leurs valeurs maximales. Les distances interréticulaires de toutes les réflexions hkl disponibles dans la direction transversale ont été mesurées pour chaque phase pendant l'essai de traction (Fig. F6.1b).

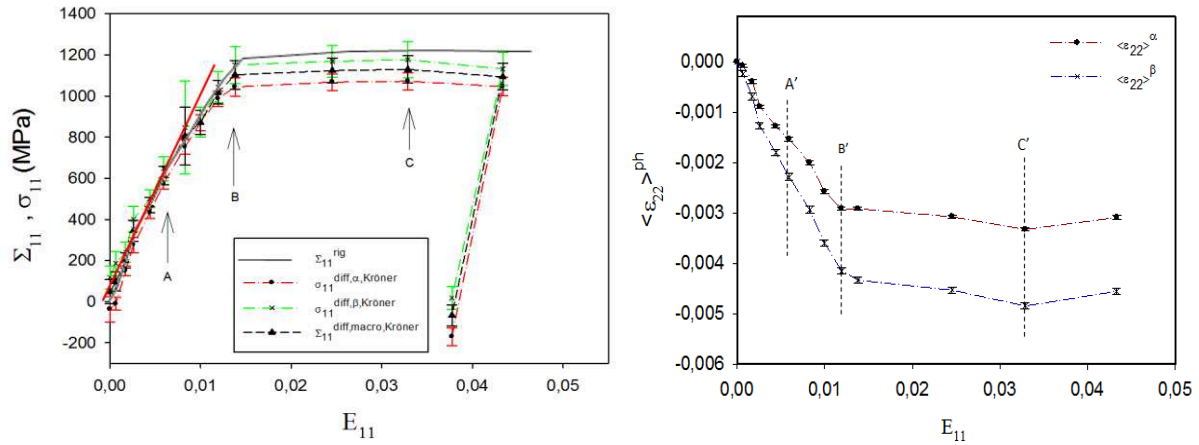


Figure F6.1 L'évolution des contraintes totale du Ti-18, de la phase α et de la phase β (a) et l'évolution des micro-déformations des phases (b).

6.2 Prédiction du modèle et confrontation aux résultats expérimentaux

La prédiction du comportement élasto-plastique du Ti-18 a été réalisée par un modèle auto-cohérent. 2000 grains sphériques sont définis comme un VER, dont 900 grains représentent la phase α (45%) et 1100 grains représentent la phase β (55%) selon l'estimation des fractions volumiques des phases (cf. section 6.1.5 de la thèse).

Le but de ce travail est de déterminer les paramètres de Voce pour chaque phase, tels que le CRSS τ_0^{ph} et les paramètres décrivant l'écrouissage linéaire θ_0^{ph} . Les valeurs des paramètres sont présentées dans le tableau F6.1 (cf. section 6.1.5.1 de la thèse).

| Paramètres de Voce | Phase | Système de glissement | Valeur (MPa) |
|--------------------|----------|---|--------------|
| τ_0^{ph} | α | (1 α) Prismatic P $\langle a \rangle$ $\{10\bar{1}0\}\langle 1\bar{2}10 \rangle$ | 300 |
| | | (2 α) Basal B $\langle a \rangle$ $\{0002\}\langle 11\bar{2}0 \rangle$ | 650 |
| | | (3 α) Pyramidal $\Pi 1 \langle a \rangle$ $\{\bar{1}011\}\langle 1\bar{2}10 \rangle$ | ≥ 650 |
| | | (4 α) Pyramidal $\Pi 1 \langle c+a \rangle$ $\{\bar{1}011\}\langle 11\bar{2}3 \rangle$ | 500 |
| | β | (1 β) $\{110\}\langle 1\bar{1}1 \rangle$ and (2 β) $\{112\}\langle 11\bar{1} \rangle$ | 520 |
| θ_0^{ph} | α | Tous les systèmes | 20 |
| | β | Tous les systèmes | 20 |

Tableau F6.1 Paramètres de Voce déterminés par l'essai de traction

Une bonne cohérence entre les déformations et les contraintes calculées et mesurées expérimentalement pour toutes les deux phases (Fig. F6.2). Veuillez voir la section 6.1.5.2 et 6.1.5.5 de la thèse pour plus d'informations.

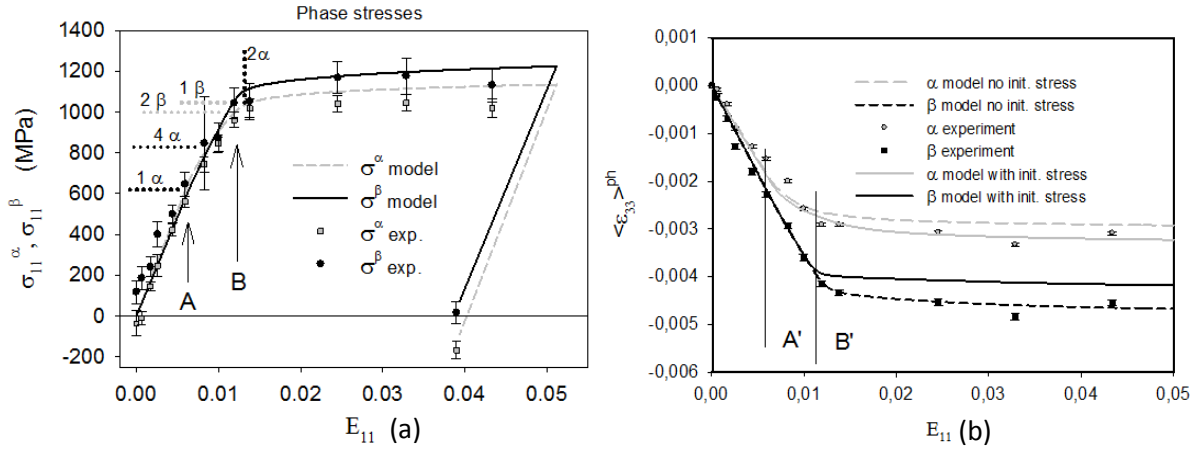


Figure F6.2 Confrontation entre les prédictions et les résultats expérimentaux des contraintes (a) et des déformations (b) des deux phases.

En analysant les figures 6.2 et 6.3, l'activation des systèmes de glissement est étudiée. On put conclure qu'au début de l'essai de traction, les deux phases se déforment élastiquement, au seuil A, le système de glissement (1α) prismatic P $\langle a \rangle \{10\bar{1}0\} \langle 1\bar{2}10 \rangle$ est le premier à s'activer, ensuite, le système (4α) pyramidal $\Pi 1 \langle c+a \rangle \{\bar{1}011\} \langle 11\bar{2}3 \rangle$ s'active. L'activation de ces deux systèmes conduit à une légère plastification de la phase α entre le seuil A et B, et provoque également une légère augmentation de la contrainte dans la phase β pour équilibrer le chargement imposé. Une incertitude importante de la contrainte déterminée dans la phase β est observée lorsque le système $\Pi 1 \langle c+a \rangle$ commence à s'activer dans la phase α . Bien que les glissements dans la phase α ne soient pas suffisants pour activer une déformation plastique globale, ils sont probablement capables de mener à une relaxation des contraintes intergranulaires ou interphase dans le matériau. Au seuil B, tous les autres systèmes de glissement dans les deux phases s'activent presque en même temps, ce qui conduit à une diminution significative de la pente de courbe contrainte-déformation macroscopique (cf. section 6.1.5.3 de la thèse).

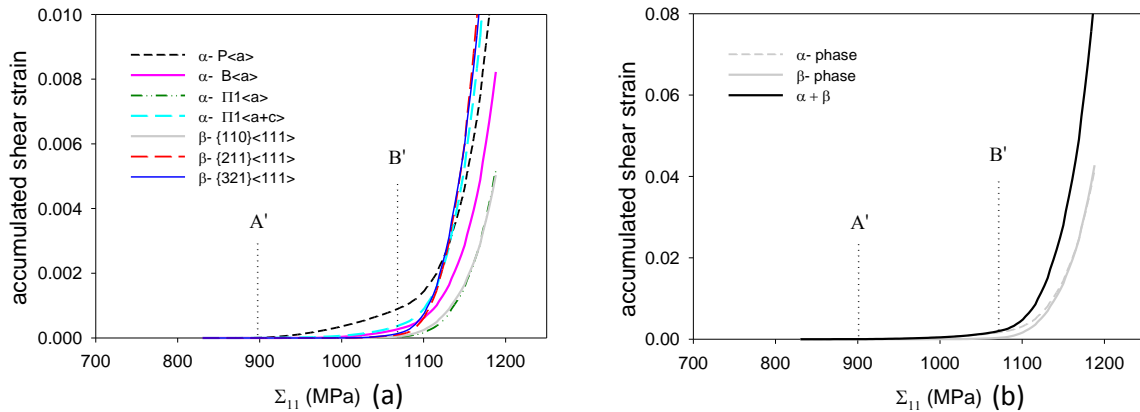


Figure F6.3 La déformation de cisaillement accumulée moyenne (par grain) pour chaque système de glissement (a), et pour les phases (b) en fonction de la contrainte appliquée Σ_{11} . Les contraintes initiales sont prises en compte.

6.3 Mesure de TKD sur la microstructure de Ti-18

La technique TKD a été appliquée pour observer l'évolution de la microstructure de Ti-18 entre l'état initial et l'état après rupture.

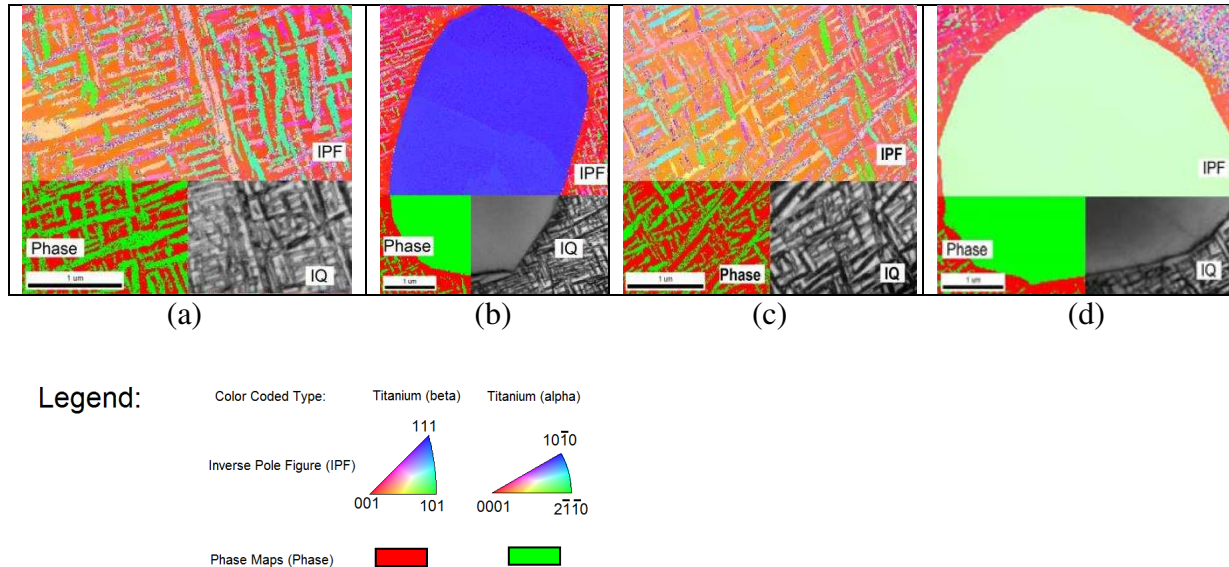


Figure F6.4 Les résultats de la mesure de TKD. La microstructure de phase α_s enrobée dans la phase β et la phase α_p dans l'état initial (a) et (b), et après rupture (c) et (d).

Ces résultats (Fig. F6.4) montrent que les orientations cristallographiques sont homogènes dans la phase α_s et β . La cartographie de la qualité de l'image (IQ) montre que la phase α_p est composée de petits grains ou que la densité des défauts est élevée dans cette phase. En outre, les orientations cristallographiques des deux phases α_s et β montre que la relation de Burgers $\{110\}_\beta \parallel \{0001\}_\alpha$ est satisfaite ou approximativement satisfaite. En outre, pas de maclage évidant se produit au cours de la déformation de matériau.

Conclusions générales et perspectives

Le but de cette thèse est de caractériser les propriétés élasto-plastique des matériaux polycristallins, ainsi que les comportements mécaniques des différentes phases lors des grandes déformations et de l'endommagement. Le modèle auto-cohérent est employé afin de comparer les résultats théoriques avec ceux expérimentaux, pour identifier les propriétés mécaniques des matériaux. Des études sur le comportement mécanique ont été réalisées aux échelles micro, méso et macroscopique.

D'une part, dans le cadre de l'étude des déformations élasto-plastiques, les méthodes de diffraction ont été appliquées lors des essais de traction uniaxiale jusqu'à la rupture de

l'échantillon. Des expériences complémentaires ont également été aussi réalisées, telles que les tests de l'indentation instrumentée et des observations des microstructures, afin de recueillir des données expérimentales à différentes échelles.

D'autre part, des simulations numériques ont été réalisées pour déterminer quantitativement les paramètres liés au comportement élasto-plastique et à l'initiation de l'endommagement. Le modèle auto-cohérent élasto-plastique a été appliqué pour étudier l'activation des systèmes de glissement et l'évolution de l'écrouissage dans les matériaux concernés. L'hétérogénéité et l'initiation du processus de l'endommagement ont également été étudiées le long de la striction lors des grandes déformations. Dans ce cas, le modèle d'endommagement intégré et une simulation de MEF ont été appliqués pour aider à l'interprétation des données expérimentales.

Grâce aux expériences expérimentales et calculs numériques, la ferrite est considérée comme la phase première à s'endommager, notamment ses grains ayant des orientations particulières contribuant aux réflexions 200 et 211. Trois critères d'endommagement sont testés, les meilleures prédictions sont obtenues par le critère d'équivalence en déformation. Ceci indique que l'accumulation des déformations dans des grains et ses histoires de déformations (y compris la variation des orientations) sont importantes pour l'initiation d'endommagement. La simulation simple de MEF montre que la triaxialité de contrainte joue un rôle important pour la relaxation de contrainte dans ferrite et aussi pour l'initiation d'endommagement. Ensuite, par le test d'indentation instrumenté, une corrélation entre la dureté et la relaxation de matériau semble être observé dans la ferrite lors des grandes déformations.

Quant à l'alliage de titane biphasé, les paramètres liés à la déformation élasto-plastique (CRSS et écrouissage linéaire) sont identifiés pour les phases α et β . L'ordre d'activation des systèmes de glissement a aussi déterminée, le système prismatique $P_{\langle a \rangle}$ de phase α est le premier à s'activer. Une observation de TKD a été aussi réalisée, grâce à laquelle la relation de Burgers $\{110\}_{\beta} \parallel \{0001\}_{\alpha}$ est confirmée, et aucun maclage évident n'est observée en grandes déformations.

Bien que des résultats fructueux aient été obtenus, certaines améliorations devraient aussi être réalisées, elles sont présentées ci-dessous:

- L'effet de bord et l'influence de la zone plastifiée ne peuvent pas être négligée pour les résultats de nanoindentation, à cause de la dimension insuffisante de l'échantillon. Un échantillon plus large serait intéressant dans le future pour bien espacer les empreintes et pour effectuer de plus nombreuses empreintes.
- Le test de traction du Ti-18 n'a pas été mené jusqu'aux grandes déformations, un alliage de titane plus ductile peut être proposé pour le futur test afin de déterminer les paramètres liés à l'écrouissage non linéaires et ceux de l'endommagement.
- La mesure de contrainte sur le Ti-18 avec diffraction de rayon X peut être appliqué que dans le volume près de la surface, une source de l'énergie plus élevée (e .g. rayonnement de synchrotron) permettrait une étude dans le volume au sein de l'éprouvette.
- Pour le calcul numérique, un objectif futur est d'implémenter la modélisation multi-échelle dans un logiciel éléments finis, ce qui permettrait de non seulement prédire les comportements mécaniques des matériaux aux différentes échelles, mais aussi d'effectuer des calculs structurels.

Appendix

| | |
|------------------|-----|
| Appendix 1..... | 195 |
| Appendix 2..... | 196 |
| Appendix 3..... | 198 |
| Appendix 4..... | 199 |
| Appendix 5..... | 201 |
| Appendix 6..... | 203 |
| Appendix 7..... | 206 |
| Appendix 8..... | 208 |
| Appendix 9..... | 212 |
| Appendix 10..... | 212 |
| Appendix 11..... | 214 |
| Appendix 12..... | 216 |
| Appendix 13..... | 218 |
| Appendix 14..... | 220 |
| Appendix 15..... | 221 |
| Appendix 16..... | 223 |
| Appendix 17..... | 224 |
| Appendix 18..... | 228 |
| Appendix 19..... | 229 |
| Appendix 20..... | 230 |
| Appendix 21..... | 232 |
| Appendix 22..... | 233 |
| Appendix 23..... | 234 |
| Appendix 24..... | 236 |
| Appendix 25..... | 242 |
| Appendix 26..... | 243 |

Appendix 1 General description of stainless steels

The stainless steels are iron-based alloys which were firstly developed in the United Kingdom and in Germany in the first decade of 20th century. The corrosion resistance of these steels is due to the rich content of chromium element, which is greater than 10.5 wt% (see table A1.6). This amount of chromium is the minimum level needed to ensure the continuous formation of a stable oxide layer (rich in chromium) on the surface of the material, preventing the rust formation in an unpolluted environment [Davis 94]. The stainless steels are generally classified by their crystallographic structure. The mechanical and chemical properties of the stainless steels depend mostly on the presence and the level of alloying elements. A brief presentation of the stainless steel grades is given in the following table A1.6 [Maetz 14].

| | AISI/SAE | EN | UNS | C | N | Cr | Ni | Mo | Autre |
|------------|----------|--------|--------|------|------|------|-----|-----|--------|
| Duplex | 2101 | 1.4162 | S32101 | 0,03 | 0,22 | 21,5 | 1,5 | 0,3 | 5 Mn |
| | 2202 | 1.4062 | S32202 | 0,03 | 0,21 | 22,7 | 2 | 0,2 | 1,3 Mn |
| | 2304 | 1.4362 | S32304 | 0,02 | 0,10 | 23 | 4,8 | 0,3 | - |
| | 2205 | 1.4462 | S32205 | 0,02 | 0,17 | 22 | 5,7 | 3,1 | - |
| | 2507 | 1.4410 | S32750 | 0,02 | 0,27 | 25 | 7 | 4 | - |
| Austenitic | 301 | 1.4310 | S30100 | 0.1 | - | 17 | 7 | - | - |
| | 304 | 1.4301 | S30400 | 0,04 | - | 18 | 8 | - | - |
| | 316 | 1.4401 | S31600 | 0,04 | - | 17 | 10 | 2 | - |
| | 254 SMO | 1.4547 | S31254 | 0.01 | 0.2 | 20 | 18 | 6 | - |
| Ferritic | 409 | 1.4512 | S40900 | 0,02 | - | 11 | 0,5 | - | - |
| | 444 | 1.4521 | S44400 | 0,02 | - | 18 | - | 2 | - |

Table A1.1 Contents of alloying elements in several stainless steels, in mass percentage (wt%).

Appendix 2 Processes occurring during structural transformation and thermal aging of duplex steels

In the present thesis the quenched and thermal aged duplex steels were studied. Therefore, a brief explanation of the structural transformation and description of the aging process during thermal treatment is presented in this chapter.

The aging mechanism and the phase transformation in the steel are strongly related to the temperature conditions. We recall here the aging mechanisms in steels under different temperature conditions according to the Time-Temperature-Transformation (TTT) curves of duplex steels presented in Fig. A2.1.

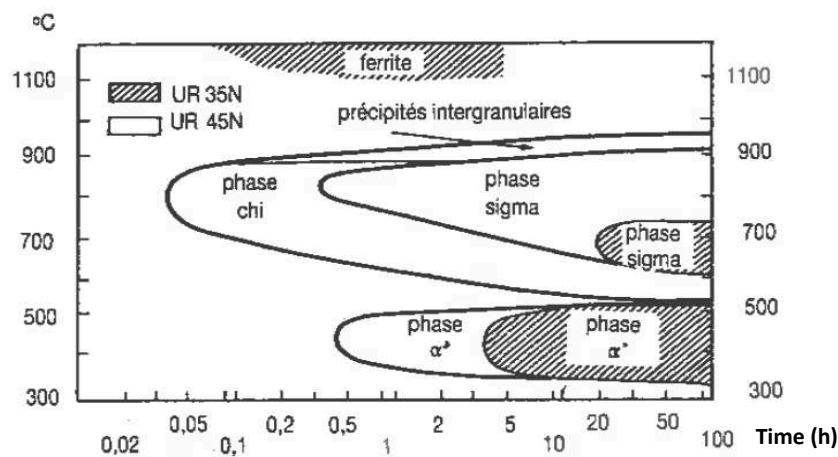


Figure A2.1 TTT diagrams of duplex stainless steels: UR35N and UR45N.

Because of the high chromium content in ferritic phase, the phenomenon of embrittlement accompanied by a significant hardening can occur in this phase at a temperature lower than 600°C. The evolution of ferrite properties leads to the embrittlement and hardening of duplex steel. As well, for the temperature lower than 600°C, a localized transformation of ferrite called “demixing” occurs [Desestret 90]. This transformation of ferritic phase is mostly caused by the decomposition of α/α' phases. The α phase is ferritic phase rich in iron, whereas the α' phases is rich in chromium and its local content level of chromium can reach probably up to 80%. The presence of α' phase is considered as the main cause of the age hardening [Calonne 01]. The different values of elastic modulus and the gaps between the crystalline lattices of α and α' phases influence the dislocation movement.

According to the following studies [Solomon-Levinson 78, Solomon-Koch 79, Eckstein 83], this phenomenon can be caused by two different mechanisms [Desestret 90]:

- by the spinodal decomposition of ferrite occurring between 280°C and 475°C.
- by the germination and its growth for a temperature about 500°C, since a process of diffusion with the creation of interfaces is needed.

The spinodal decomposition is a homogenous transformation occurring without energy intake, thus there is no energy barrier for ferrite-rich phase to cluster together, and the nucleation of ferritic phase finally causes the demixing of ferritic phase from the alloy.

The temperature range from 600°C to 1050°C is characterized by the formation of a large variety of secondary phases being able to precipitate with an incubation time, both inside ferrite and austenite. The secondary phases formed in these temperatures, such as σ phase, secondary austenite, χ phase and R phase (shown in table A2.1), as well as nitrides and carbides, are mostly affected by the effective chemical composition of materials [Charles 88]. The precipitation of above mentioned secondary phases influence strongly the mechanical properties and corrosion resistance of duplex steels [Iacoviello 97, Iacoviello 98, Iacoviello 99].

| Phase | Structure | Chemical composition |
|----------|--------------------|---|
| σ | Tetragonal | Fe-Cr / Fe-Mo / Fe-Ni |
| χ | Body centred cubic | (Fe Ni) ₃₆ Cr ₁₈ Mo ₄ ; Cr ₆ Fe ₁₈ Mo ₅ Fe ₃₆ Cr ₁₂ Mo ₁₀ |
| R | Hexagonal | Fe-Cr-Mo |

Table A2.1 Presentation of precipitated intermetallic phases [Desestret 90]

At the temperature higher than 1050°C, the duplex steel transforms completely into ferritic structure, while the solidified ferritic structure will partially turn into austenitic structure after cooling down to ambient temperature. The latter transformation from ferritic structure (bcc) to austenitic structure (fcc) is reversible. Consequently, all increases in temperature higher than 1050°C bring an increase in the volume fraction of ferrite and a decrease in the fraction of the other alloying elements [Strutt 86].

Appendix 3 General description of titanium alloys

Named after the giant “Titan” from the Greek mythology, the titanium combines high mechanical resistance with a relatively low density and relatively good ductility. The yield strength values of conventional titanium alloys are between about 800 MPa and 1200 MPa. Table A3.1 presents the values of some important characteristics of titanium and titanium based alloys compared to other structural metallic materials based on Fe, Ni and Al [Lütjering 07]. Thanks to their high strength-to-weight ratio, good creep resistance and its excellent corrosion resistance, titanium and its alloys are widely applied in nowadays industrial field, especially in the aeronautic sectors and for the aerospace applications.

| | Ti | Fe | Ni | Al |
|---|----------------------------------|-----------------------------------|-----------|-----------|
| Melting temperature (°C) | 1670 | 1538 | 1455 | 660 |
| Allotropic transformation (°C) | $\beta \xrightarrow{882} \alpha$ | $\gamma \xrightarrow{912} \alpha$ | - | - |
| Crystal structures | bcc→hcp | fcc→bcc | fcc | fcc |
| Room temperature E (GPa) | 115 | 215 | 200 | 72 |
| Yield stress (MPa) | 1000 | 1000 | 1000 | 500 |
| Density (g/cm³) | 4.5 | 7.9 | 8.9 | 2.7 |
| Comparative corrosion resistance | Very high | Low | Medium | High |

Table A3.1 Some important characteristics of titanium and titanium based alloys compared to other structural metallic materials based on Fe, Ni and Al [Lütjering 07].

However, the relatively high production cost of titanium limits its application field. In order to minimize this inherent limitation, it is necessary to take advantage of all its features and its specific properties, which can distinguish the titanium from other alternative materials. According to table A3.1, we can see that pure titanium exhibits an allotropic phase transformation at about 882°C. Fig. A3.1 illustrates the phase transition related to the cooling rate of titanium alloy Ti-6Al-4V [Ahmed 98]. The β phase of titanium with a body centred cubic (bcc) crystal structure at higher temperature will change into a hexagonal close-packed crystal structure (hcp), named α titanium, at lower temperature. The exact transformation

temperature is strongly influenced by interstitial and substitutional elements and therefore depends on the purity of titanium.

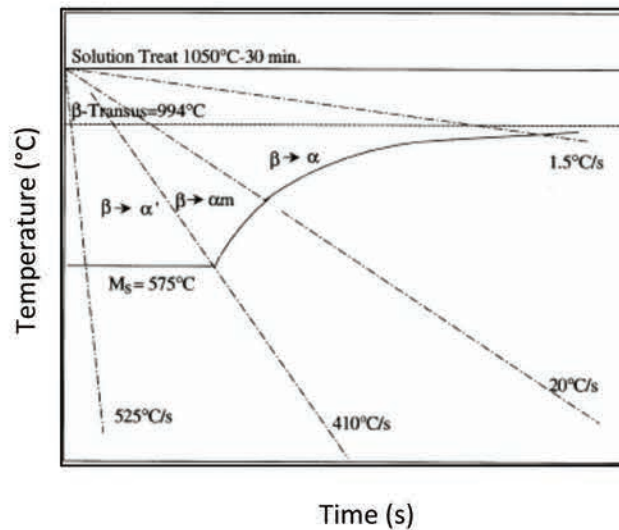


Figure A3.1 Extract of TTT diagram for Ti-6Al-4V, alloy solution annealed at 1050°C, quenched till phase transformation, observed by [Ahmed 98]

Appendix 4 Microstructure variation of TIMETAL-18 in function of temperature

The thermal treatments have also influence on the microstructure of titanium alloys. As reported by Lebrun et al. [Lebrun 14], the alloy TIMETAL-18 (one of the titanium alloys used in the studies of this thesis) presents different morphological structures under different thermal treatments. Fig A4.1 shows the microstructure variation of TIMETAL-18 in function of the treatment temperatures. It can be noticed that the thermal treatments have important influence on the structural morphology of titanium alloy. The volume fraction of α_p was much lower after a solution treatment at 832°C than that solution treated at 818°C. This phenomenon can be explained by higher treatment temperature (832°C), which was closer to the β transus temperature (882°C). As the result, the stability of α titanium was decreased and most of α titanium was transformed to β titanium.

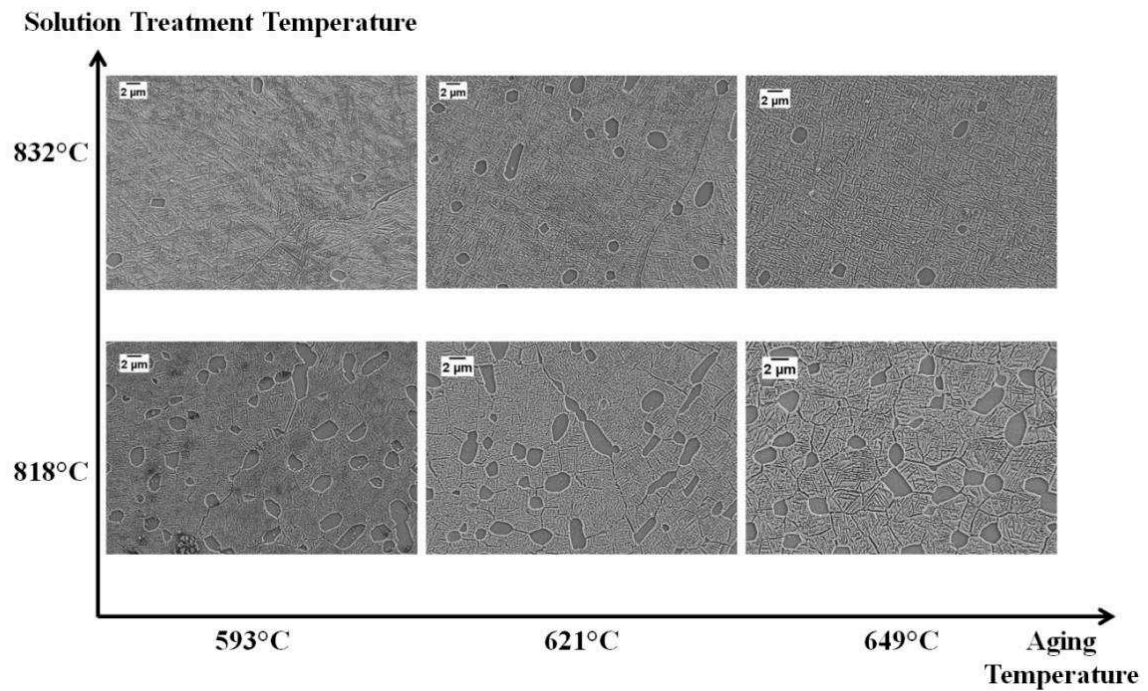


Figure A4.1 Microstructure variation of TIMETAL-18 in function of thermal treatment temperatures [Lebrun 14]. The thermal treatments have been done by material supplier (TIMET Henderson) before sample delivering.

Table A4.1 reports the volume fraction of different morphologies of α titanium under different thermal treatment conditions. We can see the volume fraction of α_p was nearly constant and the α_s slightly decreased, when the aging temperature increased. On the other hand, the volume fraction of α_s strongly increased, while the α_p phase almost disappeared with the increasing of solution treatment temperature.

| Aging temperature Solution treatment temperature | 593°C | | 621°C | | 649°C | |
|---|---------|----------|---------|----------|---------|----------|
| | primary | acicular | primary | Acicular | primary | Acicular |
| 818°C | 10 | 40 | 13 | 36 | 13 | 31 |
| 832°C | 2 | 45 | 4 | 48 | 2 | 43 |
| Volume Fraction of α phase (%) | primary | acicular | primary | Acicular | primary | Acicular |

Table A4.1 Volume fraction of α titanium in function of thermal treatment temperatures [Lebrun 14].

From the previous study we can see the volume fraction of primary and secondary α titanium can be controlled by the conditions of thermal treatment, whereas the forging or rolling deformation influences the shape of primary α phase grains.

Appendix 5 Fitting of diffraction profiles by Pseudo-Voigt function

The measured diffraction patterns were analysed using software (Winplotr, Multi-fit) in which the Pseudo-Voigt function was adjusted to the experimental diffraction peaks [Pecharsky 05, Lutterotti 14]. This method is now widely used for the structural analyses of crystalline materials.

The fitting procedure is based on the the Pseudo-Voigt function, which is defined as the superposition of Lorentzian and Gaussian functions, i.e.:

$$PV(2\theta_i - 2\theta_{k,j}) = \eta_k \left(\frac{1}{1 + S_{i,k}^2} \right) + (1 - \eta_k) e^{-S_{i,k}^2 \ln 2} \quad \text{Eq. A5.1}$$

where η_k is the Lorentz factor which defines relative proportion of the Lorentzian functions, and $S_{i,k}$ is used to characterize the evolution of peak width as a function of 2θ (see Eq. A5.2 below).

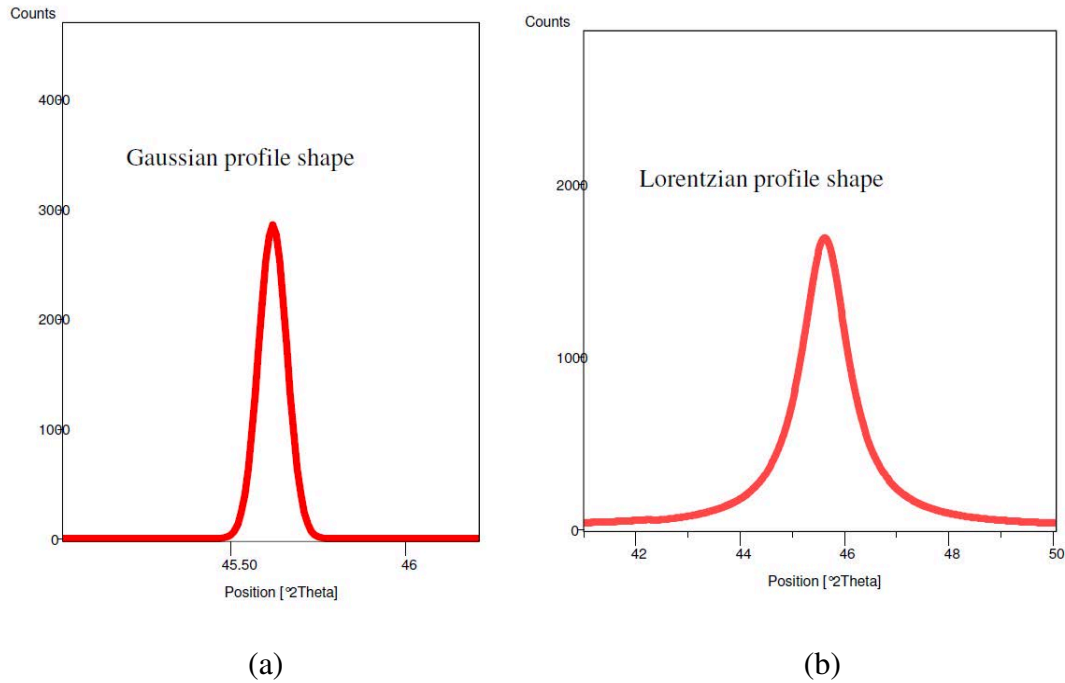


Figure A5.1 Illustration of Gaussian profile shape (a) and Lorentzian profile shape (b).

It is well known, that the peak shape evolves during the elasto-plastic deformation process. During elastic deformation of annealed polycrystalline materials, the peak shape can be better described by Gaussian function (Fig. A5.1 a, Gaussian profile shape), whereas the peak shape is closer to a Lorentzian function (Fig. A5.1b, Lorentzian profile shape) when sample is plastically deformed [Hutchings 05], as illustrated in Fig. A5.1. Furthermore, the type of diffraction beam also influences the peak shape, for instance, a peak similar to Gaussian profile is obtained for neutron diffraction, while a more Lorentzian shape profile is obtained with X-rays [Pecharsky 05]. The peak profile will be also influenced by the variation of gauge volume size or as well by the distortion of crystal lattice under the influence of dislocation or lattice defects, which leads to the peak broadening.

The term $S_{i,k}$ is expressed by the Cagliotti parameter ω_i :

$$S_{i,k} = \frac{2\theta_i - 2\theta_{k,j}}{\omega_k} \quad \text{Eq. A5.2}$$

where ω_k denotes the Full Width at Half Maximum (FWHM), which describes the half distance between the two points on x-axis corresponding to half of the peak height, see Fig. A5.2. The square of ω_k can be expressed using three adjustable parameters U, V, W, as presented in Eq. A5.3:

$$\omega_k^2 = U \tan^2 \theta_k + V \tan \theta_k + W \quad \text{Eq. A5.3}$$

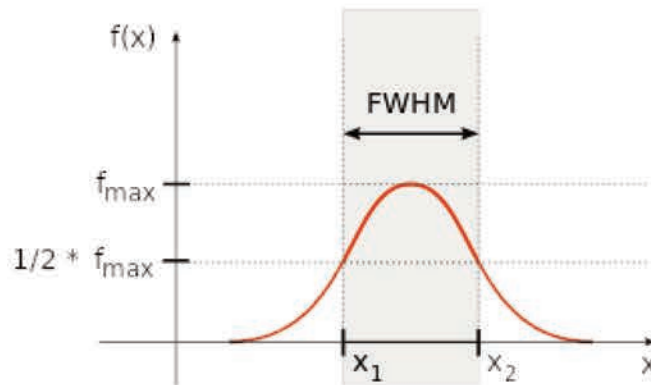


Figure A5.2 Illustration of the Full Width at Half Maximum (FWHM) for a given profile.

Appendix 6 Classification of stresses in a polycrystalline material [Baczmański05]

Polycrystalline materials consist of crystallites (grains) with different lattice orientations, belonging to one or more phases. Their different mechanical features or orientations can result in the incompatibilities between the neighboring grains and various defects in grain boundaries or within the lattice structure. These mentioned effects as well the external loading impose stress fields inside polycrystalline materials at different scales. The stress field exists not only during loading process but in general the so called residual stress remind in the sample after different irreversible processes applied to the material (e.g. mechanical or thermal treatment).

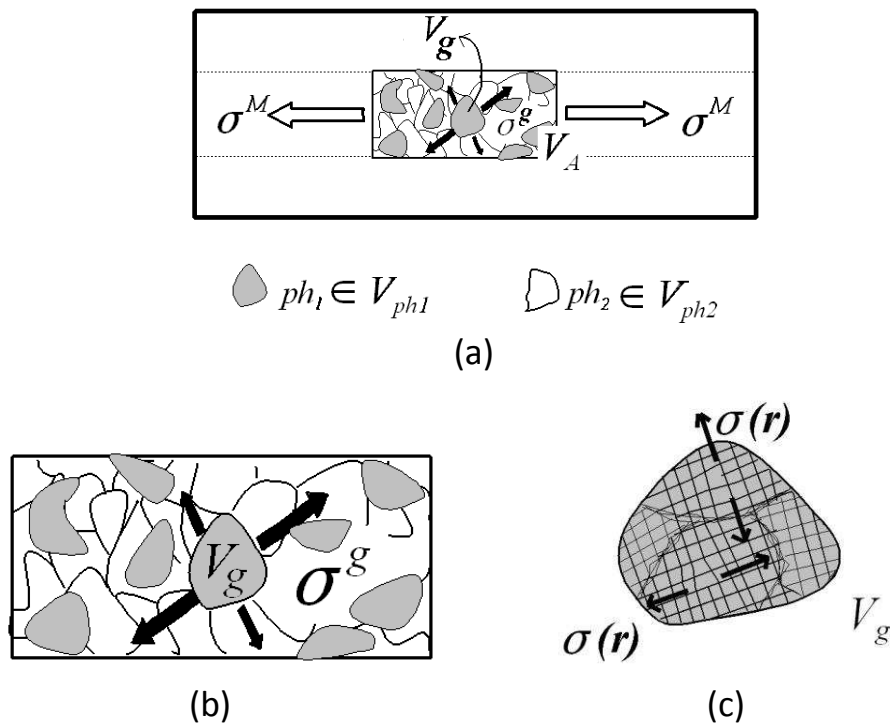


Figure A6.1 Definition of stress fields in a polycrystalline material at different scales, (a) scale of the 1st order stress σ_{ij}^I ; (b) scale of the 2nd order stress σ_{ij}^{II} ; (c) scale of the 3rd order stress σ_{ij}^{III} [Baczmański05].

The 1st order stress σ_{ij}^I is defined as the average stress over the volume containing a large number of crystallites (as figure A6.1a), which can be considered as being equivalent to the macro-stress σ_{ij}^M loaded by external force or caused by long range incompatibility of sample

volumes (residual macro-stress). For a polycrystalline material σ_{ij}^I is the weighted average stress for all grains stresses (σ_{ij}^g) within a given volume V_A , expressed by Eq. A6.1. The phase stresses can be also considered as the pseudo first order stresses (because the existence of external load or long range incompatibility, the stresses are not strictly first order one) and they can be determined independently for each phase. In this case the mean value is calculated over a large number of grains belonging to the given phase.

$$\sigma_{ij}^M = \frac{1}{V_A} \int_{V_A} \sigma_{ij}^g dV \quad \text{Eq. A6.1}$$

The 2nd order stress σ_{ij}^{II} is described as the deviation of grains stress σ_{ij}^g from the macroscopic stress, expressed by Eq. A6.2. The second order stress can be caused by the incompatibility between grains resulted from different physical behaviours and various orientations of different grains (Fig. A6.1b).

$$\sigma_{ij}^{II} = \sigma_{ij}^g - \sigma_{ij}^I \quad \text{Eq. A6.2}$$

The 3rd order stress is used to indicate the heterogeneity within a single crystal grain, which arise from the local stress fields around lattice defects (Fig. A6.1c). In this case, it can be expressed as the deviation of local stress $\sigma_{ij}(r)$ existing in position \mathbf{r} from the grain stress σ_{ij}^g (Eq. A6.3):

$$\sigma_{ij}^{III} = \sigma_{ij}(r) - \sigma_{ij}^g \quad \text{Eq. A6.3}$$

The 2nd order stress has an elastic origin varying with the orientation of grain lattice or can be generated from the incompatibility between grains, both for single phased or multi-phase materials. A brief explanation of stresses at different scales is shown in Fig. A6.2, where the relationships between stresses of different orders are illustrated. As above mentioned, the second order stress can be originated from elastic heterogeneity and anisotropy, as well from the incompatibility effects.

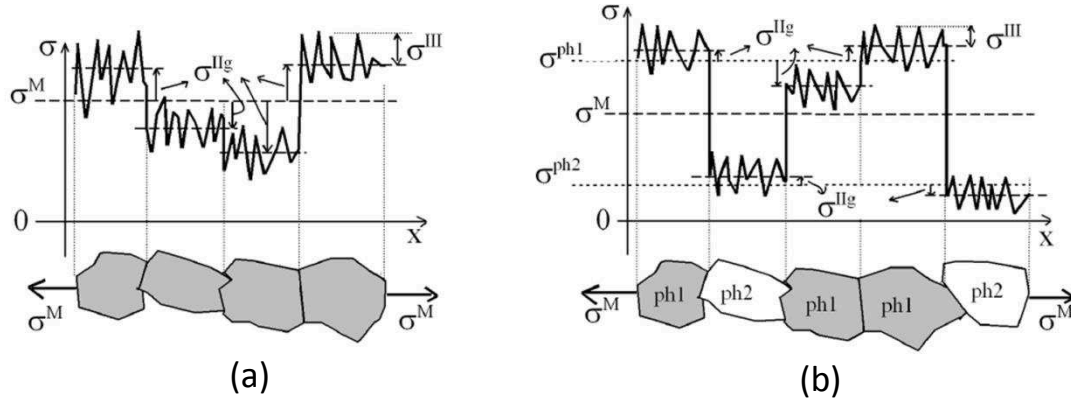


Figure A6.2 Stresses of different orders in (a) single phase material; (b) two phase material (σ^{ph} means phase stress). The first and the second order stresses are induced by external loads or interaction between large volumes or grain volumes, respectively. The third order stress characterizes the local stress field around lattice defects [Baczmanski05].

A summary of the stresses of different orders and their origins are listed in the following table A6.1.

| Scale Origin | 1 st order (Volume average) | 2nd order (Deviation from 1 st order stress) | 3rd order (Local heterogeneity in grain) |
|--|--|---|--|
| External loads or Long-scale forces | σ_{ij}^M (macro-stress) $\sigma_{ij}^{ph(el)}$ (phase elastic stress) | $\sigma_{ij}^{II(el)}$ (2 nd order elastic stress) | |
| Thermal or plastic homogenous process | $\sigma_{ij}^{ph(ic)}$ (phase incompatibility stress) | $\sigma_{ij}^{II(ic)}$ (2 nd order incompatibility stress) | σ_{ij}^{III} (local stress inside grain –lattice imperfections) |

Table A6.1 Summary of stresses of different orders with their origins [Baczmanski 05].

Appendix 7 Calculation of internal stress for macroscopic elastically anisotropic polycrystalline materials

Diffraction method plays one of the most important roles in the stress analysis field due to its selectivity, non-destructive character and possibility of in situ measurement. This method was for the first time applied in residual stress measurement in 1930 [Glockner 34, Bollenrath 39, Genzel 05]. One of the most used measurement technique in X-ray Stress Analysis (XSA), i.e. the $\sin^2\psi$ method was introduced by Macherauch and Müller in 1961 [Macherauch 61, Genzel 05].

The $\langle \rangle_{\{hkl\}}$ brackets denote the average value of a physical quantity q over the diffracting volume measured only from diffracting grains for which the scattering vector \vec{n} is perpendicular to the $\{hkl\}$ planes, as presented by Eq. A7.1

$$\langle q_{\vec{n}}(\phi, \psi) \rangle_{\{hkl\}} = \frac{\int_0^{2\pi} q(\phi, \psi, \lambda)_{hkl} f(\phi, \psi, \lambda)_{hkl} d\lambda}{\int_0^{2\pi} f(\phi, \psi, \lambda)_{hkl} d\lambda} \quad \text{Eq. A7. 1}$$

where $f(\phi, \psi, \lambda)_{hkl}$ indicates the Orientation Distribution Function (ODF) in terms of the measurement parameters for a given $\{hkl\}$ plane and the rotation by angle λ around normal to $\{hkl\}$ plane [Welzel 05]. The (ϕ, ψ, λ) angles are related to Euler angles (ϕ_1, Φ, ϕ_2) , for which the ODF is defined as usual [Bunge 69].

During diffraction experiment the average value of the interplanar spacing $\langle d_{\vec{n}}(\phi, \psi) \rangle_{\{hkl\}}$ are measured for different orientations described by two angles ϕ and ψ shown in Fig. 2.4. Thus, the average elastic strains $\langle \varepsilon_{\vec{n}}(\phi, \psi) \rangle_{\{hkl\}}$ for a plane $\{hkl\}$ can be expressed in the laboratory frame L using Eq. A7.2,

$$\begin{aligned} \langle \varepsilon_{\vec{n}}(\phi, \psi) \rangle_{\{hkl\}} &= \langle \varepsilon_{33}^L(\phi, \psi) \rangle_{\{hkl\}} \\ &= \frac{\int_0^{2\pi} \varepsilon_{33}^L(\phi, \psi, \lambda)_{hkl} f(\phi, \psi, \lambda)_{hkl} d\lambda}{\int_0^{2\pi} f(\phi, \psi, \lambda)_{hkl} d\lambda} \end{aligned} \quad \text{Eq. A7. 2}$$

where $\varepsilon_{33}^L(\phi, \psi, \lambda)_{hkl}$ means the strain parallel to the L_3 axis in the frame L. $f(\phi, \psi, \lambda)_{hkl}$ indicates the Orientation Distribution Function (ODF) in terms of the measurement

parameters for a given $\{hkl\}$. The (ϕ, ψ, λ) angles are related to Euler angles (ϕ_1, Φ, ϕ_2) , for which the ODF is defined as usual [Bunge 69].

Taking into consideration the coordinate system transformation from sample reference system **S** to laboratory reference system **L**, the averaged elastic strains $\langle \varepsilon(\phi, \psi) \rangle_{\{hkl\}}$ can be expressed in **L** system, using a transformation vector \vec{m} by Eq. A7.3:

$$\begin{aligned} \langle \varepsilon_{ij}^L(\phi, \psi) \rangle_{\{hkl\}} &= m_i^S \langle \varepsilon_{ij}^S \rangle_{\{hkl\}} m_j^S \\ &= \langle \varepsilon_{11}^S \rangle_{\{hkl\}} \cos^2 \varphi \sin^2 \psi + \langle \varepsilon_{22}^S \rangle_{\{hkl\}} \sin^2 \varphi \sin^2 \psi \\ &\quad + \langle \varepsilon_{33}^S \rangle_{\{hkl\}} \cos^2 \psi + \langle \varepsilon_{12}^S \rangle_{\{hkl\}} \sin 2\varphi \sin^2 \psi \\ &\quad + \langle \varepsilon_{13}^S \rangle_{\{hkl\}} \cos \varphi \sin 2\psi + \langle \varepsilon_{23}^S \rangle_{\{hkl\}} \sin \varphi \sin 2\psi \end{aligned} \quad \text{Eq. A7. 3}$$

$$\text{where:} \quad \vec{m}^S = \begin{pmatrix} \cos \varphi \sin \psi \\ \sin \varphi \sin \psi \\ \cos \psi \end{pmatrix} \quad \text{Eq. A7. 4}$$

In the case of macroscopically elastically anisotropic polycrystalline material, exhibiting the direction-dependent interaction between grains or/and so-called crystallographic texture, the averaged strains for $\{hkl\}$ planes can be related to its average first order stresses (macro-stresses) using X-ray Stress Factors (XSF) $F_{ij}(\phi, \psi, f)_{\{hkl\}}$:

$$\langle \varepsilon(\phi, \psi) \rangle_{\{hkl\}} = F_{ij}(\phi, \psi, f)_{\{hkl\}} \sigma_{ij}^L \quad \text{Eq. A7.5}$$

where for simplicity the S and L superscripts were skipped, i.e. $\sigma_{ij}^L = \sigma_{ij}^{L,S}$ and $\langle \varepsilon(\phi, \psi) \rangle_{\{hkl\}} = \langle \varepsilon_{\vec{n}}(\phi, \psi) \rangle_{\{hkl\}} = \langle \varepsilon^L(\phi, \psi) \rangle_{\{hkl\}}$.

In the case of textured materials, the factors XSFs and XEFs depend on the texture function f (given by ODF) and the reflection hkl (Eq. A7.5) [Hauk 97, Welzel 03]. In the case of random texture (macroscopically elastically isotropic material) the relation between the XSFs F_{ij} and the hkl -dependent XEC $S_1^{\{hkl\}}$ and $S_2^{\{hkl\}}$ can be given as follow:

$$F_{11} = \frac{1}{2}S_2^{\{hkl\}}\cos^2\varphi\sin^2\psi + S_1^{\{hkl\}}$$

$$F_{22} = \frac{1}{2}S_2^{\{hkl\}}\sin^2\varphi\sin^2\psi + S_1^{\{hkl\}}$$

$$F_{33} = \frac{1}{2}S_2^{\{hkl\}}\cos^2\varphi + S_1^{\{hkl\}}$$

Eq. A7. 6

$$F_{12} = F_{21} = \frac{1}{2}S_2^{\{hkl\}}\sin 2\varphi\sin^2\psi$$

$$F_{13} = F_{31} = \frac{1}{2}S_2^{\{hkl\}}\cos\varphi\sin 2\psi$$

$$F_{23} = F_{32} = \frac{1}{2}S_2^{\{hkl\}}\sin\varphi\sin 2\psi$$

The hkl-dependent X-ray diffraction elastic constant $S_1^{\{hkl\}}$ and $\frac{1}{2}S_2^{\{hkl\}}$ as well as the XSF stress factors $F_{ij}(\phi, \psi, f)_{\{hkl\}}$ can be evaluated experimentally by the uniaxial tension or bending tests in which a known load is applied. They can be also calculated from single-crystal elastic constants using crystallite coupling models such as Voigt, Reuss or Eshelby-Kröner models, which will be presented in Appendix 8.

Appendix 8 Grains-interaction models

Although the hkl-dependent X-ray diffraction elastic constants $S_1^{\{hkl\}}$ and $\frac{1}{2}S_2^{\{hkl\}}$ as well as the XSF stress factors $F_{ij}(\phi, \psi, f)_{\{hkl\}}$ can be evaluated experimentally applying a known load during the lattice strain measurement, this method is rarely used in reality. Generally, the determination of X-ray elastic constants and the stress factors are calculated from the single-crystal elastic constants adopting appropriate grains-interaction model [Welzel 05].

The Voigt [Voigt 28], Reuss [Reuss 29], Kröner [Kröner 61] as well as Eshelby-Kröner [Eshelby 57, Fréour 12] models are the most important grains-interaction models based on the Hook's law for single-crystal (grain) in expressed in the S-system:

$$\varepsilon_{ij}^{g,S} = S_{ijkl}^{g,S}\sigma_{kl}^{g,S} \quad \text{Eq. A8. 1}$$

The Voigt model:

The assumption in the Voigt model [Voigt 10] is that the strain is distributed homogenously in the specimen, which means single-crystal strain tensor $\varepsilon_{ij}^{g,S}$ is identical for all crystallites in the specimen as shown in Fig. A8.1 [Reimers 08]. Therefore the strain is continuous at the grain boundaries, however, in this case the single-crystal stress tensors are different for different crystallites. These stress discontinuities in the grain boundaries violate mechanical equilibrium in the sample, and the Voigt model cannot predict the real mechanical behaviour of polycrystalline materials [Welzel 05].

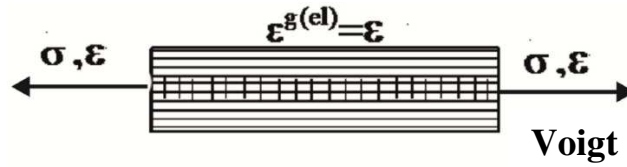


Figure A8.1 Schematic diagram of Voigt model, in which the strain distribution is homogenous in the whole sample ($\varepsilon^{g(el)}$ means the elastic strain for single-crystal) [Baczmański 05].

The stress factors $F_{ij}(\phi, \psi, f)_{\{hkl\}}$ in the Voigt model do not depend on hkl reflection and can be calculated by the formula [Brakman 87, Marciszko 13b]:

$$F_{ij}(\phi, \psi, f)_{\{hkl\}} = m_k^S m_l^S [\mathbf{C}^S]_{kli}^{-1} \quad \text{Eq. A8. 2}$$

$$C_{ijkl}^S = \frac{1}{8\pi^2} \int_0^{2\pi} d\varphi_1 \int_0^{2\pi} d\varphi_2 \int_0^\pi c_{ijkl}^{g,S}(\varphi_1, \Phi, \varphi_2) f(\varphi_1, \Phi, \varphi_2) \sin\Phi d\Phi \quad \text{Eq. A8. 3}$$

where m_k^S and m_l^S are defined in Eq. A7.4 and C_{ijkl}^S is the macroscopic stiffness tensor calculated from single crystal stiffness $c_{ijkl}^{g,S}(\varphi_1, \Phi, \varphi_2)$ for all possible orientations $\varphi_1, \Phi, \varphi_2$ in Euler space (S denotes S-system of coordinates) [Bunge 69, Brakman 87, Marciszko 13b].

The Reuss model:

Contrary to the Voigt model, the Reuss model assumes that the stress distribution is homogeneous in the sample [Reuss 29], i.e. the single-crystal stress tensor σ^S is same for all crystallites (as shown in Fig. A8.2). The single-crystal strain tensors are consequently different in each crystallite, therefore the incompatibility for strain at grain boundaries occurs.

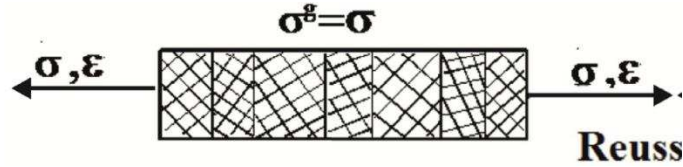


Figure A8.2 Schematic diagram of Reuss model, in which the stress distribution is homogenous in the whole sample [Baczmanski 05].

The stress factor $F_{ij}(\phi, \psi, f)_{\{hkl\}}$ in the Reuss model can be calculated by the formula in Eq. A8.4 [Hauk 97, Welzel 05].

$$F_{ij}(\phi, \psi, f)_{\{hkl\}} = m_k^S m_l^S \frac{\int_0^{2\pi} S_{klij}^{g,S}(hkl, \lambda, \phi, \psi) f(hkl, \lambda, \phi, \psi) d\lambda}{\int_0^{2\pi} f(hkl, \lambda, \phi, \psi) d\lambda} \quad \text{Eq. A8.4}$$

where $S_{klij}^{g,S}$ denotes the single-crystal elastic compliance tensor expressed in the sample frame and λ is the rotation around normal to the planes $\{hkl\}$, cf. Eqs. A7.1 and A7.2A7. .

The Eshelby-Kröner model:

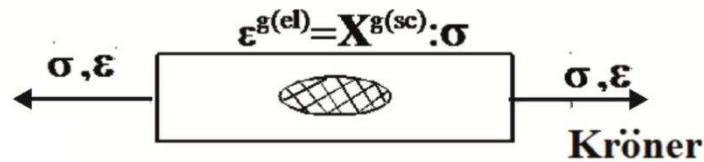


Figure A8.3 Schematic diagram of Eshelby-Kröner model, the grains are considered in shape of an ellipsoidal inclusion embedded into an elastically isotropic homogenous matrix having the elastic properties of the entire polycrystal material [Baczmanski 05].

This model is employed in the self-consistent [e.g. Lipinski 89, Lipinski 95] method. In the Eshelby-Kröner model, the grains are supposed being approximately in shape of ellipsoidal

inclusions embedded into an elastically anisotropic homogenous matrix having the elastic properties of the entire polycrystalline material, as illustrated in Fig. A8.33.

In this model the stresses and strain for inclusion are calculated using the Eshelby model [Eshelby 57], based on the elasticity theory, The analytical solutions of this model is only available for calculation with Kröner's assumptions [Kröner 58], where the matrix is elastically isotropic, the inclusion has a spherical shape and the elastic properties of inclusion is cubic symmetry. Afterwards, this model was extended to the case of crystallographically textured specimens by Kneer [Kneer 65]. The Kneer's method involves spherical anisotropic inclusions embedded in an elastically anisotropic matrix and an iterative numerical calculation is applied instead of the analytical solution.

The elastic strain of a single-crystal inclusion (grain) in a polycrystal aggregate can be expressed as follow in Eq. A8.5 [Welzel 05],

$$\varepsilon_{ij}^{g,S} = [S_{ijkl}^S + t_{ijkl}^{g,S}] \sigma_{kl}^{I,S} \quad \text{Eq. A8.5}$$

where S_{ijkl}^S is the macroscopic mechanical compliance tensor of the aggregate g , $t_{ijkl}^{g,S}$ is a tensor describing the deviation of the elastic properties of an individual grain from the average elastic properties of the entire surrounding polycrystal matrix. The tensor $t_{ijkl}^{g,S}$ depends on the shape of the inclusion, the single-crystal elastic constants and the macroscopic mechanical compliance tensor S_{ijkl}^S of the aggregate.

In this thesis, the stress calculations were carried out by using different models mentioned above, in order to avoid the errors caused by a single model. Then in comparison between the stress calculations results, more accurate stress value can be concluded, the details will be specifically described later.

Appendix 9 Technique drawings of tested samples

For neutron diffraction measurement in ISIS, Oxford, United Kingdom:

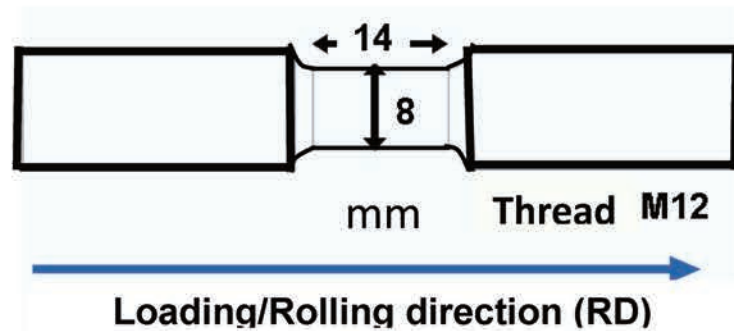


Figure A9.1 Technical scheme of sample used in neutron measurements.

For synchrotron diffraction measurement in ESRF, Grenoble, France:

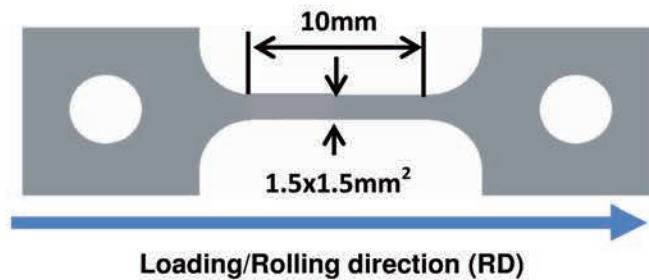


Figure A9.2 Technical scheme of samples used in synchrotron experiment.

Appendix 10 Determination of sample-detector distance L for synchrotron diffraction measurement

The calibration was carried out by two 2D patterns captured in different detector position (L and L_1 , where L is the detector position during the in situ measurement and L_1 is the additional position) and the difference between the two distances ΔL was measured

The two diffraction patterns recorded with different detector positions were treated by software FIT2D [Hammersley 96]. FIT2D enables to determine the length of radius R for each diffraction ring and the position of the diffraction patterns centre, as shown in Fig. A10.2.

By applying Thales theorem, the link between 2θ , R and L can be expressed as (Fig. A10.1A10.1):

$$\tan 2\theta = \frac{R_1}{L - \Delta L} = \frac{R_0}{L} \quad \text{Eq. A10.1}$$

which allows us to obtain the accurate sample-detector distance from each diffraction ring:

$$L = \frac{R_0 \Delta L}{R_0 - R_1} \quad \text{Eq. A10.2}$$

Then by calculating the average on sample-detector distances obtained from different diffraction rings, the accurate sample-detector distance (L) during in situ real diffraction measurement can be found.

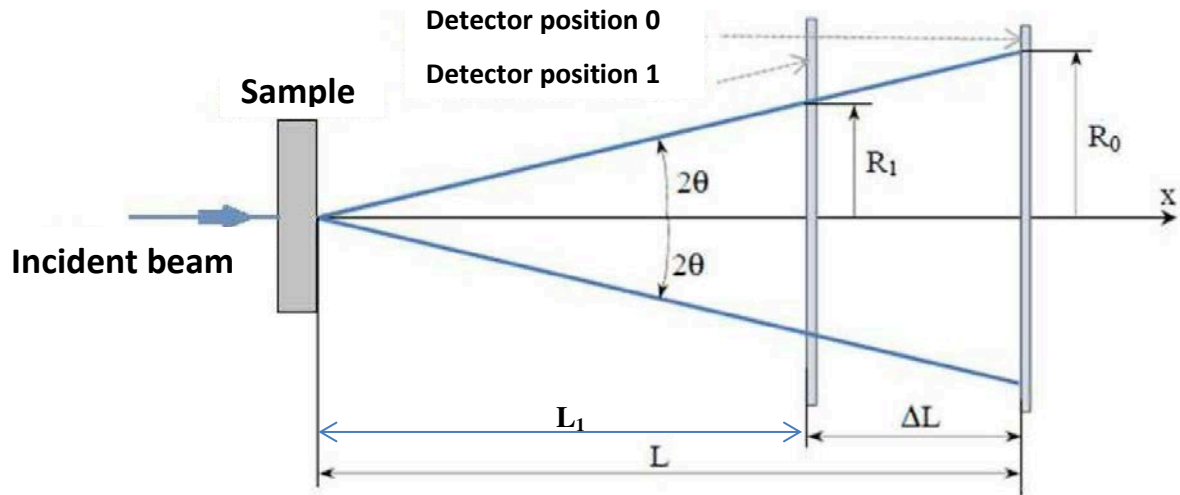


Figure A10.1 Illustration of the calibration for the distance between sample and detector position 0 before in situ tensile test. The detector was moved backward with a known displacement ΔL until the position 1. The radius R_0 and R_1 are measured on the recorded 2D diffraction patterns [François 12].

The 2D patterns recorded during the in situ diffraction measurements were treated using FIT2D [Hammersley 96] and MULTIFIT [Merkel 11] programs. Besides the determination of radius for diffraction rings, FIT2D can be also used to convert the 2D patterns into one dimensional 2θ diffractogram. The recorded beam intensity was integrated over a given azimuth angle range within a “cake shape” sector (as shown in Fig. A10.2a, the azimuth angle range is defined $\pm 7.5^\circ$) to create a one-dimensional diffractogram (Fig. A10.2). It should be mentioned that, during measurement the scattering vector is not perfectly aligned with the loading direction due to inclination from plane of detector by the θ angle. However, this effect can be neglected due to a small value of θ which changes in the range from 1° to 3.5° .

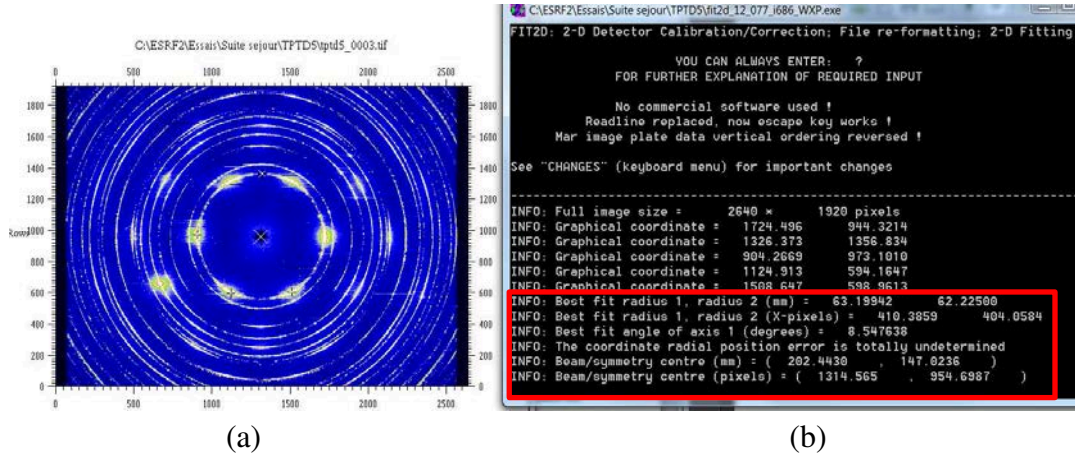


Figure A1.2 (a) An example of the determination of diffraction pattern centre and the radius length of diffraction rings using the FIT2D program and (b) the results obtained in mm and pixel.

Appendix 11 Stress calibration during necking process and macro-mechanical

The local applied stress inside gauge volume were calibrated for each test during the large deformation range using the method proposed by Baczmański et al. [Baczmański 11], in order to avoid the influence of sample narrowing effect occurred during tensile test. This stress calibration is based on the assumption that in the gauge volume, the true macro-stress Σ_{RD} (averaged over the whole gauge volume) is proportional to the arithmetic mean lattice elastic strain $\langle \varepsilon_{RD} \rangle_{mean}^{fer+aus}$ calculated over all hkl reflections belonging to both ferritic and austenitic phases. This assumption, represented by Eq.A11.1 was applied not only for the elastic range but also for the large plastic deformation and even during the initiation of damage process. The calibrated macro-stress was determined as:

$$\Sigma_{RD} = k \langle \varepsilon_{RD} \rangle_{mean}^{fer+aus} \quad \text{Eq.A11.1}$$

where: k is a scalar coefficient describing the relationship between macro-stress Σ_{RD} in the diffraction gauge volume and the arithmetic mean calculated over all available lattice strains measured for both phases $\langle \varepsilon_{RD} \rangle_{mean}^{aus+fer}$. The macro-strain $\langle \varepsilon_{RD} \rangle_{mean}^{aus+fer}$ is equal to the mean strain for both phases (Eq.A11.2 **Erreur ! Source du renvoi introuvable.**):

$$\langle \varepsilon_{RD} \rangle_{mean}^{fer+aus} = \frac{\langle \varepsilon_{RD} \rangle_{fer} + \langle \varepsilon_{RD} \rangle_{aus}}{2} \quad \text{Eq.A11.2}$$

where $\langle \varepsilon_{RD} \rangle_{fer}$ and $\langle \varepsilon_{RD} \rangle_{aus}$ are the mean strains over lattice strains measured respectively in ferrite and austenite. The raw micro-strain vs. applied stress evolution is presented in Fig. A11.1a and the compression between the plots of micro-strain in function of applied stress and calibrated stress are presented in Fig. A11.1b.

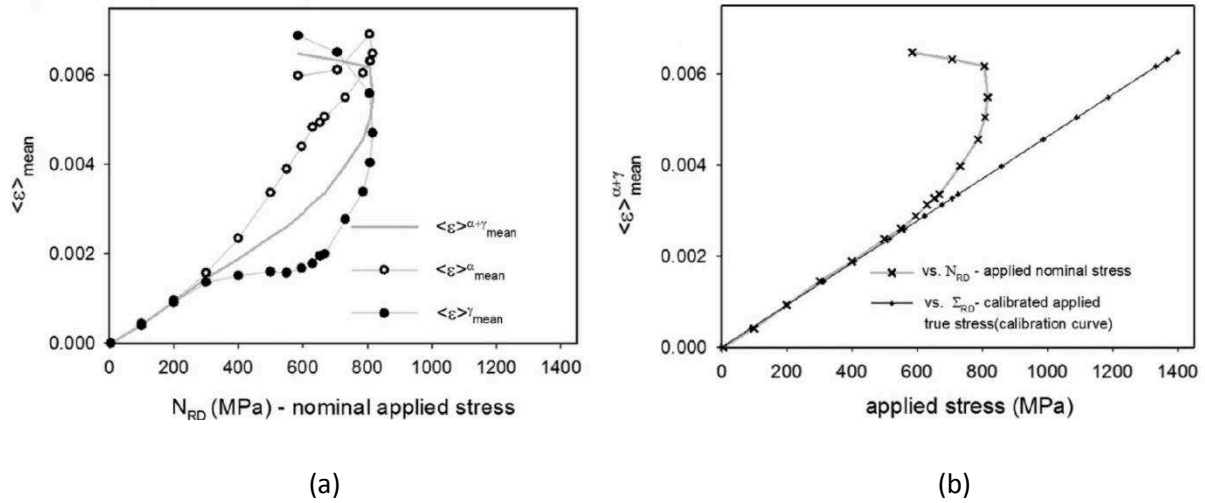


Figure A11.1 (a) Measured mean values of the elastic lattice strains $\langle \varepsilon_{RD} \rangle_{mean}^{fer}$, $\langle \varepsilon_{RD} \rangle_{mean}^{aus}$ and $\langle \varepsilon_{RD} \rangle_{mean}^{fer+aus}$ vs. the nominal applied stress N_{RD} . (b) Comparison between the dependences of $\langle \varepsilon_{RD} \rangle_{mean}^{fer+aus}$ vs. calibrated stress Σ_{RD} and $\langle \varepsilon_{RD} \rangle_{mean}^{fer+aus}$ vs. nominal stress N_{RD} (superscript α denotes ferrite and γ denotes austenite).

The real macro-stress in the heterogeneously deformed area (for example necking region) is assumed to be proportional to the average elastic macro-strain $\langle \varepsilon_{RD} \rangle_{mean}^{aus+fer}$ in both the elasto-plastic stage and large deformation stage, even in the damage stage. Therefore, the value of calibrated Σ_{RD} can be calculated for the gauge volume from the measured $\langle \varepsilon_{RD} \rangle_{mean}^{aus+fer}$ if the value of the k coefficient is known. This coefficient can be determined from the elastic range of sample deformation using linear regression. The inter-phase and inter-granular stresses were neglected in the stress calibration because the calculation of the average elastic macro-strain $\langle \varepsilon_{RD} \rangle_{mean}^{aus+fer}$ was made considering a large number of grains having various orientations. The global inter-granular and inter-phase stress, defined as the deviations from macroscopic stress, must cancel each other out and sum to zero over a diffracted volume. This assumption was confirmed in a previous work using a self-consistent model by Baczmański et al. [Baczmański 11] and [Le Joncour 10, 11].

Appendix 12 Preparation of IIT specimens

For the IIT on fractured sample, the mechanical properties of the material were measured inside the sample, after successive mechanical polishing until the symmetry plane BB in the centre of the sample, as shown in Fig. A12.1A12.1 .

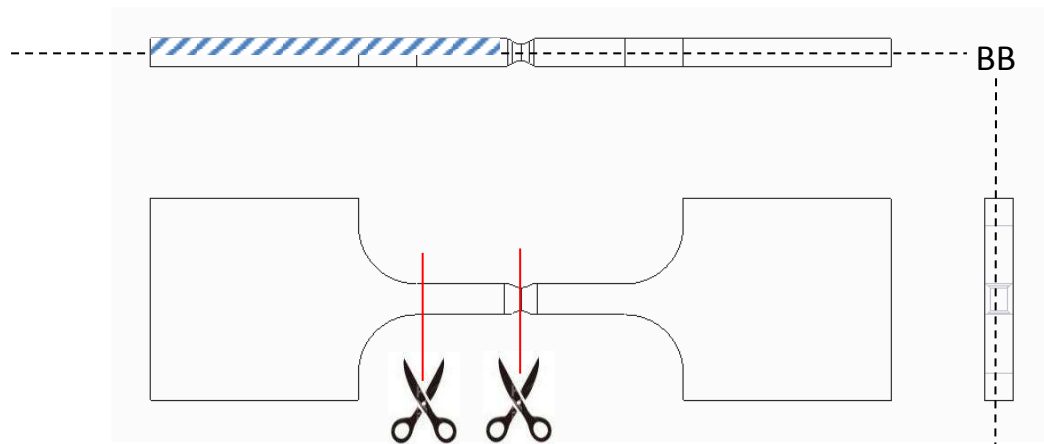



Figure A12.1 Illustration of the central plane BB, tested by instrumented indentation test. The removed layer is shown by ().

A part of the broken sample, between the fracture edge and the beginning of sample as indicated in Fig. A12.1 was embedded in a pillar-shaped resin as shown in Fig. A12.2.



Figure A12.2 The photo of specimen embedded in pillar-shaped resin.

The mechanical polishing was performed with a Vector® LC 250 automatic lapping and polishing unit provided by BUEHLER An ITW International, Lake Bluff, USA. The material layer above the symmetry plane was polished off step by step, while the thickness of the removed layer was checked by a laser gauge (KEYENCE LK-2001) after each polishing step.

A 600-grit silicon carbide abrasive film disc was firstly used for 10 min of polishing with rotation speed of 200 rpm, under load of 20 N. Subsequently, the polishing was continued for 20 min with 800-grit silicon carbide abrasive film discs (200 rpm, under load of 10N), and next the 1200-grit and 2500-grit abrasive film discs were used to refine the polished surface for respectively 5 min and 2 min, with rotation speed of 200 rpm, under load of 10 N. This material is polishing removed until the total layer of $584 \pm 10 \mu\text{m}$ was removed. After that, a smooth surface was prepared for the indentation test using the polishing cloths with respectively $3 \mu\text{m}$ and $1 \mu\text{m}$ diamond lapping suspension (provided by ESCIL, Chassieu, France), under a load lower than 10N and with a rotation speed of 150 rpm. Finally, super-finishing was performed on the specimen surface with alumina suspension of $0.3 \mu\text{m}$ (ESCIL, Chassieu, France) under a load lower than 10 N. In total, the layer of $675 \pm 10 \mu\text{m}$ was removed by polishing, i.e. almost half of the initial sample thickness ($\approx 1.4 \text{ mm}$).

In addition to the specimen taken from the fractured sample, three other specimens having TD, ND and RD directions normal to the investigated surfaces were prepared (as shown in Fig. A12.3). The preparation process of initial specimens was similar to that of the fractured specimen, but no such thick layer of material was removed. The samples made from the initial material will be named TD, ND and RD, respectively.

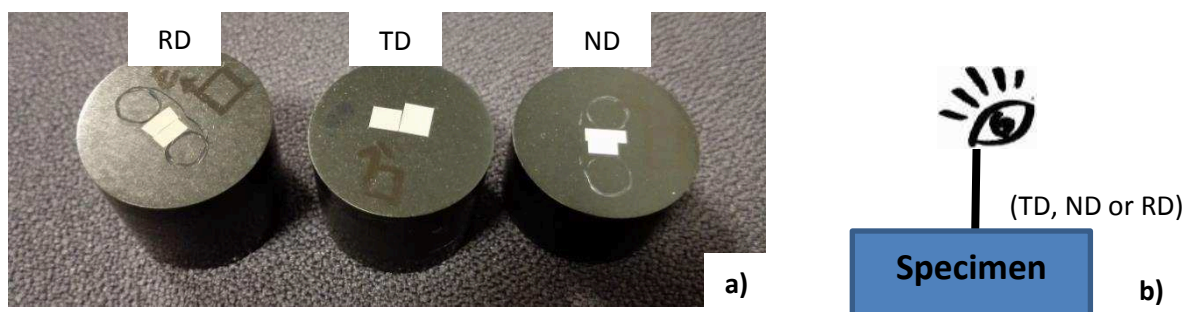


Figure A12.3 (a) The 3 specimens taken from the as-received material respectively for ND, TD and RD directions normal to the surface. (b) Illustration of normal to the specimen surface.

Appendix 13 Estimation of the plastified zone induced by nano imprint for Instrumental Indentation Tests

The plastic zone (Fig. A13.1) induced by indentation imprint is an important factor which should be taken into account during IIT, in order to avoid the interference of indentation results between test points. To this end, an estimation of plastic zone was done to help us determine the minimal distance between test points required for the measurements.

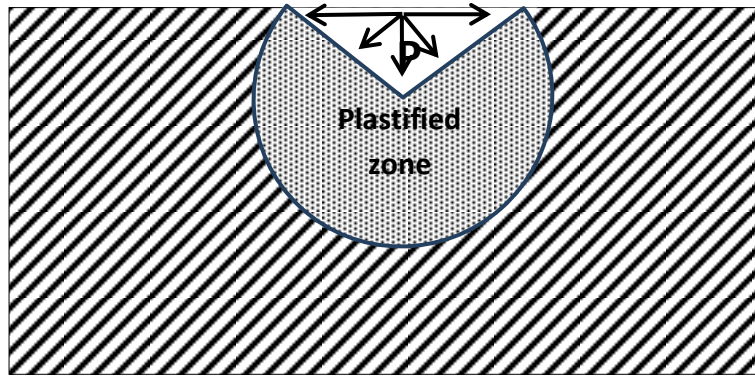


Figure A13.1 Illustration of plastified zone caused by indentation imprint.

The model proposed by Mata et al. [Mata 06] was employed to determine the upper limit and the lower limit of plastified area. This model is based on the analogy between indentation and the expansion of a spherical cavity [Bishop 45, Johnson 70, Chiang 82], which in turn provides relationships between contact parameters and the elasto-plastic mechanical properties of the material.

The employed model assumes that the indentation tip creates a spherical cavity and exerts hydrostatic pressure at the surface of cavity (illustrated by Fig. A13.1). Further inflation of the cavity during indentation process causes modifications of the stress-strain state in the surrounding medium, leading to plastic deformation around the cavity. This model is based on the formula:

$$c = R \left(\frac{2E}{3\sigma_{ys}} \right)^{\frac{1}{3}} \quad \text{Eq. A13.1}$$

where c is the radius of plastified zone, R is the radius of spherical cavity created by indentation tip, E is Young's modulus and σ_{ys} is the yield stress of the tested material.

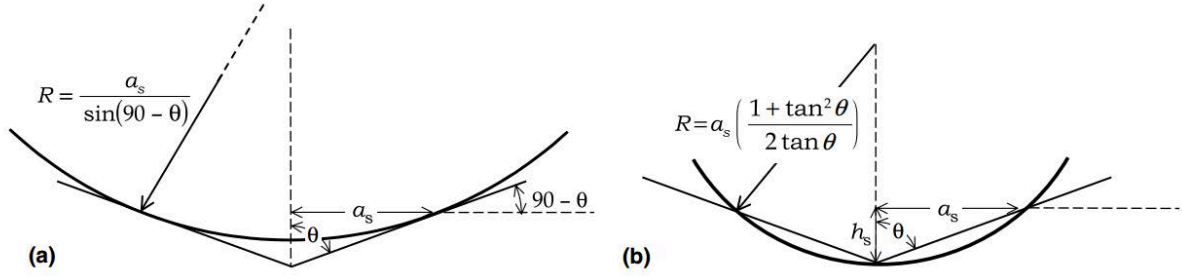


Figure A13.2 Schematic drawing of equivalent cavity created by indentation imprint. (a) The sphere is tangent to the contact radius a_s ; (b) The sphere intersects the contact radius a_s and the penetration depth h_s [Mata 06].

To estimate the upper and lower limit of the plastified zone, two assumptions were proposed by [Mata 06]. As illustrated in Fig. A13.2, two configurations can be assumed for the relation between the indentation tip (available for conical, spherical, Vickers and Berkovich tips) and the spherical cavity created during indentation.

The first configuration (Fig. A13.2 A13.2 a) assumes that the sphere of cavity is tangent at the contact boundary of an imprint (cf. section 2.2.1), which can give the lower limit of plastified zone, and the expression of the radius of spherical cavity is in function of contact radius a_s :

$$R = \frac{a_s}{\sin(90^\circ - \theta)} \quad \text{Eq. A13.2}$$

where θ is the equivalent semi-apex angle which is equal to 70.3° in the case of Berkovich tip (cf. section 2.2.2). The equivalent projected contact radius a_s can be calculated in function of the penetration depth h_s , which is equal to 500 nm for the tests in this work, using the formulas Eq. 2.11 (supposing $C=0$ to simplify the estimation) and Eq. 2.15. Finally, the a_s is approximately equal to $1.4 \mu\text{m}$ and the radius of spherical cavity R_1 , calculated with the above assumption, is equal to $4.11 \mu\text{m}$.

For the second assumption concerning relation between the indentation tip and the spherical cavity (Fig. A13.2b), the radius of sphere is calculated by equation:

$$R = a_s \left(\frac{1 + \tan^2 \theta}{2 \tan \theta} \right) \quad \text{Eq. A13.3}$$

In this case, the radius of cavity R_2 is equal to $2.20 \mu\text{m}$ for the performed tests.

Then, the radius of plastified zone was determined using Eq. A13.1. In calculations the Young's modulus E equal to 200 GPa and 220 GPa, and yield stress equal to 300 MPa and 220 MPa were assumed respectively for ferrite and austenite (cf. table 1.1 page 12). The radius of plastified zone of austenite is equal to 34.8 μm using the first assumption and 18.6 μm using the second assumption, while the radius of plastified zone of ferrite is equal to 32.4 μm for the first assumption and 17.34 for the second assumption. Hence, the average radiuses of plastified zone for these two considered assumptions are 26.7 μm and 24.9 μm for ferrite and austenite, respectively. According to the estimation about the dimension of plastified zone, and taking into account the size of specimen as well as the intended number of imprints, the minimal distance between test points in the IIT is selected as 50 μm .

Appendix 14 Calculation of hardness and Young's modulus by IIT

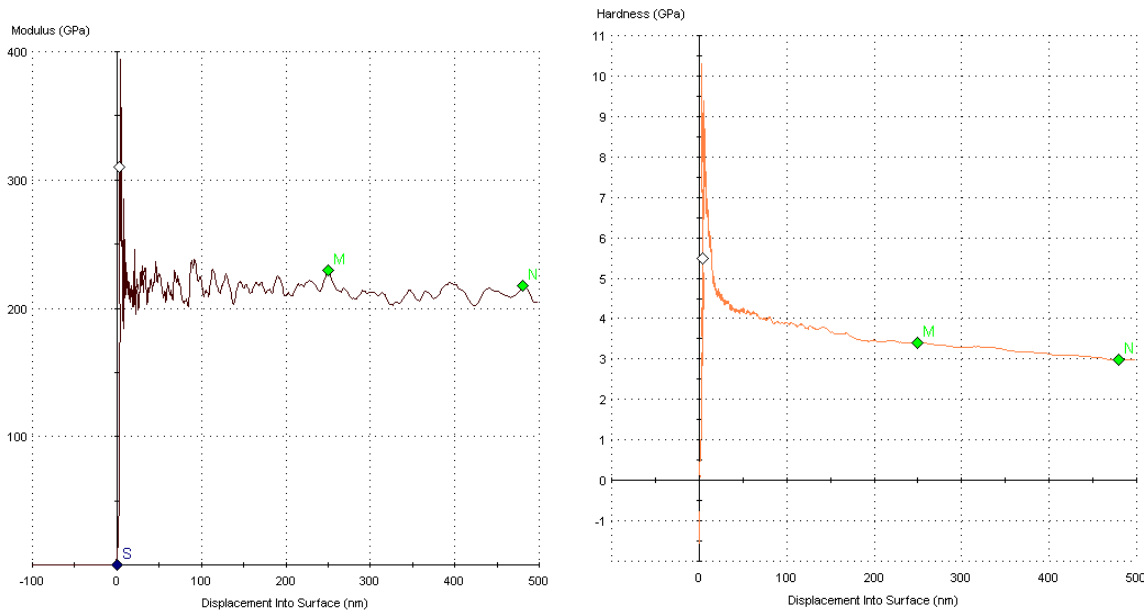


Figure A14.1, Illustration for calculations of Young's modulus and hardness by IIT. (a) The curve Young's modulus vs. imprint depth. (b) The curve hardness vs. imprint depth.

As illustrate in Fig. A14.1, the hardness an Young's modulus are determined by the average value between depth M and N. M is considered as the beginning of stabilization of physical quantities (Modules E or Hardenns H). N is the end depth around 480 nm, in order to ensure the calculation range. The total imprint depth is 500 nm.

Appendix 15 Statistic results of ITT on the initial samples

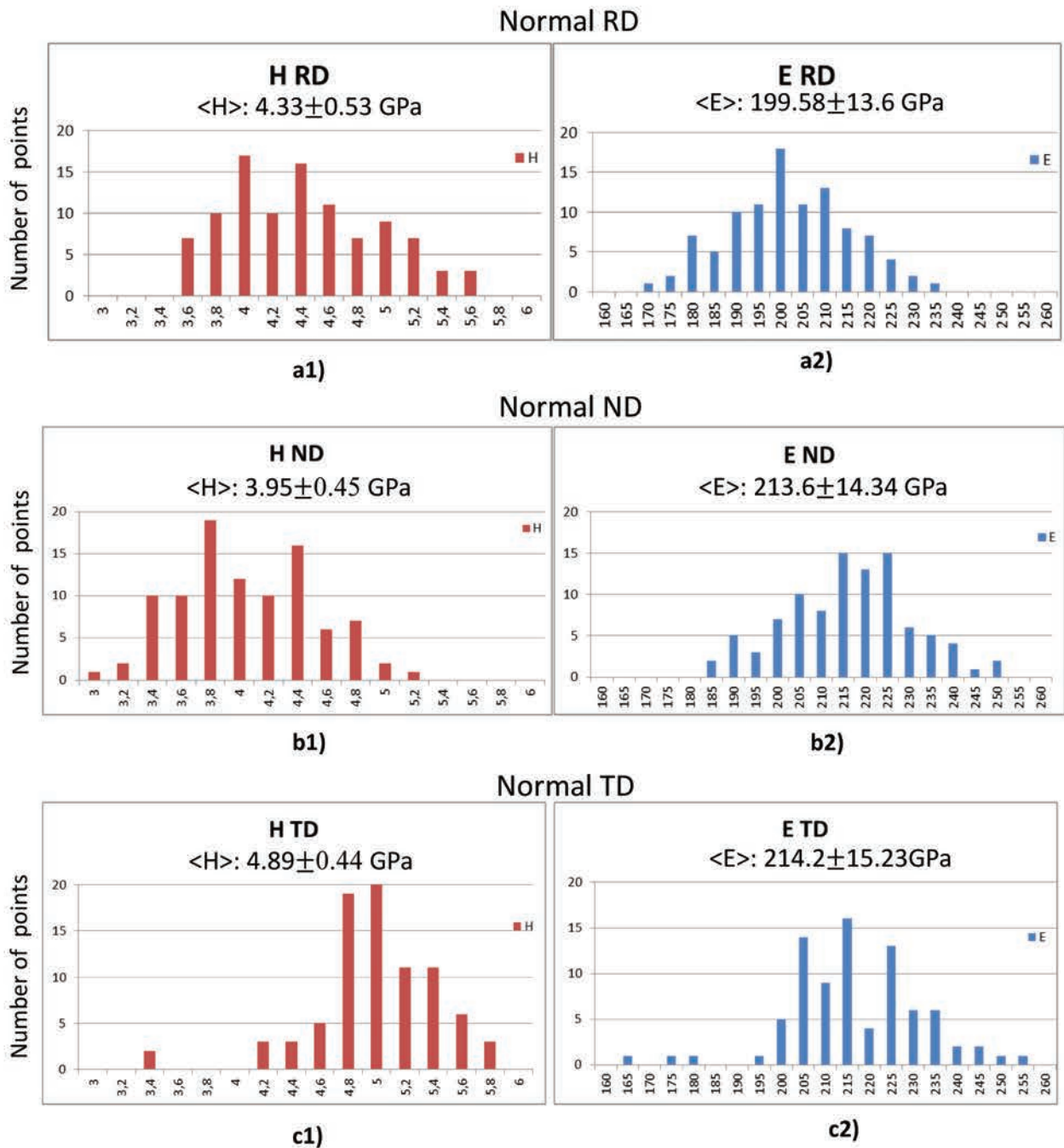


Figure A15.1 The histograms of IIT results of Vickers hardness H and Young's modulus E obtained for the initial specimen with RD (a), ND (b) and TD (c) normal to the investigated surface.

Appendix 16 Distribution maps of modulus E and hardness H for IIT with reduced points

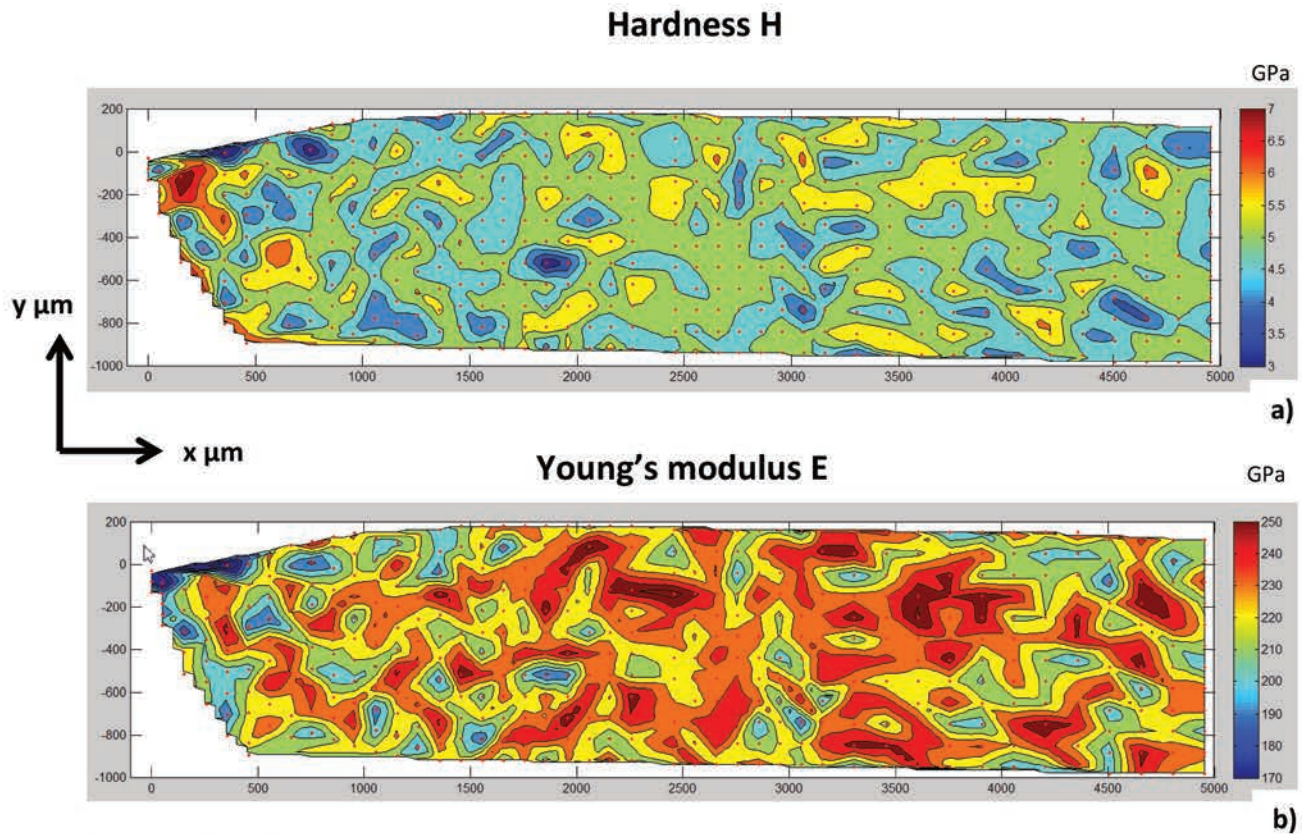


Figure A16.1 The distribution maps of (a) hardness and (b) Young's modulus on the basis of all test points for which the IIT was performed.

The distribution maps of hardness and Young's modulus with reduced IIT points are presented in Fig. A16.1, where the red points represent the test points. From these maps we can see that the deviation of hardness or Young's modulus is more significant in the range of x axis from 0 to 1200 μm , which contains much more test points than the rest of specimen.

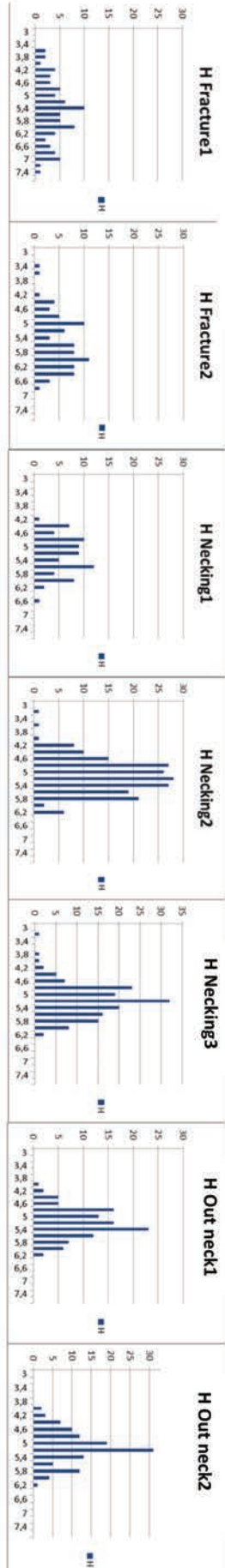
Appendix 17 Statistic results of ITT along the fractured sample

In order to analysis quantitatively the evolution of hardness and Young's modulus in differing the pressed phase, the statistical analysis was carried out in three categories. The first category is noted as Ferrite+Austenite+Boundary, with all test points (which means test points on ferrite, austenite and on the boundary between the two phases were identified by microscope, see Fig. 5.4). The second category is noted Ferrite, in which only the test points selected for ferrite were taken into account. The third category is noted Austenite, where only test points for austenite were counted in.

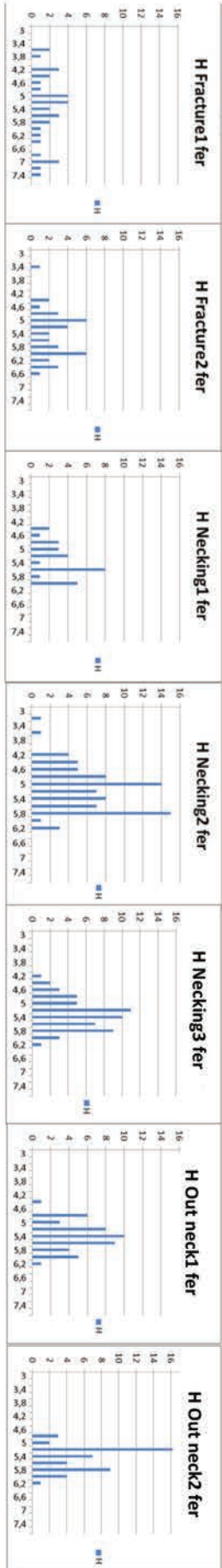
The statistics results (Fig. A17.1) show that the distribution range of hardness H exhibits a global narrowing tendency from fractured edge to the end of specimen. In the zone Fracture 1, the hardness value spreads in a broad range from 3.4GPa to 7.4GPa. In the zone Fracture 1, the hardness values are relatively low and an important fluctuation, both highest and lowest values occurred along the fracture edge. In the zone Fracture 2, the hardness values are relative higher, and no extreme fluctuation occurred in this area. Less fluctuation on hardness occurred in the other areas until the end of specimen. Then the distribution range of hardness becomes narrower with the increasing distance from the fracture edge. In conclusion, farther the zone is away from the fracture, the distribution ranges of hardness become narrower. This phenomenon corresponds to previous observation on the distribution maps (Fig. A16.1 and Fig. 5.6 page 128), the heterogeneity of material is more important in the severe deformed area close to fracture edge, in comparison with the less deformed area outside of the neck.

Fig. A17.2 reports the distribution of Young's modulus values in different zones along specimen. The range of hardness for all test points in zone Fracture 1 is from 160 to 250GPa. For austenite the distribution range become slightly narrower with the increasing distance from the fracture edge, but it keeps almost stable in different zones along the specimen. Besides, we can see that for the ferritic phase, the range of E is initially from 170 to 240GPa within zone Fracture 1, then it shifts significantly to higher values with increasing distance from the fracture edge, and finally reaches values between 215 and 265GPa in the zone Out neck2. This variation tendency of Young's modulus in ferrite is also well seen on the distribution map on which the values of E go down near the fracture edge. The reduction in the E value of ferrite near the fracture could be explained by the pronounced plastic deformation [Hordon 58].

Ferrite+Austenite+ Boundary (a)



Ferrite (b)



Austenite (c)

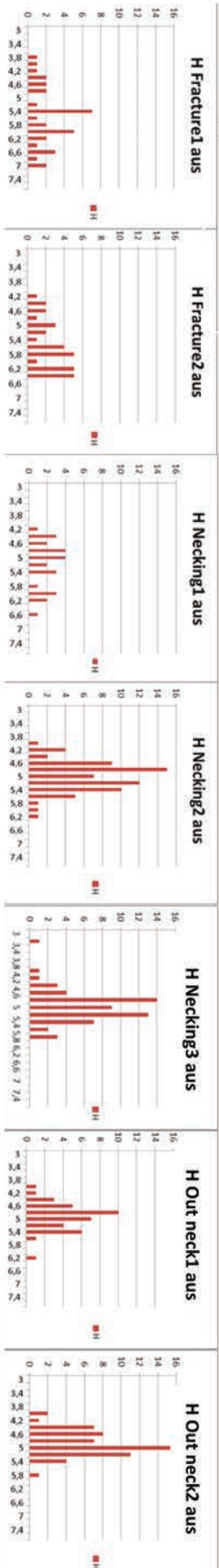
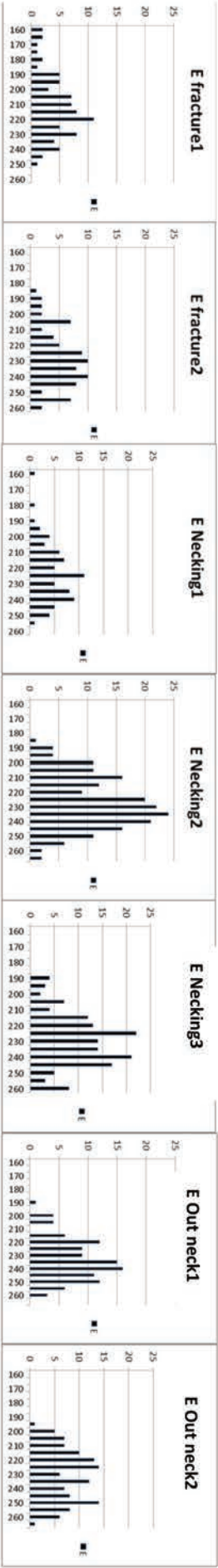
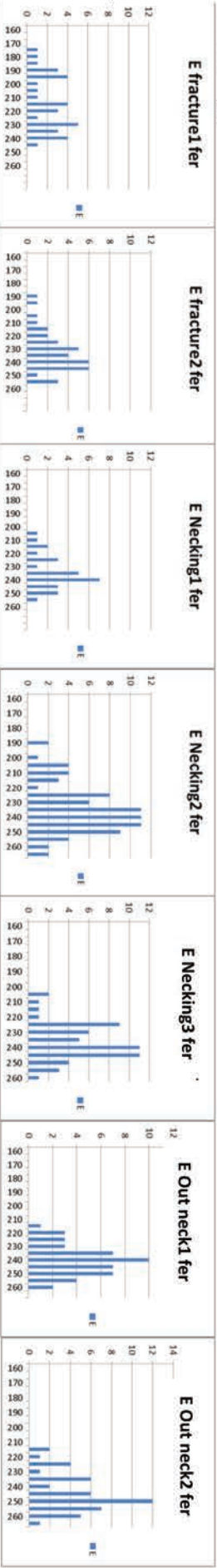


Figure A17.1 The statistical data of hardness H in different areas along fracture specimen, for all test points (a), for test points in ferrite (b) and for test points in austenite (c).

Ferrite+Austenite+ Boundary (a)



Ferrite (b)



Austenite (c)

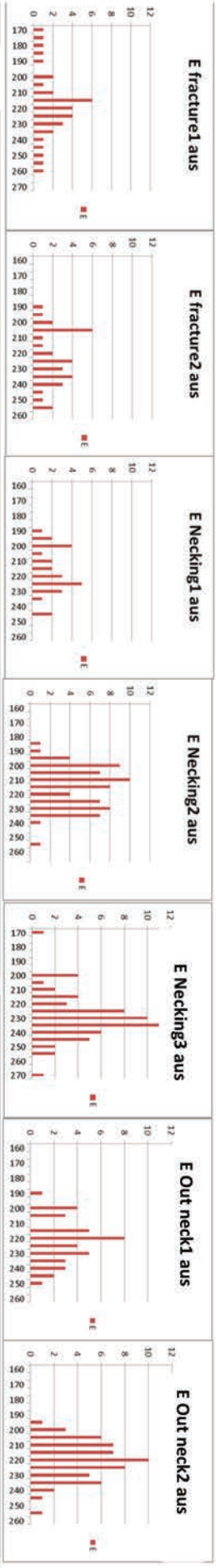


Figure A17.2 The statistical data of Young's modulus E in different areas along fracture specimen, for all test points (a), for test points in ferrite (b) and for test points in austenite (c).

Appendix 18 Estimation of volume fraction for α and β titanium in Ti-18

The binary images after conversion are shown in Fig. A18.1 and Fig. A18.2, where: Fig. A18.1a and A18.2a are binary images corresponding respectively to Fig. 1.22a and 1.23a; Fig. A18.1b and A18.2b are respectively taken from the white framed zone as shown beside them (Fig. A18.1c and A18.2c). In the binary images, the black pixels represent α titanium, the white pixels indicate β titanium. By counting respectively the percentage of black pixels in Figs A18.1a and A18.2a, the surface fraction of primary α titanium α_p in radial and axial cross sections can be obtained. As well, the percentage of black pixels in Figs A18.1b and A18.2b allows determining the surface fraction of α_s in β titanium matrix on both cross sections. The estimated surface fractions of α_p and α_s are listed in table 1.12 page 36. In calculations the following formula was used:

$$f_{\alpha} = f_{\alpha_p} + f_{\alpha_s} \times (1 - f_{\alpha_p}) \quad \text{Eq. A18.1}$$

where f_{α} , f_{α_p} and f_{α_s} are respectively the total surface fraction of α titanium, the surface fraction of α_p nodules calculated from Fig. A18.1a and Fig. A18.2a and the surface fraction of α_s lamellas calculated from Fig. A18.1b and Fig. A18.2a.

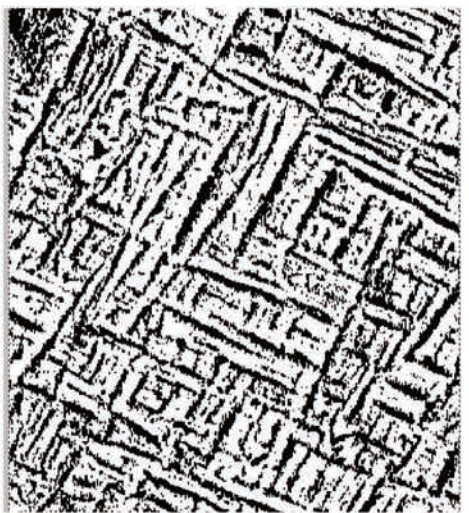
An investigation on the volume fractions of α titanium in Ti-18 has been previously carried out for different combinations of solution treatments and aging temperatures [Lebrun 14]. The results presented in table A18.1 show that depending on the conditions of thermal treatment, the volume fraction of α phase changes between 44% to 52% [Lebrun 14]. This agrees with the estimation done in the present work, where mean volume fraction of α phase determined from two measured sections is about 45% (cf. table 1.12 page 36).

| <i>Solution Treatment Temperature</i> / <i>Aging Temperature</i> | 593°C | | 621°C | | 649°C | |
|--|---------|----------|---------|----------|---------|----------|
| 818°C | 10 | 40 | 13 | 36 | 13 | 31 |
| 832°C | 2 | 45 | 4 | 48 | 2 | 43 |
| Volume Fraction of α phase (%) | primary | acicular | primary | Acicular | primary | Acicular |

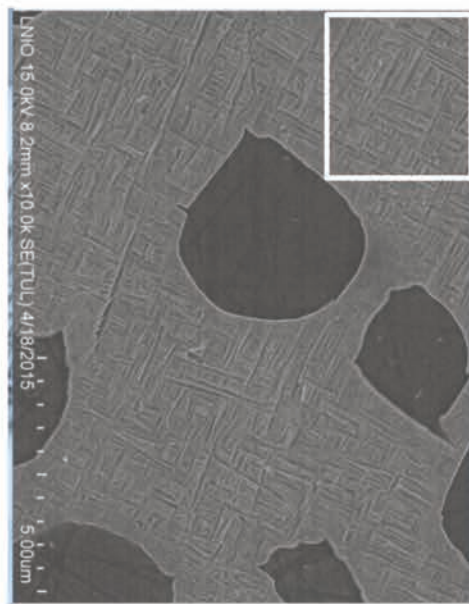
Table A18.1 Volume fraction of α titanium for different combinations of solution treatments and aging temperatures [Lebrun 14]



(a)

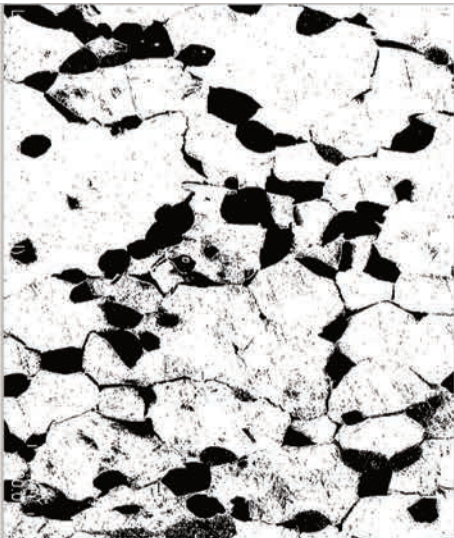


(b)

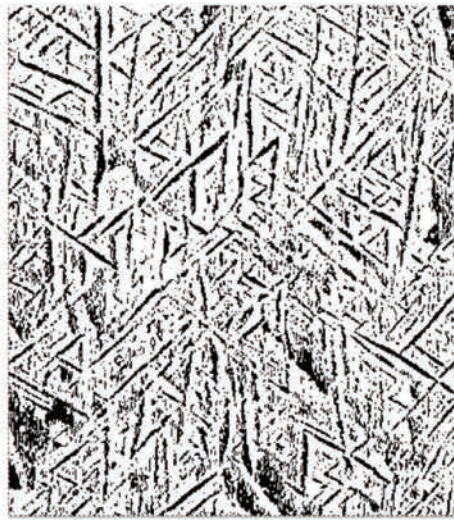


(c)

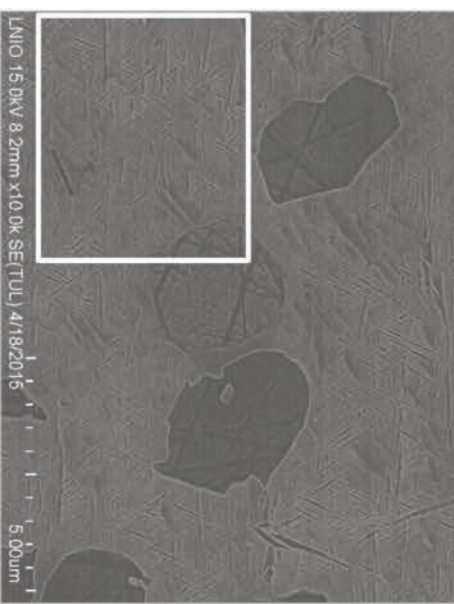
Figure A18.1 Binary images of the microstructure of Ti-18 on transverse section: (a) low-magnification, estimation of surface fraction of globular α_p ; (b) high-magnification image, estimation of surface fraction of acicular α_s ; (c) Zone taken from β matrix for image b.



(a)



(b)



(c)

Figure A18.2 Binary images of the microstructure of Ti-18 on longitudinal section: (a) low-magnification, estimation of surface fraction of globular α_p ; (b) high-magnification image, estimation of surface fraction of acicular α_s ; (c) Zone taken from β matrix for image b.

Appendix 19 Determination of initial stress in Ti-18 sample

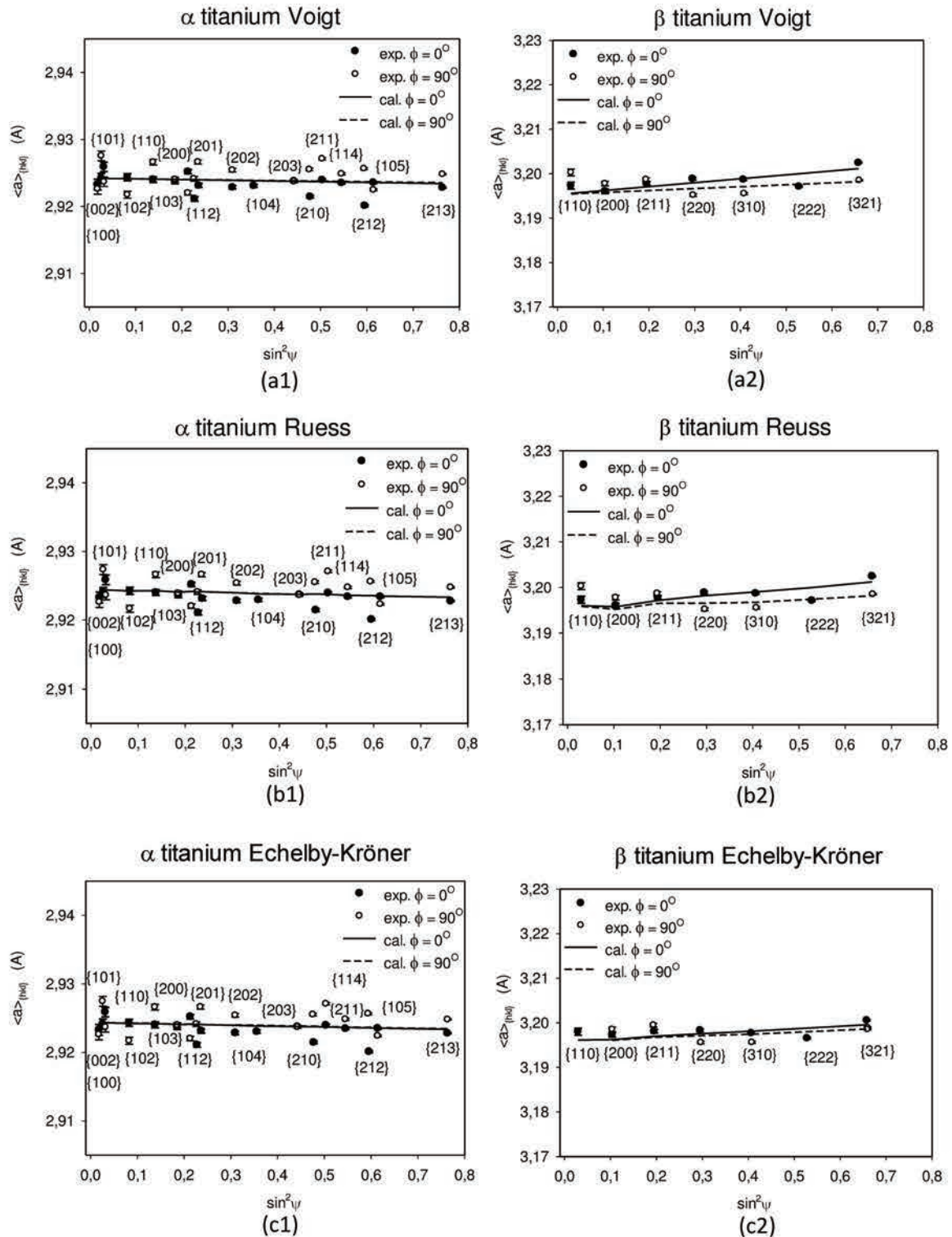


Figure A19.1 $\langle a(\phi, \psi) \rangle_{[hkl]}$ vs $\sin^2 \psi$ plots determined for the initial sample without tensile loading, plots for α and β phases were fitted using Voigt model (a), Reuss model (b) and Eshelby-Kröner model (c).

The Fig. A19.1a1, b1 and c1 show very similar tendency for the plots obtained for α titanium fitted by all three models. All experimental points spread almost linearly with only small deviations caused by the crystal anisotropy, allowing a good fitting by least square method. A tiny negative slop on the plots indicates very slight initial compressive stresses both in LD ($\sigma_{LD} = \sigma_{11}, \phi = 0^\circ$) and in TD ($\sigma_{TD} = \sigma_{22}, \phi = 90^\circ$) determined for α phase. From the figure A19.1 a2, b2 and c2, more significant positive slop for $\langle a(\phi, \psi) \rangle_{\{hkl\}}$ vs. $\sin^2 \psi$ plots can be observed for β titanium, suggesting noticeable initial tensile stress in TD and a relatively lower tensile stress in ND.

Appendix 20 $\langle a(\phi, \psi) \rangle_{\{hkl\}}$ vs $\sin^2 \psi$ plots for stress determination during tensile test of Ti-18

The experimental plots $\langle a(\phi, \psi) \rangle_{\{hkl\}}$ vs. $\sin^2 \psi$ plots fitted by theoretical lines for two angles ϕ (0° and 90°) and both phases are presented in Fig. A20.1. The example four different states during the tensile test are shown for the thresholds A, B, C and for the unloaded sample. All curves are almost linear with small deviations caused by the crystal anisotropy, however larger deviations from the mean phase stresses are not seen on these plots. Significant slope of the plots measured in the direction of applied load ($\phi = 0^\circ$) indicates large tensile stresses in both phases. The experimental results (points) are correctly adjusted using a least square minimization (lines), including small deviations from linearity during loading state. No significant spread of experimental points around the lines was observed after unloading/fracture of the sample. We can conclude that the shear stresses σ_{13}^{ph} and σ_{23}^{ph} , stress gradients as well as the second order stresses within each phase are negligible in the gauge volume analysed by X-rays. Due to the nearly orthorhombic symmetry of the texture and the symmetrical character of tensile load, the shear stress component σ_{12} is expected to be also negligible. Therefore the determined biaxial stress state (σ_{11} and σ_{22} components) completely describes the stress state in both phases.

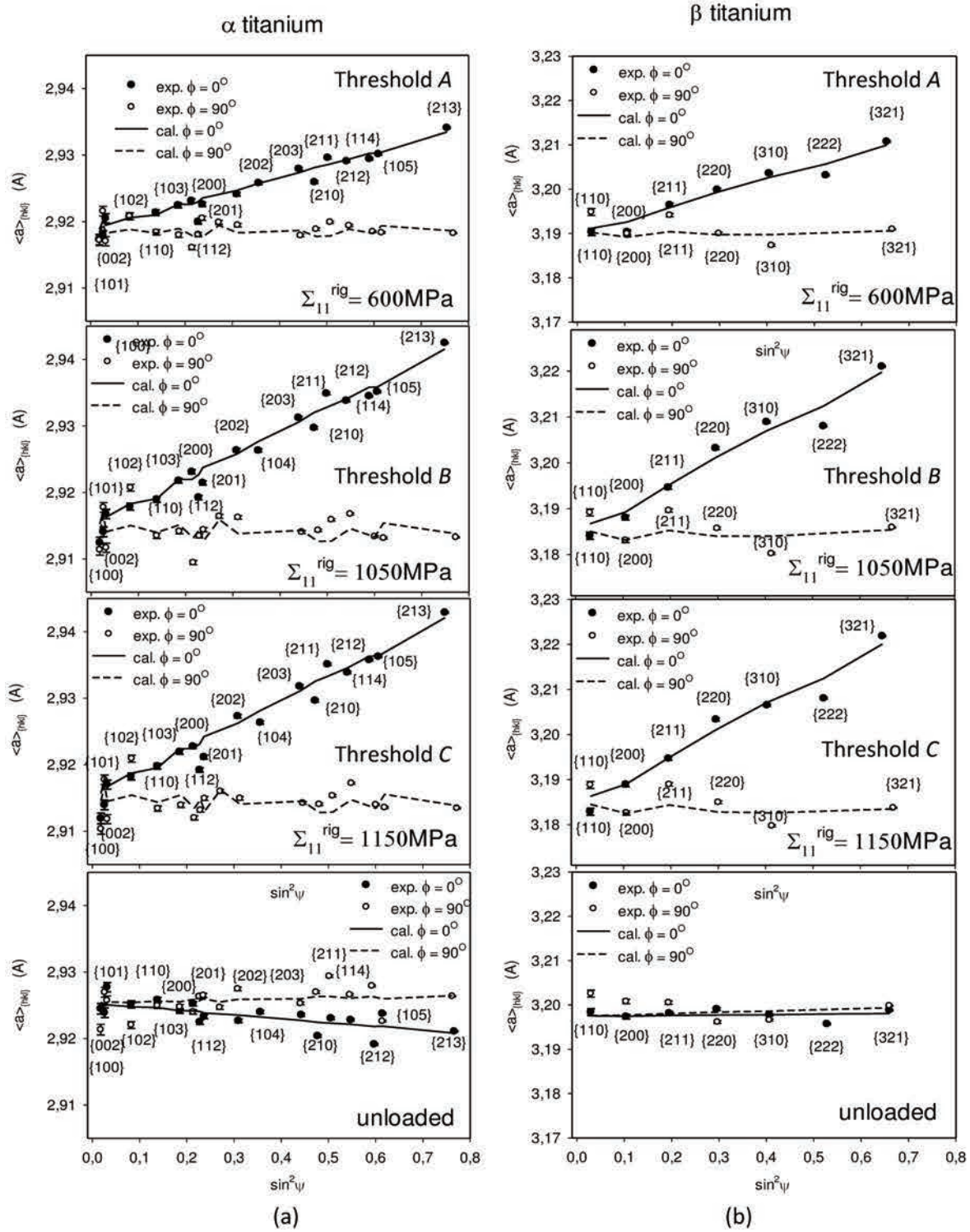


Figure A20.1 The $\langle a(\phi, \psi) \rangle_{\{hkl\}}$ vs $\sin^2 \psi$ plots determined for the applied loads: $\Sigma_{11}=600$ MPa (threshold A), $\Sigma_{11}=1050$ MPa (threshold B), $\Sigma_{11}=1150$ MPa (threshold C) and for the unloaded sample after fracture. The experimental points and fitted lines are presented for α phase (a) and β phase (b).

Appendix 21 Evolution of individual hkl reflections for α and β titanium in transverse direction during tentiles test of Ti-18

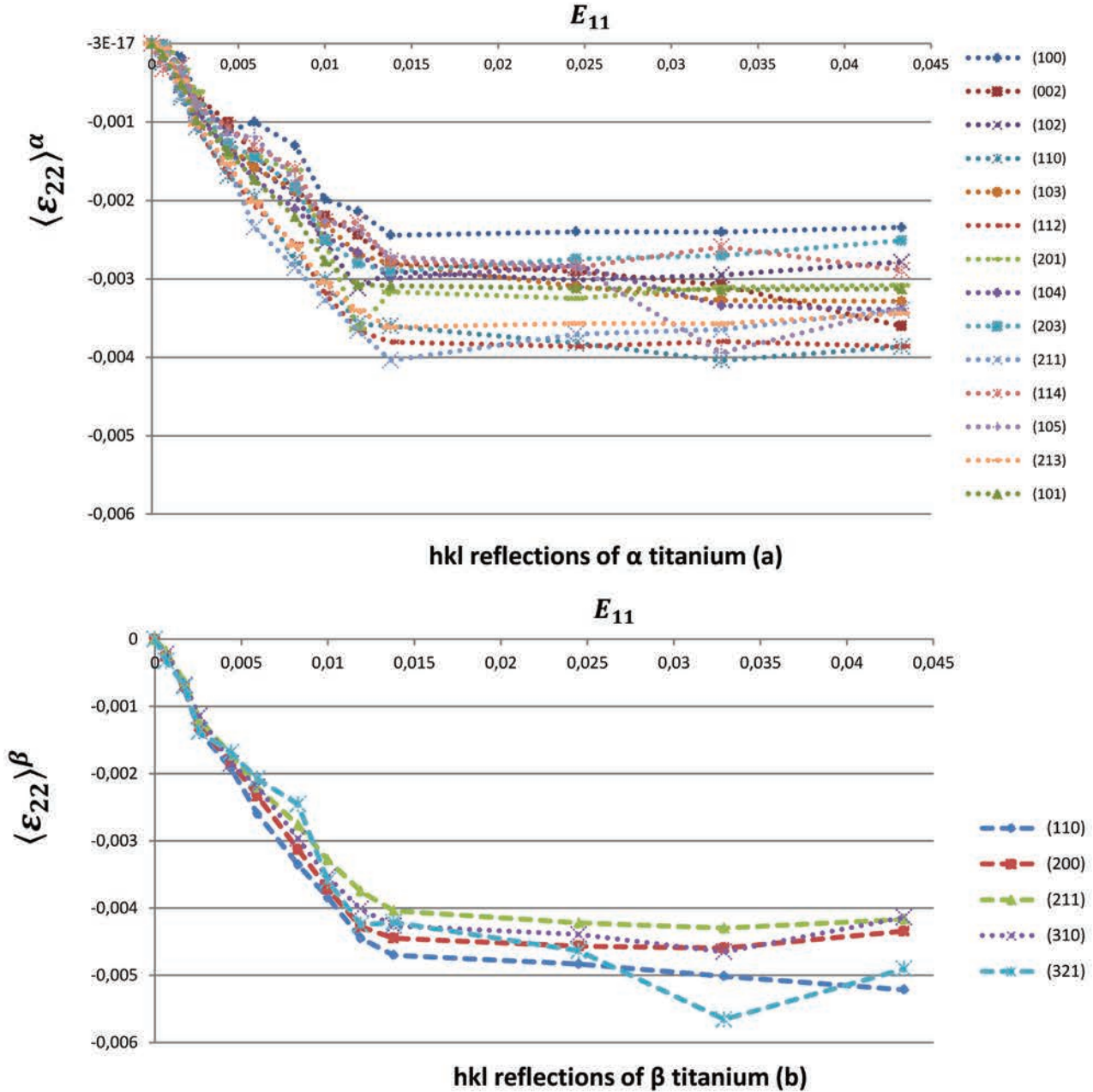
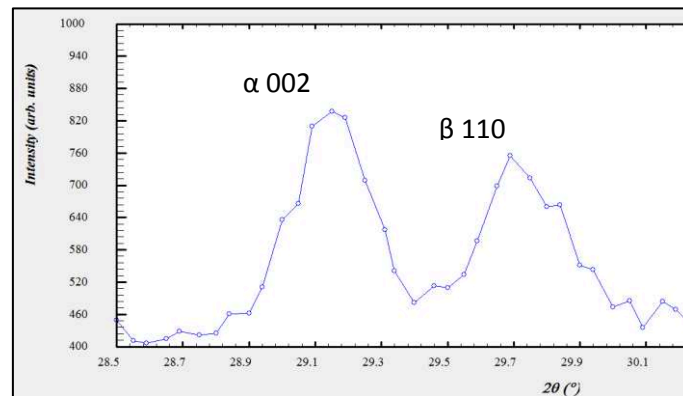


Figure A21.1 Evolution of lattice strain $\langle \varepsilon_{33} \rangle_{hkl}^{ph}$ in the normal direction (ND) for all available hkl reflections belonging to α titanium (a) and β titanium (b) during the tensile test, plotted as a function of macrostrain E_{11} .

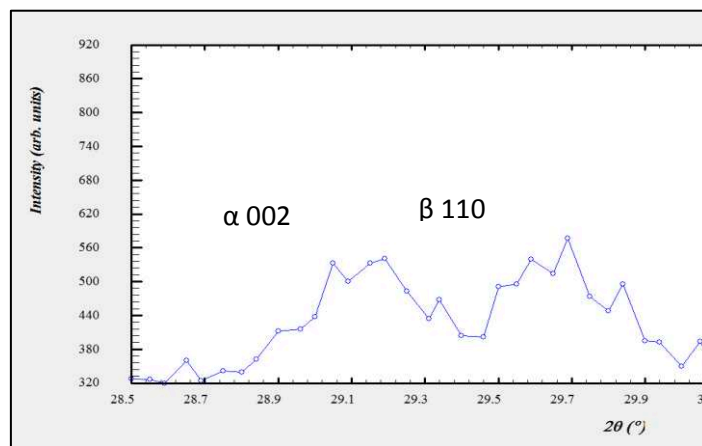
Owing to the hcp lattice much more hkl reflections can be observed for α phase comparing with phase β having bcc lattice.

Appendix 22 Illustration for weak diffracted intensity on Ti-6246 by neutron diffraction

Due to the low coherent scattering for the neutrons in the case of titanium, the intensities of diffraction peaks were very low for most of the measured hkl reflections. Therefore, limited number of hkl reflections measured for the texture maxima were taken into account, but still the intensities of these peaks are not high (see Fig. A22.1 A22.1).



(a)



(b)

Figure A22.1 Illustration of diffraction intensity by two spectrums of reflections α 002 and β 110 respectively taken before tensile test (a) and before the sample fracture (b). We can see the diffraction intensity was already not very strong to be fit, and it was weaker and weaker during the tensile test.

Appendix 23 Characterisation of Ti-6246

The studied Ti-6246 titanium alloy consists of α and β phases, and it was received as a round cylinder with a diameter of 250mm. The chemical composition in weight percentage of this alloy is shown in table A23.1.

| Elements | Al | Mo | Fe | Sn | Zr | O | C | N | Ti |
|----------|---------|---------|------|-----------|---------|------|------|------|---------|
| Wt% | 5.5-6.5 | 5.5-6.5 | 0.15 | 1.75-2.25 | 3.5-4.5 | 0.15 | 0.04 | 0.04 | Balance |

Table A23.1 The chemical composition in weight percentage of Ti-6246 alloy.

As previously for Ti-18, two small specimens were cut from the delivered cylinder. The observed surface of first specimen is parallel to the radial cross section of ingot, for the second specimen the observed surface is parallel to the axial cross section of delivered bar (cf. Fig. 1.21 page 34). Both specimens were polished with SiC abrasive papers and finally polished by polishing pastes. Then specimens were chemically etched using a nitric-perchloric acid solution, the concentration of each component is shown in table 1.11 page 34. All above mentioned surface treatment were operated at room temperature.

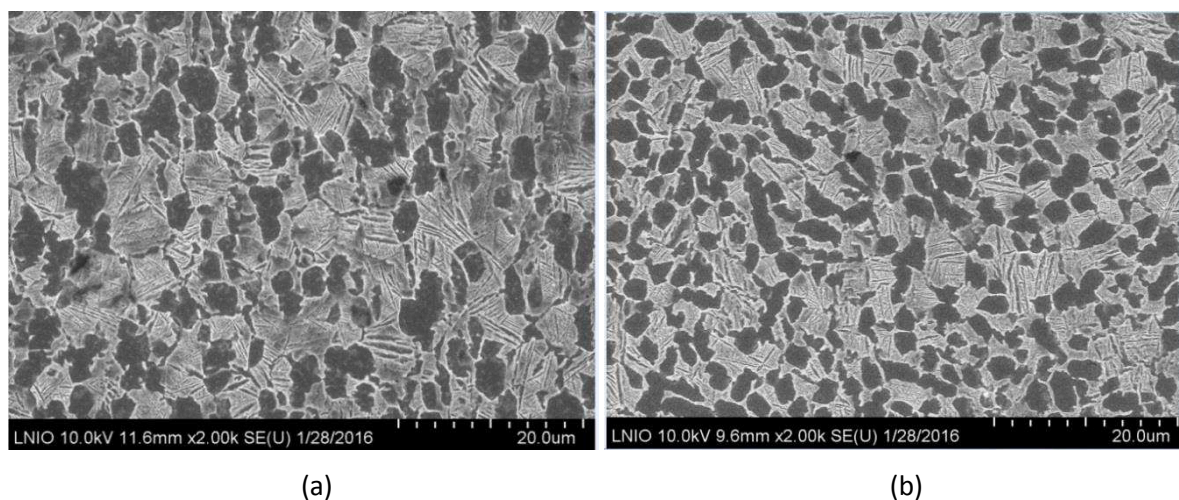


Figure A23.1 SEM images at 2000x magnification of the microstructure of Ti-6246 on axial section (a) and radial section (b). Typical bimodal structure can be observed.

A HITACHI SU-8030 Scanning Electron Microscope (SEM) was employed to perform surface observation. A typical bimodal structure of titanium alloys (cf. section 1.) can be observed, as shown in Fig. A23.1. At 2000x magnification level uniformly spread globular

primary α -titanium α_p nodules and lamellar secondary α -titanium α_s nodules can be observed embedded in the matrix of β titanium on both cross sections.

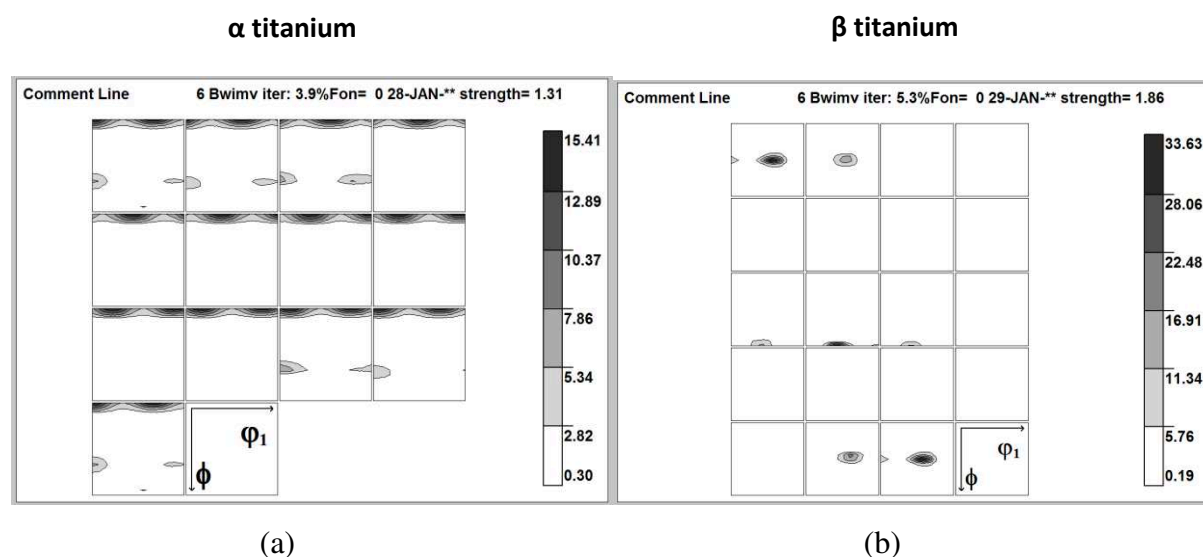


Figure A23.2 Orientation Distribution Functions for α titanium (a) and for β titanium (b) of the studied Ti-6246 alloy determined by X-ray diffraction (Cu radiation). The sections through Euler space with the step of 5° along the ϕ_2 axis are shown for both phases.

To characterize crystallographic texture in both phases of the studied Ti-6246 alloy, two sets of pole figures, i.e. $\{0001\}$, $\{0110\}$, $\{0111\}$, $\{0112\}$, $\{1120\}$, $\{1122\}$ and $\{011\}$, $\{002\}$, $\{112\}$, $\{013\}$ were measured respectively for α and β titanium on the radial surface. The Orientation Distribution Functions were determined using the WIMV method [Kallend 90] for both phases and shown in Fig. A23.2.

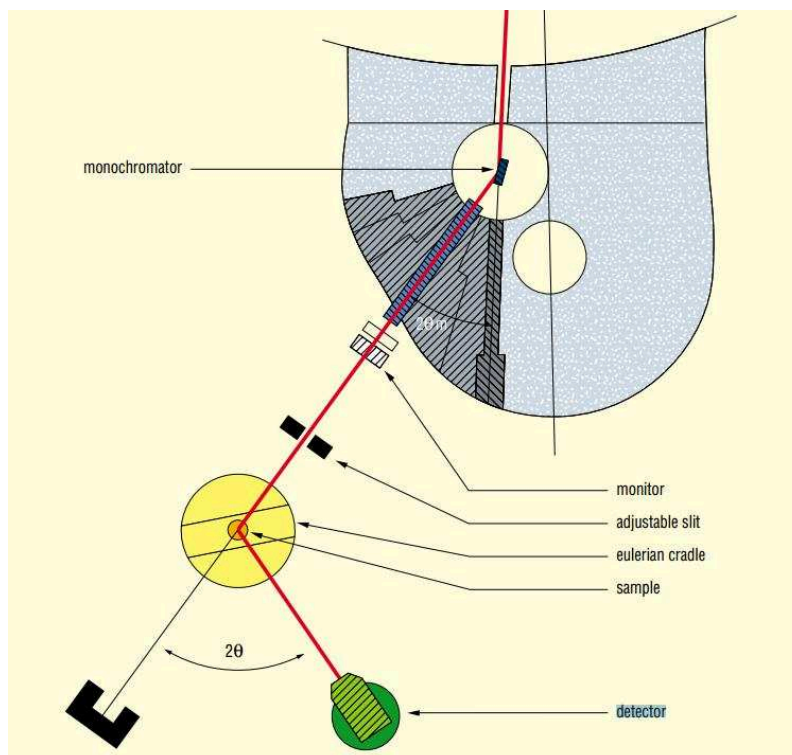


Figure A24.2 Illustration for the set-up of neutron diffraction equipment in LLB.

Fig. A24.2 presents the set-up of neutron diffraction equipment (facility description see reference document [6T1 03]). The diffraction measurement was performed for the whole cross section of sample. The wavelength of incident neutron beam was 1.159\AA , selected by a Cu (111) monochromator. The diffractometer is equipped with an Eulerian cradle, allowing sample rotations and various collimations of the incident and diffracted beam.

Due to the low coherent scattering for the neutrons in the case of titanium, the intensities of diffraction peaks were very low for most of the measured hkl reflections. Therefore, limited number of hkl reflections measured for the texture maxima were taken into account, but still the intensities of these peaks are not high (see Appendix 22, Fig. A22.1).

The reflections 100, 002, 101 of α titanium, and 110 of β titanium were measured in loading direction LD ($\phi = 0^\circ$, $\psi = 90^\circ$). The reflection 110 of α titanium was measured in transverse direction TD ($\phi = 90^\circ$, $\psi = 90^\circ$). In addition, 002, 101 of α titanium were respectively measure in the directions ($\phi = 90^\circ$, $\psi = 30^\circ$) and ($\phi = 60^\circ$, $\psi = 30^\circ$), as well as the 110 of β titanium were measured in the direction ($\phi = 60^\circ$, $\psi = 90^\circ$). The measurement orientations are summerised in table A24.1.

| | hkl reflections | ϕ° | ψ° |
|--------------------------|-----------------|--------------|--------------|
| Loading direction LD | α 100 | 0 | 90° |
| | α 002 | 0 | 90° |
| | α 101 | 0 | 90° |
| | β 110 | 0 | 90° |
| Transversal direction TD | α 110 | 90 | 90 |
| | α 002 | 90 | 30 |
| | α 101 | 60 | 30 |
| | β 110 | 60 | 90 |

Table A24.1 Summary of orientations for each hkl reflections during the neutron diffraction measurement.

A24.2 Neutron diffraction measurement during in-situ tensile test

The relative lattice strains were measured in-situ during tensile test for several applied loads. The tensile machine was driven by applied stress during the elastic deformation of sample and then controlled by displacement of the grip, when the sample underwent plastic deformation. All in-situ neutron diffraction measurements were performed after the stabilization of the applied load.

The evolution of nominal macro-stress recorded by tensile rig $\Sigma_{11}^{rig,nominal}$ vs. macro-strain E_{11} in loading direction is presented in Fig. A24.3. The neutron diffraction measurement was performed at different loading steps (step 1 to 7). The steps were selected for the elasto-plastic transition, during the plastic deformation and necking process until the damage of sample, in order to observe the variation of the lattice strains in two phases for the whole tensile test.

The neutron diffraction measurements were performed with a maximum detector 2θ range of 7° during 16000s for each 2θ position. All diffraction measurements were done at a quasi-static state, after a long time ($\approx 50 - 60$ min) needed for stabilization of material. During this time the macro-stress decreased as seen in Fig. A24.4.

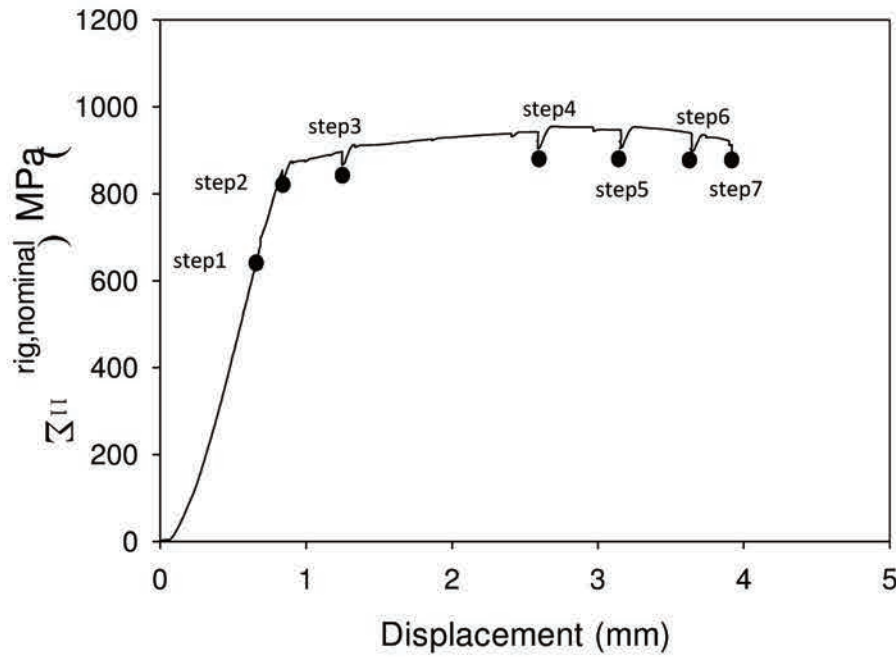
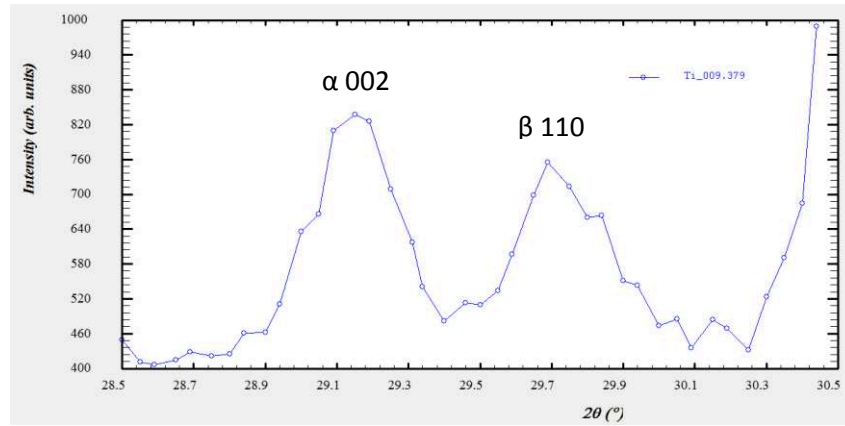


Figure A24.3 Evolution of nominal stress $\Sigma_{33}^{rig,nominal}$ in loading direction with different steps of neutron diffraction measurement.

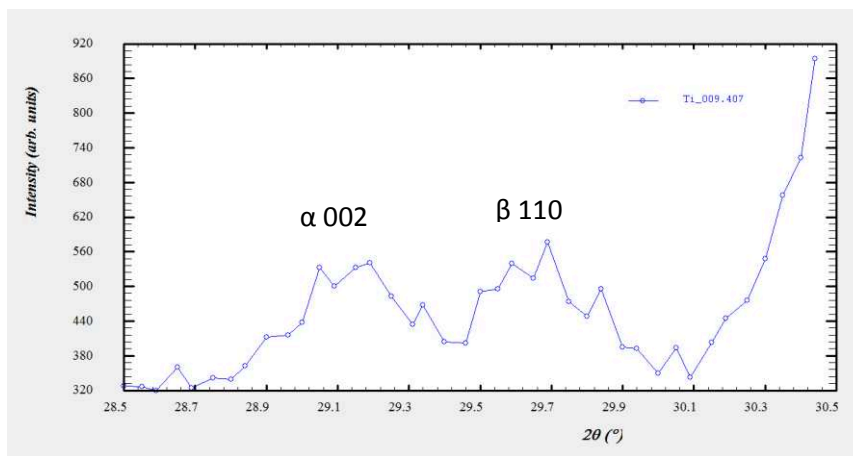
The measured diffraction peaks were fitted by program WinPLOTTR [Winplotr] using Pseudo-Voigt function (cf. Eq. A5.1). The 2θ peak positions and the the interplanar spacing d_{hkl} were determined for different hkl reflections (cf. Eq.6.2). Then the relative lattice strains were calculated from Eq. A19.1.

The evolutions of lattice strains in different scattering vector directions ($\langle \epsilon_{33} \rangle_{\{hkl\}}$, $\langle \epsilon_{22} \rangle_{\{hkl\}}$ and $\langle \epsilon_{(\phi,\psi)} \rangle_{\{hkl\}}$) are plotted in function of the sample strain E_{33} (Fig. A24.5 a and b). The corresponding steps are also indicated on the plots.

Due to the low coherent scattering of neutron [Willis 09] reacting with titanium atoms, the intensities of diffraction peaks are very low for most of measured hkl reflections. Therefore, only limited number of hkl reflections measured with maxima texture could be correctly recorded, but their intensities are still not strong enough. The Fig A24.4 illustrates weak intensities on some of the best recorded reflection peaks.



(a)



(b)

Figure. A24.4 Illustration of diffraction intensity by two spectrums of reflections α 002 and β 110 respectively taken before tensile test (a) and before the sample fracture (b). We can see the diffraction intensity was already not very strong to be fit, and it was weaker and weaker during the tensile test.

From Fig. A24.5a we can see that the α and β titanium exhibit similar behavior in loading direction, i.e. at beginning of the test the strains $\langle \varepsilon_{33} \rangle_{\{hkl\}}$ went up linearly up to the yield point of material (step 2). Then for all reflections the $\langle \varepsilon_{33} \rangle_{\{hkl\}}$ strains tend to saturate, indicating that the slip systems have been activated and material started plastic deformation. Very small work hardening can be observed during the plastic deformation. Then after the step 5 strain relaxation of $\langle \varepsilon_{33} \rangle_{\{hkl\}}$ strains occurred for reflections 100, 002 and 101 in α phase. The strain $\langle \varepsilon_{33} \rangle_{\{110\}}$ in β phase firstly relaxed but suddenly increased just before the sample fracture. This phenomenon possibly means that evolution of intergranular stresses occurred, however, due to the poor diffraction spectrum quality and lack of such prove from

other hkl reflections of β titanium, we cannot identify if this phenomena means load transfer between two phases or it is caused by experimental errors.

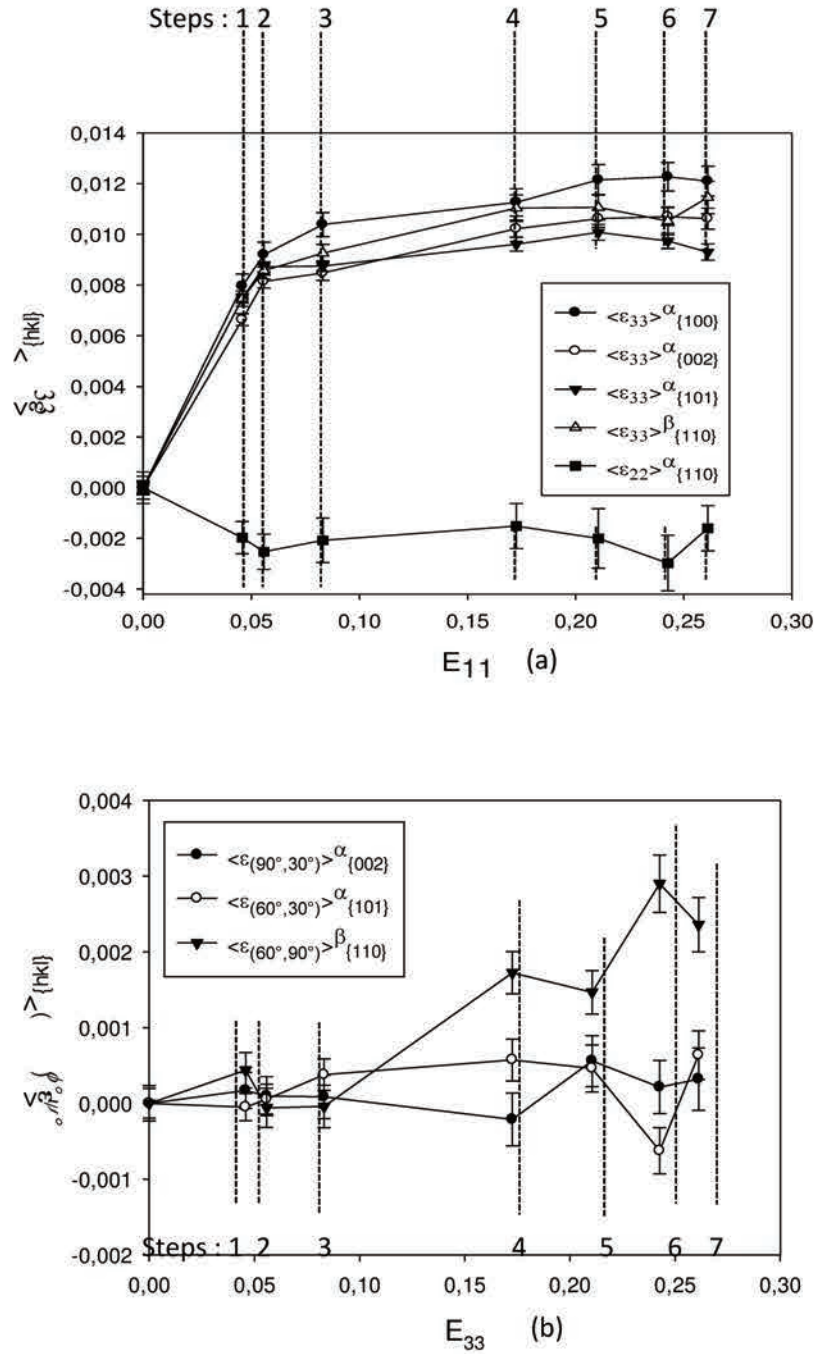


Figure A24.5 Evolutions of lattice strains measured in function of sample strain E_{11} along the directions: LD ($\langle \varepsilon_{33} \rangle_{\{hkl\}}$), TD ($\langle \varepsilon_{22} \rangle_{\{hkl\}}$) (a); as well as directions determined by angles ϕ and ψ ($\langle \varepsilon_{\phi,\psi} \rangle_{\{hkl\}}$) (b). The corresponding step numbers are also indicated on the plots.

In the case of the only measurable in strain $\langle \varepsilon_{22} \rangle_{\{110\}}$ (in α phase), we can see negative evolution during elastic deformation. Then the $\langle \varepsilon_{22} \rangle_{\{110\}}$ strain kept almost stable during the

plastic deformation, and finally slightly went up, indicating the possible initiation of damage in α titanium.

Then the Fig. A24.5b shows the evolution of micro-strain $\langle \varepsilon_{(\phi,\psi)} \rangle_{\{hkl\}}$ in two phases for other directions defined by ϕ, ψ angles. We can see the two plots for hkl reflections coming from α titanium are almost constants along the tensile test. And the lattice strain for reflection 110 from β phase increased and kept at a relatively high level when material was plastically deformed.

Summarizing, it can be stated that the neutron diffraction experiment showed that a significant plastic deformation started in both phases almost at the same time, which agrees with the conclusion drawn on the basis of the previous X-ray diffraction measurements. However, the activation of slip systems cannot be analyzed from neutron diffraction data because they are much poorer comparing with the results of X-ray experiment.

Appendix 25 SEM image of fracture surface of Ti-18

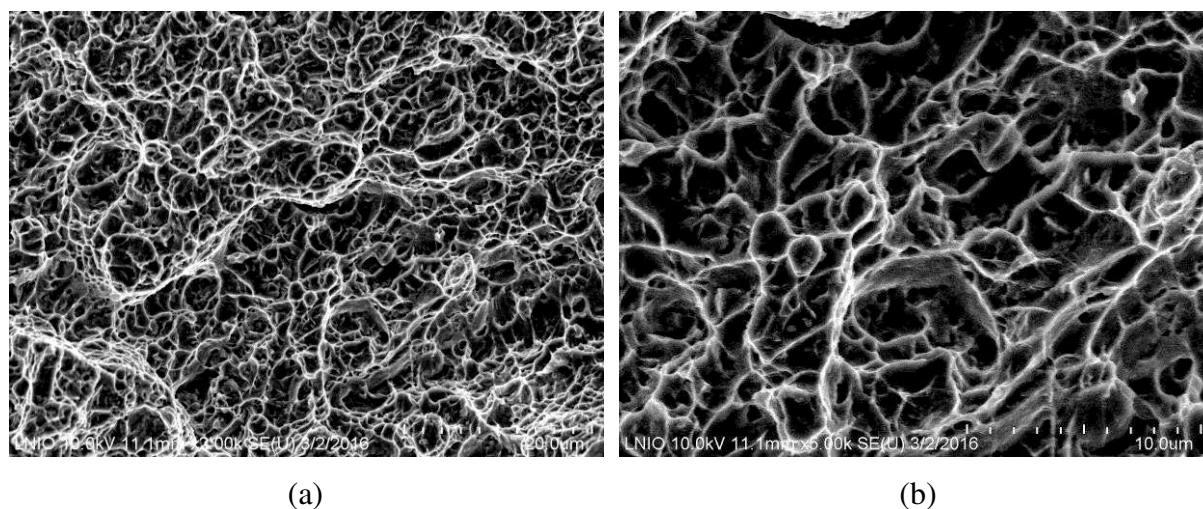


Figure A25.1 SEM images of fracture surface of Ti-6246. The fracture surface presents large numbers of “dimples” with more uniform sizes (a). The inclusions are hardly observed in the dimples (b).

The morphology of fracture surface of Ti-6246 alloy was investigated using Scanning Electron Microscope (SEM). The fracture surface was directly observed after the tensile test without any preparation or treatment. The microscopic pictures presented in Fig. A25.1, show many “dimples” having different sizes. The “dimples” on the surface of Ti-6246 are fine and uniform, which confirms the ductility of material during the damage process.

Appendix 26 Tomographic images of initial Ti-18

The tomography is applied to try to identify α and β phases in Ti-18 alloy. The tomography instrument Nanotom 180N, fabricated by GE Sensing & Inspection Technologies phoenix|X-ray GmbH, equipped with a Hamamatsu 2300x2300 pixel detector.

The tomography imaging is performed with X-ray beam of 160KV and 80 μ A, the specimen is rotated $\varphi = 360^\circ$ during the whole imaging process with 1800 steps. At each step the specimen is exposed 500ms under incident beam.

The Fig. A26.1 shows us the tomography images at rotation angle $\varphi = 0^\circ$, 45° and 90° . No significant contrast can be seen from the image, which means it is difficult to identify the α and β titanium with X-ray tomography. This difficult can be owned to the close X-ray absorption coefficient for both α and β phases.

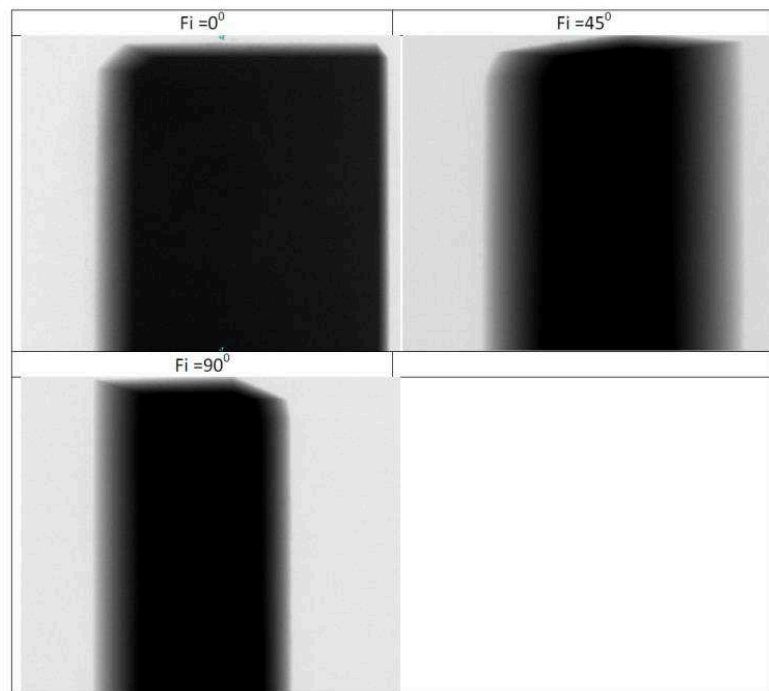


Figure A26.1 Tomography images of Ti-18 at rotation angle $\varphi = 0^\circ$, 45° and 90° .

References

[6T1 03] www-llb.cea.fr/fr-en/pdf/6t1-llb.pdf

[Ahmed 98] Ahmed, T., and H. J. Rack. Phase transformations during cooling in α β titanium alloys. *Materials Science and Engineering: A* 243, no. 1 (1998): 206-211.

[Akhtar 75] Akhtar A. Basal slip and twinning in α -titanium single crystals[J]. *Metallurgical Transactions A*, 1975, 6(5): 1105-1113.

[Alfonsson 10] E. Alfonsson, Lean duplex - the first decade of service experience, Duplex stainless steel, Conference Proceedings, BEAUNE, France, 2010, page 787.

[Almer 03] Almer J, Lienert U, Peng R L, et al. Strain and Texture Analysis of Coatings Using High-Energy X-Rays[J]. *Journal of Applied Physics*, 2003, 94(1):697-702.

[Alvarez-Armas 07] Alvarez-Armas I, Marinelli M C, Malarri A J A, et al. Microstructure associated with crack initiation during low-cycle fatigue in a low nitrogen duplex stainless steel[J]. *International Journal of Fatigue*, 2007, 29(4):758-764.

[Alvarez-Armas 12] Alvarez-Armas I, Krupp U, Balbi M, et al. Growth of short cracks during low and high cycle fatigue in a duplex stainless steel[J]. *International Journal of Fatigue*, 2012, 41(8):95-100.

[Arfken 00] Arfken, G. B.; Weber, H. J., *Mathematical Methods for Physicists* 5th, Boston, Massachusetts: Academic Press, 2000, ISBN 978-0-12-059825-0

[ASTM 07] ASTM E2546-07, Standard Practice for Instrumented Indentation Testing, ASTM International, West Conshohocken, PA, 2007, www.astm.org

[Attanasio 13] Attanasio, A.; Gelfi, M.; Pola, A.; Ceretti, E.; Giardini, C. Influence of Material Microstructures in Micromilling of Ti6Al4V Alloy. *Materials* 2013, 6, 4268-4283.

[Aubin 01] V. Aubin. Plasticité cyclique d'un acier inoxydable austéno-ferritique sous chargement biaxial non proportionnel. Thèse de doctorat, Université des Sciences et Technologie de Lille, 2001

[Baczański 93] A. Baczański, K. Wierzbowski, W.G. Haije, R.B. Helmholtz, G. Ekambaranathan, B. Pathiraj, *Cryst. Res. Technol.* 28 (1993) 229–243.

[Baczański 94] A. Baczański, K. Wierzbowski, P. Lipinski, R.B. Helmholtz, G. Ekambaranathan, B. Pathiraj, *Phil. Mag. A* 69 (1994) 437–449.

[Baczański 97] A. Baczański, K. Wierzbowski, J. Tarasiuk, M. Ceretti, A. Lodini, *Rev. de Metall.* 42 (1997) 1467–1474.

[Baczański 03] Baczański, A., Braham, C., Seiler, W., 2003. Micro-stresses in Textured Polycrystals Studied by Multireflection Diffraction Method and Self-consistent Model. *Phil. Mag.* 83, 3225-3246.

[Baczański 04a] Baczański, A., Braham, C., 2004. Elasto-plastic Properties of Duplex Steel Determined Using Neutron Diffraction and Self-Consistent Model. *Acta Mater.* 52, 1133-1142.

[Baczmański 04b] Baczmański A., Braham C., Seiler W., Shiraki N., Multi-reflection method and grazing incidence geometry used for stress measurement by X-ray diffraction, *Surface and Coating Technology*, vol. 182, p. 43, 2004.

[Baczmański 05] Andrzej Baczmański, I. S. Academia and H. Krak, "Stress field in polycrystalline materials studied using diffraction and self-consistent modelling". 2005.

[Baczmański 11] Baczmański, A., Le Joncour L., Panicaud, B., Francois M., Braham, C., Paradowska, A. M., Wroński, S., Amara, S. and Chiron, R., 2011. Neutron time-of-flight diffraction used to study aged duplex stainless steel at small and large deformation until sample fracture. *J. Appl. Cryst.* 44, 966-982.

[Baczmański 16] A. Baczmański, Y. Zhao, E. Gadalińska, L. Le Joncour, S. Wroński, C. Braham, B. Panicaud, M. François, T. Buslaps, and K. Soloducha, "Elasto-plastic deformation and damage process in duplex stainless steels studied using synchrotron and neutron diffractions in comparison with a self-consistent model," *Int. J. Plast.*, vol. 81, pp. 102–122, 2016.

[Baker 99] Baker, Hugh D. R.; Avedesian, Michael (1999). *Magnesium and magnesium alloys*. Materials Park, OH: Materials Information Society. p. 4. ISBN 0-87170-657-1.

[Barkia 15] B. Barkia, V. Doquet, J.P.Couzinié, I.Guillot, E.Héripuré, *Mat. Sci. Eng. A*, 636 (2015) 91-102

[Bakasubramanian 02] S. Balasubramanian, L. Anand, 2002 Plasticity of Initially Textured Hexagonal Polycrystals at High Homologous Temperatures: Application to Titanium, In: *Acta Materialia*, 50 133 148 , 1359-6454

[Balzar 02] Balzar D, Popa N. Improved Modeling of Residual Strain/Stress and Crystallite-Size Distribution in Rietveld Refinement. 2002.

[Bavay 90] J. Bavay, *Les aciers inoxydables*, Chapitre XVI, p. 565-610, Les éditions de physique, 1990.

[Beausir 09] Benoît Beausir, Somjeet Biswas, Dong Ik Kim, László S. Tóth, Satyam Suwas, Analysis of microstructure and texture evolution in pure magnesium during symmetric and asymmetric rolling, *Acta Materialia*, Volume 57, Issue 17, October 2009, Pages 5061-5077, ISSN 1359-6454

[Benmhenni 13] N. Benmhenni, S. Bouvier, R. Brenner, T. Chauveau, B. Bacroix, *Mat. Sci. Eng. A*, 573 (2013) 222–233

[Berkovich 50] E.S. Berkovich, "Three-Faceted Diamond Pyramid for Studying Microhardness by Indentation," *Zavodskaya Laboratoria*, Vol. 13 #3, 1950, p 345-347 (in Russian).

[Berveiller 79] M. Berveiller, A. Zaoui, *J. Mech. Phys. Solids* 26, 1979, 325.

[Besson 01] J. Besson, G. Cailletaud, J-L. Chaboche, S.Forest. *Mécanique non linéaire des Matériaux*. Hermès, 2001.

[Beyerlein 10] I.J. Beyerlein, L. Capolungo, P.E. Marshall, R.J. McCabe, and C.N. Tome: Statistical analyses of deformation twinning in magnesium. *Philos. Mag.* 90, 4073 (2010).

[Bhattacharyya 03] D. Bhattacharyya, G.B. Viswanathan, R. Denkenberger, D. Furrer, H.L. Fraser, *Acta Mater.* 51 (2003) 4679–4691.

[Bishop 45] Bishop, R.F., Hill, R., Mott, F.R.S., 1945. The theory of indentation and hardness tests. *Proc. Phys. Soc.* 57, 147–159

[Boersch 37] Boersch *Physikalische Zeitschrift*, 38 (1937) 1,000.

[Bollenrath 39] Bollenrath F., Hauk V., Osswald E., Röntgenographische Spannungsmessungen beiüberschreiten der Fließgrenze an Zugstäben aus unlegiertem Stahl, *VDI Z.*, vol. 83, p. 129, 1939.

[Bonfoh 03] N. Bonfoh, A. Carmasol, P. Lipinski, *Int. J. Plasticity* 19 (2003) 1167-1193.

[Bonnet 90] Bonnet, S., Bourgoïn, J., Champredonde, J., Guttman, D., Guttman, M., 1990. Relationship between evolution of mechanical properties of various cast duplex stainless steels and metallurgical and aging parameters: outline of current EDF programmes. *Mater. Sci. and Tech.* 6, 221-229.

[Bornert 01] M. Bornert, T. Bretheau, P. Gilormini, *Homogénéisation en mécanique des matériaux*, vol 2, Hermès, Paris, 2001.

[Bouvier 05] Bouvier, S., et al. "Modelling of anisotropic work-hardening behaviour of metallic materials subjected to strain-path changes." *Computational Materials Science* 32.3 (2005): 301-315.

[Boyer 94] Boyer R., Welsch G., Collings E. W., eds.: *Materials Properties Handbook: Titanium Alloys*, ASM, Materials Park, USA, (1994)

[Brakman 87] Brakman C.M., The Voigt model case, *Phil. Mag. A*, vol. 55, p. 39, 1987.

[Brakman 88] Brakman, C.M. Ph.D Thesis, Technische Universiteit Delft 1988, The Netherlands

[Bridier 05] F. Bridier, P. Villechaise, and J. Mendez, "Analysis of the different slip systems activated by tension in α/β titanium alloy in relation with local crystallographic orientation," *Acta Mater.*, vol. 53, no. 3, pp. 555–567, 2005.

[Bridier 08] Bridier, F., P. Villechaise, and J. Mendez. "Slip and fatigue crack formation processes in an α/β titanium alloy in relation to crystallographic texture on different scales." *Acta Materialia* 56.15 (2008): 3951-3962.

[Britannica 16] Britannica Online for Kids, s.v. "microscope," accessed May 11, 2016, <http://kids.britannica.com/comptons/article-204632/microscope>.

[Bugat 00] Bugat, B., 2000, Comportement et endommagement des aciers austéno-ferritiques vieillis : une approche micromécanique. PhD thesis, Ecole Nationale Supérieure des Mines de Paris, France

[Bugat 01] Bugat, S., Besson, J., Gourgues, A.F., N’Guyen, F., Pineau, A., 2001. Microstructure and damage initiation in duplex stainless steel. *Mater. Sci. Eng. A* 317, 32–36.

[Bunge 69] Bunge H J. *Mathematische Methoden der Texturanalyse: Mit 86 Abbildungen und 31 Tabellen, sowie 7 Abbildungen und 9 Tabellen im Anhang*[M]. Akademie-Verlag, 1969.

[Bunge 82] H.J. Bunge, 1982. Texture analysis in material science: Mathematical methods. London: Butterworth.

[Burgers 34] W.G. Burgers, *Physica* 1 (7–12) (1934) 561–586.

[Burgers 39] J.M. Burgers, Some considerations of the field of stress connected with dislocations in a regular crystal lattice, *Koninklijke Nederlandse Akademie van Wetenschappen*, 42 (1939), pp. 293–325 (Part 1); 378–399 (Part 2)

[Calonne 01] V. Calonne. Propagation de fissures par fatigue dans les aciers austéno-ferritiques moulés ; influence de la microstructure, du vieillissement et de la température d'essai. Thèse de doctorat, Ecole des mines de Paris, 2001.

[Capron 99] A. Capron, J. Edelson, C. Thibault. Etude de la fragilisation d'un acier austéno-ferritique par vieillissement à 475°C. Rapport de Stage, Ecole Nationale Supérieure des Mines de Paris, 1999.

[Charles 88] J. Charles, P. Pugeault, F. Dupoirion, D. Catelin, *Bulletin du Cercle des Métaux* XV (1988) 24.

[Chateigner 13] Chateigner D. Combined analysis[M]. John Wiley & Sons, 2013.

[Cheng 98] Cheng, Yang-Tse, and Che-Min Cheng. "Relationships between hardness, elastic modulus, and the work of indentation." *Applied physics letters* 73.5 (1998): 614-616.

[Chiang 82] Chiang, S.S., Marshall, D.B., Evans, A.G., 1982. The response of solids to plastic/plastic indentation. I. Stresses and residual stresses. *J. Appl. Phys.* 53, 298–311.

[Chun 08] Chun. L, "Inelastic neutron scattering and lattice dynamics," vol. 71, no. 4, pp. 819–828, 2008.

[Clausen 98] Clausen, Bjørn, T. Lorentzen, and T. Leffers. "Self-consistent modelling of the plastic deformation of fcc polycrystals and its implications for diffraction measurements of internal stresses." *Acta Materialia* 46.9 (1998): 3087-3098.

[Courant 00] B. Courant, B. Bourniquel, M. François, M. Bessière "Observations on two commonly used profile shape functions" *Mater. Sci. Forum*, 347 (3) (2000), pp. 161–165

[Cullity 78] Cullity, B.D. Elements of X-ray Diffraction, Second Edition, Addison-Wesley, Massachusetts 1978

[Dakhlaoui 06] R. Dakhlaoui, A. Baczmanski, C. Braham, S. Wronski, K. Wierzbanski and E.C. Oliver, Effect of residual stresses on individual phase mechanical properties of austeno-ferritic duplex stainless steel, *Acta Materialia*, 54, 5027-5039 (2006)

[Dakhlaoui 07] R. Dakhlaoui C. Braham, A. Baczmanski, Mechanical Properties of Phases in Austeno-ferritic Duplex Stainless Steel - Surface Stresses Studied by X-ray Diffraction, *Materials Science and Engineering (A)*, 444, 6-17

[Daniels 09] Daniels J.E. and Drakopoulos, M., 2009. High-Energy X-Ray Diffraction Using the Pixium 4700 Flat Panel Detector. *Synchrotron Rad.* 6, 463-468.

[Danoix 00] F. Danoix, P. Auger, *Materials Characterisation* 44 (2000) 177.

- [Dao 01] Dao, M., et al., Computational modeling of the forward and reverse problems in instrumented sharp indentation. *Acta materialia*, 2001. 49(19): p. 3899-3918.
- [Davis 94] J. Davis, Ed., *ASM Specialty Handbook : Stainless Steels*, 1994
- [Day 01] A. P. Day et al., *Channel 5 User Manual*, HKL Technology A/S, Hobro, Denmark (2001).
- [DeBold 89] Terry A. DeBold, Duplex stainless steel—Microstructure and properties, *JOM*. March 1989, Volume 41, Issue 3, pp 12-15
- [Desestret 90] A. Desestret, J. Charles. Les aciers inoxydables austéno-ferritiques. In : *Les aciers inoxydables*,. Les éditions de la physique. 1990, 31-677
- [Devillers-Guerville 98] L. Devillers-Guerville. Rupture d'aciers inoxydables austéno-ferritiques moulés, fragilisés par vieillissement à 350-400°C : Aspect microstructuraux—Simulation numérique de la dispersion et des effets d'échelle. Thèse de doctorat, Ecole Nationale Supérieure des Mines de Paris. 1998
- [Di Gioacchino 15] Di Gioacchino, Fabio, and João Quinta da Fonseca. "An experimental study of the polycrystalline plasticity of austenitic stainless steel." *International Journal of Plasticity* 74 (2015): 92-109.
- [Dingley 84] D. J. Dingley, *Proc. Roy. Microsc. Soc.*, 19 (1984) 74.
- [Dolle 79] H. Dolle, *J. Appl. Cryst.* 12 (1979) 489–501.
- [Duval 92] C. Duval. Contribution à l'étude de l'endommagement des aciers austéno-ferritiques viellis. Thèse de Doctorat, Ecole Centrale de Paris, 1992.
- [Eckstein 83] Eckstein H.J., Serchen R. *Prakt. Met.* 20(1983) 596
- [El Bartali 07] A. El Bartali. Apport des mesures de champs cinématiques à l'étude des micromécanismes d'endommagement en fatigue plastique d'un acier inoxydable duplex. Thèse de doctorat, Ecole Centrale de Lille, 2007.
- [El Bartali 08] El Bartali, Ahmed, et al. "Identification and analysis of slip systems activated during low-cycle fatigue in a duplex stainless steel." *Scripta Materialia* 59.12 (2008): 1231-1234.
- [Emley 66] E.F. Emley, *Principles of Magnesium Technology*, Pergamon Press, London, 1966.
- [Eshelby 57] Eshelby J D. The determination of the elastic field of an ellipsoidal inclusion, and related problem, *Proceedings of the Royal Society of London A: Mathematical, Physical and Engineering Sciences*. The Royal Society, 1957, 241(1226): 376-396.
- [Evrard 08] P. Evrard. Modélisation polycristalline du comportement élastoplastique d'un acier inoxydable austéno-ferritique. Thèse de doctorat, Ecole Centrale de Lille, 2008.
- [Fanning 10] UK Patent Application, GB2470613A, 2010.
- [Follansbee 88] Follansbee, P. S., and U. F. Kocks. "A constitutive description of the deformation of copper based on the use of the mechanical threshold stress as an internal state variable." *Acta Metallurgica* 36.1 (1988): 81-93.

- [Field 95] Field, J. and M. Swain, Determining the mechanical properties of small volumes of material from submicrometer spherical indentations. *Journal of Materials Research*, 1995. 10(01): p. 101-112.
- [Fischer-Cripps 11] A. C. Fischer-Cripps, "Nano-indentation," pp. 21–38, 2011.
- [Franckel 93] Frankel, J., A. Abbate, and W. Scholz. "The effect of residual stresses on hardness measurements." *Experimental mechanics* 33.2 (1993): 164-168.
- [François 00] M. François, B. Bourniquel, C. Not, R. Guillén, C. Duval "Parameters influencing peak localization repeatability for X-ray stress measurements – use of experiment designs technique" *Zeitschrift Für Metallkunde*, 91 (5) (2000), pp. 414–420
- [François 08] François M., Unified description for the geometry of X-ray stress analysis: proposal for a consistent approach. *Journal of Applied Crystallography*, 2008. 41(1): p. 44-55.
- [François 12] François M., (2012), « Relation entre forme d'un anneau et contraintes ». *Journal d'études*, Université de Technologie de Troyes.
- [Franz 09] G. Franz, F. Abed-Meraim, T. Ben Zineb, X. Lemoine, M. Berveiller. *Computational Materials Science* 45, 2009, 768–773
- [Fréhard 06] Fréhard, S., et al. "AFM and EBSD combined studies of plastic deformation in a duplex stainless steel." *Materials Science and Engineering: A* 418.1 (2006): 312-319.
- [Fréour 05] S. Freour, D. Gloaguen, M. François, A. Perronnet, R. Guillen, Determination of single-crystal elasticity constants in a cubic phase within a multiphase alloy: X-ray diffraction measurements and inverse-scale transition modelling, *J. Appl. Crystallogr.* 38 (2005) 30-37
- [Fréour 12] S. Fréour and J. Fajoui, "Eshelby-Kröner self-consistent elastic model: The geometric mean versus the arithmetic mean - A numerical investigation," *ZAMM Zeitschrift für Angew. Math. und Mech.*, vol. 92, no. 4, pp. 329–338, 2012.
- [Friedel 53] J. Friedel *Phil.Mag.* 44.444 (1953)
- [Furuhara 95] T. Furuhashi, T. Ogawa, T. Maki, *Phil. Mag. Lett.* 72 (3) (1995) 175–183
- [Genzel 05] Genzel Ch., X-ray residual stress analysis in thin films under grazing incidence – basic aspects and applications, *Mat. Scienc. Tech.*, vol. 21, p. 10, 2005.
- [Glavicic 04] Glavicic M G, Salem A A, Semiatin S L. X-ray line-broadening analysis of deformation mechanisms during rolling of commercial-purity titanium[J]. *Acta materialia*, 2004, 52(3): 647-655.
- [Gloaguen 02] Gloaguen, D., François, M., Guillen, R., & Royer, J. (2002). Evolution of internal stresses in rolled Zr702 α . *Acta materialia*, 50(4), 871-880
- [Gloaguen 04] Gloaguen D, François M, Guillen R. Mesoscopic residual stresses of plastic origin in zirconium: interpretation of X-ray diffraction results[J]. *Journal of Applied Crystallography*, 2004, 37(6):934-940.
- [Gloaguen 15] D. Gloaguen, G. Oum, V. Legrand, J. Fajoui, M.-J. Moya, T. Pirling, W. Kockelmann, *Metall. Mater. Trans. A*, 46 (2015) 5038-5046

- [Glockner 34] Glockner R., Z. Techn. Phys., vol. 15, p. 421, 1934.
- [Gologanu 95] M. Gologanu, J-B. Leblond, G. Perrin. Micromechanically based Gursontype model for ductile porous metals including strain gradient effects. American Society of Mechanical Engineers, Applied Mechanics Division, AMD, 1995, 216, Pages 47-56.
- [Greenfield 72] M.A. Greenfield and H Margolin, Met. Trans., 3, 1972, 2649.
- [Guttmann 91] M. Guttmann, Duplex stainless steel _91, Beaune, France, October 1991, p. 79.
- [Gympel 90] Gympel, P. & Norbert, A. Constitution et propriétés. Les aciers inoxydables : Propriétés, mise en oeuvre, emploi, normes, 1990, Technique et Documentation-Lavoisier.
- [Hammersley 96] Hammersley, A.P., Svensson, S.O., Hanfland, M., Fitch, S.O. and Häusermann, D., 1996. Two-dimensional detector software: From real detector to idealised image or two-theta scan. High Pressure Research, 14, 235-248.
- [Hao 07] Hao, Y. L., et al. "Elastic deformation behaviour of Ti-24Nb-4Zr-7.9 Sn for biomedical applications." Acta biomaterialia 3.2 (2007): 277-286.
- [Hauk 86] V.M. Hauk, Adv. X-Ray Anal. 29 (1986) 1–15
- [Hauk 97] Hauk V., Structural and Residual Stress Analysis by Nondestructive Methods, Elsevier, Amsterdam, 1997.
- [Hay 09] J. Hay, "Introduction to instrumented indentation testing," Exp. Tech., vol. 33, no. 6, pp. 66–72, 2009.
- [He 11] He, B.B., Two-dimensional X-ray diffraction. 2011: John Wiley & Sons.
- [Helbert 96] Helbert, A. L., X. Feaugas, and M. Clavel. "The influence of stress trlaxiality on the damage mechanisms in an equiaxed α/β Ti-6Al-4V alloy." Metallurgical and Materials Transactions A 27.10 (1996): 3043-3058.
- [Hill 65] R. Hill, "A self-consistent mechanics of composite materials," J. Mech. Phys. Solids, vol. 13, no. March 1962, pp. 213–222, 1965.
- [Hordon 58] Hordon M J, Lement B S, Averbach B L. Influence of plastic deformation on expansivity and elastic modulus of aluminum[J]. Acta Metallurgica, 1958, 6(6): 446-453.
- [Hu 10] Hu, C.-E., Zeng, Z.-Y., Zhang, L., Chen, X.-R., Cai, L.-C. & Alfe`, D. (2010). J. Appl. Phys. 107, 093509.
- [Hutchings 05] M.T. Hutchings, P.J. Withers, T.M. Holden, T. Lorentzen. Introduction to the characterisation of residual stress by neutron diffraction. Taylor & Francis, 2005.
- [Hutchinson 06] Hutchinson, Bevis, and Norman Ridley. "On dislocation accumulation and work hardening in Hadfield steel." Scripta Materialia 55.4 (2006): 299-302.
- [Iacoviello 97] F. Iacoviello, M. Habashi, M. Cavallini, Materials Science and Engineering A 224 (1997) 116.
- [Iacoviello 98] F. Iacoviello, J. Galland, M. Habashi, Corrosion Science 260, 40, 8 (1998) 1281.

- [Iacoviello 99] F. Iacoviello, M. Boniardi, G.M. La Vecchia, *International Journal of Fatigue* 21 (October) (1999)957.
- [Inal 99] K. Inal, P. Gergaud, M. Francois, J-L Lebrun. X-ray diffraction methodologies of macro and pseudo-macro stress analysis in a textured duplex stainless steel. *Scand. J. Metall.*, 1999, 28, 139–50.
- [Jang 08] Jang, J.-i. and G. Pharr, Influence of indenter angle on cracking in Si and Ge during nano-indentation. *Acta Materialia*, 2008. 56(16): p. 4458-4469.
- [Ji 89] Ji, N. "Characterization of Microstructure and Mechanical State of Metallic Materials by X-Ray Diffraction Profile Analysis.(Dissertation)." 116 (1989): 1989.
- [Ji 03] Ji, V. "Contribution to the X-ray diffraction analysis method of the micro-structural and mechanical state of heterogenous materials." (2003).
- [Jia 08] N Jia, Ru Peng, D W Brown, B Clausen and Y D Wang. Tensile Deformation Behavior of Duplex Stainless Steel Studied by In-Situ Time-of-Flight Neutron Diffraction Metallurgical and materials transactions a-physical metallurgy and material science, 2008, 39A(13), 3134-3140.
- [Joly 92] P. Joly. Etude de la rupture d'aciers inoxydables fragilisés par vieillissement à 400°C. Thèse de doctorat, Ecole Nationale Supérieure des Mines de Paris, 1992.
- [Jonas 05] J.J. Jonas, Y. He, S. Godet. The role of partial dislocation in facilitating transformations of the Nishiyama-Wassermann type. *Scripta Materialia*, 2005, 52, 175-179.
- [Jones 81] Jones I. P., Hutchinson W. B.: *Acta Met.* 29, (1981) p. 951
- [Johnson 70] Johnson, K.L., 1970. The correlation of indentation experiments. *J. Mech. Phys. Solids* 18, 115–126.
- [Jun 16] Jun, Tea-Sung, et al. "Local deformation mechanisms of two-phase Ti alloy." *Materials Science and Engineering: A* 649 (2016): 39-47.
- [Kaiser 03] F. Kaiser, J. Bohlen, Deitmar, K.U. Kainer Anisotropic properties of magnesium sheet AZ31 *Mat. Sci. Forum*, 419–422 (2003), pp. 315–320
- [Kallend 90] Kallend, J.S., Kocks, U.F., Rollet, A.D., Wenk, H.R., 1990. Operational Texture Analysis, Raport LA-UR-90-2852, Centre for Material Sciences, Los Alamos National Laboratory, USA.
- [Kim 99] Kim, Hyoungh Seop, and Mark B. Bush. "The effects of grain size and porosity on the elastic modulus of nanocrystalline materials." *Nanostructured materials* 11.3 (1999): 361-367.
- [Kneer 65] Kneer, G. (1965). *Phys. Status Solidi*, 9, 825–834.
- [Kocks 88] Kocks, U. F., M. G. Stout, and A. D. Rollett. "The influence of texture on strain hardening." *ICSMA*. Vol. 8. 1988.
- [Kröner 58] Kröner, E. (1958). *Z. Physik*, 151, 504–518.

[Kröner 61] Kröner, E., On the plastic deformation of polycrystals, *Acta Metall.*, vol. 9, p. 55, 1961.

[Kruml 97] Kruml, Tomáš, et al. "Dislocation structures in the bands of localised cyclic lastic strain in austenitic 316L and austenitic-ferritic duplex stainless steels." *Acta materialia* 45.12 (1997): 5145-5151

[Kurdjumov 30] G. Kurdjumov and G. Sachs. 2. *Fhxs.* 64,325 (1930).

[Lacombe 90] P. Lacombe, B. Baroux, G. Béranger, Eds., *Les aciers inoxydables*, Les éditions de physique, 1990.

[Larson and Von Dreele 94] Larson A. and Von Dreele RB. GSAS – general structure analysis system. Technical Report LA-UR-86-748, Los Alamos National Laboratory; 1994.

[Lebensohn 93] Lebensohn, Ricardo A., and C. N. Tomé. "A self-consistent anisotropic approach for the simulation of plastic deformation and texture development of polycrystals: application to zirconium alloys." *Acta metallurgica et materialia* 41.9 (1993): 2611-2624.

[Lebrun 14] Lebrun E, Svec P, Nowak S, et al. Phase Transformations of TIMETAL-18 as a New Titanium Alloy with Bimodal Microstructure[C]//Advanced Materials Research. Trans Tech Publications, 2014, 922: 418-423.

[Leffler 05] B. Leffler. Stainless steels and their properties. 2005 URL: <http://www.outokumpu.com/files/Group/HR/Documents/STAINLESS20.pdf>

[Le Joncour 10] Le Joncour L, Panicaud B, Baczmański A, et al. Damage in duplex steels studied at mesoscopic and macroscopic scales[J]. *Mechanics of Materials*, 2010, 42(12): 1048-1063.

[Le Joncour 11] Le Joncour L. Analyses expérimentales et modélisations multi-échelles de l'endommagement d'un acier UR45N laminé vieilli. Université de Technologie de Troyes, 2011

[Lemaitre 94] Lemaitre, Jean, and Jean-Louis Chaboche. *Mechanics of solid materials*. Cambridge university press, 1994.

[Lemaitre 01] J. Lemaitre, J.-L. Chaboche, *Mécanique des matériaux solides*, 2nd édition, Dunod, France, 2001.

[Le Roux 99] Le Roux, J. C.. Etude du comportement et de l'endommagement en fatigue d'un acier inoxydable austéno-ferritique moulé vieilli (Doctoral dissertation),1999.

[Li 14] Li, Y.G., P. Kanoute, and M. François. Characterization of Residual Stresses and Accumulated Plastic Strain Induced by Shot Peening through Simulation of Instrumented Indentation. in *Advanced Materials Research*. 2014. Trans Tech Publ.

[Li 15] Li.Y.G., Shot-peening and low-cycle fatigue of titanium alloys: instrumented indentation and X-ray diffraction, Université de Technologie de Troyes, 2015

[Lim 87] Lim, G., et al. "Grazing incidence synchrotron x-ray diffraction method for analyzing thin films." *Journal of Materials Research* 2.04 (1987): 471-477.

- [Lin Peng 02] Peng R L, Odén M, Wang Y D, et al. Intergranular strains and plastic deformation of an austenitic stainless steel[J]. *Materials Science & Engineering A*, 2002, 334(1):215-222.
- [Lipinski 89] P. Lipinski and M. Berveiller, “*Elasto-plasticity of micro-inhomogeneous metals at large strains*”, *Int. J. Plast.*, vol. 5, no. 2, pp. 149–172, 1989.
- [Lipinski 95] P. Lipinski, M. Berveiller, E. Reubrez, and J. Morreale, “*Transition theories of elastic-plastic deformation of metallic polycrystals*”, *Arch. Appl. Mech.*, vol. 65, no. 5, pp. 291–311, 1995.
- [Lütjering 07] Gerd Lütjering, James C. Williams, *Titanium*, 2nd edition, 2007, chapter 2.
- [Lutterotti 14] L. Lutterotti, “Introduction to Rietveld refinements,” 2014.
- [Ma 02] Ma, C-H., J-H. Huang, and Haydn Chen. "Residual stress measurement in textured thin film by grazing-incidence X-ray diffraction." *Thin Solid Films* 418.2 (2002): 73-78.
- [Macherauch 61] Macherauch E., Müller P., Das $\sin^2 \psi$ -Verfahren der röntgenographischen Spannungsmessung, *Z. Angew. Phys.*, vol. 13, p 305, 1961.
- [Maetz 14] Jean-Yves Maetz. Evolution de la microstructure d'un acier inoxydable lean duplex lors du vieillissement. *Matériaux*. INSA de Lyon, 2014.
- [Maitland 07] Maitland T, Sitzman S. Electron backscatter diffraction (EBSD) technique and materials characterization examples[M]. Berlin: Springer, 2007.
- [Manoj 11] Manoj Gupta, Nai Mui Ling Sharon. *Magnesium, magnesium alloys, and magnesium composites*, 2011 ISBN 978-0-470-49417-2
- [Marciszko 13a] Marciszko M., Baczmański A., Wróbel M., Seiler W., Braham C., Donges J., Śniechowski M., Wierzbowski K., Multireflection grazing incidence diffraction used for stress measurements in surface layers, *Thin Solid Films* vol. 530, p.81, 2013.
- [Marciszko 13b] Marciszko M. thèse de l'Ecole Nationale Supérieure d'Arts et Métiers, Diffraction study of mechanical properties and residual stresses resulting from surface processing of polycrystalline materials, 2013
- [Marciszko 16] Marciszko, Marianna, et al. "Analysis of stresses and crystal structure in the surface layer of hexagonal polycrystalline materials: a new methodology based on grazing incidence diffraction." *Journal of Applied Crystallography* 49.1(2016).
- [Marrow 14] Marrow, James, et al. "3D studies of damage by combined X-ray tomography and digital volume correlation." *Procedia Materials Science* 3 (2014): 1554-1559. [Mata 06] Mata M, Casals O, Alcala J. The plastic zone size in indentation experiments: The analogy with the expansion of a spherical cavity. *International Journal of Solids and Structures*, 2006, 43(20): 5994-6013.
- [Mateo 97] Mateo, A., Llanes, L., Anglada, M., Redjaimia, A., Metauer G., 1997. Characterization of the intermetallic G-phase in an AISI 329 duplex stainless steel., *J. Mater. Sci.* 32, 4533–4540.
- [Matthies 95] Matthies S. Moment pole figures in residual stress analysis. *Textures and Microstructures*, 1996, 25(2): 229-236.

[Matthies 01] Matthies S, Priesmeyer H G, Daymond M R. On the diffractive determination of single-crystal elastic constants using polycrystalline samples[J]. Journal of Applied Crystallography, 2001, 34(5): 585-601.

[Maud] <http://maud.radiographema.com/>

[M'Cirdi 01] M'Cirdi, L., Lebrun, J.L., Inal, K., 2001. Experimental approach of a crystallographic cleavage criterion in a cast aged duplex stainless steel. Acta Mater. 29, 3879-3887.

[Merkel 11] Merkel S., 2011. Multifit/ Polydefix Polycrystal Deformation using X-rays, <https://code.google.com/p/multifit-polydefix>.

[Millet 12] Y. Millet, Développement d'un nouvel alliage à hautes caractéristiques mécaniques : le Ti18; Journées Titane Nantes 2012

[Mott 52] N.F.Mott Phil.Mag. 43.1157 (1952)

[Motyka 12] Motyka, Maciej, et al. "Hot Plasticity of Alpha Beta Alloys." Titanium Alloys-Towards Achieving Enhanced Properties for Diversified Applications (2012): 88-116.

[Mura 93] Mura, T., 1993, Micromechanics of defects in Solids, Kluwer Academic Publisher, Dordrecht, Boston, London. 1993.

[Myers 02] H. P. Myers. Introductory Solid State Physics. Taylor & Francis. ISBN 0-7484-0660-37, 2002

[Nano-indentation 02] Nano-indentation, X., User's manual. version16. Test Works, 2002. 4.

[Newkirk 53] Newkirk J B, Geisler A H. Crystallographic aspects of the beta to alpha transformation in titanium[J]. Acta Metallurgica, 1953, 1(3): 370-374.

[Nicaise 10] N. Nicaise, S. Berbenni, F. Wagner, M. Berveiller, X. Lemoine, Int. J. Plasticity Coupled effects of grain size distributions and crystallographic textures on the plastic behaviour of if steels. International Journal of Plasticity, 2010.

[Nishikawa 28] Nishikawa S, Kikuchi S. The diffraction of cathode rays by calcite[J]. Proceedings of the Imperial Academy, 1928, 4(8): 475-477.

[Noyan 87] Noyan I.C., Cohen J.B., Residual Stress. Measurement by Diffraction and Interpretation, New York, 1987.

[Olivier 92] Oliver, W.C. and G.M. Pharr, An improved technique for determining hardness and elastic modulus using load and displacement sensing indentation experiments. Journal of materials research, 1992. 7(06): p. 1564-1583.

[Panicaud 11] B. Panicaud, K. Saanouni, A. Baczmański, M. François, L. Cauvin, and L. Le Joncour, "Theoretical modelling of ductile damage in duplex stainless steels - Comparison between two micro-mechanical elasto-plastic approaches," Comput. Mater. Sci., vol. 50, no. 6, pp. 1908–1916, 2011.

[Park 02] Park, C.J., Kwon, H.S., 2002. Effects of Aging at 475°C on Corrosion Properties of Tungsten Containing Duplex Stainless Steels. Corros. Sci. 44, 2817-2830.

- [Partridge 67] Partridge P. G.: Met. Rev. 12, (1967) p. 169
- [Paton 73] Paton N. E., Williams J. C., Rauscher G. P.: Titanium Science and Technology, Plenum, Press, New York, USA, (1973) p. 1049
- [Pearson 67] Pearson WB. A hand book of lattice spacings and structure of metals and alloys, vol. 2. London: Pergamon Press; 1967. p. 908.
- [Pecharsky 05] V.K.Pecharsky, P.Y. Zavalij, Fundamentals of Powder Diffraction and Structural Characterization of Materials, Springer, 2005.
- [Pecharsky 08] P. Pecharsky, K. Vitalij, Y. Zavalij "Fundamentals of powder diffraction and structural characterization of materials" Springer (2008)
- [Peng 06] Peng, J., et al. "Residual stress gradient analysis by the GIXRD method on CVD tantalum thin films." Surface and Coatings Technology 200.8 (2006): 2738-2743.
- [Perrin 92] G. Perrin. Contribution à l'étude théorique et numérique de la rupture ductile des métaux. Thèse de doctorat. Ecole polytechnique, Palaiseau, 1992.
- [Peters 03] Dr.-Ing. M. Peters, Dr.-Ing. J. Hemptenmacher, Dr.-Ing. J. Kumpfert and Dr.-Ing. C. Leyens Structure and Properties of Titanium and Titanium Alloys, Chapter 1, Titanium and Titanium Alloys, WILEY-VCH Verlag GmbH & Co. KGaA, Weinheim, 2003, ISBN: 3-527-30534-3
- [Petit 11] S. Petit, "Inelastic Neutron Scattering," CEA Saclay, Laboratoire Léon Brillouin, August, 2011.
- [Pochettino 92] Pochettino A A, Gannio N, Edwards C V, et al. Texture and pyramidal slip in Ti, Zr and their alloys[J]. Scripta metallurgica et materialia, 1992, 27(12): 1859-1863.
- [Popa 98] Popa N C. The (hkl) dependence of diffraction-line broadening caused by strain and size for all Laue groups in Rietveld refinement[J]. Journal of Applied Crystallography, 1998, 31(2): 176-180.
- [Popa 01] Popa N C, Balzar D. Elastic strain and stress determination by Rietveld refinement: generalized treatment for textured polycrystals for all Laue classes[J]. Journal of applied crystallography, 2001, 34(2): 187-195.
- [Prakash 10] Leo Prakash, D. G., Ding R, Moat R.J, Jones I, Withers P J, Quinta da Fonseca J, Preuss M (2010). "Deformation twinning in Ti-6Al-4V during low strain rate-moderate strains at room temperature." Materials Science and Engineering A 527: 5734–5744.
- [Pumphrey 90] Pumphrey, P.H., Akhurst, K.N., 1990. Aging kinetics of CF3 steel in range 300-400°C. Mater. Sci. Tech. 6, 211-219.
- [Qi 14] Qi, M. L., et al. "A metallography and x-ray tomography study of spall damage in ultrapure Al." AIP Advances 4.7 (2014): 077118.
- [Raabe 07] D. Raabe, D. Ma, and F. Roters: Effects of initial orientation, sample geometry and friction on anisotropy and crystallographic orientation changes in single crystal microcompression deformation: A crystal plasticity finite element study. Acta Mater. 55, 4567 (2007)

- [Randle 00] Randle V, Engler O. Introduction to texture analysis: macrotexture, microtexture and orientation mapping[M]. CRC press, 2000.
- [Reimers 08] Reimers W., Pyzalla A.R., Schreyer A., Clemens H., Neutrons and Synchrotron Radiation in Engineering Materials Science, WILEY-VCH Verlag GmbH & Co. KGaA, Weinheim, 2008.
- [Reuss 29] Reuss A., Berechnung der Fließgrenze von Mischkristallen auf Grund der Plastizitätsbedingung für Einkristalle, Z. Angew. Math. Mech., vol. 9, p. 49, 1929.
- [Rice 69] J. Rice, D. Tracey. On the ductile enlargement of voids in triaxial stress fields. J. Mech. Phys. Solids 17, 1969, 201–217.
- [Roberts 60] C.S. Roberts, Magnesium and Its Alloys, John Wiley and Sons, New York, 1960.
- [Rousselier 87] G. Rousselier. Ductile fracture models and their potential in local approach of fracture. Nuclear Engineering and Design 105, 1987, 97–111.
- [Sachs 28] Sachs, G., 1928, Zeit. Der V.D.I., **72**, 739.
- [Santisteban 06] Santisteban, J., James, J., Daymond, M., Edwards, L., 2006. ENGIN-X: A third-generation neutron strain scanner. J. Appl. Cryst. 39, 812-825.
- [Sannouni 96] K. Saanouni, A. Abdul-Latif, Int. J. Plasticity 12 (1996) 1111-1121.
- [Schmid 50] Schmid, E. & Boas, W. Plasticity of crystals. 1950. Hughes, London.
- [Schwartz 09] Schwartz, Adam J., et al., eds. Electron backscatter diffraction in materials science. Vol. 2. New York: Springer, 2009.
- [Skrzypek 01] Skrzypek S.J., Baczmański A., Ratuszek W., Kusior E., New approach to stress analysis based on a grazing-incidence X-ray diffraction, J. Appl. Cryst., vol.34, p.427, 2001.
- [Simons 71] G. Simons and H. Wang, Single Crystal Elastic Constants and Calculated Aggregate Properties: A Handbook, 2nd edition, The M.I.T. Press, Cambridge, Massachusetts and London, 1971.
- [Solomon-Koch 79] Solomon-Koch, Scr. Metall. 13(1979) 971
- [Solomon-Levinson 78] Solomon-Levinson, Acta Metall. 26(1978) 429
- [Simons 71] G. Simons, H. Wang. Single Crystal Elastic Constants and Calculated Aggregate Properties: A Handbook. 2nd edition, 1971, The M.I.T. Press, Cambridge, Massachusetts and London.
- [Stroh 57] A.N. Stroh, Advances in Physics, 6, 1957, 418
- [Strutt 86] A.J. Strutt, G.N. Lorimer, C.V. Roscoe, K.J. Gradwell, Duplex stainless steel _86, The Hague, Netherlands, October 1986, p. 310.
- [Swain 98] Swain, M., Mechanical property characterisation of small volumes of brittle materials with spherical tipped indenters. Materials Science and Engineering: A, 1998. 253(1): p. 160-166.

- [Suresh 14] Suresh K S, Kitashima T, Yamabe-Mitarai Y. Effects of orientation on hardness, strain accumulation, and fracture[J]. *Materials Science & Engineering A*, 2014, 618:335-344.
- [Suri 99] S. Suri, G.B. Viswanathan, T. Neeraj, D.-H. Hou, M.J. Mills, *Acta Mater.* 47 (1999) 1019–1034.
- [Tan 94] X.L. Tan, H.C. Gu, S.F. Zhang, C. Laird, *Mater. Sci. Eng. A* 189 (1994) 77–84.
- [Taylor 26] Taylor, G. I., and C. F. Elam. "The distortion of iron crystals." *Proceedings of the Royal Society of London. Series A, Containing Papers of a Mathematical and Physical Character* 112.761 (1926): 337-361.
- [Taylor 38] Taylor, G.I., 1938, *J. Inst. Metals*, **62**, 307.
- [Teirlinck 88] D. Teirlinck, F. Zok, J.D. Embury, and M.F. Ashby: *Acta Metall.*, 1988, vol. 36 (5), pp. 1213-28.
- [Terada 08] M.Terada et al. *J Mater Sci* (2008) 43:425–433
- [Thomasson 90] M.H. Thomasson: *Ductile Fracture of Metals*, Pergamon Press, New York, NY, 1990.
- [Tompson 73] Thompson, Anthony W., Michael I. Baskes, and William F. Flanagan. "The dependence of polycrystal work hardening on grain size." *Acta Metallurgica* 21.7 (1973): 1017-1028.
- [Thompson 77] A.W. Thompson and J.C. Williams, *Nuclei for Ductile Fracture in Titanium, Fracture 1977*, vol.2, ICF4, Waterloo, Canada, June 19-24, 1977
- [Thompson 87] Thompson, P., Cox, D. E. and Hastings, J. B., 1987. Rietveld refinement of Debye-Scherrer synchrotron X-ray data from Al_2O_3 . *J. Appl. Cryst.*, 20, 79-83.
- [Ti-6246] <http://www.titaniumengineers.com/uploads/1/7/9/5/17957627/6246datasheet.pdf>
- [Tokarski 16] T. Tokarski, G. Cios, A. Kula, P. Bała, High quality transmission Kikuchi diffraction analysis of deformed alloys - Case study, *Mater. Character.* 121 (2016) 231–236.
- [Tomé 84] C. Tomé, G.R. Canova, U.F. Kocks, N. Christodoulou, J.J. Jonas. The relation between macroscopic and microscopic strain hardening in fcc polycrystals. *Acta Metall.* 32, 1984, 1637.
- [Trimby 12] Trimby, Patrick W. "Orientation mapping of nanostructured materials using transmission Kikuchi diffraction in the scanning electron microscope." *Ultramicroscopy* 120 (2012): 16-24.
- [UCSB] <http://www.mrl.ucsb.edu/centralfacilities/x-ray/basics>
- [Van 14] Van Phan T. Grain scale simulation of local deformation behavior[J]. *Asia Pacific Journal on Computational Engineering*, 2014, 1(1): 1-24.
- [Van Acker 93] Van Acker, K., et al. Internal stress measurement on CVD diamond coatings by X-ray diffraction and Raman spectroscopy. in *MRS Proceedings*. 1993. Cambridge Univ Press.
- [Venables 73] J. A. Venables and C. J Harland, *Phil. Mag.*, 27 (1973) 1193.

- [Verhaeghe 96] B. Verhaeghe. Etude microstructurale des modes de déformation et de rupture d'un acier austéno-ferritique vieilli thermiquement. Rapport de thèse de doctorat "Sciences et Génie des Matériaux". Institut National Polytechnique de Grenoble, 4 avril 1996.
- [Verhaeghe 97] Verhaeghe, Bénédicte, et al. "Damage and rupture mechanisms in an austenoferritic duplex steel." *Acta materialia* 45.5 (1997): 1811-1819.
- [Voigt 10] Voigt, W. *Lehrbuch der Kristallphysik*. Leipzig: Teubner. 1910.
- [Voigt 28] *Lehrbuch der Kristallphysik*, Leipzig, BG Teubner Verlag, 1928.
- [Wang 07] Wang, Xiufang, et al. "Nanoindentation Characterization of Mechanical Properties of Ferrite and Austenite in Duplex Stainless Steel." (2007).
- [Wang 10] L. Wang, P. Eisenlohr, Y. Yang, T. Bieler, and M. Crimp: Nucleation of paired twins at grain boundaries in titanium. *Scr. Mater.* 63, 827 (2010).
- [Welzel 03] Welzel, U. & Mittemeijer, E. J. (2003). *J. Appl. Phys.* 93, 9001–9011.
- [Welzel 05] Welzel U., Ligot J., Lamparter P., Vermeulen A.C., Mottemeijer E.J., Stress analysis of polycrystalline thin film and surface regions by X-ray diffraction, *J. Appl. Cryst.*, vol.38, p. 1, 2005.
- [Williams 80] Williams JC, Luetjering G. In: Kimura H, Izumi O, editors. *Titanium 80*, Kyoto, Japan, 1980. p. 671.
- [Willis 09] Willis, Bertram Terence Martin, and Colin J. Carlile. *Experimental neutron scattering*. Vol. 30. Oxford: Oxford University Press, 2009.
- [Winkelmann 07] Winkelmann A, Trager-Cowan C, Sweeney F, et al. Many-beam dynamical simulation of electron backscatter diffraction patterns[J]. *Ultramicroscopy*, 2007, 107(4): 414-421.
- [Winplotr] <http://www.cdifx.univ-rennes1.fr/winplotr/winplotr.htm>
- [Wright 06] Wright, Stuart I., and Matthew M. Nowell. "EBSD image quality mapping." *Microscopy and Microanalysis* 12.01 (2006): 72-84.
- [Wroński 07] Wroński, S., Baczmański, A., Dakhloui, R., Braham, C., Wierzbowski, K., Oliver, E.C., 2007. Determination of Stress Field in Textured Duplex Steel Using TOF Neutron Diffraction Method. *Acta Mater.* 55, 6219–6233.
- [Wroński 12] Wroński S, Tarasiuk J, Bacroix B, et al. Investigation of plastic deformation heterogeneities in duplex steel by EBSD[J]. *Materials Characterization*, 2012, 73: 52-60.
- [Yoo 81] Yoo H. M.: *Met. Trans.* 12A, (1981) p. 409
- [Young 93] Young, Donald S., Bruce S. Sachais, and Leigh C. Jefferies. "The rietveld method." (1993).
- [Zaefferer 03] Zaefferer S. A study of active deformation systems in titanium alloys: dependence on alloy composition and correlation with deformation texture[J]. *Materials Science and Engineering: A*, 2003, 344(1): 20-30.
- [Zambaldi 12] C. Zambaldi, Y. Yang, T. R. Bieler, D. Raabe, *J. Mater. Res.*, 27 (2012) 356-367

[Zattarin 00] P. Zattarin, A. Baczyński, P. Lipiński, K. Wierzbowski. Modified Self-Consistent Model for Time Independent Plasticity of Polycrystalline Material. Archives of Metallurgy, 2000, 45, 163-184.

[Zecevic 15] Zecevic, Milovan, et al. "An elasto-plastic self-consistent model with hardening based on dislocation density, twinning and de-twinning: application to strain path changes in HCP metals." Materials Science and Engineering: A 638 (2015): 262-274.

[Zevin 12] Zevin, Lev S., and Giora Kimmel. Quantitative X-ray diffractometry. Springer Science & Business Media, 2012.

[Zhrebtsov 10] S. Zhrebtsov, G. Salishchev, S.L. Semiatin, Phil. Mag. Lett. 90 (12) (2010) 903–914.

Yuchen ZHAO

Doctorat : Matériaux, Mécanique, Optique et Nanotechnologie

Année 2017

Etude multi-échelle du comportement mécanique de matériaux biphasés lors de grandes déformations et de l'endommagement ductile

Cette thèse est dédiée à l'étude du comportement élasto-plastique des matériaux polycristallins multiphasés ainsi que de l'endommagement ductile à différentes échelles. Les hétérogénéités microscopiques ont une influence importante sur la réponse mécanique macroscopique des matériaux. Et l'endommagement ductile est encore difficile à mesurer aux échelles fines.

Cette thèse traite des problématiques suivantes :

1. L'évolution du comportement des phases et des grains sous chargements jusqu'à la rupture.
2. L'influence de l'hétérogénéité intrinsèque au niveau micro, sur le comportement macroscopique des matériaux biphasés.
3. L'influence de la striction et de l'endommagement sur le comportement de familles d'orientation de grains.
4. La mesure indirecte de l'endommagement échelle fine par diffraction.

Afin d'enquêter sur ces questions, l'acier duplex et le titane biphasé sont testés. La diffraction est utilisée pour effectuer des mesures in situ non-destructive au cours d'essais de traction et jusqu'à la rupture. Des simulations sont réalisées grâce à un modèle auto-cohérent élasto-plastique, dans lequel est introduite la modélisation de l'endommagement ductile. Les données expérimentales aux différentes échelles y sont comparées. En outre, des tests de nano-indentation et observation micrographiques sont effectués pour observer l'évolution spatiale des propriétés mécaniques des phases le long de la striction et jusqu'à la surface de rupture.

Mots clés : polycristaux - analyse multiéchelle - elastoplasticité - endommagement, mécanique de l' (milieux continus) - diffraction - simulation par ordinateur

Multi-scale Study of Mechanical Behaviour of Two-phase Materials during Large Deformation and Ductile Damage

The thesis is dedicated to the study of elasto-plastic behavior of multiphase polycrystalline materials and ductile damage at different scales. The microscopic heterogeneities have important influence on the macroscopic mechanical behavior of materials. Ductile damage is still difficult to measure at small scales.

The following issues are the main topic involved in this thesis:

1. The evolution of mechanical behavior in phases and groups of grains, under external load until fracture.
2. The influence of intrinsic heterogeneity on the macroscopic behavior of two-phase materials.
3. The influence of necking and ductile damage, on the behavior of grains with different orientation families.
4. The indirect measurement of ductile damage at small scales by diffraction.

To answer these questions, duplex steels and two-phase titanium are tested. The diffraction method is used to perform in situ measurements during tensile test until fracture. Predictions are carried out by an elasto-plastic self-consistent model, in which ductile damage have been integrated. Experimental data on different scales are compared with these predictions. In addition, nano-indentation tests are carried out to study the evolution of phases' mechanical properties along the neck until fracture edge. Microscopic images were also taken in order to observe the fracture surfaces of studied materials.

Keywords: polycrystals - multi-scale analysis - elastoplasticity - continuum damage mechanics - diffraction - computer simulation.

Thèse réalisée en partenariat entre :



Ecole Doctorale "Sciences et Technologies"